UNIVERSITÀ DEGLI STUDI DI PADOVA
DIPARTIMENTO DI FISICA E ASTRONOMIA
SCUOLA DI DOTTORATO DI RICERCA IN ASTRONOMIA
XXXVI CICLO

Star Formation in Young Stellar Clumps of Ram-Pressure Stripped Galaxies as seen by *HST*

Coordinator: Prof. Giovanni Carraro

Supervisor: Dr. Bianca M. Poggianti

Co-supervisor: Dr. Marco Gullieuszik

Co-supervisor: Dr. Alessia Moretti

Ph.D. student: Eric Giunchi

Febraury 29, 2024

Contents

List of Figures

List of Tables

Abstract

Star-forming Hα- and UV-emitting clumps are found embedded in the gaseous tails of galaxies undergoing intense ram-pressure stripping in galaxy clusters, so-called jellyfish galaxies. These clumps offer a unique opportunity to study star formation under extreme conditions, in the absence of an underlying disk and embedded within the hot intracluster medium. Yet, a comprehensive, high-spatial resolution study of these systems is missing. We obtained UVIS/*HST* data to observe with a resolution of ~ 140 pc the first statistical sample of clumps in the tails and disks of six jellyfish galaxies from the GASP survey; we used a combination of broad-band (UV to I) filters and a narrow-band Hα filter.

After the data are reduced minimizing residual cosmic rays, I detect and select Hα- and UV-bright clumps, tracing star formation on different timescales, and optical star-forming complexes in this sample of galaxies. I consider clumps located in galaxy disks, in the stripped tails and those formed in stripped gas but still close to the disk, called extraplanar. I detect 2406 Hα-selected clumps (1708 in disks, 375 in extraplanar regions, and 323 in tails), 3745 UV-selected clumps (2021 disk clumps, 825 extraplanar clumps and 899 tail clumps) and 424 optical star-forming complexes (all in the tails). Only $\sim 15\%$ of star-forming clumps are spatially resolved, meaning that most are smaller than ~ 140 pc. I study the luminosity and size distribution functions (LDFs and SDFs, respectively) and the luminosity-size relation. The average LDF slope is 1.79 ± 0.09, while the average SDF slope is 3.1 ± 0.5, suggesting that also in this peculiar environment clumps form through the turbulent scale-free collapse of the interstellar medium, as in main-sequence galaxies. All the clumps, whether they are in the disks or in the tails, have an enhanced Hα luminosity at a given size, compared to the clumps in main-sequence galaxies. Indeed, their Hα luminosity is closer to that of clumps in starburst galaxies, indicating that ram pressure is able to enhance this quantity, most likely as a consequence of gas compression. No striking differences are found among disk and tail clumps, suggesting that the different environments in which they are embedded play a minor role in influencing the star formation.

After that, I characterize the morphological properties of the optical complexes in the tails, by connecting them with those of the Hα and UV clumps that they contain. I find that more than half of the complexes contain no Hα clumps, while most of them host at least one UV clump. The clump number and size increase with the complex size, while the median complex filling factor is larger for UV clumps (0.27) than for Hα clumps (0.10) and does not correlate with almost any morphological property. This suggests that the

clump number and size grow with the complex keeping the filling factor constant. When studying the position of the clumps inside their complexes, Hα clumps, and UV clumps to a lesser extent, show a displacement from the complex center of $0.1 - 1$ kpc and, in $\sim 60\%$ of the cases, they are displaced away from the galactic disk. This is in accordance with the fireball configuration, already observed in the tails of stripped galaxies. Furthermore, the filling factor and the clump radius increase with the distance from the galactic disk, suggesting that the reciprocal displacement of the different stellar generations increases as a consequence of the velocity gradient induced by ram pressure.

Finally, I parameterize the clump mass completeness and the possible discrepancy between the intrinsic and observed mass by performing a large set of clump mock observations, generated by modelling the real clumps and spanning a wide range of masses. These two effects are taken into account when fitting the tail clumps mass function to a single power law in a Bayesian framework. I obtain slopes equal to 2.07 ± 0.10 and 2.28 ± 0.08 for Hα and UV tail clumps, respectively, which further confirm the fact that even the gas undergoing ram-pressure stripping and embedded in the intracluster medium collapses following a scale-free cascade driven by turbulence.

To conclude, the high-resolution statistical sample of clumps that I obtain helped answering some of the open questions about the effects of ram-pressure stripping on the star-formation mechanism, showing that this process highly enhances the star-forming clumps Hα luminosity at a given size and affects their morphology, yet not affecting their formation channel, which is the same observed and theorized for clumps in main-sequence galaxies.

Riassunto della Tesi

Clump brillanti in Hα e UV, e in piena formazione stellare, sono già stati osservati nelle code di gas delle galassie di ammasso in cui tale gas viene rimosso fal disco, a causa della pressione d'ariete esercitata dal caldo mezzo intra-ammasso (le cosiddette galassie medusa). Questi clump offrono l'opportunità unica di studiare la formazione stellare in condizioni estreme, in assenza di un disco stellare e immersi nel mezzo intra-ammasso. Tuttavia, uno studio di questi sistemi su grande scala e ad alta risoluzione spaziale non è stato ancora compiuto. Abbiamo così ottenuto dati UVIS/*HST* per osservare il primo campione statistico di clump stellari con una risoluzione di $\sim$ 140 pc, usando una combinazione di filtri a banda larga (da UV a I) e un filtro Hα a banda stretta. Dopo aver effettuato la riduzione dei dati minimizzando i raggi cosmici residui, ho individuato e selezionato in questo campione di galassie sia clump brillanti in Hα e UV, in modo da tracciare la formazione stellare su diverse scale temporali, che complessi stellari in banda ottica. Ho considerato clump localizzati nei dischi galattici, nelle code gassose e quelli formati nel gas rimosso dal disco ma ancora vicini al disco stesso, chiamati extraplanari. Ho così individuato 2406 clump Hα (1708 nei dischi, 375 nelle regioni extraplanari e 323 nelle code), 3745 clump UV (2021 clump di disco, 825 extraplanari e 899 di coda) e 424 complessi stellari in banda ottica (tutti quanti nelle code). Solo il $\sim$ 15% di questi clump è spazialmente risolto, il che comporta che la maggior parte di essi sono più piccoli di $\sim$ 140 pc. Ho poi studiato le funzioni di distribuzione di luminosità e dimensione dei clump (LDF e SDF, rispettivamente), e la relazione luminosità-dimensione. Il coefficiente angolare medio delle LDF è 1.79 ± 0.09, mentre per le SDF è 3.1 ± 0.5, il che suggerisce che anche in ambienti peculiari i clump si formino attraverso un collasso turbulento del gas, privo di una qualunque lunghezza di scala, come accade nelle galassie di sequenza principale. Inoltre tutti i clump, siano essi nei dischi o nelle code, mostrano un aumento della luminosità Hα a una data dimensione, se comparati ai clump di galassie di sequenza principale. Infatti, la loro luminosità Hα è più vicina a quella dei clump delle galassie starburst, indicando che la pressione d'ariete è capace di intensificare questa quantità, molto probabilmente come conseguenza della compressione del gas. Nessuna differenza degna di nota è stata invece osservata tra clump di disco e coda, il che suggerisce come i diversi ambienti in cui questi clump sono immersi giochino un ruolo minore nell'influenzare la formazione stellare.

Successivamente, ho caratterizzato le proprietà morfologiche dei complessi ottici nelle code, mettendole in relazione con quelle dei clump Hα e UV che essi contengono. Ne risulta

che più di metà dei complessi non contiene alcun clump Hα, mentre la maggior parte di essi ne ospita almeno uno UV. Il numero di clump e la loro dimensione crescono con le dimensioni del complesso, mentre la mediana del filling factor nei complessi è più grande per i clump UV (0.27) che per quelli Hα (0.10), e non correla con praticamente nessuna proprietà morfologica. Ciò suggerisce che il numero e le dimensioni dei clump crescano insieme ai complessi in modo tale da mantenere costante il filling factor. Nello studiare la posizione dei clump dentro ai loro complessi, i centri dei clump Hα, e anche di quelli UV in misura minore, sono spostati rispetto al centro del complesso, di circa $0.1 - 1$ kpc, e nel $\sim 60\%$ dei casi, tale spostamento è diretto lontano dal disco galattico. Ciò è in accordo con la configurazione fireball, già osservata in alcune code di galassie medusa. Per di più, il filling factor e il raggio dei clump crescono con la loro distanza dal disco galattico, suggerendo che lo spostamento reciproco tra le diverse generazioni stellari cresca come conseguenza del gradiente di velocità indotto dalla pressione d'ariete.

Infine, ho parametrizzato la completezza in massa dei clump e la possibile discrepanza tra la loro massa intrinseca e quella stimata dalle osservazioni, effettuando una vasta serie di osservazioni simulate di clump, generate modellando i clump reali e coprendo un ampio intervallo di masse. Questi due effetti sono presi in considerazione per effettuare un fit Bayesiano della funzione di massa dei clump di coda a una funzione a legge di potenza. I coeffiencienti angolari da me ottenuti sono 2.07 ± 0.10 e 2.28 ± 0.08 per clump Hα e UV di coda, rispettivamente, che confermano ulteriormente come il gas rimosso dalla pressione d'ariete e immerso nel mezzo intra-ammasso collassi in modo turbolento e del tutto privo di una qualunque lunghezza di scala.

In conclusione, il campione statistico di clump ad alta risoluzione spaziale che ho ottenuto ha aiutato a rispondere ad alcune delle domande ancora aperte circa gli effetti della pressione d'ariete sul meccanismo di formazione stellare, mostrando come questo processo intensifichi notevolmente la luminosità Hα dei clump a una data dimensione e ne modifichi la morfologia, tuttavia senza cambiarne il canale di formazione, che rimane lo stesso osservato e teorizzato per i clump nelle galassie di sequenza principale.

Chapter 1

Introduction

The aim of this work is to understand if and how ram-pressure stripping affects the formation and the evolution of young stellar clumps in cluster galaxies. When a galaxy is accreted by a galaxy cluster, it experiences for the first time the ram pressure exerted by the intracluster medium (ICM) and its interstellar medium (ISM) gets compressed. If the ram pressure is strong enough the ISM gets stripped out of the galactic disk and pushed in the hot and dense ICM. Understanding whether this process and peculiar environment have effects on the properties of the stellar clumps is fundamental to understand which processes drive star formation.

This Chapter gives an overview of the scientific framework in which this work is set. The Chapter is organized as follows: I begin describing some basic properties of stars (Section 1.1) and galaxies (Section 1.2); Section 1.3 introduces galaxy clusters and groups, the environments in which the taget galaxies of this work are located, with a specific focus on the physics of ram-pressure stripping (Section 1.3.2) and on the GASP survey (Section 1.3.3), from which the galaxies of our sample are selected. In Section 1.4 I introduce the main properties of star-forming clumps, especially referring to the aspects that I have analyzed throughout my work, like their luminosity, size and distribution functions (Section 1.4.1) and the luminosity-size relation (Section 1.4.2); finally, in Section 1.5 I describe the observed and predicted peculiar properties of star-forming clumps in galaxies undergoing ram-pressure stripping.

1.1. *Spectra and lifetimes of stars as a function of stellar mass*

Stars dominate the emission of the vast majority of galaxies at optical wavelengths. To derive the galaxy properties it is therefore fundamental the knowledge of the stellar main properties. Stars are self-gravitating bodies of gas in which the internal temperature and density are such that thermonuclear reactions are triggered in their internal regions and able to sustain the pressure of the gas against the gravitational attraction, preventing the collapse of the structure. For most of their life (during the so-called Main-Sequence phase) stars produce energy by converting hydrogen into helium. Typically, the mass and radius of

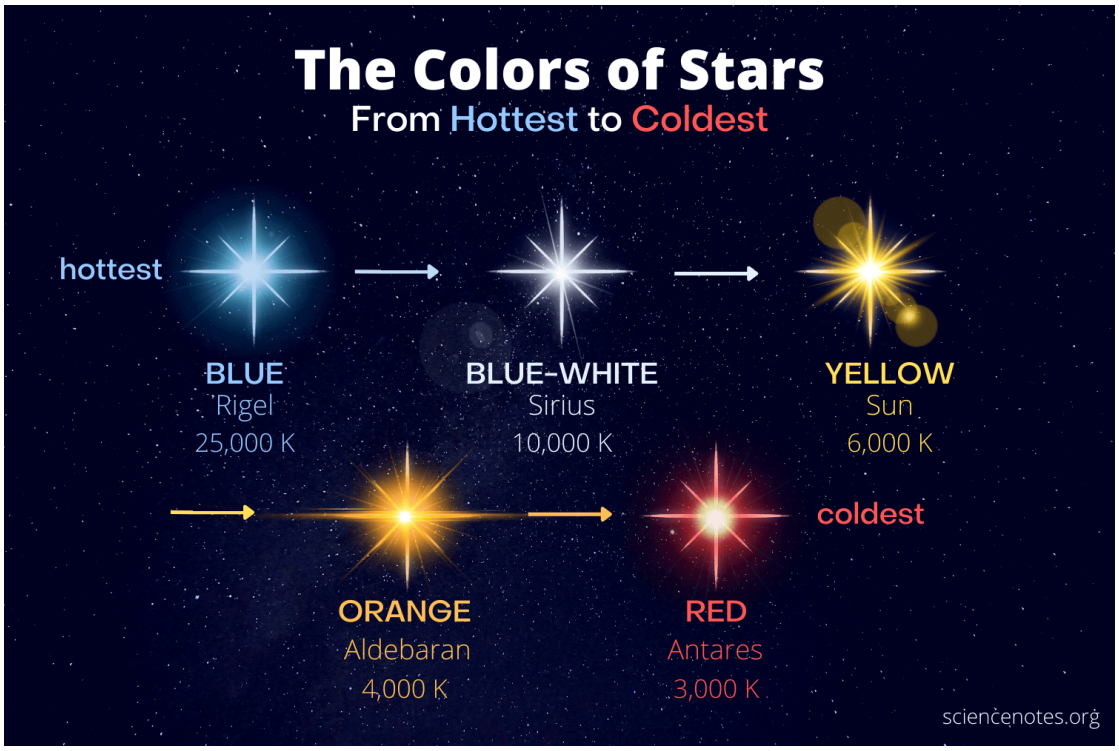

Figure 1.1: The colors of stars from the hottest ones (blue) to the coldest ones (red). Credits to A. Helmenstine `https://sciencenotes.org/the-colors-of-the-stars-from-hottest-to-coldest/`.

stars are given relatively to those of the Sun, which are $M_\odot = 2 \times 10^{33}$ g and $R_\odot = 7 \times 10^{10}$ cm.

The Morgan–Keenan (MK) system is the most commonly used stellar classification and assigns to stars a spectral class (a sequence of letters: O, B, A, F, G, K and M) according to the properties of their spectrum, and a luminosity class (I, II, III, IV, V). The reason for which this classification became widely used is that it is closely related to the intrinsic physical properties of stars, even starting from pure observable quantities (Cox, Becker & Pesnell, 2000). The shape of the spectrum and therefore the spectral classes are strongly related to the stellar surface temperature (at the photosphere). This happens because stellar spectra can be well described by a Black Body curve, featuring also absorption lines due to hydrogen, helium and heavier elements (metals) in the photosphere. Therefore, depending on the stellar surface temperature, the spectrum can peak at blue wavelengths ($\lambda \lesssim 3000\,\text{Å}$) for hot O- and B-class stars ($\gtrsim 12000\,\text{K}$) or at redder wavelengths for cold M-class stars ($2000 - 3700\,\text{K}$). A cartoon summary of this correlation is shown in Figure 1.1. Throughout this work, I am going to call *blue* all the stars having spectra peaking at wavelengths shorter than 3000 Å, i.e. OB stars. On the other hand, the luminosity class is related to the surface gravity, which varies depending on the evolutionary stage of the star (from I for supergiant stars, to V for dwarf stars). For example, according to this classification the Sun is a GV star, with a surface temperature of 5777 K.

Now, both the surface temperature and the evolutionary path of a star are mainly determined by its mass (Stroemgren, 1933; Iben, 1965; Iben & Renzini, 1984; Humphreys & Davidson, 1979; Gamow, 1938; Mo, van den Bosch & White, 2010). When almost all the

hydrogen contained in the stellar core is converted into helium, the star undergoes a series of phases which includes the production and consumption of heavier elements. The final stage is the death of the star, which typically consists on the release of the most external layers leaving a compact object as a remnant. For low-mass stars ($M_* \lesssim 8\,\mathrm{M}_\odot$) the release will be slow while explosive for more massive stars, leaving a white dwarf as a remnant in the first case, a neutron star or a black hole in the second one. Furthermore, the surface temperature T_e of a star roughly scales with its mass as $T_e \propto M_*^{1/2}$. Therefore massive stars have also a hotter surface temperature than low-mass stars, and their spectra peak at bluer wavelengths. Finally, stellar evolution models predict that the lifetime of a star scales with mass roughly as M_*^{-3}, implying that massive and bright stars live shorter than low-mass stars. For example, a G-class star like our Sun has a lifetime of about 10 Gyr, while O-class stars ($M_* \gtrsim 10\,\mathrm{M}_\odot$) live less than 10 Myr and B-class stars ($3\,\mathrm{M}_\odot \lesssim M_* \lesssim 10\,\mathrm{M}_\odot$) between 10 and 200 Myr.

The observed spectrum of a galaxy is given by the integrated light of all the stars underlying the observed region of the sky, being it a relevant portion of the galaxy (as in the case of fiber/MOS spectroscopy of distant galaxies) or a more spatially resolved region (as in the case of IFU spectra of more nearby objects). In order to correctly interpret the galaxy spectra it is therefore fundamental to be able to assess the stellar properties. For what stated above, one of the main ingredients is the mass distribution of the stars when they started to shine, i.e. their Initial Mass Function (IMF, Salpeter 1955; Kroupa 2001; Chabrier 2003), which specifies the relative number of stars in a group of coeval stars as function of their initial mass. If this is mostly sufficient to predict the observed properties of simple stellar populations, in the case of a galaxy many different populations coexist and such properties depend on the star formation history (SFH) of the galaxy. This encodes the knowledge of the IMF, but also of the Star Formation Rate (SFR) at each time in the history of the galaxy. Therefore the overall galactic spectrum depends on the age distribution of stars, i.e. the SFH. A passive galaxy, with an almost null current star formation rate (SFR) is expected to be red, since blue massive stars already completed their evolutionary paths. On the other hand, systems with ongoing star formation are still populated by young massive OB stars, which are expected to produce a strong blue continuum.

As previously said, the continuum emission of O stars (with a surface temperature larger than $\sim 30000\,\mathrm{K}$) peaks in the high-energy regime of their spectra. Therefore a large fraction of the photons emitted by this class of stars is capable of ionizing the surrounding gaseous medium (the condition is $\lambda_{\mathrm{photon}} < 912\,\text{Å}$). The classic modelling of this process is the so-called "Strömgren sphere" (Strömgren, 1939; Osterbrock, 1989). A study of the physics of Strömgren spheres is beyond the scope of this work, and therefore here it is just briefly summarized.

The ionizing radiation emitted by the O star gets absorbed by the gaseous medium in which it is embedded. As the medium is ionized, it emits continuum free-free radiation, with the addition of recombination lines of the hydrogen Balmer series and helium and forbidden lines from the metals that pollute the interstellar medium (like oxygen, nitrogen and neon). In particular, this work is going to focus on the Hα line of the Balmer series as a tracer of these gas regions ionized by O stars. The model of the Strömgren sphere

predicts the Hα luminosity $L_{\mathrm{H}\alpha}$ and the size R of the ionized region to follow a correlation of the form $L_{\mathrm{H}\alpha} \propto R^3$, more specifically

$$L_{\mathrm{H}\alpha} = \frac{4\pi}{3} \frac{N_{\mathrm{H}}^2 \alpha_{\mathrm{B}} hc}{\lambda_{\mathrm{H}\alpha}} R^3, \tag{1.1}$$

where N_{H} is the ionized hydrogen number density and α_{B} is the Case-B recombination coefficient assuming a hydrogen temperature $T_{\mathrm{H\,II}} = 10^4 K$ (Osterbrock, 1989).

One consequence of this process is that regions populated by stars younger than 10 Myr are expected to be particularly bright in Hα, too, in addition to be characterized by a strong blue continuum. After this interval of time, OB stars die and the most massive stars of the populations are A stars (with a lifetime of $\sim$ 200 Myr) which, yet being quite bright in the blue part of the optical electromagnetic spectrum, do not emit ionizing photons, with the consequent fading of the Hα emission line.

1.2. *Properties of galaxies in the local Universe*

Stars in the Universe are typically are assembled into self-gravitating systems called galaxies, which are the building blocks of the Universe (Hubble 1926, 1936; Kennicutt 1998; Salaris & Cassisi 2005; Mo, van den Bosch & White 2010; Kormendy & Bender 2012; see also Conselice et al. 2004 and references therein). Their size is typically of the order of tens-to-hundreds of kpc (1 pc is the distance at which the semi-major axis of Earth orbit subtends an angle of 1 arcsecond; this corresponds to $\sim$ 326 light years, where one light year is the distance travelled by light in one year, i.e. 9.4607×10^{17} cm). Galaxies can be divided in three main morphological types: spirals, ellipticals and irregulars. In addition to those, spirals and ellipticals are bridged by the so-called lenticular galaxies. An illustration of all the different galaxy morphologies is shown in Figure 1.2, disposed according to the so-called Hubble fork (Hubble, 1936; Kormendy & Bender, 2012).

Elliptical galaxies constitute the so called *early-type* galaxies. They account for $\sim$ 10% of the bright galaxies, have an ellipsoidal shape of varying axial ratios and a mass range between $\sim 10^5\,\mathrm{M}_\odot$ and $\sim 10^{12}\,\mathrm{M}_\odot$. They show no sign of complex sub-structures nor of dust and young stars, therefore their morphology is typically round and smooth and their spectra peaks at red wavelengths (indeed they are named *quiescent* galaxies). The kinematics of their stars is typically dominated by random motions. As shown in Figure 1.2, ellipticals are named as "En", where "n" is the major-to-minor axes ratio of the galaxy.

Spiral galaxies (also called *late-type* galaxies) constitute more than half of the bright galaxies in the Local Universe (within $\sim$ 100 Mpc of the Sun). They are generally composed by a disk formed by both stars and gas (the so-called interstellar medium, ISM) and containing luminous spiral arms, a bright bulge (the central nucleus, looking very similar to a small elliptical galaxy), and a faint spherical halo. Spirals have typical masses of the order of $10^{9-11}\,\mathrm{M}_\odot$ and, as shown in Figure 1.2, are divided into barred and normal spirals, depending on whether the spiral arms start from a bar emerging from the central regions or directly from the bulge. They can show different bulge-to-disk luminosity ratio. These two properties determine the acronym of the galaxy, which consists of either two or three letters: "Sx" for unbarred galaxies and "SBx" for barred galaxies, where "x" is a letter,

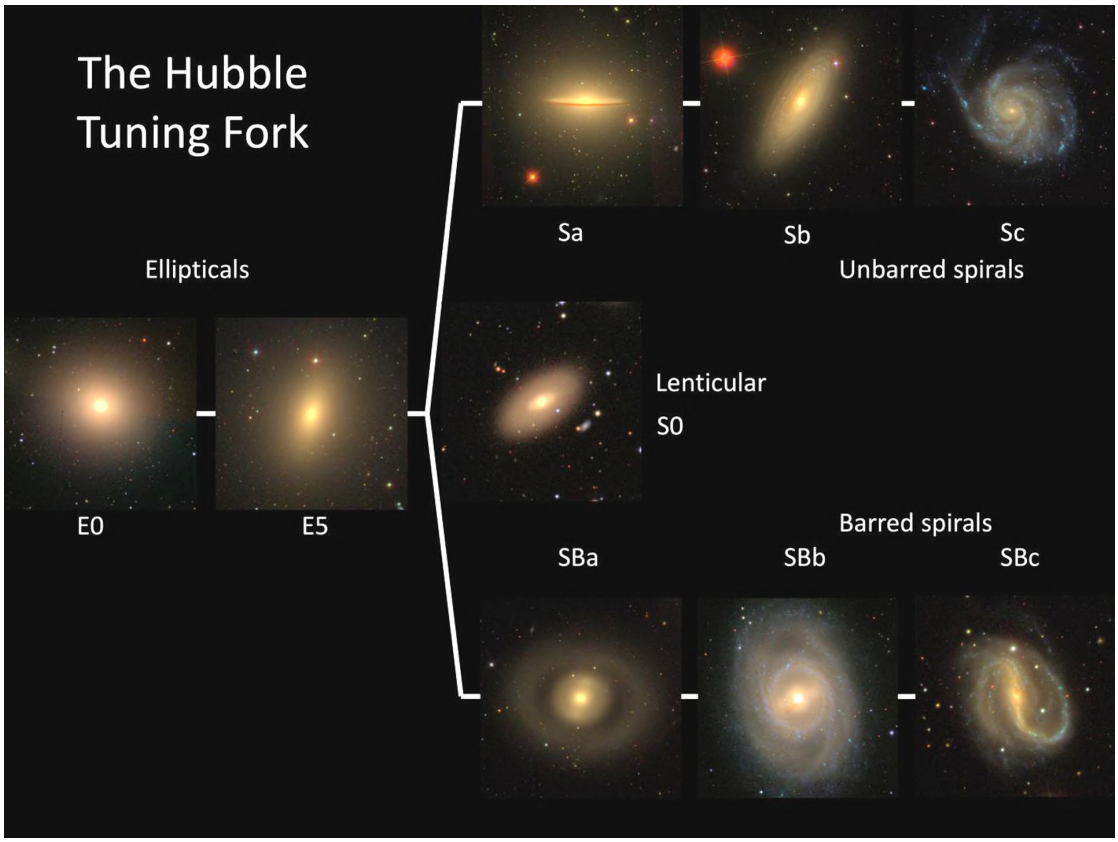

Figure 1.2: A summary of the so-called Hubble fork (Hubble, 1936; Kormendy & Bender, 2012) with images of galaxies from the Sloan Digital Sky Survey, showing all the main galactic morphological types and how they can be connected by common features. Image credit: Karen Masters, Sloan Digital Sky Survey `https://www.sci.news/astronomy/hubble-tuning-fork-07280.html`.

either a, b or c, increasing for a decreasing bulge-to-disk luminosity ratio. Most dust and young stars are contained in the disk, whose spectra therefore show strong blue continuum (reason for which they are also named *star-forming* galaxies), whereas the bulge and halo are populated by older stars. Stars in spiral galaxies show ordered rotational motion, especially in the disk.

These two broad categories of galaxies are bridged morphologically by the so-called lenticular galaxies (S0), which make up about 20% of the galaxies. These galaxies show a smooth light distribution like elongated ellipticals, without bars and spiral structure, but are characterized by a strong flattening and a disky shape like spiral galaxies, yet being dominated by the bulge. The last broad group of galaxies are the irregulars, that show no regular structure, and no rotational symmetry. They typically present young stars and are therefore characterized by a blue spectrum and bright Hα-line emission, even if less massive than most of the other star-forming galaxies.

The variety of galactic morphologies in the Local Universe brings up the question about how galaxies should form and evolve to reach these stages. Galaxies are not isolated systems: the merging of active disk galaxies can lead to the formation of passive elliptical galaxies, the accretion of external gas can let the galaxy sustain star formation for a longer period of time just like the ejection of the ISM outside the galactic potential well (either because of

Active Galactic Nuclei activity or bursty and violent star-formation episodes) can abruptly quench it. In addition to that, high-z observations and SFH studies of ellipticals suggest that high-mass galaxies have short and bursty SFHs. From these results one can conclude that most of the stellar mass of elliptical galaxies built up on relatively short timescales, contrary to star-forming galaxies for which the mass assembly is thought to be less intense but rather constant with time. This is in marked contrast to naive expectations based on the hierarchical assembly of dark matter haloes in cold dark matter (CDM) cosmology models (White & Frenk, 1991; Kauffmann, White & Guiderdoni, 1993; Cole et al., 2000; De Lucia & Blaizot, 2007) and compatible with the so-called *downsizing* scenario for star formation (Faber et al., 1995; Cowie et al., 1996; De Lucia et al., 2006).

Looking at these processes, it becomes clear that the environment in which these galaxies are located can highly affect their evolutionary paths: as we will see in Section 1.3, a galaxy embedded in a hot and dense medium, with a high local density of galaxies, will experience much more external interactions than an isolated galaxy. But before trying to understand how galaxy evolution can be affected, we need to know how star formation proceeds inside the galaxy itself.

1.2.1. *Star formation in galaxies and SFR-stellar mass relation*

The formation of new stars in galaxies is thought to be regulated by the so-called *baryon cycle* (Anglés-Alcázar et al., 2017; Christensen et al., 2016; Davé, Finlator & Oppenheimer, 2012; Krumholz & Dekel, 2012; Rasera & Teyssier, 2006; Bouché et al., 2010; Dutton, van den Bosch & Dekel, 2010), which is here briefly summarized and shown in the cartoon of Figure 1.3.

What is thought to happen is that the warm neutral medium (WNM) in the ISM, mainly composed by hydrogen and at a temperature of $6000 - 10000$ K (Ferrière, 2001), cools down to the cold phase with a temperature of ~ 100 K. This happens not only thanks to the 21 cm-emission line of the hydrogen, but also and mostly thanks to the many emission lines due to recombination of which the metals polluting the ISM are responsible. The cold neutral medium (CNM) can subsequently keep cooling down to the molecular phase, with a temperature of a few tens of kelvin, which is typically characterized by a clumpy and clustered morphology, with ~ 80 pc-scale molecular clouds (Ferrière, 2001). The molecules and the dust of which these clouds are formed can protect the innermost regions by the radiation of external sources, especially the ionizing emission of O stars, which may prevent the further cooling of the gas. The density and temperature of these regions (the so-called cores and clumps) are such that the gas pressure is unable to compensate the self-gravity. In particular, this happens when the cloud reaches a certain critical mass, which is known in literature as the *Jeans mass*, after the author of the first work focused on this idea (Jeans, 1902), and is typically of the order of $\sim 10^{5-6}\,\mathrm{M}_{\odot}$. The cloud therefore collapses and reaches the values of density and temperature needed to trigger thermonuclear reactions and the formation of stars, in such a way that from a cloud an entire population of stars is formed following the IMF (Section 1.1).

Among the newly formed stars, some of those are going to be blue and massive (Section 1.1), capable of heating the surrounding medium and prevent the further collapse of the cloud by means of ionizing radiation and stellar winds. In addition to that, the violent and

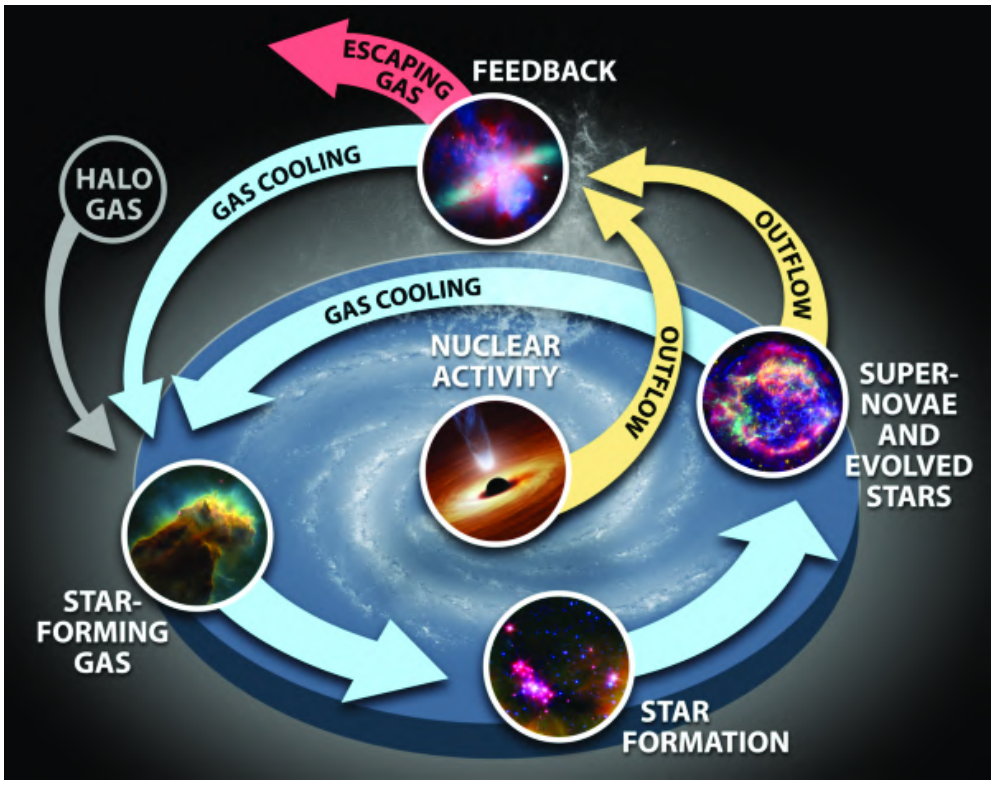

Figure 1.3: A cartoon summarizing those that thought to be the main steps of the baryon cycle, summarized in Section 1.2.1. Credits of the plot to Leisawitz et al. (2019).

explosive death of these massive stars, the supernovae, further heats and shocks the gas. This is the so-called *stellar feedback* and in some cases can result also in the ejection of the surrounding gas by means of outflows. Such gas, now heated and even ionized by the stellar feedback, can now start cooling down again and re-start the baryon cycle.

Many more factors are at play: stellar feedback implies the chemical enrichment of the ISM, as a consequence of the mixing of the processed gas expelled by dead stars with the surrounding medium (however, some of the gas remains locked in white dwarfs, neutron stars and black holes). Furthermore, cold gas can sink to the central regions of galaxies, where the gravitational interactions with the supermassive black hole hosted in the nucleus of the galaxy can trigger a phase of Active Galactic Nuclei, which heats and expels the ISM similarly to stellar feedback, but ever more efficiently. Finally, gas accretion from out of the galactic halo can replenish the gas consumed in star formation and sustain the process.

All these phenomena, combined together, are thought to create a self-regulated stationary process in which, for example, strong bursts of star formation are naturally followed by strong phases of stellar feedback and, viceversa, phases with a lower star formation rate let the gas cool down in an environment with a weaker stellar feedback.

The galactic stellar mass seems to be the main parameter driving the regulation of this complex mechanism. Many studies have demonstrated that there is a correlation between the SFR and the stellar mass M_* of star-forming galaxies, with a slope very close to 1, a bending at $M_* \gtrsim 10^{11}\,\mathrm{M}_\odot$ and a relatively small intrinsic scatter of $0.2 - 0.3$ dex (Daddi et al., 2007; Brinchmann et al., 2004; Speagle et al., 2014; Elbaz et al., 2007; Noeske et al.,

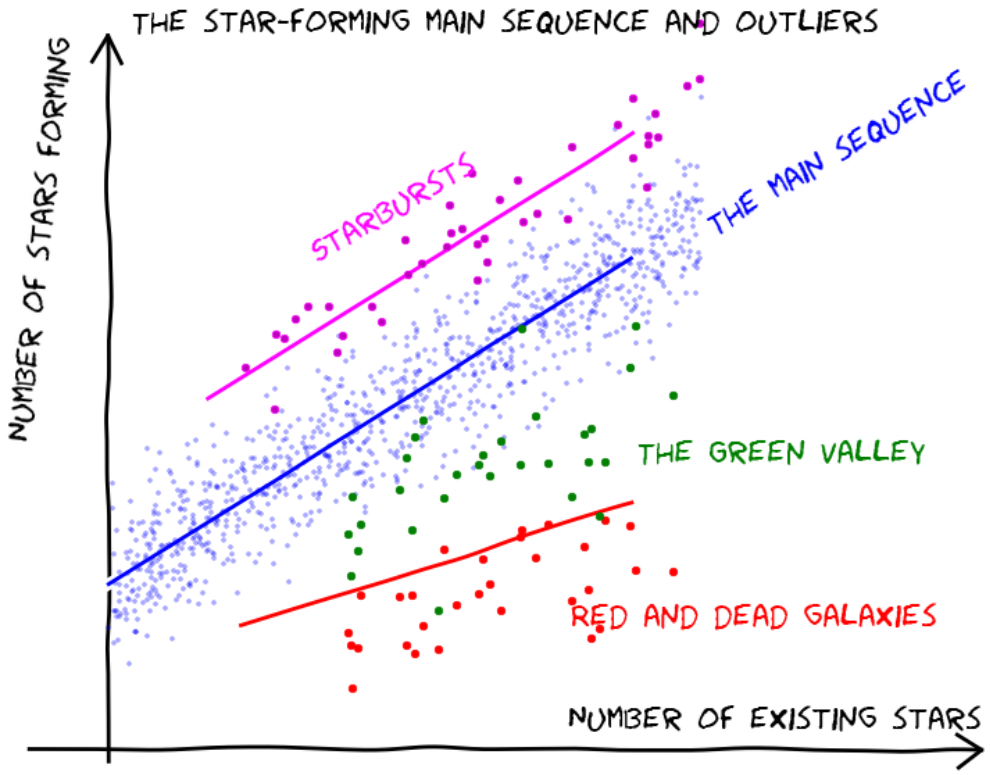

Figure 1.4: A cartoon of the galactic SFR-stellar mass plane. In blue, the so-called *main sequence* of galaxies at $z \simeq 0$ is shown, populated mainly by star-forming disk galaxies like the Milky Way. Above it, in purple, the sequence of the starburst galaxies, characterized by a very intense SFR, if compared to the one of main-sequence galaxies of the same mass. Below it, passive galaxies are plotted in red and are bridged with the main sequence by the green valley, populated by galaxies at an intermediate stage of star-formation quenching. Credits for the plot to Dr. Harry Ferguson and the CANDELS team[1].

2007; Salim et al., 2007; Whitaker et al., 2014; Pannella et al., 2015). Such correlation is called *main sequence* (MS) and is displayed in the cartoon shown in Figure 1.4.

The presence of such tight correlation implies that star-forming galaxies of very different mass (between 10^9 and 10^{11} $M_\odot$) are characterized by similar specific SFR sSFR $=$ SFR$/M_*$, that is essentially a proxy of the galactic mass growth relative to the actual mass. Therefore galaxies of different masses have relatively similar SFH and their stellar mass is the main driver of star formation. Interestingly, the normalization of the MS strongly grows with the redshift (up to a factor ~ 20 at $z \sim 2$), yet maintaining the same slope (Daddi et al., 2007; Elbaz et al., 2007; Noeske et al., 2007; Speagle et al., 2014): this is thought to occur because at high-z the gas reservoir in galactic disks and gas accretions rates were higher, supplying more fuel necessary to the formation of new stars.

In the SFR-stellar mass plane, red passive galaxies occupy a region characterized by a very low level of SFR per given stellar mass with respect to MS galaxies, and therefore smaller sSFR as well ($\log(sSFR) \lesssim -11$ typically). This demonstrates that the present growth of these galaxies is negligible and most of their mass has already been formed. Interestingly, galaxies in the region in between the MS and the passive galaxies (the so-

called *green valley*) are relatively rare: this testifies that the quenching mechanisms driving a MS galaxy to the passive area are quite efficient and this intermediate stage is relatively short. Finally, another sequence of galaxies is observed in this plane, the sequence of *starburst galaxies*. These galaxies lie above the MS, with higher SFR and sSFR at a fixed mass than MS galaxies. Typically these galaxies are characterized by peculiar morphologies and/or are undergoing a merging process that is able to trigger a strong perturbation in the gas causing a strong burst of star formation. The whole variety of mechanisms that could trigger such a burst has not been fully explored yet, and in this work we aim at understanding if environmental processes in galaxy clusters could be a trigger (Section 1.3.1).

1.3. *Clusters and groups*

Many galaxies in the local Universe show a tendency to gather together in aggregations in which the number density of galaxies is a few tens to a few hundred times higher than the average, which constitute the most massive, virialized objects in the Universe (Mo, van den Bosch & White, 2010). Galaxy clusters are the densest and most populous of these structures, and typically contain hundreds to thousands galaxies in a volume of only a few megaparsecs (Schneider, 2015), while less populous aggregations are called "groups", although the transition between the two classes of objects is smooth. An RGB image of a cluster (MACS 0416) is shown in Figure 1.5 (Yan et al., 2023), where one can appreciate the high concentration of galaxies of different morphologies and colors, from elliptical red galaxies to spiral blue galaxies.

The total mass range extends over $10^{12} - 10^{15}\,\mathrm{M}_\odot$, with average masses $10^{13}\,\mathrm{M}_\odot$ and $10^{14}\,\mathrm{M}_\odot$ for groups and clusters, respectively. However, just a few per cent of the total mass is constituted by galaxies: last-decades improvements in X-ray astronomy brought to the discovery that clusters are particularly bright in this interval of the electromagnetic spectrum. The source of this emission is the hot gas ($T \sim 3 \times 10^7$ K) in which cluster galaxies are embedded, the so-called intracluster medium (ICM), which contains most of the baryonic mass in clusters (Schneider, 2015). Furthermore, the dynamics of cluster galaxies, the properties of the gas and the results from gravitational lens effects confirmed that even gas can account for only $\sim 17\%$ of the total mass in clusters (Schneider, 2015; Laganá et al., 2013), which is mostly constituted by dark matter (DM).

Clusters of galaxies play a very important role in testing cosmology models. Being the most massive bound structures in the present-day Universe, as mentioned before, their evolution across redshift is directly related to the growth of cosmic structures. Due to their high densities in terms of both galaxies and gas, clusters and groups are also ideal laboratories to study the effects of galaxy-to-galaxy and ICM-to-galaxy interactions on the galaxy population (Schneider, 2015).

1.3.1. *Environmental effects*

Nowadays it is well established that the environment in which galaxies are located plays a critical role in their evolution (see Boselli, Fossati & Sun 2022 for a review about

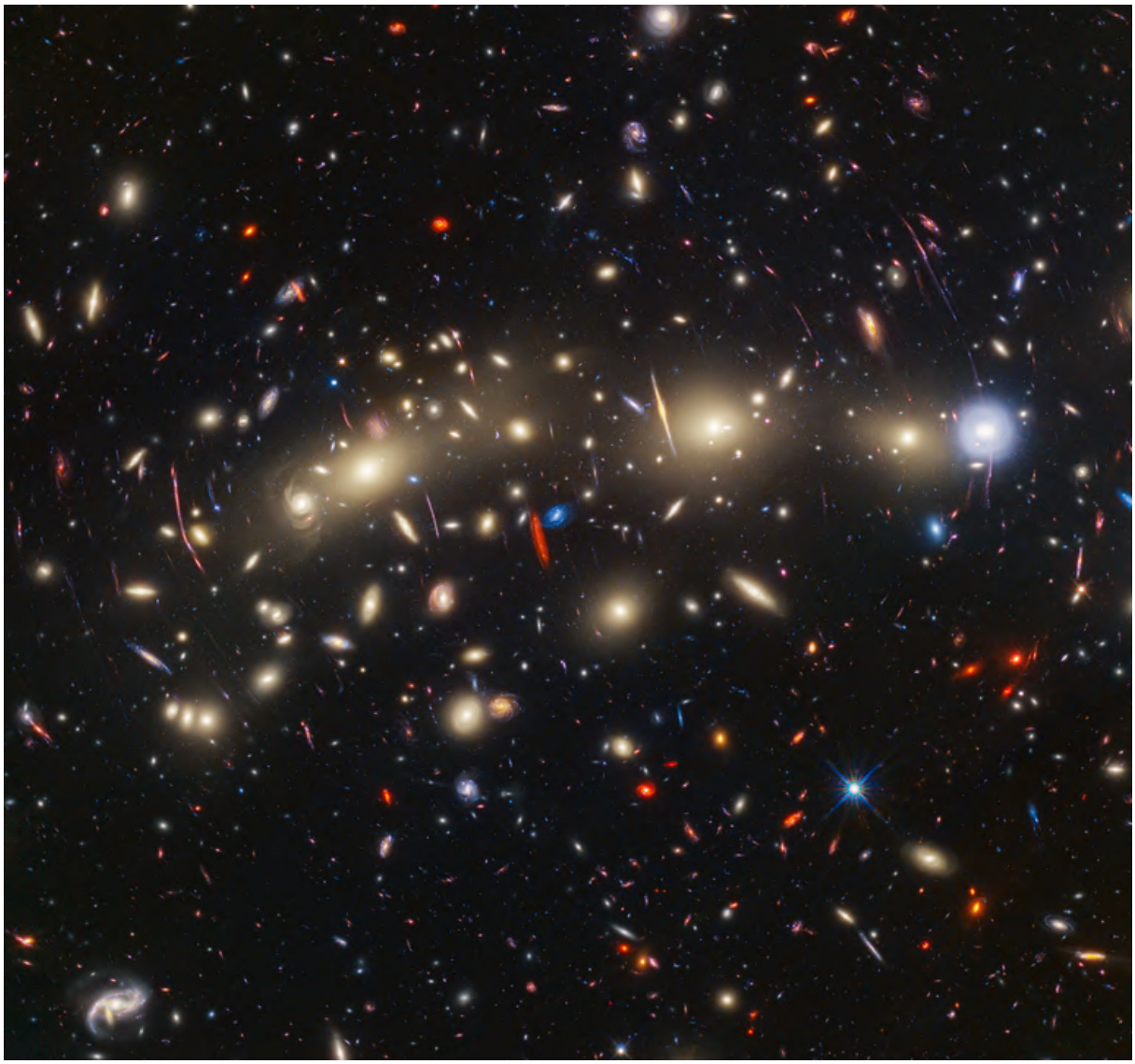

Figure 1.5: RGB image of the galaxy cluster MACS 0416 obtained combining HST and JWST photometric data. Credits to Yan et al. (2023).

environmental processes). The first evidence of the different evolutionary paths followed by galaxies in high-density aggregations was the seminal work by Dressler (1980), showing how rich environments show a larger fraction of early-type (Oemler, 1974; Postman & Geller, 1984; Goto et al., 2003; Postman et al., 2005; Whitmore, Gilmore & Jones, 1993; Dressler et al., 1997; Blanton et al., 2005) and quiescent galaxies (Lewis et al., 2002; Gómez et al., 2003; Peng et al., 2010) with respect to the field. Furthermore, even limiting the comparison to late-type galaxies, those observed in clusters show systematic differences with respect to those found in the field, including deficiency of atomic (Haynes & Giovanelli, 1984; Solanes et al., 2001; Boselli & Gavazzi, 2006; Catinella et al., 2013; Ramatsoku et al., 2020) and molecular gas (Fumagalli et al., 2009; Boselli et al., 2014).

The dynamics of the galaxies inside the cluster and the properties of the ICM influence

the galactic evolution and properties. Different perturbing mechanisms have been proposed to affect the evolutionary path of galaxies, in most cases leading to a rapid quenching of the star formation (Boselli & Gavazzi, 2014; Vulcani et al., 2021). Among these processes, some affects both the stellar and the gaseous components, drastically changing the morphology of the involved galaxies. Examples include galaxy-galaxy interactions, mergers and galaxy harassment (Toomre & Toomre, 1972; Moore et al., 1996; Moore, Lake & Katz, 1998; Merritt, 1983; Byrd & Valtonen, 1990). Some other mechanisms are hydrodynamic interactions caused by the high-speed orbital motion of galaxies ($\sigma \simeq 500 - 1000\,\mathrm{km/s}$) inside the hot ($T_{\mathrm{ICM}} \simeq 10^{7-8}$ K) and dense ($n_{\mathrm{ICM}} \simeq 10^{-3}\,\mathrm{cm}^{-3}$) ICM (Sarazin, 1986), which affect only the galactic ISM leaving instead the stellar component mostly undisturbed, such as ram pressure (RPS, Gunn & Gott 1972; Abadi, Moore & Bower 1999), thermal evaporation (Cowie & Songaila, 1977), starvation/strangulation (Larson, Tinsley & Caldwell, 1980; Balogh, Navarro & Morris, 2000; Kawata & Mulchaey, 2008).

Some processes can also feed galaxies with gas and trigger a bursts in star formation. Gas accretion from the external regions in nearby galaxies has been both observed (Sancisi et al., 2008) and predicted (Semelin & Combes, 2005). Interestingly, even the aforementioned processes causing the quenching of the galactic SFR can trigger short bursts of star formation: RPS via the compression of the available gas (Bekki & Couch, 2003; Gavazzi et al., 2003; Vulcani et al., 2018; Tomičić et al., 2018); gas rich mergers via galaxy encounters (Fujita et al., 2003; Brinchmann et al., 2004; Ostriker & Shetty, 2011).

In particular, the environmental process on which this work focuses is ram-pressure stripping, therefore in the next Section I will give more details about the physics involved in this phenomenon and which consequences it can have on cluster galaxies and their star formation.

1.3.2. *Ram-pressure stripping and jellyfish galaxies*

As described in the previous Section, when a galaxy is accreted by a galaxy cluster, it experiences for the first time the ram pressure exerted by the hot and dense ICM. Under certain conditions, such pressure is able to strip the galactic ISM, which is pushed outside the galactic disk and eventually produces tails up to more than 100 kpc long, but leaving the stellar disk almost undisturbed (Poggianti et al., 2017b). Gunn & Gott (1972) gave an analytical prescription of the conditions under which the ISM can be stripped, with the strong assumption of a disk galaxy moving face-on with respect to the ICM. The ram pressure P_{ram} exerted by the ICM is

$$P_{\mathrm{ram}} = \rho_{\mathrm{ICM}}\, v_{\mathrm{cl}}^2, \tag{1.2}$$

where $\rho_{\mathrm{ICM}}(r_{\mathrm{cl}})$ is the ICM mass density at the distance r_{cl} from the center of the cluster (often modelled as a β-model, Cavaliere & Fusco-Femiano 1976), and v_{cl} is the relative velocity of the galaxy with respect to the ICM (Section 1.3). The ICM ram pressure is opposed by the anchoring gravitational force of the galactic disk, which tries preventing the gas loss and can be modelled as the combined contribution of the stellar and gaseous components $\Pi_{\mathrm{gal}} = 2\pi\Sigma_g\Sigma_*$, where σ_g and Σ_* are the density profiles of stars and gas, respectively, and can be described by an exponential function

$$\Sigma(r) = \left(\frac{M_d}{2\pi r_d^2}\right) e^{-r/r_d}, \tag{1.3}$$

where M_d and r_d are the total mass and the scale radius of the disk, respectively. Under these assumptions, the stripping occurs when $P_{\rm ram} > \Pi_{\rm gal}$ which is a condition that, given Equation 1.3, can be met for galactic radii $r > r_{\rm tr}$, where $r_{\rm tr}$ is the so-called *truncation radius* at which $P_{\rm ram} = \Pi_{\rm gal}$. Therefore this simple model predicts outside-in quenching starting from the outskirts of the disk (Owers et al., 2019; Gullieuszik et al., 2017; Boselli et al., 2020), leading to Hα truncated disks (Koopmann & Kenney, 2004; Fritz et al., 2017) and eventually to post-starburst/post-SF disk galaxies (Vulcani et al., 2020a; Werle et al., 2022). Even if the final stage of RPS is the quenching of the galaxy (Cortese, Catinella & Smith, 2021), a number of works finds that the early stages of RPS are able to shortly enhance the galaxy star formation in the disk (Vulcani et al. 2018, 2019, 2020b for observational data, Göller et al. 2023 for evidence from TNG simulation) and to trigger in-situ star formation in compact knots of gas stripped out of the galactic disks (Yoshida et al., 2008; Smith et al., 2010; Jáchym et al., 2019), as confirmed by the discovery of large numbers of Hα-emitting clumps and Hα diffuse emission in the tails of stripped gas, up to 100-150 kpc away from the disk (Fossati et al., 2016; Merluzzi et al., 2013; Consolandi et al., 2017; Poggianti et al., 2019). Galaxies showing such peculiar tails are called "jellyfish galaxies", and they are mainly observed in the central regions of galaxy clusters where they move at high speed with respect to the intracluster medium (ICM) (Jaffé et al., 2018; Gullieuszik et al., 2020). Star formation in stripped tails was seen by some hydrodynamical simulations, though they lack the capability to predict the characteristics of star-forming complexes (Kapferer et al., 2009; Tonnesen & Bryan, 2010, 2012; Roediger et al., 2014; Tonnesen, 2019; Lee et al., 2022). Observationally, Hα clumps, as well as inter-clump diffuse Hα emission, are common in the tails of jellyfish galaxies.

In the last few years, the study of jellyfish galaxies has moved from a few individual cases to statistical samples that have unveiled a number of results related to the properties of the tails of stripped material (Boselli et al., 2018; Jáchym et al., 2019; Poggianti et al., 2019; Poggianti et al., 2019; Moretti et al., 2018; Moretti et al., 2020): a) the diffuse emission in the tails is due to a combination of photo-ionization by young stars and heating (via shock heating or heat conduction), the latter most probably due to mixing of stripped gas with the hot ICM; b) following the discovery of large amounts of molecular gas in the stripped tails obtained with single dishes, molecular gas clumps have now been directly observed with ALMA; c) the properties of $\sim$ 500 Hα clumps in jellyfish tails have been studied at 1 kpc-resolution (Poggianti et al., 2019; Gullieuszik et al., 2020), finding associated stellar masses between 10^5 and $10^8 M_\odot$ (similar to high-z clumps). At these resolutions, the tail clumps seem to follow scaling relations (Hα luminosity-gas velocity dispersion, etc) similar to disk clumps.

The emerging picture is that gas stripped by ram pressure finds itself embedded in the hot ICM plasma but manages to collapse and form new stars. The light of these young stars is directly observable in the UV (Smith et al., 2010; George et al., 2018; George et al., 2023). Depending on the galaxy, stars formed in the tails represent between a few % and 20% of the total ongoing SFR of the system disk+tail (Poggianti et al., 2019; Gullieuszik

et al., 2020; Werle et al., 2022). Overall tail clumps form stars at a higher rate than clumps in the disk with the same stellar mass density; however, if only the mass formed in the last 100 Myr is considered, the differences are reconciled, suggesting that the local mode of star formation is similar in the disks and in the tails on timescales of 100 Myr (Vulcani et al., 2020b).

1.3.3. *GASP: GAs Stripping Phenomena in galaxies with MUSE*

GASP[2] (GAs Stripping Phenomena in galaxies with MUSE, Poggianti et al. 2017a) is an ESO Large Program aiming at studying the properties of galaxies affected by different gas removal processes in the field, in groups and clusters. This includes 114 galaxies, 64 of which are observed at different RPS stages, from pre-stripping to post-stripping (Fritz et al., 2017). Targets were chosen from the catalog in Poggianti et al. (2016) as galaxies with long unilateral tail-like structures in B-band images. The final sample includes galaxies in the mass range $10^9 - 10^{11.5}\,M_\odot$ and at redshift $0.04 < z < 0.07$. Targets were observed with MUSE@VLT (details about the MUSE data are given in Section 2.6) Being an integral-field spectrograph, MUSE can produce photometric data and spectra for each spaxel, allowing a spatially resolved study of the properties of the ionized gas phase and the stellar component both in the galactic disks and in the stripped tails.

Results of GASP have confirmed the presence of clumps with in-situ star formation in the tails of individual jellyfish galaxies of the sample (Bellhouse et al., 2017; Gullieuszik et al., 2017; Moretti et al., 2018; Moretti et al., 2020; Poggianti et al., 2019). In particular, Poggianti et al. (2019) analyzed star-forming clumps at ~ 1 kpc-scale in the tails and in the disks of 16 GASP galaxies, finding that tail clumps are less massive, both in terms of stellar and gas mass, and with a smaller gas velocity dispersion than the clumps in the disks.

GASP MUSE data are complemented by observing campaigns with JVLA, APEX and ALMA, MeerKAT, LOFAR, UVIT, and Chandra to probe all the gas phases and galaxy components. The coverage given by all these instruments allowed a characterization of the whole stripping process, including: study of recently formed stars in UV (George et al., 2018; George et al., 2019, 2023), confirmation of the deficiency of H I (Ramatsoku et al., 2019; Luber et al., 2022; Deb et al., 2020; Ramatsoku et al., 2020), study of the interplay between the galaxy and the cluster environment (Bartolini et al., 2022; Lourenço et al., 2023; Campitiello et al., 2021), fraction of molecular gas (Moretti et al., 2020), kinematic effects on the molecular gas disks (Bacchini et al., 2023), properties of the plasma in the radio-tails (Ignesti et al., 2022b,a; Müller et al., 2021), correlation with AGN activity (Radovich et al., 2019; Peluso et al., 2022, 2023), dynamics of the galaxies in the cluster (Ignesti et al., 2023; Smith et al., 2022; Jaffé et al., 2018; Sanchez-Garcia et al., 2023). GASP also exploited state-of-art simulations to study the interplay between AGN, stellar feedback and RPS (Akerman et al., 2023a,b) and to track the evolution of these galaxies across different redshifts (Kulier et al., 2023).

For what concerns star-forming clumps, GASP results are hampered by the spatial resolution of the observations that is, in the case of MUSE and ALMA data, ~ 1 arcsec,

[2]https://web.oapd.inaf.it/gasp/

which corresponds to ~ 1 kpc at the redshift of GASP galaxies. As a consequence, GASP observations sample only the largest scales of the star forming structures. The unique spatial resolution of *HST* overcomes this limitation and allows us to gather a fundamental piece of information for understanding RPS and SF processes in general.

1.4. *Star-forming clumps*

It is widely accepted that the formation of new stars in galaxies occurs in the density peaks of the cold molecular gas, where the gas is the coldest and therefore the self-gravity can generate the conditions of high density necessary to trigger the thermonuclear activity in the stellar nuclei (Lada & Lada, 2003; Bressert et al., 2010). These dense and cold regions represent the final stage of a process, including turbulence, gas cooling and the growth of non-linear perturbation, driving the condensation of atomic gas (mainly neutral hydrogen, H I) from galactic to sub-kpc scales down to the pc/sub-pc dense cores of cold molecular gas ((Kennicutt & Evans, 2012)). The bridge between the galactic- and core-scale regimes is represented by $\gtrsim 10$ pc-scaled star-forming clusters, with masses $\gtrsim 10^4$ $M_\odot$ (Portegies Zwart, McMillan & Gieles, 2010). These stellar clusters form in the peaks of the molecular gas density distributions, in the so-called *cores* of the Giant Molecular Clouds (GMCs), and represent the smallest structures in galaxies containing enough stars to fully sample the stellar IMF (Section 1.1). Therefore, they represent the suitable sites to study in a statistical way how the star-formation mechanism proceeds as a function of the clump environment, like the global properties of the host galaxy, whether the host galaxy itself is in the field or in a cluster and the local conditions of the medium in which the stellar clumps and the GMCs are embedded.

Now, when observing galaxies with a spatial resolution of a few tens of parsecs to 100 pc, the direct observation of stellar clusters is made very difficult by the combined effects of this limited spatial resolution and the clustering of star formation, which causes stellar cluster to be spatially close to each other. The net results is that, in these galaxies, groups of stellar clusters are observed as a single object called *clump*. The study of clumps is fundamental also in the framework of galaxy evolution; clumps are the sites in which galaxies form the bulk of their stellar content, therefore it is vital to understand how their stars get re-distributed over within the galactic plane. Indeed simulations are still contradictory in understanding whether clumps evaporate on short timescales either by stellar feedback, relaxation and interactions within the galactic environment (Murray, Quataert & Thompson, 2009; Genel et al., 2011; Hopkins et al., 2012; Tamburello et al., 2015; Oklopčić et al., 2016), or if they survive for much longer timescales (~ 500 Myr), eventually sinking to the galaxy center as a consequence of gravitational torque and dynamical friction and contributing to the formation of the bulge and the accretion onto the central supermassive black hole (Bournaud, Elmegreen & Elmegreen, 2007; Bournaud et al., 2013; Elmegreen, Bournaud & Elmegreen, 2008; Ceverino, Dekel & Bournaud, 2010; Gabor & Bournaud, 2013; Mandelker et al., 2014). This is especially true at high redshift, where more and more recent works confirm that high-z star-forming galaxies are formed by compact massive clumps with strong ongoing star formation (Elmegreen & Elmegreen, 2005; Elmegreen et al., 2007; Elmegreen et al., 2009; Genzel et al., 2008, 2011; Wisnioski et al., 2011; Förster

Schreiber et al., 2011; Wuyts et al., 2012; Murata et al., 2014; Tadaki et al., 2013; Shibuya et al., 2016; Zanella et al., 2015; Guo et al., 2012; Guo et al., 2018; Zanella et al., 2019), although spatial resolution is clearly an important factor for the determination of clump properties as shown by the analysis of lensed high-z galaxies (Jones et al., 2010; Livermore et al., 2012; Dessauges-Zavadsky et al., 2017; Cava et al., 2018; Meštrić et al., 2022). Since these galaxies are still undergoing the bulge formation process, understanding the global contribution of clumps is important to properly model galaxy evolution.

Our knowledge about these structures has greatly improved in the last decade thanks to observational surveys of low redshift galaxies with the *Hubble Space Telescope* (*HST*), which is the only instrument able to achieve the resolution necessary to study their morphology and size properties (LEGUS, Calzetti et al. 2015; DYNAMO, Fisher et al. 2017; LARS, Messa et al. 2019; PHANGS-HST; Lee et al. 2022). These surveys explored the properties of young stellar clumps in different galaxies and environment, from isolated main-sequence galaxies (like galaxies in LEGUS and PHANGS) to starburst galaxies with turbulent disks (DYNAMO), to merging and peculiar galaxies (LARS). Furthermore, also the properties of the stellar clumps as a function of the local environment, like spiral-arms or inter-arm regions, were explored. However, yet the full understanding of how the environment affects the formation and the final properties of the clumps is not achieved. In this context, the study of star-forming clumps in jellyfish galaxies can put strong constraints on how gas compression and changes in the thermodynamic properties of the gaseous medium surrounding the clumps can affect the clumps themselves. As examples, in Figure 1.6 I show zoomed-in *HST* RGB images of two star-forming galaxies from the LEGUS atlas[3], namely NGC 3344 and NGC 6503, where one can appreciate the compact young star clusters, very bright in the blue band, with a very high resolution ($\sim$ 1 pc). In addition, in Figure 1.7 I also show lower resolution images ($\sim$ 200 pc and $\sim$ 1 kpc, respectively) of a galaxy of the DYNAMO sample (G04-1, Fisher et al. 2017, left panel) and of a $z \simeq 1.877$ galaxy (ID123, Zanella et al. 2019, right panel). The former is a two-color image obtained with *HST* with the Hα emission line as the blue color, where one can appreciate the big, compact and bright clumps distributed in the disk of the galaxy; the latter is a rest-frame UV single-filter *HST* image where one can notice the few very big and bright stellar clumps which characterize the morphology of galaxies at cosmic noon, when the spatial resolution is not high enough.

In the following Sections, I am going to list the main observables and relations that can be studied to probe environmental effects in clump formation and evolution.

1.4.1. *Distribution functions*

Models describing the fragmentation of star-forming regions as a scale-free, turbulence-driven process predict that the mass distribution function (MDF) of these regions (i.e. the number of objects per mass bin) is a power law in the form

$$\frac{dN}{dM} \propto M^{-\alpha}, \tag{1.4}$$

[3] `https://legus.stsci.edu/legus_quickview.html`

Figure 1.6: RGB images of the LEGUS galaxies NGC 3344 (lef panel) and NGC 6503 (right panel). The colour images are created using the following *HST* filter combination: F814W (red), F555W or F606W (green), and F435W or F438W (blue). Image scale varies, spatial resolution of $\sim$ 1 pc. Credits to the LEGUS collaboration[4].

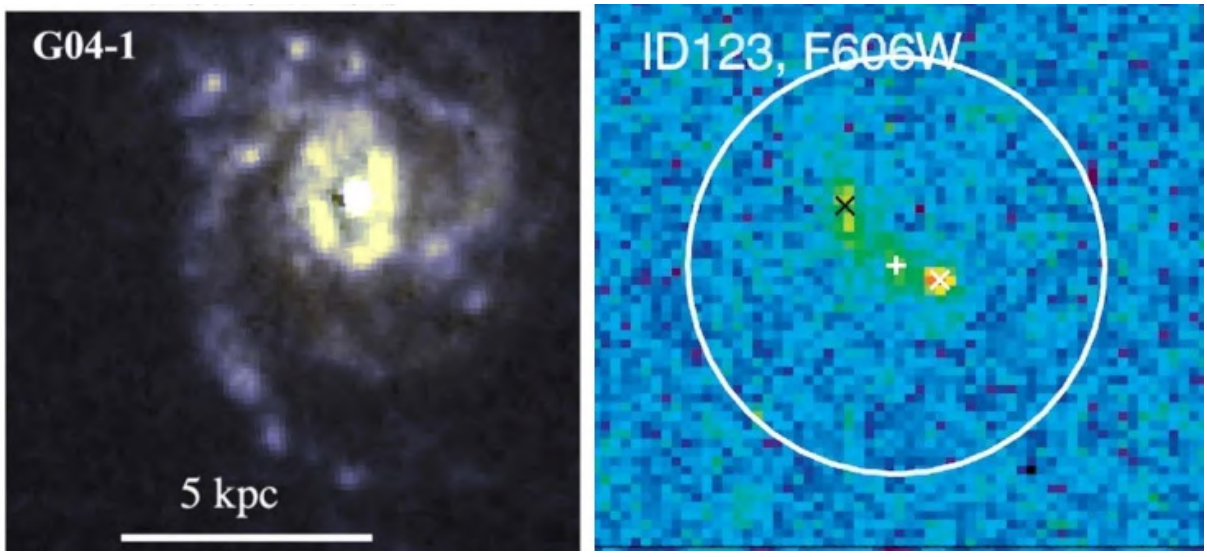

Figure 1.7: Left panel: *HST* two-color image of the DYNAMO galaxy G04-1. Blue represents Hα and yellow represents 600 nm continuum. The spatial resolution is $\sim$ 200 pc. Right panel: *HST* F606W (rest-frame UV) image of the high-z ($z \simeq 1.877$) clumpy galaxy ID123. The spatial resolution is about 1 kpc. Images taken from Fisher et al. (2017) and Zanella et al. (2019), respectively, only for display purpose.

with $\alpha = 2$ (Elmegreen, 2002, 2006). Similar results are found in simulations (Hennebelle & Audit, 2007; Audit & Hennebelle, 2010; Fensch et al., 2023), even if with the slope found in these works is slightly flatter ($1.7 - 1.8$). As time proceeds after the clump formation, the slope of the clump mass function is thought to change, as a consequence of many processes, including their dynamical evolution, their relaxation and the interactions within the surrounding environment, even if it is still debated whether the net effect is a steepening or a flattening of the mass function (Gieles, 2009; Fujii & Portegies Zwart, 2015). The corresponding luminosity distribution function (LDF), if derived using a tracer of a narrow age range, is expected to have a similar slope, provided that 1) the IMF is

well sampled and independent of the mass of the initial cloud from which the clumps are formed and 2) the SFH and therefore the stellar age distributions of all clouds are the same (Elmegreen & Falgarone, 1996; Elmegreen, 2006).

Exploiting LEGUS data, many studies find confirmation of the turbulence cascade as the formation channel of stellar clumps (Elmegreen et al., 2014; Gouliermis et al., 2015; Gouliermis et al., 2017), reflected also in the emerging spatial distribution of stars formed from such gas (Elmegreen & Falgarone, 1996; Elmegreen, 2006; Grasha et al., 2017).

Further confirmations come from observational studies of both MDFs and LDFs of recently formed star-forming regions, which are known to be well described by a power law, independently of wavelength (e.g., Hα: Kennicutt, Edgar & Hodge 1989; Santoro et al. 2022; Paα Liu et al. 2013 UV Cook et al. 2016; Messa et al. 2017; Messa et al. 2019; V-band Larsen 2002; Bastian et al. 2007; R-band Whitmore et al. 2014; IR and radio Mascoop et al. 2021). Indeed, observed slopes are found to be consistent with the one predicted by the turbulent cascade (2, Zhang & Fall 1999; Hunter et al. 2003; de Grijs et al. 2003; Gieles et al. 2006 for MDFs, Adamo et al. 2017; Messa et al. 2017; Messa et al. 2018 for both MDFs and LDFs of clumps in LEGUS galaxies), even in tidal debris (Rodruck et al., 2023) and $z \sim 1 - 1.5$ lensed galaxies (Livermore et al., 2012). Very often a cut-off at high masses/luminosities ($> 10^5\,M_\odot$) is observed (Haas et al., 2008; Adamo et al., 2017; Messa et al., 2017; Livermore et al., 2012). In some cases the distribution is found to be shallower (de Grijs & Anders 2006: 1.85 ± 0.05; Cook et al. 2016: 1.76 ± 0.3; Santoro et al. 2022: 1.73 ± 0.15).

Interestingly, some of these works find the value of the slope to be affected by the local environment (Haas et al., 2008). Cook et al. (2016) and Santoro et al. (2022) show that the LDF is flatter in regions with high star-formation rate (SFR) surface density ($\Sigma_{\rm SFR}$). Similarly, Messa et al. (2019) find steeper LDFs in regions with low $\Sigma_{\rm SFR}$ when studying the galaxies of the LARS sample. The same trend is then reflected in the LDF of clumps in different intergalactic environments: Messa et al. (2018) show that the LDF of UV clumps in the spiral arms of the LEGUS galaxy M51 is flatter than that of clumps in the inter-arm region (with likely lower $\Sigma_{\rm SFR}$), while no strong differences are found as a function of the galactocentric distance.

The characterization of the cluster MDF is fundamental not only to study the gas collapse and condensation when it forms new stars, but also for studies of the stellar IMF in external galaxies. In fact, the IMF describes the mass distribution of coeval stars formed in a unique GMC, and only under certain conditions the IMF at galactic scales is comparable to the one in a single cluster. As pointed out in Kroupa & Weidner (2003) and further studied in Elmegreen (2006), if 1) massive clumps are more likely to host massive stars, and 2) the clump mass function favors the formation of too many massive clumps, then the galactic IMF is shallower than the one that could be inferred by the stellar populations of a single clump. Elmegreen (2006) analytically demonstrated that if the clump MDF has $\alpha \leq 2$, then the galactic IMF should be approximately equal the cluster IMF.

Another important tracer of the clustering properties of the clump is the size distribution function (SDF) of star-forming clumps (Bresolin, Kennicutt & Stetson, 1996; Bresolin et al., 1998; Magnier et al., 1993; Pietrzyński et al., 2001, 2005; Gusev, 2002; Borissova

et al., 2004; Bruevich, Gusev & Guslyakova, 2011), which is strictly connected to the fragmentation properties and the maximum length at which the GMCs collapse into stellar clumps. Gouliermis et al. (2010) found that the SDF of stellar structures in the Local Group dwarf galaxy NGC 6822 is well described by a Gaussian function, while Bastian et al. (2012) got a better fit in M83 using a log-normal function. Other works find instead that the SDF can be described as a power law with slopes between 2.5 and 4.5 (Kennicutt & Hodge, 1980; Gusev, 2014). In particular, Gusev (2014) found that regions characterized by a high level of complexity, with many sub-structures, show a flatter SDF than the one of regions in which clumps are simple and isolated.

As stated above, the environmental effects on these distribution functions and, more in general, on the clump formation mechanism has not been studied in detail yet, except for a few cases. In this context, jellyfish galaxies give the unique opportunity to study very young clumps in peculiar conditions and these distribution functions can be the right tool to assess how star formation proceeds in this environment.

Hα luminosity function: deviation from single power law

Beckman et al. (2000) hypothesized that the Hα LDF of H II regions is better described by a double power law, with the knee occurring at $\sim 4 \times 10^{38}$ erg/s and a steeper slope for luminosities brighter than the knee. The difference in the slope is thought to be caused by the fact that faint H II regions are embedded in enough neutral medium and all the ionizing photons they emit are absorbed in accordance with the Strömgren sphere (Section 1.1). In such regime the H II is *ionization bound*. If the H II region is surrounded by less medium than the one necessary to absorb the ionizing photons, then regions is defined *density bound*. In such H II regions, the photons in excess escape without contributing to the production of the Hα-line emission, and the H II region is fainter than expected, causing the LDF to steepen in the bright-end regime.

1.4.2. *Luminosity-size relation*

As described in Section 1.1, stellar populations younger than ~ 10 Myr present also OB stars which are able to ionize the surrounding medium and trigger bright Hα-line emission, within the volume of the so-called Strömgren sphere. According to Strömgren (1939); Osterbrock (1989), the Hα luminosity of the Strömgren spheres of each OB star scales with its cubed radius. Therefore young stellar clumps are particularly bright in Hα, resulting from the combined emission of all the single Strömgren spheres.

Observational studies focusing on the correlation between the clumps Hα luminosity $L_{\mathrm{H}\alpha}$ and the clumps radius R showed that clumps in isolated main-sequence galaxies follow the same scaling relation of a single Strömgren sphere, with $L_{\mathrm{H}\alpha} \propto R^3$ (Beckman et al., 2000; Wisnioski et al., 2012; Cosens et al., 2018). These results favor the idea that the clumps morphology as observed through their Hα emission is close the one of H II regions, and tend to disfavor models according to which it should resemble the one of the parent GMC, for which the predicted slope of the correlation should be 5/2 in place of 3. Nonetheless, there are nowadays strong indications (Fisher et al., 2017; Cosens et al., 2018) that

the correlation flattens ($L_{\mathrm{H}\alpha} \propto R^{\sim 2}$) when considering clumps in starburst and/or high-z galaxies. Furthermore, such clumps show also an enhanced Hα luminosity at a fixed size compared to the one of clumps in main-sequence galaxies (Wisnioski et al., 2012; Cosens et al., 2018), and this enhancement has been shown to coincide also with an enhanced clump SFR surface density Σ_{SFR}. Simulations of the expansion of ionized bubbles in a Milky Way-like ISM environment by Nath, Das & Oey (2020) predict slope equal to 2, but this cannot explain the bimodality in the value of the slope. A possible explanation is proposed by Cosens et al. (2018) and relates the size of a clump with the properties of the galaxy disk where the clump is born. In fact, the H II regions we observe are constituted by ionized ISM inside the galactic disk, which is a relatively thin structure, with a scale-height H_{disk} of a few kpc at most, outside of which the neutral gas is essentially absent. Therefore, as long as the size of the H II region is smaller than the H_{disk}, the ionized region can grow along all the possible directions, with a slope equal to 3 as predicted for the Strömgren sphere. But if the H II region is too bright, condition that occurs more frequently in the highly star-forming starburst galaxies, then the predicted size becomes larger than H_{disk} and the H II region can not grow perpendicularly to the galactic plane anymore, since there is no neutral medium to ionize. That is, the H II can only grow over the galactic plane, a 2−dimensional structure, varying the predicted slope of the $L_{\mathrm{H}\alpha} - R$ relation to 2.

In Figure 1.8, I show the plot presented by Cosens et al. (2018) in their paper, in which they collected results from the literature of Hα clumps in different types of galaxies (main-sequence, starburst, high-z galaxies) and put them in the Hα luminosity-size relation, noticing the abovementioned flattening of the power-law slope (from 2.767 to 1.741) for clumps with a large SFR surface density and observed in starburst and high-z galaxies.

1.5. *Effects of ram-pressure stripping on star-forming clumps*

A complete view of the effects of RPS on the properties, formation and evolution of star-forming clumps is far from complete. Abramson & Kenney (2014) and Kenney, Abramson & Bravo-Alfaro (2015) observed galaxies undergoing RPS in the Virgo cluster (NGC 4402 and NGC 4522) and in the Coma cluster (NGC 4921) with *HST*, respectively, showing that RPS is able to decouple the high-density component of the ISM (and in particular the Giant Molecular Clouds) from the low-density one, which is more prone to stripping. Also the dust is characterized by elongated morphology and filaments aligned with the stripping direction. To our knowledge, until now only two works have presented sub-kpc scale studies of young clumps in galaxies undergoing RPS. One of them is by Cramer et al. (2019), who studied the long and narrow Hα tail of D100 in the Coma cluster with *HST* and found 10 unbound young UV sources with sizes $\sim 50 - 100$ pc, which they consider likely to disperse with ageing. The other one is by Boselli et al. (2021); this study, however, is focused on IC 3476, a low mass galaxy in the Virgo cluster that hosts a very low star-formation activity in the tail, much lower than typical SF of GASP galaxies (Gullieuszik et al., 2020). In addition to these, we mention also the work by Canning et al. (2014) for star formation in the accretion filaments of NGC 1275, the central galaxy in the Perseus cluster.

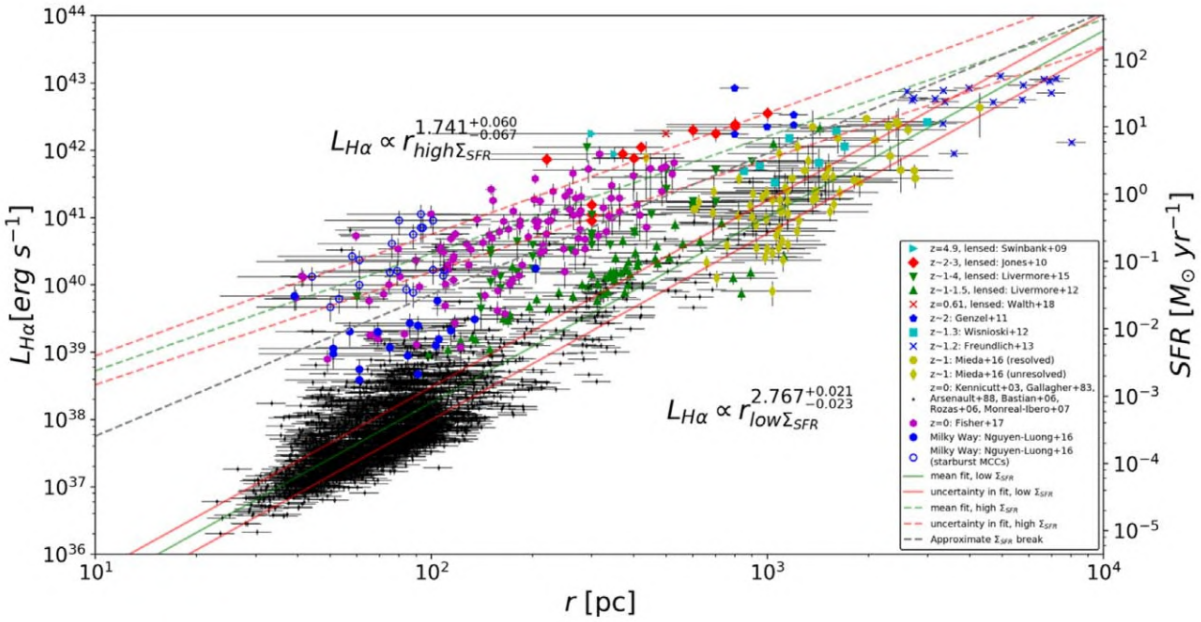

Figure 1.8: Clump Hα luminosity and size relation taken from different studies. The dashed red and green lines show the best fit to the clumps with high SFR surface density $\Sigma_{\rm SFR}$, while the solid red and green lines show the best fit of the low $\Sigma_{\rm SFR}$ data. The gray dashed line marks approximately $\Sigma_{\rm SFR} = 1\,{\rm M}_\odot/{\rm yr/kpc}^2$, where the cutoff lies when converted to luminosity. Plot taken from Cosens et al. (2018) to show state-of-art results of the clumps luminosity-size relation.

When focusing on the morphology of the star-forming clumps in the tails, one of the most peculiar structures that are found are the so-called *fireballs* (Cortese et al., 2007; Yoshida et al., 2012; Kenney et al., 2014; Jáchym et al., 2017; Waldron et al., 2023), in which the different stages of star formation are spatially displaced from each other, from the pre-collapse molecular gas clumps, to actively star forming clumps, to stellar-only clumps not actively forming new stars (Poggianti et al., 2019). These stages are spatially correlated in coherent elongated structures a few hundreds of parsecs long, in which the early ones are typically displaced further away from the galactic disk than the late ones. What is thought to occur is that, as the stars form in the stripped gas, they do not feel the ram pressure exerted by ICM anymore, being a collisionless component. Therefore they retain their initial velocity, the one that the stripped gas had at the moment of the star-formation episode. On the other hand, the ICM keeps decelerating the stripped gas, introducing a difference in velocity between gas and stars. As a consequence of that, the stellar and gaseous components decouple and once the stripped gas undergoes new star-formation events, the young generations of stars that are formed are located further away from the galactic disk than the old ones. The result is that the stellar component is spatially distributed in elongated structures and the stellar age anti-correlates with the distance from the galaxy (Kenney et al., 2014). A cartoon plot by Kenney et al. (2014) is shown in Figure 1.9 and summarizes the morphological properties of the fireball configuration, with young stars displayed further away from the disk and very close to the molecular gas, while the old stars are close to the disk and spatially displaced from stellar populations of different ages.

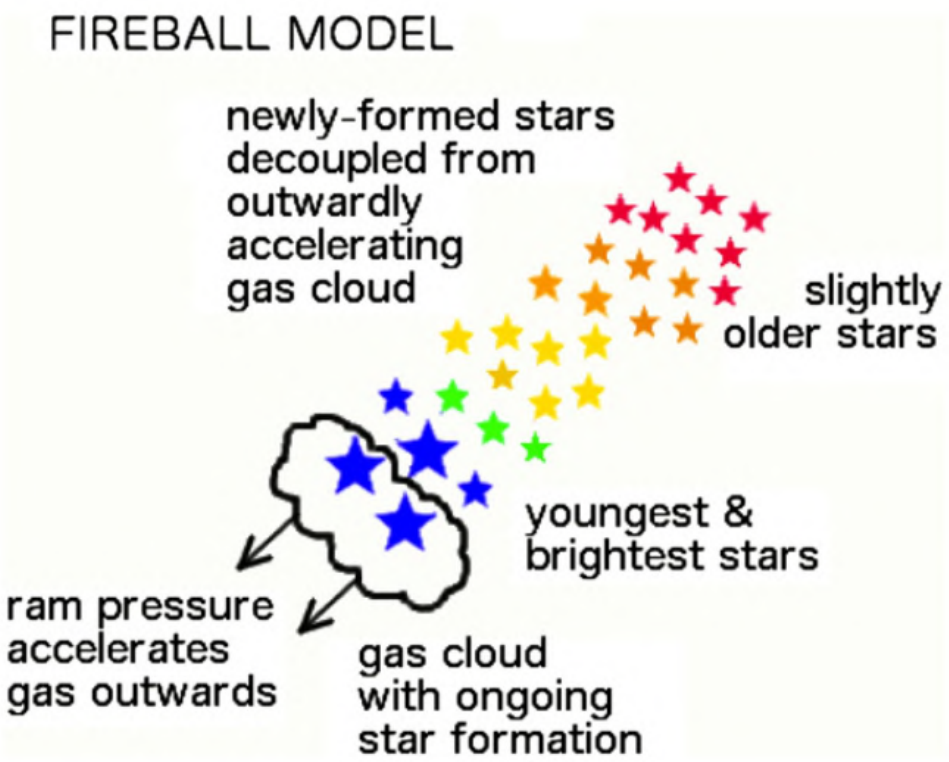

Figure 1.9: A cartoon of the fireball model from the paper by Kenney et al. (2014). A gas cloud is accelerated outward by ongoing strong ram pressure. The young stars are displayed further away from the galactic disk, close to the gas cloud, and form the *head* of the fireball, while stellar associations gets older and older and we move far from the cloud and in the direction opposite to the ram-pressure wind. Stars are collisionless system and therefore they decouple from the accelerated gas cloud on short timescales. The color differences of the stars along the tail are greatly exaggerated to emphasize the difference in ages.

The fate of these objects is debated. If their self-gravity is stronger than the tidal field of the parent galaxy, they may either become dark matter-free low-mass dwarf galaxy orbiting in the cluster, or a satellite of the parent galaxy to be eventually accreted. If the galactic tidal field is too strong, the clumps are disrupted, either contributing to the intracluster light of the cluster or to the stellar halo of the galaxy.

The crucial missing piece of the puzzle and main aim of the work presented in this thesis is the obtaining of a statistically-relevant, high-spatial resolution study of star-forming clumps in jellyfish galaxy tails and disks, that can allow a systematic description of the morphology of these clumps, how star formation proceed in these peculiar environment with respect to what happens in isolated galaxies, what is the fate of the stellar structures born from stripped material and their role in the ecosystem of the galaxy and of the cluster.

Chapter 2

Data

In this Chapter I present and describe the *HST* and MUSE data that are going to be used throughout this work, including the *HST* data reduction and analysis. The Chapter is structured as follows: in Section 2.1 I list the properties of target galaxies and of the *HST* observations; after this introduction, I describe the procedure adopted to reduce and calibrate the *HST* data (2.2), to extract the Hα emission (2.3) and to evaluate the detection limits of the images (2.4); in Section 2.5 I show how the denoising of the images (2.5.1) is performed, aimed at minimizing the background flux fluctuations and removing residual cosmic rays, and the determination of the field of view in which the clump detection is performed (2.5.2). Both these steps are fundamental to make the dataset suitable for the clumps detection. Finally, in Section 2.6, I characterize the main properties of the MUSE observations of the target galaxies, which are used to test the *HST* data calibration and to confirm the detection of the clumps in the *HST* data.

2.1. *Observations*

Observations were carried out with the UVIS channel of the WFC3 camera onboard the *HST* between October 2020 and April 2021 (GO 16223; PI Gullieuszik). All the *HST* data used in this paper can be found in MAST: 10.17909/tms2-9250.

Target galaxies were selected from the sample of GASP ram pressure stripping galaxies (Poggianti et al., 2017b) with long Hα emitting tails. The selection was based on the number of Hα clumps in the tails detected with MUSE (Poggianti et al., 2019). The main properties of the 6 target galaxies are reported in Table 2.1. The papers published so far using available multi-wavelength observations are listed in the last column; more data (e.g. with MeerKAT, LOFAR, ATCA, and Chandra) are available and will be published in forthcoming papers.

Since I am going to compare the properties of these galaxies with those of galaxies taken from different samples, in Figure 2.1 I show the SFR-stellar mass relation (Section 1.2.1) of the GASP galaxies (Vulcani et al., 2018), compared with the GASP control sample (containing field galaxies or cluster galaxies showing no signs of any environmental process) and to the DYNAMO-*HST* sample of starburst galaxies (Kauffmann et al., 2003; Green

ID_{P16}	RA	Dec	M_*	$\frac{H\alpha}{H\alpha+[N\,II]}$	z_{gal}	N_{knots}^{MUSE}	cluster	σ_{clus}	z_{clus}	ref
	(J2000)	(J2000)	$10^{10}\,M_\odot$		10^{-2}			km/s	10^{-2}	
(1)	(2)	(3)	(4)	(5)	(6)	(7)	(8)	(9)	(10)	(11)
JO175	20:51: :17.593	-52:49: :22.34	$3.2^{3.7}_{2.7}$	0.705	4.68	53	A3716	753^{+36}_{-38}	4.57	(4,10,14)
JO201	00:41: :30.295	-09:15: :45.98	$6.2^{7.0}_{2.4}$	0.660	4.46	94	A85	859^{+42}_{-44}	5.59	(3,4,5,6,8, 9,10,13,14, 15,16,18)
JO204	10:13: :46.842	-00:54: :51.27	$4.1^{4.7}_{3.5}$	0.660	4.24	87	A957	631^{+43}_{-40}	4.51	(2,4,6, 12,18)
JO206	21:13: :47.410	+02:28: :35.50	$9.1^{10.0}_{8.2}$	0.703	5.13	93	IIZW108	575^{+33}_{-31}	4.86	(1,4,6,10, 13,18,19)
JW39	13:04: :07.719	+19:12: :38.41	17^{20}_{14}	0.650	6.50	93	A1668	654	6.34	(14,18, 19,21)
JW100	23:36: :25.054	+21:09: :02.64	29^{36}_{22}	0.530	6.02	96	A2626	650^{+53}_{-49}	5.48	(4,6,7,10, 11,15,17, 18,19,20)

Table 2.1: Summary of the main properties of the galaxies studied in this paper and of their host clusters. Columns are: GASP ID of the galaxy as in Poggianti et al. 2016 (1), RA and Dec of the galaxy (2 and 3), galaxy stellar mass (4), median value for $H\alpha/(H\alpha + [N\,II])$ from the MUSE knots listed in Poggianti et al. (2019) (5), galaxy redshift (6), number of MUSE $H\alpha$ in the galaxy tails defined as in Section 3.1.3 (7), ID of the host cluster (8), cluster velocity dispersion (9), cluster redshift (10), references (11). References are: 1) Poggianti et al. (2017a), 2) Gullieuszik et al. (2017), 3) Bellhouse et al. (2017), 4) Poggianti et al. (2017b), 5) George et al. (2018), 6) Moretti et al. (2018), 7) Poggianti et al. (2019), 8) Bellhouse et al. (2019), 9) George et al. (2019), 10) Radovich et al. (2019), 11) Moretti et al. (2020), 12) Deb et al. (2020), 13) Ramatsoku et al. (2020), 14) Bellhouse et al. (2021), 15) Tomičić et al. (2021a), 16) Campitiello et al. (2021), 17) Ignesti et al. (2022b), 18) Tomičić et al. (2021b), 19) Ignesti et al. (2022a), 20) Sun et al. (2021), 21) Peluso et al. (2022). Masses are taken from Vulcani et al. (2018). Cluster redshifts and velocity dispersions are taken from Biviano et al. (2017) and Cava et al. (2009).

et al., 2013; Fisher et al., 2017). As one can notice, GASP jellyfish galaxies show an enhanced SFR at a given stellar mass, if compared to the control sample, most likely due to a short burst in star formation at the early stages of the stripping, as already shown by Vulcani et al. (2018). The six GASP galaxies for which *HST* data were collected (in red) occupy the high-mass end of the GASP distribution (above $3 \times 10^{10}\,M_\odot$), as expected since they are selected to have the largest number of clumps, but just two of them show enhanced SFR, namely JO201 and JO206. On the contrary, the starburst galaxies of the DYNAMO sample, selected to be particularly bright in $H\alpha$ (Fisher et al., 2017), are displaced much above the main sequence by almost an order of magnitude in SFR, with a particularly large specific SFR.

To probe star formation in both the tail and the disk of the galaxies, Gullieuszik et al. (2023) required observations in the broad band filters F275W and F336W and the narrow band F680N, which includes the $H\alpha$ spectral line at the redshift of the target galaxies. To subtract the continuum stellar emission from F680N and to probe the visible band light we also used the broad-band filters F606W and F814W (Section 2.3). In Figure 2.2 I show

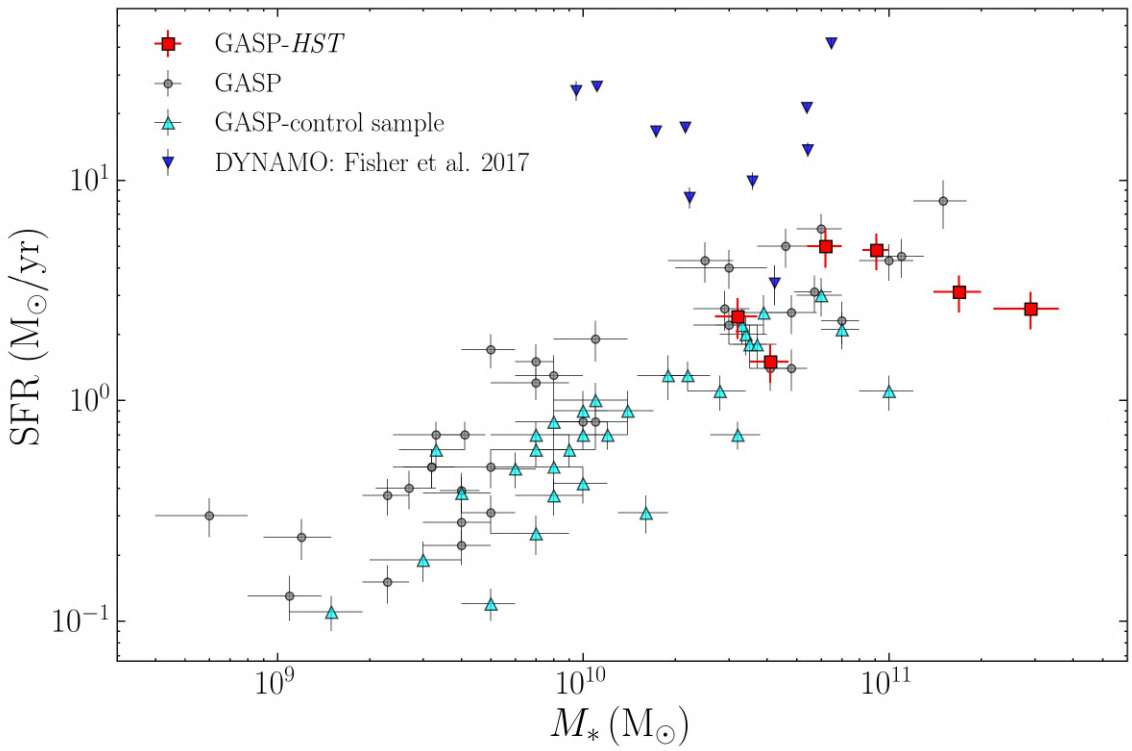

Figure 2.1: SFR-stellar mass relation for the GASP and DYNAMO sample. The six GASP jellyfish galaxies for which *HST* observations were taken (JO175, JO201, JO204, JO206, JW39 and JW100) are plotted as red squares, the other GASP jellyfish galaxies as grey dots, the GASP control sample (containing field galaxies or cluster galaxies showing no signs of any environmental process) as cyan triangle and the DYNAMO galaxies as blue triangles. GASP values are taken from (Vulcani et al., 2018), DYNAMO values from (Fisher et al., 2017).

the transmittance curves of the filters compared with three stellar spectra of different ages (0.01, 0.1 and 1 Gyr, respectively) to show the spectral features to which the filters are sensitive. The spectra are generated by BAGPIPES assuming a simple stellar population with solar metallicity and Kroupa IMF (Kroupa, 2001). As one can notice, the F275W and F336W can put strong constraints on the age of stellar populations older than 10 Myr, since the death of blue stars (Section 1.1) flattens more and more the near-UV slope, to which we are sensitive. Furthermore, the Hα, [N II]6548 and [N II]6583 triplet is completely covered by the F680N filter even considering the redshift spread of our galaxies, meaning that we can neglect variations in the sensitivity of the filter to these lines.

The UVIS PSFs in all the 5 filters does not change significantly and have a FWHM of 0.07 arcsec[1], corresponding to ~ 70 pc at the redshifts of the clusters hosting these galaxies ($0.0424 - 0.0650$, see Table 2.1). Gullieuszik et al. (2023) obtained five HST orbits[2] for each of the 6 target galaxies (2 orbits in F275W, 1 orbit each in F336W and F680N, and 0.5 orbit each in F606W and F814W) for a total of 30 orbits. For all observations a linear dither pattern to cover the gap between the 2 UVIS chips was adopted, and the exposure time was splitted in 4 single exposures for F275W and 3 exposures for all the other 4 filters. Details

[1]https://hst-docs.stsci.edu/wfc3ihb/chapter-6-uvis-imageing-with-wfc3/6-6-uvis-optical-performance
[2]An HST orbit is about 52 minutes long.

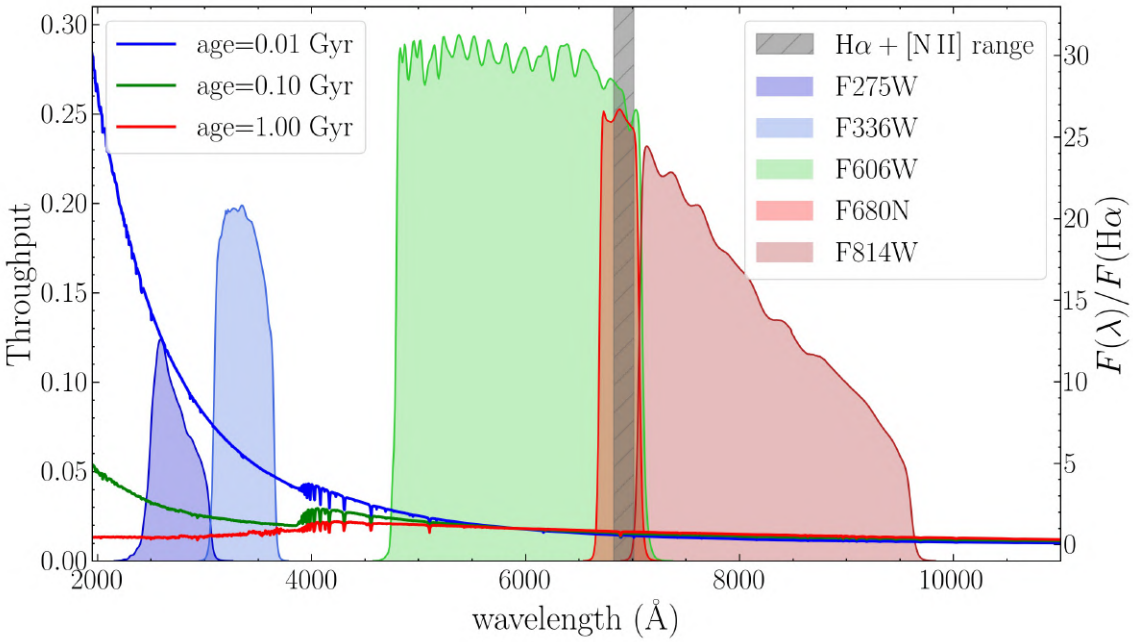

Figure 2.2: Transmission curves of the chosen *HST* filters compared to stellar spectra of different ages. The filters are (from left to right): F275W (blue), F336W (light blue), F606W (green), F680N (red), F814W (dark red). The stellar spectra are generated by BAGPIPES assuming a simple stellar population with solar metallicity, Kroupa IMF (Kroupa, 2001) and age of 0.01 (blue), 0.1 (green) and 1 Gyr (red), respectively. The grey shaded area marks the range of wavelengths in which the redshifted Hα, [N II]6548 and [N II]6583 triplet may fall.

Filter	Orbits	N exp	exptime	5σ mag	5σ mag
			sec	point src	1 arcsec $\times$1 arcsec
F275W	2	4	5283	26.9	25.0
F336W	1	3	2512	26.8	24.9
F606W	0.5	3	1038	27.4	25.4
F814W	0.5	3	1058	26.5	24.5
F680N	1	3	2507	26.1	24.1

Table 2.2: Description of the observations: filter name (1), number of orbits (2), number of sub-exposures (3) total exposure time – it is slightly different for each galaxy and here we report the mean value; (5) 5σ magnitude limit representative for point sources, computed using 5×5 pixels regions; (5) 5σ magnitude limit for 1 arcsec $\times$ arcsec regions. The computation of the last 2 columns is described in Sect 2.4.

are given in Table 2.2. Following STScI's recommendations (Instrument Science Report WFC3 2020-08), post-flash was used to mitigate the effects of UVIS CTE degradation. By using the calculations made with the Astronomer's Proposal Tool (APT), the post-flash was set to bring the average background level at 20 e^- per pixel to ensure that CTE losses remain at a manageable level.

2.2. *Data reduction and calibration*

We retrieved from the STScI archive the FLC files with the calibrated images (including the CTE correction) for each sub-exposure. All files were reduced and calibrated with the CALWF3 code v3.6.0, including the 2.0 version of the CTE algorithm, that was released in April 2021.

While individual FLC images taken with the same filters are perfectly astrometrically aligned, in most cases there are small misalignments between images taken with different filters. This is most likely due to the low number of stars bright enough in all filters. As described in Gullieuszik et al. (2023), to tweak the astrometric solution all sub-exposures taken with each filter were combined, with the F606W taken as an astrometric reference. After that, a number of astrometric reference sources in common with the F606W were selected for each of the other 5 combined images, preferentially non saturated stars, but also compact extragalactic sources. The star-forming regions spread along the tails of ionized gas were not used as astrometric references, as their emission can be displaced in observations at different wavelengths (see Section 5.3). In all cases a sufficient (> 10) number of sources evenly distributed in the field of view was found. These were then used to align all combined images to the F606W one using the TWEAKREG task; the astrometric solution was then propagated back to the FLC files using TWEAKBACK[3].

Cosmic ray removal is a critical task from *HST* data, especially considering that the main focus of this work is the detection and study of compact and bright stellar clumps in the tails of the target galaxies, objects that can be flagged as cosmic rays if the parameters are not correctly tuned. AstroDrizzle flags pixels in each FLC file as cosmic rays by computing the median and the standard deviation image of the available FLC files and comparing the counts in each pixel of the FLC files with those of the corresponding pixel in the median image. If the count difference between the two pixels (and the adjacent ones) is above a certain threshold, the pixel in the FLC file is flagged as a cosmic ray. The threshold is defined as a multiple of the standard deviation σ computed in the same pixel; the default threshold is 3σ, which is the one I adopted for most of the filters. However, the narrow-band F680N frames turned out to be particularly problematic, as the exposure time is relatively long and we have only 3 frames for each galaxy. Standard procedures could not provide a satisfactory result and I therefore adopted a slightly modified approach. The approach is similar to the one described in Cramer et al. (2019) to remove cosmic rays from areas of the images not covered by multiple exposures, in which they detected cosmic rays candidates, computed their emission in every available filter and cleaned from the image any source found in only one filter to higher than 12σ significance. Similarly to them, I computed the cosmic ray maps for the F680N by merging one cosmic ray map computed for the F680N with default parameters, following the same procedure adopted for the other filters, and one resulting by the combination of all the 9 FLC frames in filters F606W, F680N, and F814W, which were taken during the same visit. I systematically tested thresholds ranging from 7σ to 13σ, and I opted for a flag threshold of 9σ as the best compromise between an efficient flagging of cosmic rays and the need to avoid masking out emission coming from

[3]TWEAKREG, TWEAKBACK and AstroDrizzle, that is used for the following step, are included in the DrizzlePac Python package.

real sources.

Then I stacked together all FLC frames taken with each filter using AstroDrizzle. Following standard recommendations[4], I resampled the stacked images with a pixel-scale of 0.04 arcsec. An important parameter to take into account when performing the drizzling is `pixfrac` (p): p is the fraction by which input pixels are "shrunk" before being drizzled onto the output image grid, given as a real number between 0 and 1. It is important to regulate this parameter if one wants to avoid that the counts of a single pixel influence the counts of more than one output pixel. It is suggested to lower p with increasing number of input images. Therefore I set $p = 0.8$ for the F275W images (for which we have 4 exposures) and $p = 1$ for all the other filters (for which the exposures are 3).

I visually inspected the output images to look for residual cosmic-rays. The inspection was done by comparing the images of each galaxy in the 5 filters, flagging as cosmic-rays compact, bright and sharp-shaped emitting regions detected in one filter only.

Finally, I corrected the final stacked images for the Milky Way dust extinction using Schlafly & Finkbeiner (2011) reddening maps and the Cardelli, Clayton & Mathis (1989) extinction curve.

The RGB images shown in Figure 2.3 and published in Gullieuszik et al. (2023) are obtained using the F814W and F606W output images for the R and G channels, respectively; given the large difference in wavelength between the F814W/F606W and the F336W/F275W filters, for the B channel we created a pseudo B-band image as:

$$F_{\rm B} = 0.25\,(F_{\rm F275W} + F_{\rm F336W}) + 0.5\,F_{\rm F606W} \tag{2.1}$$

We then performed a non-local mean denoising on the 3 images used in the 3 channels using the scikit-image python package[5] (van der Walt et al., 2014). All the images in the 3 channels have been normalized using lower and upper limits of 0 and 10^{-19} erg/s/cm^2/Å and an arcsinh stretching function. The 6 RGB images were scaled to have the same spatial scale in kpc/pixel in Figure 2.3.

2.3. *Computing the Hα flux*

This Section describes the procedure to evaluate the Hα emission flux from the F606W, F680N and F814W observations. The procedure I followed for the extraction of emission-line maps has already been adopted and validated in the literature (Venemans et al., 2005; MacKenty et al., 2000). First, I assumed that the only line contributing to the F606W and F680N observed fluxes is Hα and that no line contributes to the F814W flux. Indeed other emission lines (Hβ and the [O III], [N II] and [S II] lines being the strongest) are in the spectral range covered by the three filters, but they have a minor contribution in most cases, as I will show in the following. This assumption can be written as:

[4] https://www.stsci.edu/scientific-community/software/drizzlepac.html

[5] `https://scikit-image.org/`

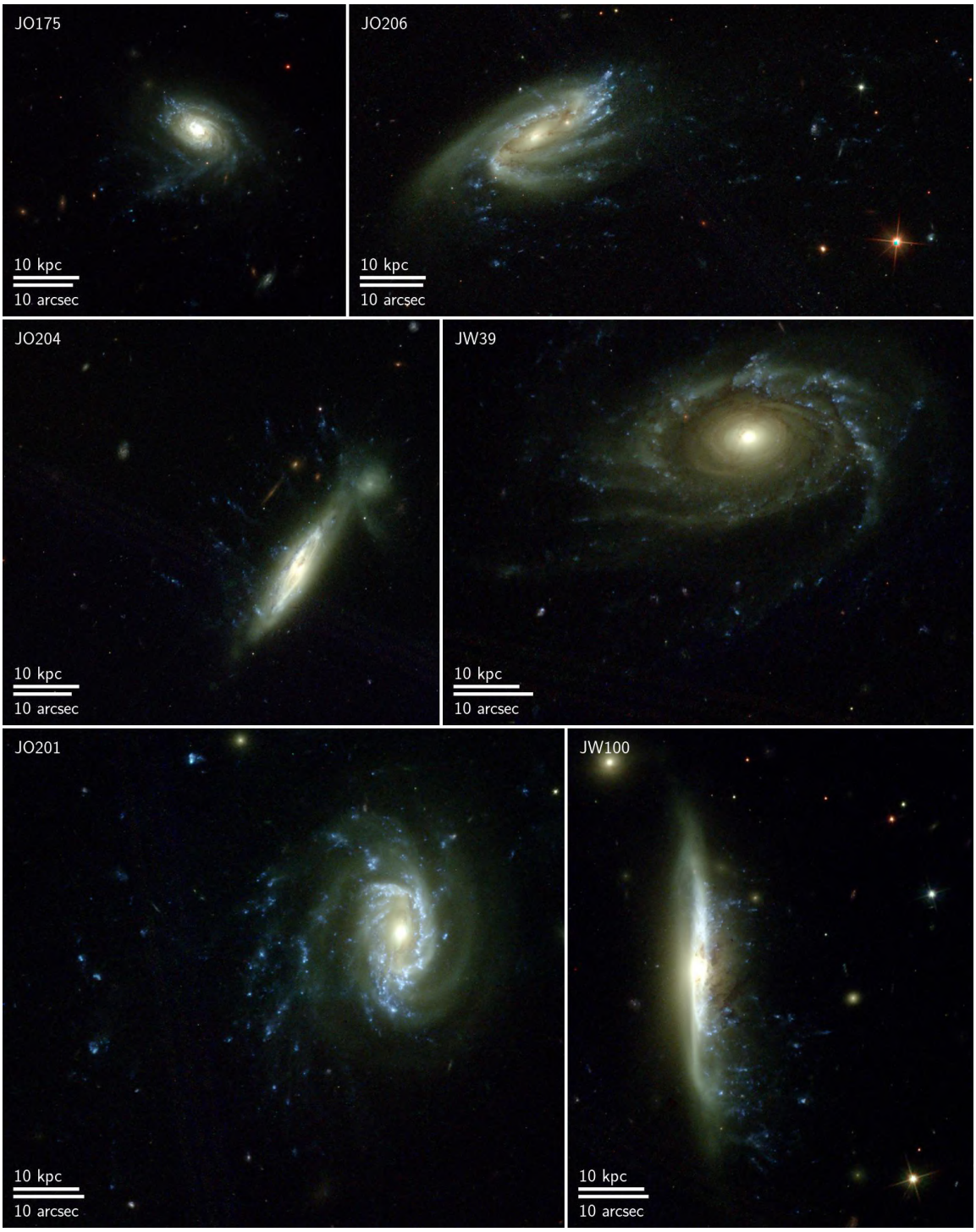

Figure 2.3: *HST* WFC3 images of the six observed galaxies (a description of the data used in each of the RGB channels is given at the end of Section 2.2). The scale in linear (kpc) and angular (arcsec) units are shown on the lower-left corner of each panel. All images have been zoomed to have the same scale in linear units (kpc per pixel). The luminosity cuts and stretching function are the same for all galaxies. North is up ad East is left. Images from (Gullieuszik et al., 2023).

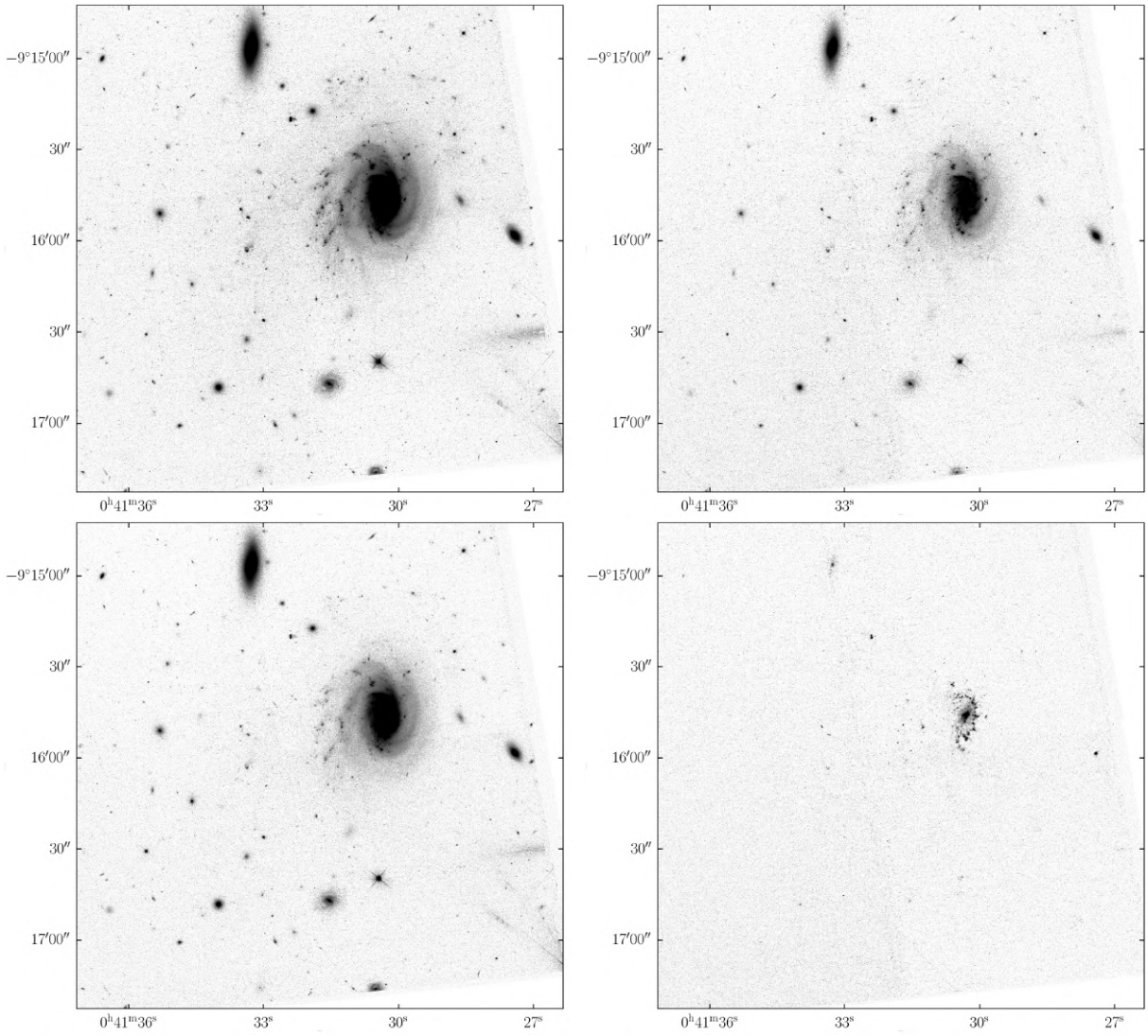

Figure 2.4: m
ap.]*HST* WFC3 images of JO201 in the filters F606W (top left), F680N (top right) and F814W (bottom left), and the Hα+[N II] map obtained from the continuum-subtracted F680N filter, as described in Section 2.3. The shown field of view is reported in Table 2.3.

$$\begin{aligned} F_{\mathrm{F606W}} &= F^{\mathrm{cont}}_{\mathrm{F606W}} + F_{\mathrm{H}\alpha}/w_{\mathrm{F606W}} \\ F_{\mathrm{F680N}} &= F^{\mathrm{cont}}_{\mathrm{F680N}} + F_{\mathrm{H}\alpha}/w_{\mathrm{F680N}} \\ F_{\mathrm{F814W}} &= F^{\mathrm{cont}}_{\mathrm{F814W}} \end{aligned} \tag{2.2}$$

where $F_{\mathrm{H}\alpha}$ is the line flux (in erg/s/cm^2) and for each filter f:

- F_f is the PHOTFLAM calibrated average measured spectral flux density;
- F_f^{cont} is the average spectral continuum flux density;

- w_f is the effective filter width. This was calculated using the RECTWIDTH method from the STSDAS package SYNPHOT (STScI Development Team, 2020), a python tool able to simulate photometric and spectroscopic data[6].

I also assumed that the spectral continuum flux density is a linear function of the wavelength in the spectral region of F606W, F680N and F814W:

$$\begin{aligned} F^{\rm cont}_{\rm F680N} =& a\ F^{\rm cont}_{\rm F606W} + b\ F^{\rm cont}_{\rm F814W} \\ a =& \frac{\lambda_{\rm F814W} - \lambda_{\rm F680N}}{\lambda_{\rm F814W} - \lambda_{\rm F606W}} \\ b =& \frac{\lambda_{\rm F680N} - \lambda_{\rm F606W}}{\lambda_{\rm F814W} - \lambda_{\rm F606W}} \end{aligned} \tag{2.3}$$

λ_f values have been calculated by creating a flat spectrum in F_λ and using the SYNPHOT EFFECTIVE_WAVELENGTH method. The resulting equation is

$$F_{\rm H\alpha} = 411.6\ F_{\rm F680N} - 242.3\ F_{\rm F606W} - 169.4\ F_{\rm F814W} \tag{2.4}$$

As mentioned at the beginning of this paragraph, the procedure I adopted assumes that Hα is the only emission line present in the observed wavelength range.

In the following the systematic effects due to the presence of other emission lines in star forming regions is quantitatively assessed, as described in Gullieuszik et al. (2023). At the redshift of the target galaxies the [N II]6548 and [N II]6583 lines are included in the spectral range of both the F606W and the F680N filters. Since the two lines are very close to Hα, their contribution is simply summed up to the contribution of Hα.

Therefore Equation 2.4 actually provides the sum of the flux of Hα and of the [N II] lines. In Gullieuszik et al. (2023) we compute the ratio $Q_{\rm N\,II}$ between the flux of Hα and the total flux of the three lines for different values of [N II]6583/Hα, assuming a fixed line ratio [N II]6583/[N II]6548 = 3.071 (Storey & Zeippen, 2000). $Q_{\rm N\,II}$ is equivalent to the ratio between the actual value of the Hα flux and the value obtained from Equation 2.4. Results are shown in Figure 2.5. For star forming regions ($\log$ [N II]6583/H$\alpha \lesssim -0.3$, red symbols) $Q_{\rm N\,II}$ is always larger than 0.6 which means that estimating the Hα flux using Equation 2.4 would overestimate the true flux by less than a factor ~ 1.6. Even for the regions with the most extreme AGN- or Liner-like line ratios the real Hα flux is at least $\sim 40 - 50\%$ of the estimated value.

Evaluating the effects of Hβ and [O III] is less straightforward. At the redshift of the target galaxies these lines are in the F606W band and therefore their emission flux contributes to over-estimate the F606W stellar continuum and consequently also the computed continuum in F680N (see Equation 2.3); this results in a systematic underestimation of the Hα flux computed from Equation 2.4. To quantify this effect, synthetic spectra with different line ratios were used to compute the fluxes in the UVIS photometric band and then

[6] `https://synphot.readthedocs.io/en/latest/`

the results of Equation 2.4 were compared with the value of the input Hα flux. Both input spectra creation and synthetic photometry computation were carried out with SYNPHOT. For the model spectra a continuum described by a linear function of the wavelength was adopted; quantitative tests were made to verify that the shape of the continuum has negligible effects on the results. Hβ, Hα, and the [O III] doublet at 4959 and 5007 Å emission lines were modeled using Gaussian profiles[7]. We adopted a fixed line ratio of 3.013 for [O III]5007/[O III]4959 (Storey & Zeippen, 2000) and 2.86 for Hα/Hβ and created a series of synthetic spectra for different values of the [O III]5007/Hα ratios. Using SYNPHOT, Gullieuszik et al. (2023) computed the fluxes in the UVIS photometric bands which were then used to evaluate the $F_{\mathrm{H}\alpha}$ from Equation 2.4; the ratio between the input Hα flux and the resulting value is reported as $Q_{\mathrm{O\,III}}$ in Figure2.5.

As expected, the Hα flux is always underestimated ($Q_{\mathrm{O\,III}} > 1$); when the [O III] emission is weak the effect is dominated by the Hβ emission and it is $\sim 5\%$, which is negligible considering all the sources of uncertainty. In general, for star forming regions ($\log$ [O III]5007/Hα)$\lesssim 0.25$, see central panel in Figure 2.5) $Q_{\mathrm{O\,III}}$ is smaller than 1.2 which means that Hα is never underestimated by more than $\sim 15\%$.

The throughput of the F680N filter is essentially constant between 6800 and 7000 Å with variations of a few percent; at 7040 Å its value is decreased by 10% and at redder wavelengths it drops rapidly. This might be an issue only for JW39, which is the galaxy at the highest redshift (see Table 2.1); using results from GASP observations with MUSE we can safely assume that there should not be any Hα or [N II] emission at wavelength longer than 7040 Å. We therefore conclude that the dependency of the filter throughput on wavelength has no significant effects on the Hα flux estimate.

I finally note that these considerations do not take into account dust effects; as dust attenuates Hβ and [O III] more than Hα emission it would therefore decrease the $Q_{\mathrm{O\,III}}$ value; as a consequence, the values discussed above are upper limits as any star-forming regions would have a non-negligible dust extinction.

It can therefore be concluded that the main source of uncertainty in my method to derive the Hα flux is due to the contribution of the [N II] lines. All other emission lines play a second order role that would in any case act in opposite direction to the one of [N II]; their contribution would therefore reduce the systematic effect due to the [N II] lines. In Section 3.4.1 I will describe how Hα fluxes have been corrected exploiting the already available MUSE data.

2.4. *Background variation, noise and detection limit*

This Section presents a statistical analysis of our images and an assessment of the noise level and the magnitude limit of our observations.

By construction, the average background in the final images is zero, but small-amplitude residuals are present on large spatial scales. These are shown in Figure 2.6 for two galaxies as an example. With the aim of enhancing large-scale structures and minimizing the local

[7]The actual shape of the line profile is negligible for this analysis, as it is based on synthetic photometry on bands much wider than the line profiles.

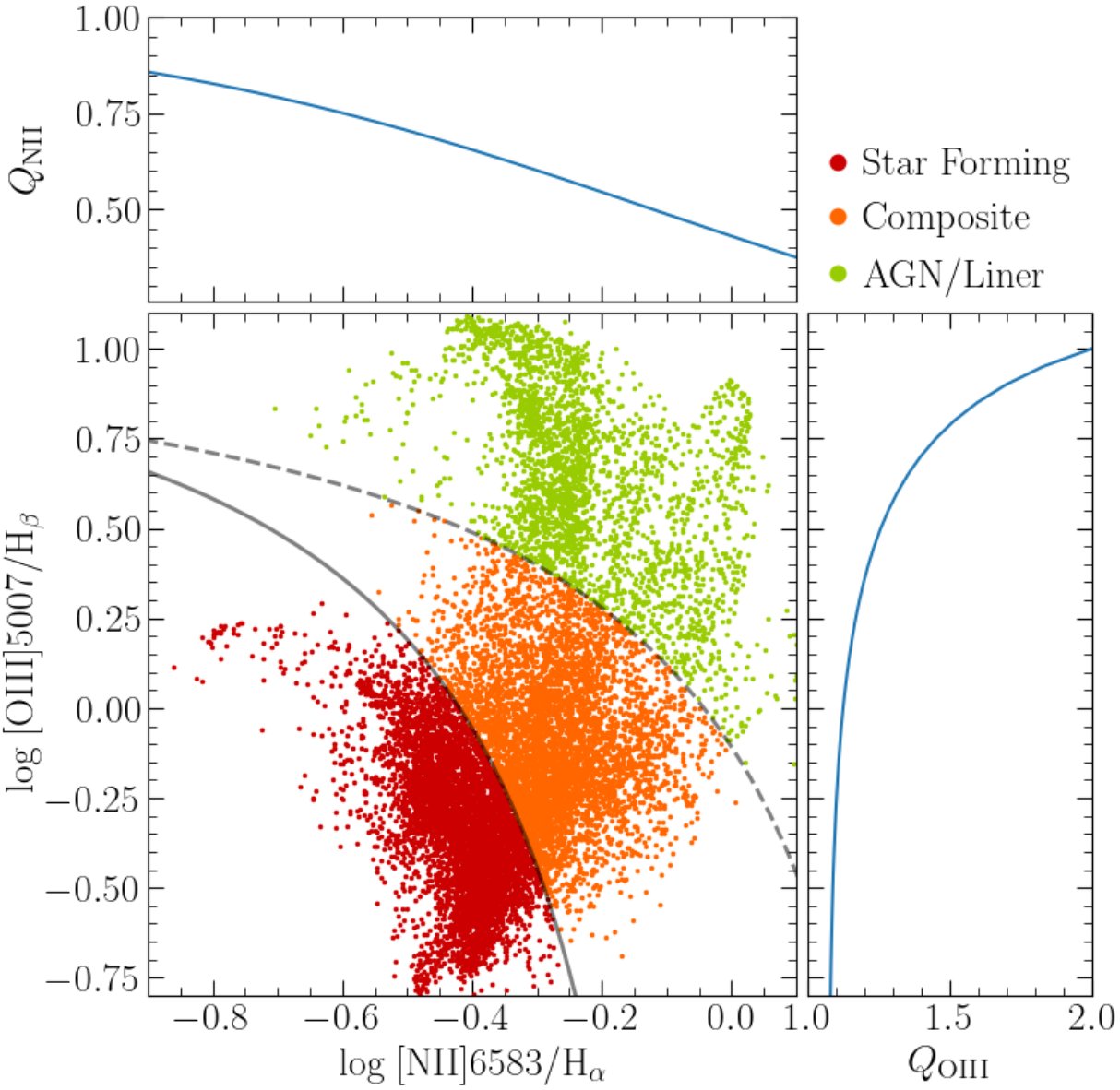

Figure 2.5: Values of $Q_{\rm N\,II}$ (top panel) and $Q_{\rm O\,III}$ (right panel) as a function of [O III]/Hβ and [N II]/Hα line ratios, respectively. We remind that Q is the ratio between the true Hα flux, as it is simulated, and the one derived as in Equation 2.4. The largest panel shows the range of [O III]/Hβ and [N II]/Hα line ratios using as a reference the BPT diagram obtained from MUSE observations of JO204 (Gullieuszik et al., 2017). Plot credits to Gullieuszik et al. (2023).

noise, in Figure 2.6 we binned 10×10 the DRC images and the results were divided by 100; the values in the resulting image can be therefore interpreted as spatially-averaged image with the same intensity scale as the original image. We then smoothed the image by convolving it with a 2D Gaussian kernel with a standard deviation of 3 pixels. The rightmost panels in Figure 2.6 show also results for the Hα emission maps obtained as described in Section 2.3.

First of all we note that in some of the images there are discontinuities corresponding

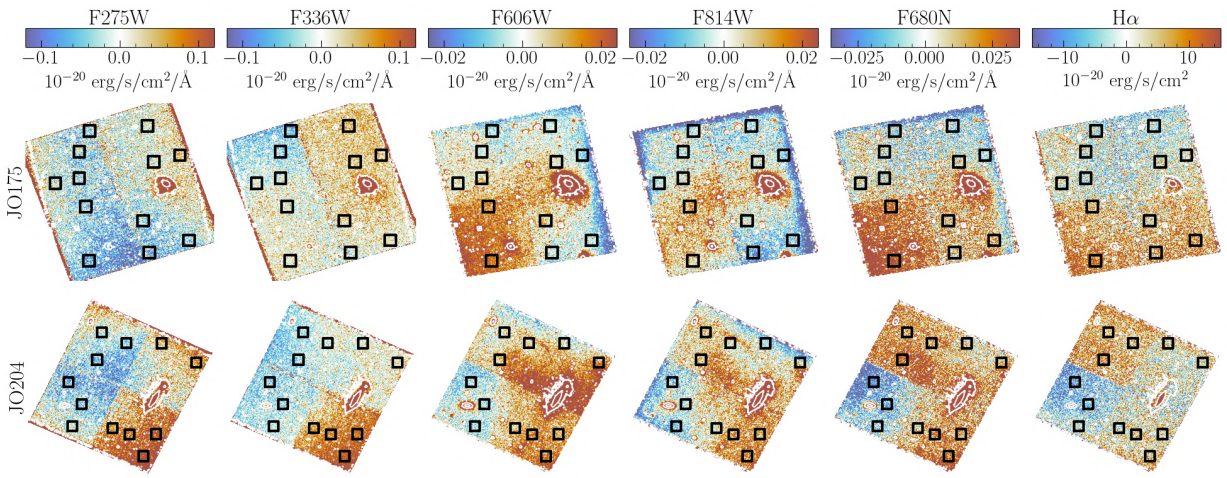

Figure 2.6: Images in the 5 UVIS filtes and the Hα emission map for two target galaxies. Images were smoothed and convoluted with a gaussian kernel to reduce the noise on small spatial scales and to highlight large scale background variations. The white contours are isophotes from the F606W image shown to visualize the stellar sources as a reference. The black squares show the 12 regions that were used to evaluate the statistical properties of the images. Plot credits to Gullieuszik et al. (2023).

to the edges of the 2 UVIS chips and of the two readout amplifiers in each of them. Besides these, all other large scale patterns are different from one image to the other; they might be due to a combination of uncertainties in the image reduction and calibration and/or to stray light components. We note that background variations are in all cases very small, of the order of 10^{-21} and 10^{-22} erg/s/cm^2/Å for the images in the two UV and the three visible filters, respectively. As we will show in the following, this is smaller than the average value of the local 1σ noise in the images. A further characterization of the background variations and investigation of its origin are therefore beyond the scope of this work as they do not significantly affect any of our conclusions.

The drizzling procedure induces correlated noise (Gonzaga et al., 2012) which was evaluated by carrying out a statistical analysis on regions of different size, from 1 (40 mas) to 25 pixels (1 arcsec). As described in Gullieuszik et al. (2023), first of all, for each galaxy we selected 12 regions of 300×300 pixels with no bright sources (see Figure 2.6). Since some faint and therefore not detected sources might be present, for each region, the background mean brightness value m and the rms noise σ were estimated with an iterative procedure. First guess values were estimated as the mean and the standard deviation of the counts in the region. We then fitted a Gaussian function to the values lower than $m + \sigma$. The m and σ values derived by the fitting procedure were then used to update the selection procedure and the fitting procedure was repeated to obtain a final value for the mean and rms noise of the counts. Then each of the 12 cutout images (one for each of the 12 regions) was re-binned using binning factors from 2 to 25, to estimate the statistical properties of the images on scales up to 1arcsec (25 pixels).

The standard deviation of the count rate in each of the 12 regions for all re-binning factors gives the noise on the corresponding spatial scale. The 12 noise values are consistent with each other indicating, as expected, that the noise level of the background is substantially constant across the images. For each spatial scale we calculated the average

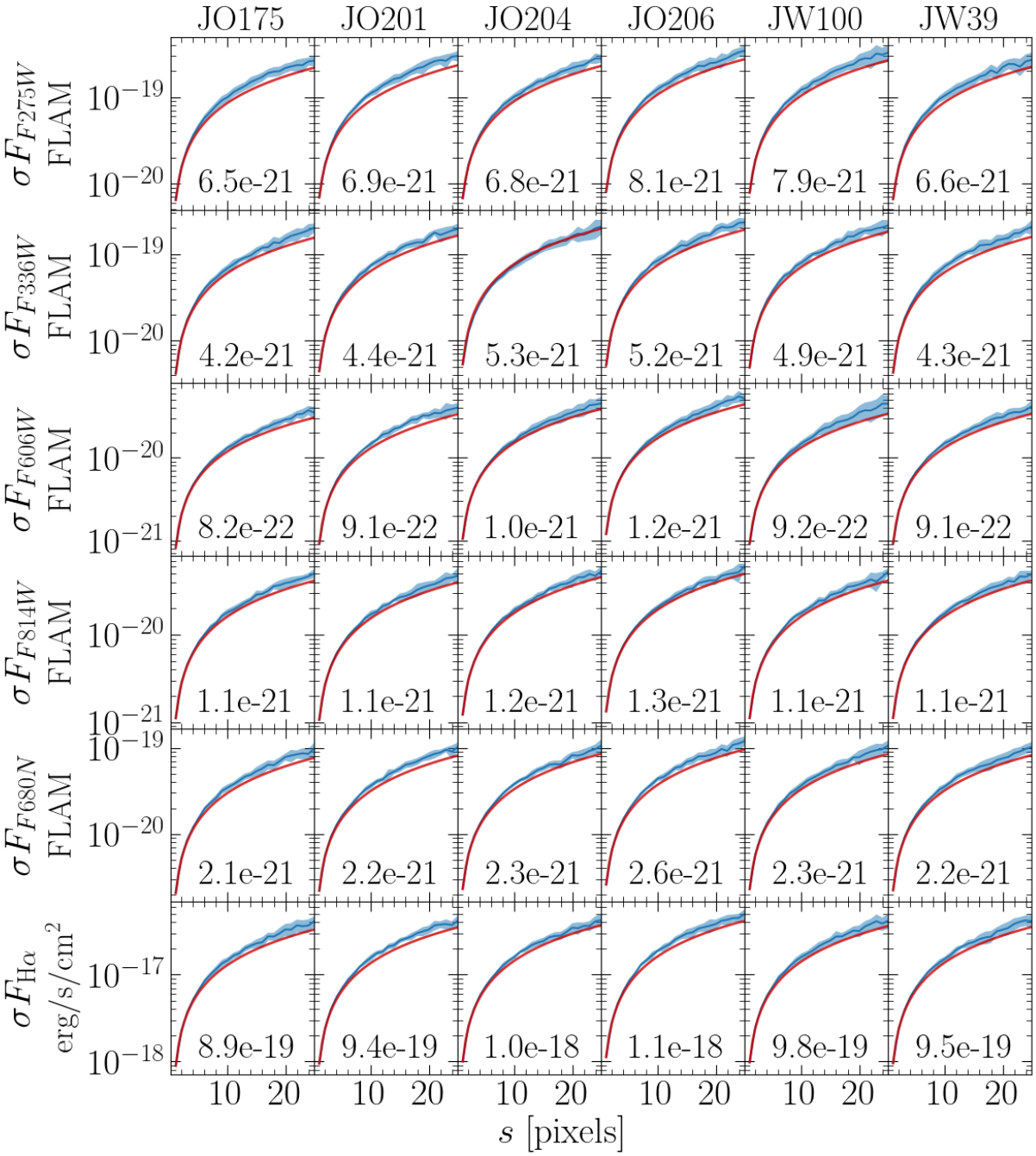

Figure 2.7: Mean value and dispersion (blue area) of the noise level at different scales computed in 12 different regions on each image. The red lines are predictions using the formula in Casertano et al. (2000). The values of the noise on 1 pix scales σ_1 are reported in each panel. Noise values are in erg/s/cm^2/Å for the images in the 5 filters (panels in the top 5 rows) and in erg/s/cm^2 for the Hα emission map (bottom row). Plot from Gullieuszik et al. (2023).

and the standard deviation of the noise values obtained for each of the 12 regions; these are shown in Figure 2.7 as blue shaded regions. The figure shows also predictions for the correlated noise using the formula from Casertano et al. (2000); for images drizzled with a PIXFRAC parameter equals to p, the noise on scales corresponding to N pixels is:

$$\begin{aligned} \bar{\sigma} &= \sigma(1)/(1-p/3) \\ \sigma(N) &= \bar{\sigma}\, N\, (1-p\, N/3) \end{aligned} \tag{2.5}$$

for our images $p = 0.8$ for F275W observations, 1.0 for all other filters (Section 2.2). These relations are shown as a red line in Figure 2.7 and show a good agreement with our data; the noise model from Casertano et al. (2000) underestimates the observed values in particular at large spatial scales. This is a well known fact that is commonly associated to a combination of the presence of very faint sources and small irregularities in the background, as was already found by Casertano et al. (2000).

These results were used to compute the magnitude limit of our observations. For each filter, the mean values of the noise levels in Figure 2.7 are computed and converted into AB magnitudes using the UVIS zero-points; to estimate the detection magnitude limit for point sources we used the noise computed on 5×5 pixels regions, corresponding to the values generally used on exposure time calculator; a magnitude limit more representative for extended sources was computed from the values obtained for 1 arcsec $\times$1 arcsec. The results are shown in Table 2.2; they are in good agreement with the values obtained with the UVIS exposure time calculator. For the Hα flux we obtained a 1σ detection limit of 7×10^{-18} erg/s/cm^2 for point sources and 4×10^{-17} erg/s/cm^2/ arcsec^2 for diffuse emission.

At the redshift of the target galaxies ($z \sim 0.05$) the Hα point source detection limit corresponds to a luminosity $L_{\mathrm{H}\alpha} = 4{\times}10^{37}$ erg/s. This value is very similar to the luminosity of the faintest knots detected for GASP galaxies with MUSE (Poggianti et al., 2019). We note, however, that clumps larger than the UVIS resolution ($\sim$ 70pc FWHM) can not be approximated by point-like sources; in this case their flux would be spread on a larger area and consequently the detection limit would be brighter than the one estimated for point-like sources.

2.5. *Preparing the data for clump detection: denoising and field of view*

The clump detection (that I will describe in detail in Section 3.2) is a process that may take a lot of computational time, both to individuate clump candidates and to select and clean the sample from spurious detections. Therefore I decided to treat the images in order to make this procedure more efficient and less time consuming: the first step is the denoising of the images (Section 2.5.1), which can erase local noise fluctuations, allowing us to detect faint clumps without being overwhelmed by spurious clump candidates; the second step is a limit in the field of view (Section 2.5.2), in order to avoid to run the clump detection algorithm over an area pointlessly large.

ID_{P16}	RA_{center}	Dec_{center}	width
JO175	20:51:17.6169	-52:49:47.189	2.00'
JO201	0:41:31.7471	-9:16:02.613	2.67'
JO204	10:13:47.2256	-0:54:46.617	1.60'
JO206	21:13:44.1417	+2:28:06.535	3.27'
JW39	13:04:08.8132	+19:12:17.151	2.20'
JW100	23:36:23.0832	+21:04:47.508	1.93'

Table 2.3: Properties of the *HST* images sub-FOV used to detect clumps. For each galaxy (ID_{P16}) the center coordinates (RA_{center} and Dec_{center}) and the width of the sub-FOV (width) are listed. Sub-FOV are always squared.

2.5.1. *Denoised HST images*

I performed the denoising using a Python software package called PySAP[8] (Farrens et al., 2020).

This algorithm expands the image in Fourier series and The parameters were set to remove the high-frequency components, which are typically due to noise, with a pixel-scale for which the denoising is performed of 2 pixels. In particular, PySAP includes a set of sub-packages particularly well suited for solving linear inverse imaging problems of the following form

$$\mathbf{y} = \mathbf{H}\mathbf{x} + \mathbf{n}, \tag{2.6}$$

where $\mathbf{y}$ is the observed image, $\mathbf{H}$ is a degradation matrix that could constitute blurring, sub-sampling, distortion, etc., $\mathbf{x}$ is the true image that one aims to recover and $\mathbf{n}$ is noise. Denoising basically consists of solving the equation above to find the noise $\mathbf{n}$ and remove it from the image, though it can slightly decrease the resolution of the observed image. This procedure allows us to detect also fainter regions without being dominated by noise, but does not yield reliable sizes. This is the reason for not working with denoised images only.

2.5.2. *Choice of the field of view*

Throughout this work, we work on a smaller squared field-of-view (see Table 2.3) with respect to the entire *HST*-WFC3/UVIS images (2.67 arcmin $\times$2.67 arcmin), still sufficient to cover the entire extension of the galaxies and their tails.

2.6. *MUSE data*

Throughout this work, I also exploit the information obtained from the GASP survey to remove regions powered by AGN or shocks using BPT maps (Baldwin, Phillips & Terlevich, 1981), to confirm the redshift of star-forming clump candidates and to correct the F680N filter for the line emission of [N II]. All galaxies were observed in service mode with the Multi

[8] `https://cea-cosmic.github.io/pysap/index.html`

Unit Spectroscopic Explorer (MUSE, Bacon et al. 2010). MUSE is an integral-field-unit spectrograph with a 1 arcmin ×1 arcmin field of view, sampled with 0.2 arcsec ×0.2 arcsec pixels. The typical seeing of the MUSE observations is 1 arcsec (0.7−1.3 kpc at the redshifts of these galaxies, Table 2.1). Furthermore, MUSE spectra cover a spectral range going from 4500 to 9300 Å, sampled at ∼ 1.25 Å/pixel and with a spectral resolution of 2.6 Å. The data were reduced using the most recent version of the MUSE pipeline available at the time of each observation (Bacon et al. 2010, from version 1.2 to 1.6), as described in details in Poggianti et al. (2017a). The datacubes were then corrected for Galactic extinction using the extinction law and the reddending map by Cardelli, Clayton & Mathis (1989) and Schlegel, Finkbeiner & Davis (1998) (considering the recalibration introduced by Schlafly & Finkbeiner 2011), respectively. Fluxes, velocities and velocity dispersions of the gas emission lines were obtained using KUBEVIZ (Fossati et al., 2016), after subtracting the stellar-only component derived with SINOPSIS (Fritz et al., 2017).

As example, in Figure 2.8 I show the MUSE Hα contours overplotted to the white images (obtained integrating the MUSE over the whole spectra range) of the six target galaxies. One can appreciate the huge improvements brought by *HST* in terms of spatial resolution with respect to this images, even if the MUSE of course gives important spectral information unavailable with the purely photometric *HST* dataset.

2.6.1. *MUSE knots*

Star-forming knots in the disks and tails of the target galaxies were already observed and studied using MUSE observations (Poggianti et al., 2017b, 2019). The sample comprises 778 knots, 516 in the tails (defined as described in Section 3.1.3 and listed galaxy per galaxy in Table 2.1), detected in Hα with a spatial resolution of 1 kpc. The Hα surface brightness of these knots ranges between $10^{-16.5}$ and 10^{-15} erg/s/cm^2/arcsec^2. The spatial resolution that can be achieved with MUSE (∼ 1 kpc) does not allow a study of the morphological properties of these structures, which is why *HST* observations were necessary. Nonetheless, this sample is useful to confirm the detection of an *HST* clump candidate, especially in the tails and for clumps detected in UV. Indeed the photometric dataset available with *HST* can not confirm the redshift of clump candidate if the Hα emission line is too weak or absent, which may occur if the clump is too faint or, even if rather young, has already quenched star formation. The absence of the emission line makes it tricky to constrain the redshift of UV-detected clump candidates and confirm their connection to the target galaxy. Therefore spectroscopic redshifts available for MUSE Hα knots can be used to confirm the belonging of *HST* tail clump candidates to the jellyfish galaxy by spatially matching the two samples.

As extensively described in Poggianti et al. (2017b), the location and radius of these knots are found through a purposely devised shell script that includes IRAF and FORTRAN packages. In the first step, the centers of knot candidates are identified as local minima onto the laplace+median filtered Hα image derived from the MUSE datacube. A "robustness index" based on the counts gradient toward the knot center for pixels around it is used to confirm the detection.

The radii of the knots are computed through a recursive (outward) analysis of three at a time, consecutive circular annuli (of one pixel thickness) around each knot center. The

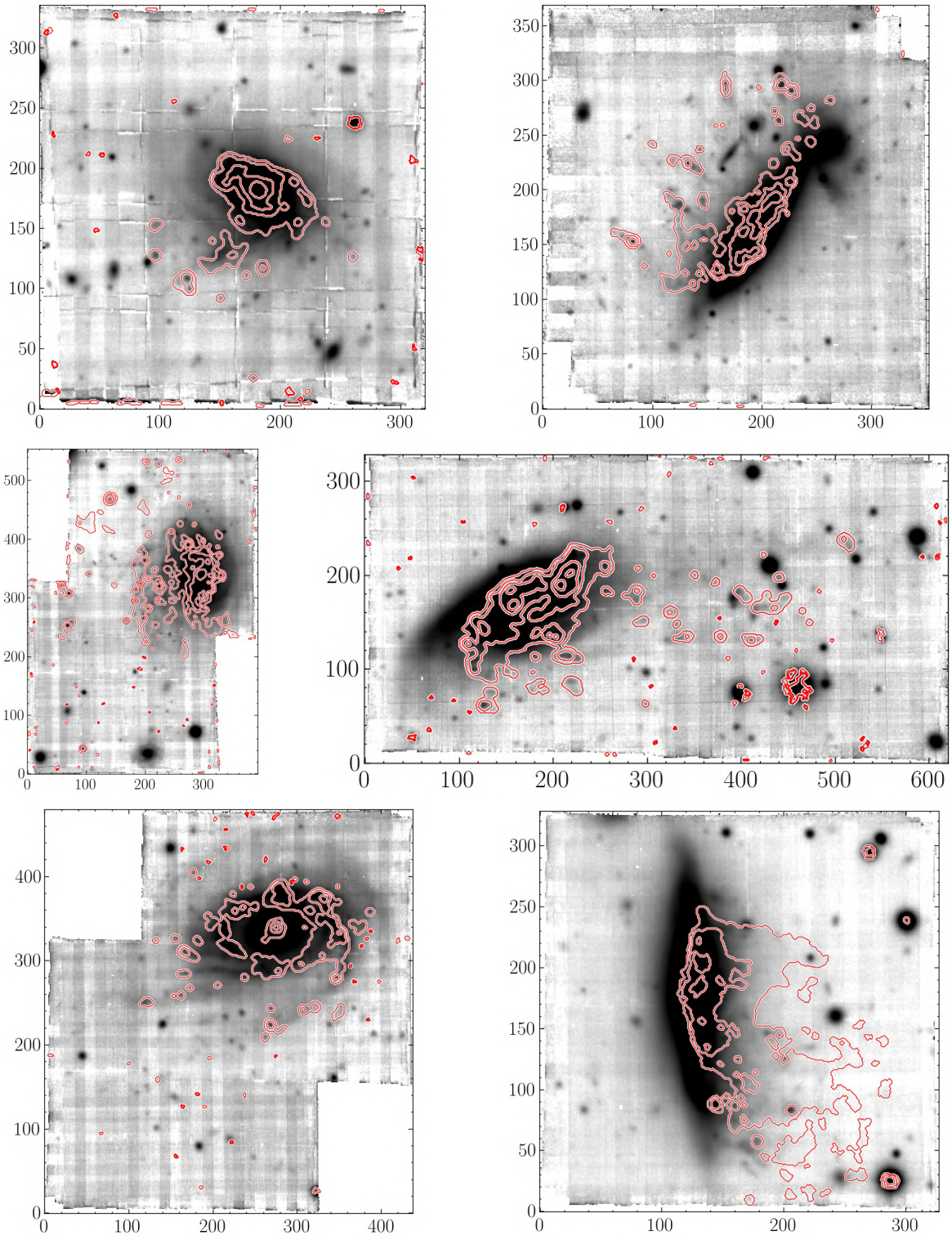

Figure 2.8: MUSE Hα contours (in red) overplotted to the white images (obtained integrating the MUSE over the whole spectra range) of the six target galaxies. The contours are at fluxes of 1, 4, 15 and 60×10^{-18} erg/s/cm^2. From left to right and top to bottom: JO175, JO206, JO201, JO204, JW39, JW100.

algorithm stops and the knot's radius is computed after the occurrence of at least one of the following four conditions: (1) at least one pixel exceeds in counts those of the peak pixel; (2) the fraction of pixels with counts larger than the average counts of the preceding shell ("bad" pixels) exceeds a given threshold (typically 1/3); (3) the average counts of "good" pixels are below a given maximum value; and (4) the image borders are reached. All the integrated quantities of the knots, including fluxes, are computed within the area defined by the knot radius.

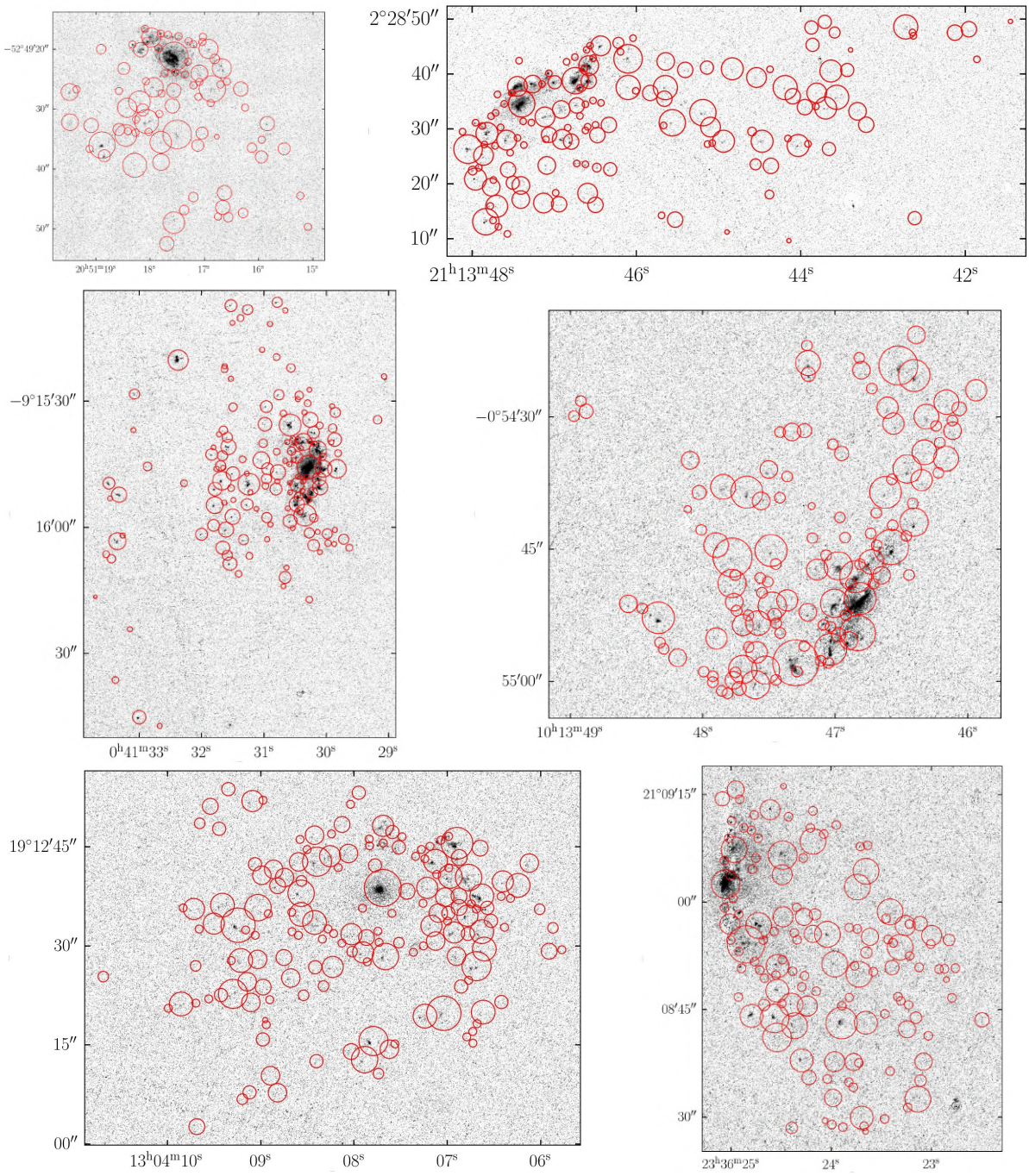

Figure 2.9: Star-forming knots detected in Hα from MUSE images (Poggianti et al., 2019) plotted on the Hα *HST* images for the six target galaxies. Each knot is plotted as a red circle as large as the size of the knot. From left to right and top to bottom: JO175, JO206, JO201, JO204, JW39, JW100.

Chapter 3

Method

This Chapter starts with a qualitative description of the images in Section 3.1, followed by the procedure adopted to select and classify the star-forming clumps and complexes of our sample (Section 3.2). The number of sources is presented in Section 3.3, together with their spatial distribution in the images, while in Section 3.4 I define all the samples used thereafter and describe their properties. Finally, in Section 3.5, I present the catalog of clumps that was publicly released.

3.1. *Galactic centers and evidence of stripped clumps inside disks*

In this Section I start from a visual inspection of the single filters and RGB images of the target galaxies, focusing on their disks. Since the *HST* spatial resolution is higher than the one obtained with MUSE, we can better observe both the morphology of the central regions powered by AGNs (Section 3.1.1), firstly identified with MUSE, and of the clumps inside the galactic disk (Section 3.1.2). The latter ones show in many cases an elongated and filamentary morphology (especially in UV) that is most likely caused by ram-pressure stripping. In order to disentangle clumps born from stripped gas still observed inside the optical disk (most likely because of projection effects), in Section 3.1.3 I define the three *spatial categories* (*disk*, *extraplanar*, *tail*) under which the clumps are classified. Such categories are based on the definition of the optical galactic disk contour (updating the definition given in Gullieuszik et al. 2020 from the MUSE images) and the UV inner disk contour.

3.1.1. *Central regions of the galaxies*

This Section focuses on the central region of the 6 target galaxies; the UVIS data allow us to study with unprecedented high resolution the source of the bright central emission and to complement the available MUSE spectroscopy to better constrain its nature. Results from the GASP survey showed that JO201, JO204, JO206 and JW100 galaxies host an AGN (Radovich et al., 2019); the JW39 central region has a LINER-like spectrum (Peluso

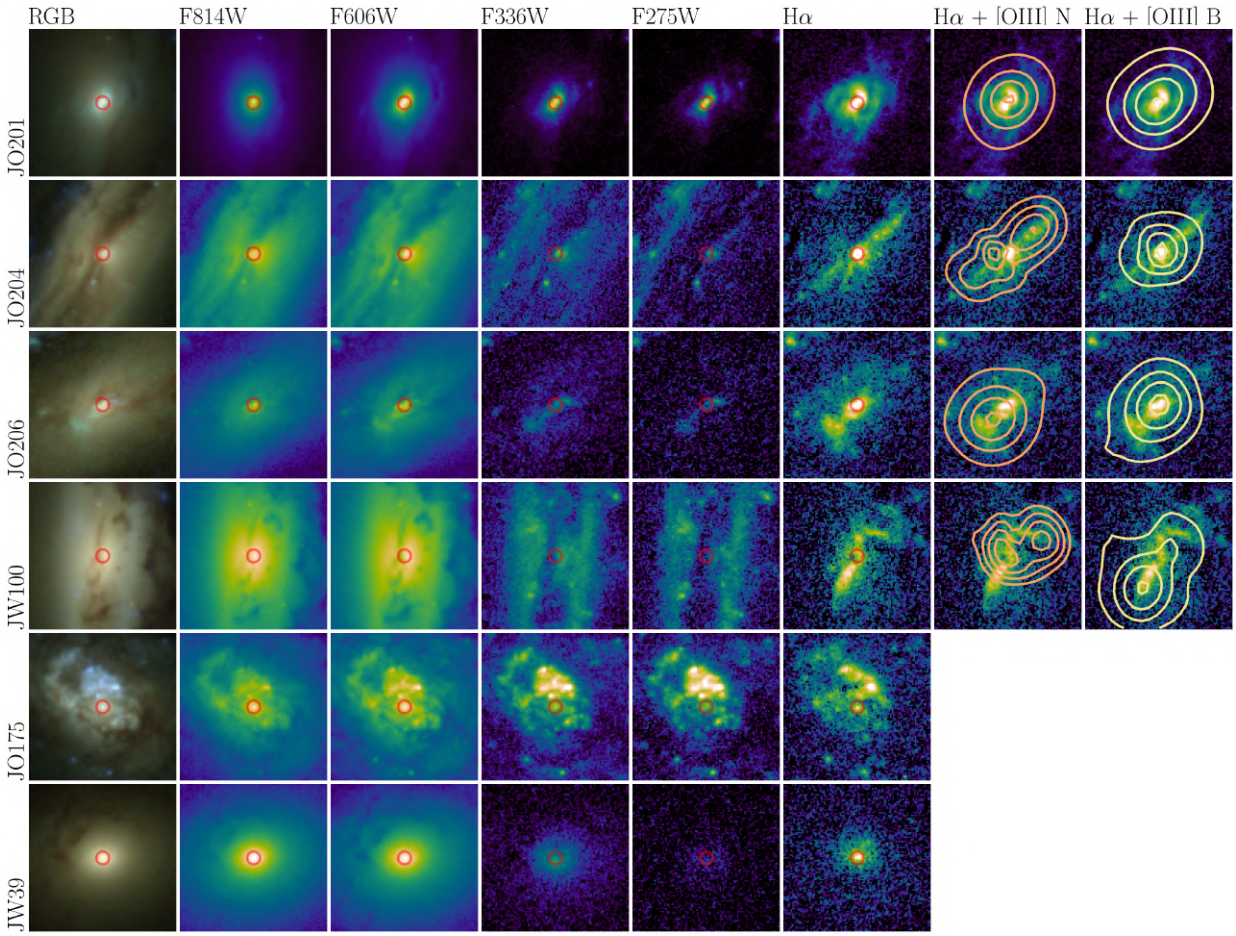

Figure 3.1: RGB image, Hα emission map, and broad-band images of the central 4 arcsec $\times$4 arcsec of the 6 target galaxies. The red circle marks the center of the galaxies. The RGB images in the leftmost column are obtained as the other ones presented in this paper but using different luminosity cuts to better visualize the bright central regions. The background image in the two rightmost panels is the Hα emission map; the contours show the flux of the broad (light yellow) and narrow (light orange) components of the [O III]5007 detected with MUSE (Radovich et al., 2019). An interactive visualization of the data presented here is available at `https://web.oapd.inaf.it/gullieuszik/hst_gasp_centers` and in the online version of Gullieuszik et al. (2023).

et al., 2022); finally, ionization in the central region of JO175 is dominated by star-forming activity (Poggianti et al., 2019; Radovich et al., 2019).

The central regions of the galaxies are shown in Figure 3.1. A large number of very compact sources are detected in the central region of JO175; they are bright both in the UV and in the Hα maps and faint in F814W; we can therefore conclude they are young star-forming regions, confirming the results obtained from MUSE (Poggianti et al., 2019; Radovich et al., 2019). JW39 emission is dominated by a source with a regular elliptical morphology at the center of the galaxy; it is clearly detected in Hα and in F336W and extremely faint in the F275W; indeed among the 6 central sources it is the one with the reddest F275W-F336W color; the most plausible scenario is that the central region is obscured by dust and/or older than the central regions of the other galaxies.

All the other 4 galaxies host an AGN; the [O III]5007 line is therefore expected to be

extremely strong in the central regions and therefore the Hα flux we computed could be significantly underestimated as discussed in Section 2.3; we note that none of the conclusions of this work will be based on the Hα flux of the regions dominated by AGNs.

The morphology of the central regions for these galaxies varies significantly at the different wavelengths (Figure 3.1). Multiple dust lanes are present in the nuclear regions, in particular in JO204, JO206 and JW100: this is often observed in *HST* images of type-2 AGN (see e.g. Keel et al., 2015; Ma et al., 2021). In particular, Keel et al. (2015) attributed the presence of irregularly distributed dust lanes, similar to those observed here, in local galaxies of the Sloan Digital Sky Survey to ongoing or past interaction processes.

HST observations also reveal the detailed morphology of the bright Hα emission already observed with MUSE, that was proved to be predominantly ionized by the AGN based on the analysis of the emission line ratios in MUSE (Radovich et al., 2019). MUSE data also showed that emission lines in JO201, JO204 and JW100 clearly present at least two components in the line profiles, one *broader* ($\sigma_v \sim 200-500$ km s^{-1}) and the other *narrower* ($\sigma_v < 200$ km s^{-1}). Both components can be related to outflows, which in Radovich et al. (2019) were defined as those cases where the line velocities deviate significantly from the rotational field traced by stellar velocities measured at the same positions (see also e.g. Davies et al., 2020). In Figure 3.1 we overlay on the *HST* Hα images the contour maps of the [O III]5007 flux in these two components. This allows us to compare the *HST* Hα properties with the analysis of outflow properties done in Radovich et al. (2019), to which we refer for more details. In JO201 both [O III] components overlap well with the Hα central, more compact emission; this agrees with the interpretation that in JO201 the outflow orientation is close to the line of sight. In JO204 the Hα emission shows a more extended structure: the broader [O III] component overlaps with the central emission, the narrower one is peaked at two opposite positions along the Hα emission; both components were associated to the outflow. Similarly, in JW100 there are two [O III] components of similar width ($\sigma_v < 200$ km s^{-1}) emitted by distinct regions along the Hα emission and merging into a double peaked profile in the inner regions, which were also associated to an outflow. Finally, [O III] shows a very faint broader component in the central MUSE spaxels of JO206, and Radovich et al. (2019) concluded that it was not possible to detect a meaningful outflow component: we notice however that this component overlaps well with the Hα peak. The dominant, narrower component still follows the Hα emission, but there is an offset between the peaks of the two maps. To summarize, though both the broader and narrower components may be related to outflows and the Hα maps include the contribution from both, it can be seen that the emission from the broader component is peaked on the central Hα emission, thus confirming that it is mostly emitted by the inner nuclear regions. The narrower components are instead coincident with a more extended Hα emission.

3.1.2. *Galaxy disk and stripped gas in the inner regions*

The high potential of the diagnostic power of UVIS observations can be appreciated in Figure 3.2 in which I show a zoom on the galaxy disk of JO204, JO206, and JW100 of the RGB images from Figure 2.3. The same figure also shows the F275W and F814W images, to probe star-forming and intermediate-old stellar populations. In each panel I also show, as a reference, the line derived from GASP data to define the stellar disk and the stripped

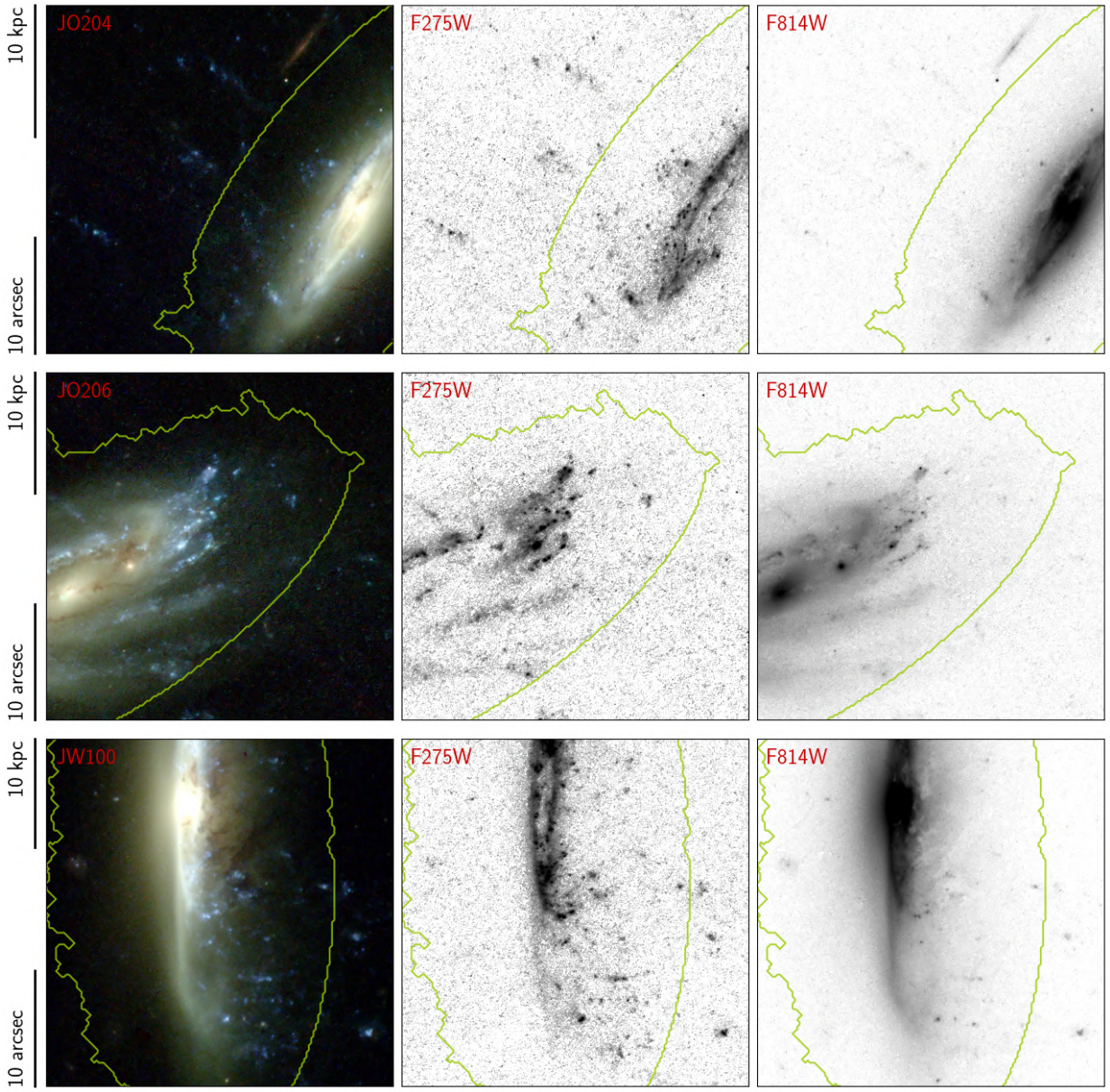

Figure 3.2: RGB, F275W, and F814W images of JO204, JO206, and JW100. The green line is the galaxy disk contour derived from MUSE observations (Gullieuszik et al., 2020). Images from Gullieuszik et al. (2023).

gas tail (Gullieuszik et al., 2020).

HST observations provide a detailed view of the complex structure of the galaxy disk and of the inner galactic regions; the 1 kpc spatial resolution of MUSE and UVIT observations does not allow to clearly resolve and characterize sub-structures, in particular for galaxies with a substantial inclination in the plane of the sky. As a consequence, it is also extremely difficult to clearly disentangle structures belonging to the disk and to the stripped tail; previous GASP works therefore adopted a conservative approach to define star-forming regions that can be safely classified as being formed in the stripped gas tail. This was

done by considering the stellar continuum emission and using the isophote corresponding to a surface brightness 1σ above the average background; the isophote is not symmetric due to RPS and hence an ellipse was fitted to the undisturbed side of the isophote; this ellipse was used to replace the isophote on the disturbed side (for details see Gullieuszik et al., 2020). The resulting contour line is shown in green in Figure 3.2. *HST* data allow us to go beyond this simple approach and they provide robust clues on how RPS affects the inner region of galaxies. Figure 3.2 shows bright regions in the disk that are particularly bright in the UV and barely visible -or not visible at all- in the F814W image; they hence stands out as bright and blue sources in the RGB images; most of them have also Hα emission associated with the UV bright emission. We also note that they are organized in filamentary structures aligned in the direction of the tail. For these reasons we can safely conclude that the observed bright regions are young stellar clumps that are formed in gas stripped from the stellar disk by ram pressure. Being so close to the galactic disk, we can not say whether they are still gravitationally bound to the galaxy, eventually falling back in the galaxy disk, or not and hence they will be completely stripped and lost in the ICM.

Many star-forming regions are organized in filamentary structures, in agreement with cloud-crushing simulations of cold clouds in a hot wind; these have been able to produce long tails of cold, dense gas that are about the cloud width and extend for tens of cloud radii when the radiative cooling time is shorter than the cloud destruction time (e.g. Gronke & Oh, 2018; Abruzzo, Bryan & Fielding, 2022; Tan, Oh & Gronke, 2022). Recent simulations have found star formation within these streams from individual dense $\sim$ 100 pc clouds (Tonnesen & Smith, in prep).

Since one of the interests of this work is to study the effects of local environment on star formation, in the following Section I exploit the high resolving power given by *HST* to refine the definition of galactic disk given in Gullieuszik et al. (2020) and Poggianti et al. (2019), in order to better distinguish star-forming regions originating from stripped gas embedded in the cluster environment from those that are not.

3.1.3. *Definition of disk, extraplanar and tail regions*

In analogy with what was done for the MUSE observations (Gullieuszik et al., 2020), the starting point to define the stripped tails is the definition of the galaxy stellar disk. As already noted in Section 3.1.2 (see also Figure 3.2), the high spatial resolution of *HST* allows us to characterize the galaxy substructures and the stellar disk in more detail than what is possible with MUSE. I used the 2σ contour of the reddest photometric band available (F814W) to draw the most external boundary of the stellar optical disk. 2σ values range from 2.14 to 2.67 $\times$ 10^{-21} erg/s/cm^2/Å per pixel. I will refer to this contour as the galaxy optical contour (white dashed lines in Figure 3.3) and I define as *tail* the region beyond it.

As already pointed out in the previous Section, in the disks of these galaxies there are some regions particularly bright in UV (band F275W), faint in optical (band F814W), elongated and aligned in the same direction of the tails. Therefore, they are likely to be young stellar populations formed in gas already stripped by ram pressure, but still inside the galaxy optical contour because of projection effects or because RPS is at an early stage: I call these regions *extraplanar*. In order to separate the extraplanar regions from those still in the disk, I visually inspected the UV contours (green contours in Figure 3.3) over-

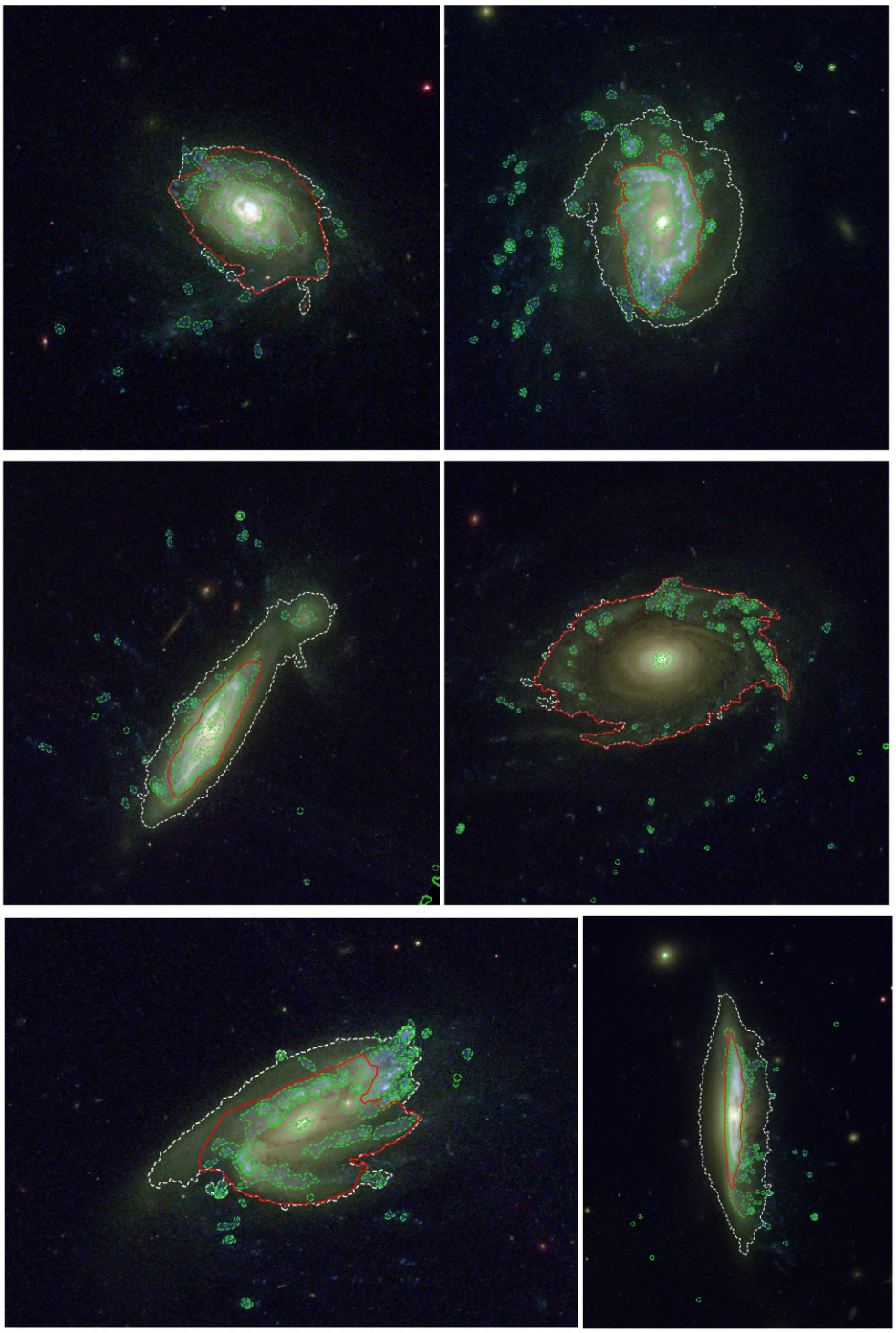

Figure 3.3: Zoomed-in version of RGB images in Figure 2.3 of JO175, JO201, JO204, JO206, JW39, JW100 (from top left to bottom right). The three colours of the RGB images are: F814W (red), F606W (green), a combination of F275W, F606W and F814W (blue). Details are given in Section 2.2. The white dashed contours are the optical disks, defined as the 2σ contour in F814W. The green dashed contours are the 1σ, 2σ, 3σ and 5σ UV (F275W+F336W) contours (smoothed for clarity). The red line is the inner disk contour, traced as described in Section 3.1.3. Images from Giunchi et al. (2023a).

plotted to RGB images of the target galaxies. Looking at the UV morphology of the clumpy sources, I traced an inner disk contour (red solid lines in Figure 3.3) to separate clumps with an elongated appearance and aligned along the likely stripping direction from those looking round and undisturbed. I define as *disk* the region within the inner disk contour and as *extraplanar* the region within the galaxy optical contour but outside the inner disk UV contour. We point out that projection effects make it difficult to completely separate undisturbed and stripped gas.

3.2. *Clumps and complexes detection*

This Section presents the procedure we developed to detect star-forming clumps and to measure their properties. This procedure was applied independently to both the F275W and Hα images (Section 3.2.2), in order to trace star formation on different timescales ($\sim$ 200 Myr and $\sim$ 10 Myr, respectively, Kennicutt 1998; Kennicutt & Evans 2012; Haydon et al. 2020). In addition, a slightly modified version of the same procedure is also applied to the F606W images to fully recover the stellar content in the galaxy tails and will be described in (Section 3.2.3).

3.2.1. *The* Astrodendro *software package*

The clump detection is performed using ASTRODENDRO[1], a software package created to compute dendrograms of observed or simulated Astronomical data. This software detects bright clumps and sub-clumps inside them, classifying them in a hierarchical tree structure.

Clumps are defined as local maxima on the image; then the image is analyzed at fainter and fainter flux levels and the clumps grow by including fainter pixels. Eventually, at some point, adjacent clumps might blend together. In this case, those clumps stop growing and are defined as children of a common parent clump; for the following steps, when fainter flux levels are considered, only the parent clump keeps growing. When the flux threshold reaches a given value (see MIN_VALUE below), the algorithm stops and the tree structure is built: starting from the clumps at the base of the tree (i.e. the most extended ones), to which a level equal to 0 is assigned. ASTRODENDRO retraces the tree and assigns to the sub-clumps a level equal to the level of their parent clump +1. It also generates a mask to define all pixels corresponding to each clump.

Three parameters regulate how ASTRODENDRO builds the tree structure:

- MIN_VALUE: the algorithm stops when the flux threshold reaches this value, instead of zero;
- MIN_NPIX: minimum number of pixels for a clump to be included to the tree structure;
- MIN_DELTA: the threshold is not lowered in a continuum way, but at steps of MIN_DELTA. If no MIN_DELTA is given, the algorithm identifies each local maximum as a new sub-clump. MIN_DELTA should be high enough to avoid the detection of noise peaks in the surface brightness distribution as sub-clumps.

[1]http://www.dendrograms.org/

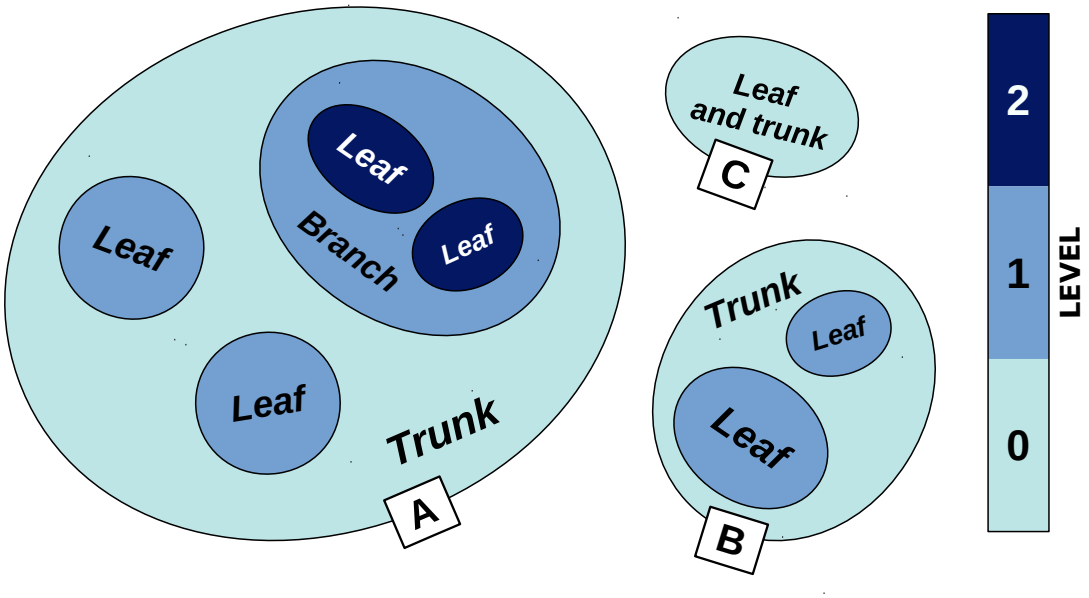

Figure 3.4: Illustration of the dendrogram structures built by ASTRODENDRO. Each clump is labelled with its position (trunk, branch and leaf) and colored according to its level in the tree hierarchy (from 0 to 2).

The naming convention used to define the position of the clump in the tree hierarchy is as follows:

- *trunk*: clump with level = 0, regardless of whether it contains sub-clumps or not;
- *branch*: clump with level > 0 and parent of other clumps;
- *leaf*: clump with no children sub-clumps. Notice that, according to this definition, a trunk can be also a leaf.

Figure 3.4 shows an illustration of 3 possible structures that ASTRODENDRO can generate.

3.2.2. *Star-forming clumps*

I identified star-forming clumps in the F275W (UV-selected clumps) and Hα (Hα-selected clumps) images running ASTRODENDRO with a flux threshold of 2.5σ on the original images and 2σ on the denoised images[2].

As a first step to achieve this sensitivity, I masked out foreground and background sources. This is done using, when available, the spectroscopic information from MUSE and by visually inspecting the RGB images in Figure 2.3 constructed as described in Section 2.2, searching for red elliptical or blue spiral-armed sources.

[2]We remind that the detection limit σ varies from galaxy to galaxy and is computed as described in Section 2.4.

Then I performed three runs of ASTRODENDRO adopting the following parameters (MIN_NPIX= 5 in all the runs):

- RUN A: MIN_VALUE= 2.5σ; MIN_DELTA= 5σ;
- RUN B: MIN_VALUE= 2.5σ; no MIN_DELTA. Given that a clump candidate is detected only if its brightest pixel is brighter than about MIN_VALUE+MIN_DELTA, regions for which each pixel has counts between MIN_VALUE and MIN_VALUE+MIN_DELTA are not detected. Since I want to detect also these fainter clumps, I ran ASTRODENDRO a second time without defining MIN_DELTA. This run is executed on an image masked for the clumps detected in run A and only trunk clumps are retained, to avoid including spurious local maxima.
- RUN C: MIN_VALUE= 2σ; no MIN_DELTA. This run is performed on an image masked for the clumps detected and kept in runs A and B. For the same reasons explained for run B, I kept only the trunks clumps of run C. Also, as a consequence of removing the high-frequency components of the image, denoising introduces a sort of smoothing, and part of the light of the brightest regions of the image, already detected as clumps, may eventually smooth out of the masks defined from runs A and B. Thus, even masking the image for the clumps already detected, the residual smoothed emission adjacent to these masks may be possibly flagged as a clump in run C. Since such an emission is clearly not due to a real clump, I excluded from the sample generated by run C all the clump candidates adjacent to the clumps found in the previous runs.

UV and Hα-selected samples are computed independently, meaning that, in principle, some UV- and Hα-selected clumps may overlap if the same region is bright enough in both filters. Throughout this work, we use only leaf and trunk clumps (*LT sample*), unless otherwise stated, to avoid considering the same region too many times.

ASTRODENDRO detected an initial total of 6090 Hα and 6259 UV candidates. To minimize the number of spurious detections I adopted the following procedure, which is schematised in the flow chart shown in Figure 3.5.

Firstly, for each of the 5 photometric bands, I flagged a clump as detected if its flux has a signal-to-noise ratio SNR[3] higher than 2. Then I exclude all clumps that were not detected in at least 3 photometric bands or in both F275W and F680N[4]. These criteria yield a reliable detection of clumps, as confirmed by subsequent visual inspection. A total 3611 Hα and 2293 UV spurious detections were removed. As an example, in Figure 3.6 I show the images in the 5 filters and in Hα of four Hα-selected clump candidates of JO201: the first one (upper left panel) is clearly detected in all images; the second one (upper right panel) does not show UV emission but is detected in three optical filters and in Hα; the third one (lower left panel) is detected only in F680N, F275W and Hα; all these three are therefore confirmed star-forming clumps. The last one (lower right panel) shows emission only in F680N and Hα and was therefore rejected.

[3]Defined as the ratio between the total flux inside the clump contour and the noise of the image in an area as large as that of the clump.

[4]The reason for this is that a star-forming clump might be in principle bright in UV and Hα only.

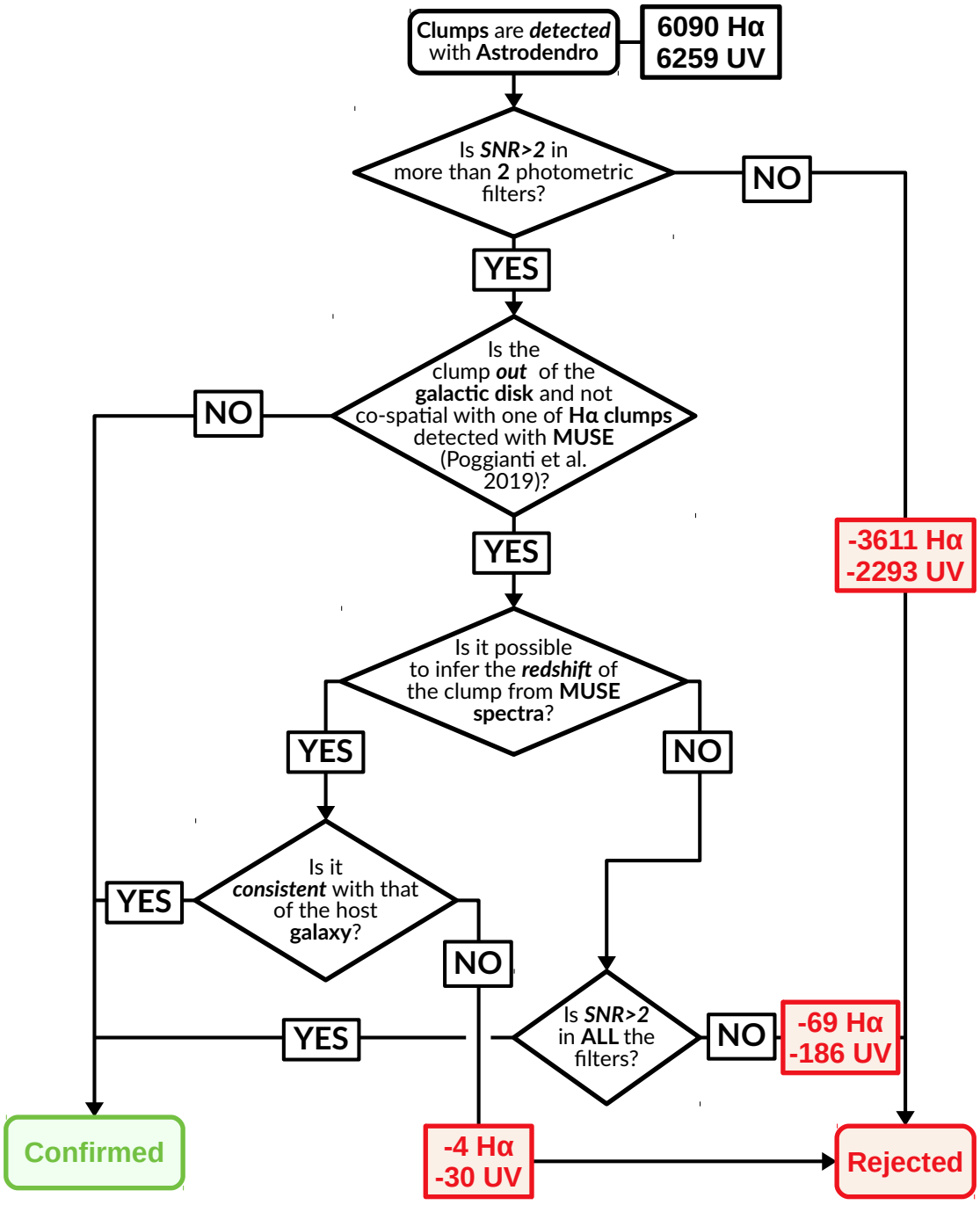

Figure 3.5: Flow chart summarizing the selection procedure adopted in this paper to confirm (green checkmark) or reject (red cross) clump candidates detected by ASTRODENDRO.

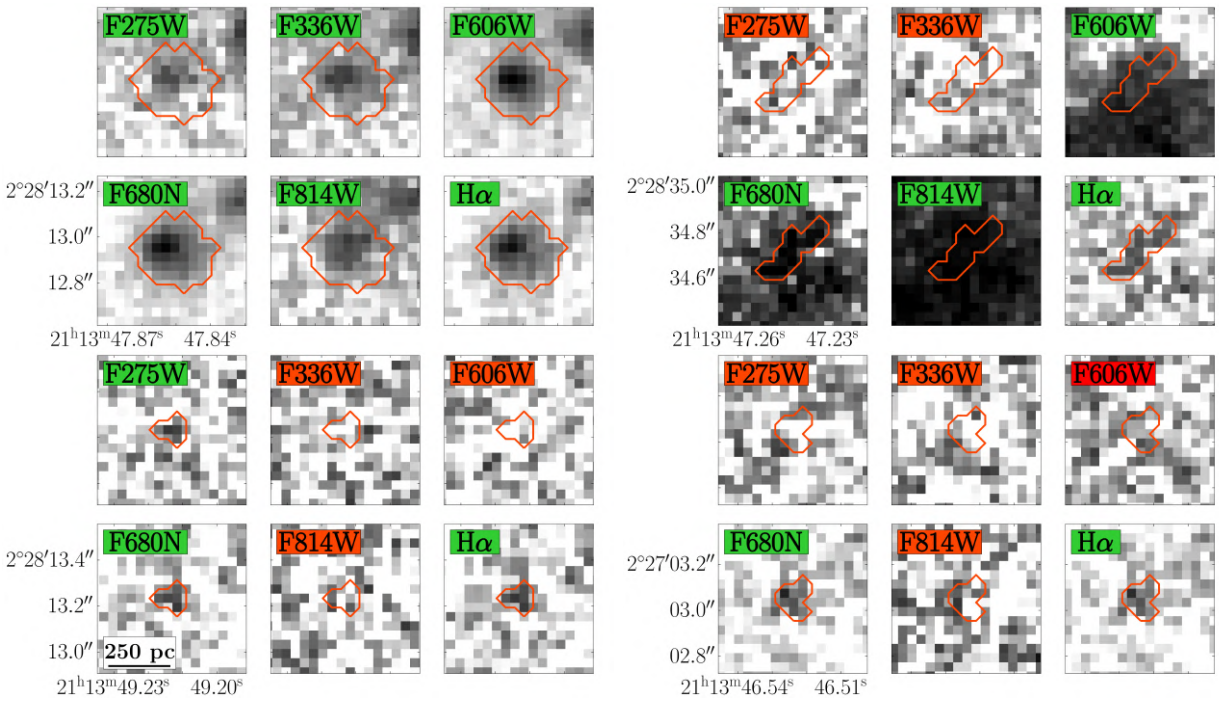

Figure 3.6: Images of 4 Hα clumps of JO206 in all the filters. Each clump is shown in 6 different filters, which are (from upper left to lower right): F275W, F336W, F606W, F680N, F814W, Hα. Each filter is labelled in green or red whether we have a detection or not, according to our definition (Section 3.2.2). The FOV is constant for all the clumps (a lengthscale equal to 250 pc is plotted in lower left panel of the third clump). Images from Giunchi et al. (2023a).

Outside the stellar disk, ASTRODENDRO can include noise peaks and cosmic rays as clump candidates, since both are bright and compact sources. Indeed, despite the procedure described in Section 2.4 and developed to mask out cosmic rays, some residual sources can still be present in the images. For these reasons, I perform an additional check for clumps in the tails. Both the Hα- and UV-selected tail clumps are matched with the corresponding catalogs of Hα knots detected with MUSE observations and described in Poggianti et al. (2019). If a match is found, the *HST* clump is validated; if not, the clump is validated only if either the redshift from the MUSE spectrum at the corresponding position of the clump is consistent with that of the galaxy, or no redshift can be inferred from the MUSE spectrum, but the clump is detected in all *HST* filters. The latter case lets us include clumps which are located outside the MUSE FOV, for which there is no spectroscopic data, and UV-selected clumps which are too faint in Hα emission to be detected as an Hα knot by MUSE. In particular, 10 Hα- and 53 UV-selected clumps are found outside the MUSE FOV, while 30 confirmed UV-selected clumps are located in the MUSE FOV, but outside any MUSE knot. The redshift is inferred from the shift of specific emission lines such as the [N II] $6548, 6583 - $ Hα and Hβ $-$ [O III] $4958, 5006$ triplets and the [SII] $6716, 6730$ doublet, which are visually identified in the MUSE spectra, obtained within a circular aperture as close as possible to that of the clump. 73 Hα candidates (69 with no MUSE redshift and no detection in all filters and 4 with redshift incompatible with that of the galaxy) and 216 UV candidates ($186 + 30$) were rejected after this selection.

Finally, 5 UV-selected trunk clumps in the disks of the JO201, JO204, JO206 and JW100

are removed as their morphologies are such that they cannot be considered clumps, rather than more likely big portions of the stellar disks.

When specified in the following, I removed clumps located in regions whose emission is powered by an AGN. In order to do that, I used the BPT maps (Baldwin, Phillips & Terlevich, 1981) of the MUSE images of the corresponding galaxies (Poggianti et al., 2017b). Adopting the boundary lines by Kauffmann et al. (2003), Kewley et al. (2001) and Sharp & Bland-Hawthorn (2010), the MUSE spaxels were flagged as star forming, composite, AGN or LINER regions according to the line ratios $\log([\mathrm{N\,II}]/\mathrm{H}\alpha)$ and $\log([\mathrm{O\,III}]/\mathrm{H}\beta)$ (for the spaxels with S/N> 3 for each line). The *HST* clumps are flagged as the MUSE spaxels they fall into and in the following I remove those flagged as AGN or LINER when studying the luminosities of the Hα-selected clumps.

3.2.3. *Star-forming complexes*

UV- and Hα-selected clumps probe the emission coming from or due to stars younger than $\sim 10^8$ yr and $\sim 10^7$ yr, respectively. The contribution from stellar components older than such timescales can be better detected in other optical bands used in this analysis, in order to trace the whole stellar populations formed from the stripped gas in the tails.

Therefore we decided to run ASTRODENDRO also on the F606W filter images, which are deeper than the UV images (Table 2.2) and are sensitive to older stellar populations with respect to F275W and Hα. ASTRODENDRO was run on the denoised F606W images, with MIN_VALUE= 3σ and no MIN_DELTA, in order to avoid the inclusion of faint and diffuse emission from the outskirts of the galactic disks. Only trunk tail F606W clumps are considered, and among them I retain the ones overlapping with at least one pixel of any Hα- or UV-selected clump. In the following, I call *star-forming complex* the union of a F606W clump and each star-forming clump overlapped it. Such star-forming clumps are considered *matched* to the complex.

As examples, in Figure 3.7 three complexes are shown as representatives of the variety of nesting configurations that our sample contains. In the left, I show an elongated complex containing one Hα-selected clump on one side of it (in gold) and one UV-selected clump (in magenta) covering a larger fraction of the optical emission (in dark violet). In the middle, a similar case but for a round complex is presented. In this case, there is almost no displacement among the centers of the Hα-selected clump, the UV-selected clump and the optical star-forming complexes. In the right, I show a complex containing no Hα-selected clumps and three UV-selected clumps, which cover almost the whole optical complex.

3.3. *Number of detected clumps and complexes*

The distributions of all clumps with respect to the host galaxy are shown in Figures 3.8-3.14. Here the disk, extraplanar and tail clumps (definitions of the spatial categories in Section 3.1.3) can be seen in different colors, and their hierarchical tree structure can be appreciated from the color shading. In Figure 3.9, I show zoomed-in examples of Hα-selected clumps in JO201, to illustrate the hierarchical structure and the irregular morphologies of these clumps.

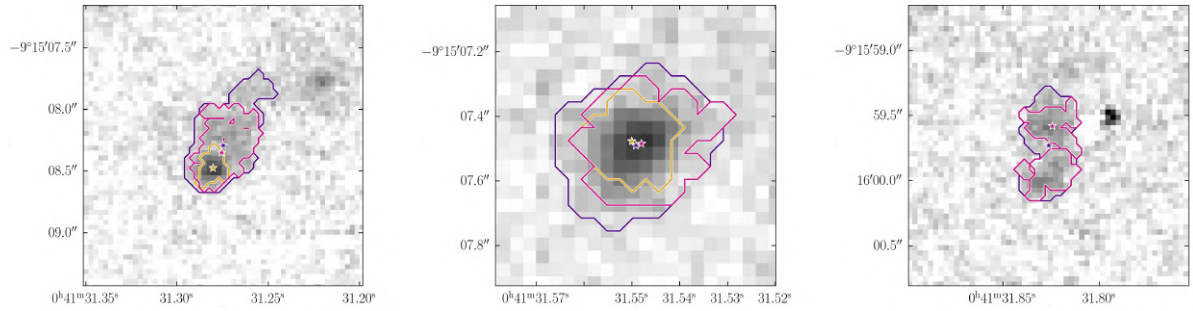

Figure 3.7: Images of 3 star-forming complexes (in dark violet) together with the matched UV- (in purple) and Hα- (in golden, when present) selected trunk clumps. Geometrical centers of the complex and the brightest Hα- and UV-selected matched clumps are plotted as violet, purple and golden stars, respectively. Underlying images are in the optical F606W band. Credits to Giunchi et al. (2023b).

The largest clumps are found in the disks of JO175, JO201 and JO206 and in the extraplanar region of JO206. As shown by Figure 3.9, large disk clumps (red contours) typically contain several sub-clumps (yellow contours), while extraplanar and especially tail clumps often have only one level. One can also appreciate the effects of RPS on extraplanar clumps, like the filamentary structures in JO206 and JW100, which are particularly bright in UV (lower right panels in Figures 3.12 and 3.14).

In the tails, clumps are often aligned in extended linear or arched structures, suggesting the presence of many sub-tails in each galaxy (as already noticed in Bellhouse et al. 2021 and Franchetto et al. 2020, who found sub-tails in these galaxies from MUSE images). Whether clump and complex properties correlate with distance from the galaxy or along its sub-tailsùis investigated in Chapter 5.

Figure 3.15 shows a zoomed-in F606W image of some structures in the tails of JO201, to better appreciate the different spatial distributions of star-forming complexes (dark violet contours), Hα-selected clumps (dark orange) and UV-selected clumps (violet). Typically, an Hα-selected clump has a corresponding UV-selected clump, while the viceversa is not true. Indeed, the number of UV-selected clumps is higher than the number of Hα-selected ones (see below). Furthermore, the corresponding UV-selected clump is generally bigger and almost completely encompasses the Hα-selected clump. Similarly, star-forming complexes contain many UV- and Hα-selected clumps, embedded in fainter, optical regions.

The number of star-forming clumps per galaxy is given in Table 3.1.In total, including all galaxies, our LT sample comprises 2406 Hα-selected clumps (1708 disk clumps, 375 extraplanar clumps and 323 tail clumps), 3745 UV-selected clumps (2021 disk clumps, 825 extraplanar clumps and 899 tail clumps) and 424 optical star-forming complexes in the tails (31 in JO175, 129 in JO201, 53 in JO204, 92 in JO206, 73 in JW39, 46 in JW100). Typically, 98-99% of the selected clumps are leaves (including also simple trunks with no substructures inside), while the trunks containing leaves represent only 1-2% of the whole sample (the fraction increases to 7-14% when restricting the analysis only to resolved clumps). The trunks with no sub-structures are 84-87% of the sample (49-54% for resolved clumps), therefore the majority of the clumps in these galaxies are simple and small structures. In Table 3.2 the same clumps are listed but divided per run of ASTRODENDRO (see Section 3.2).

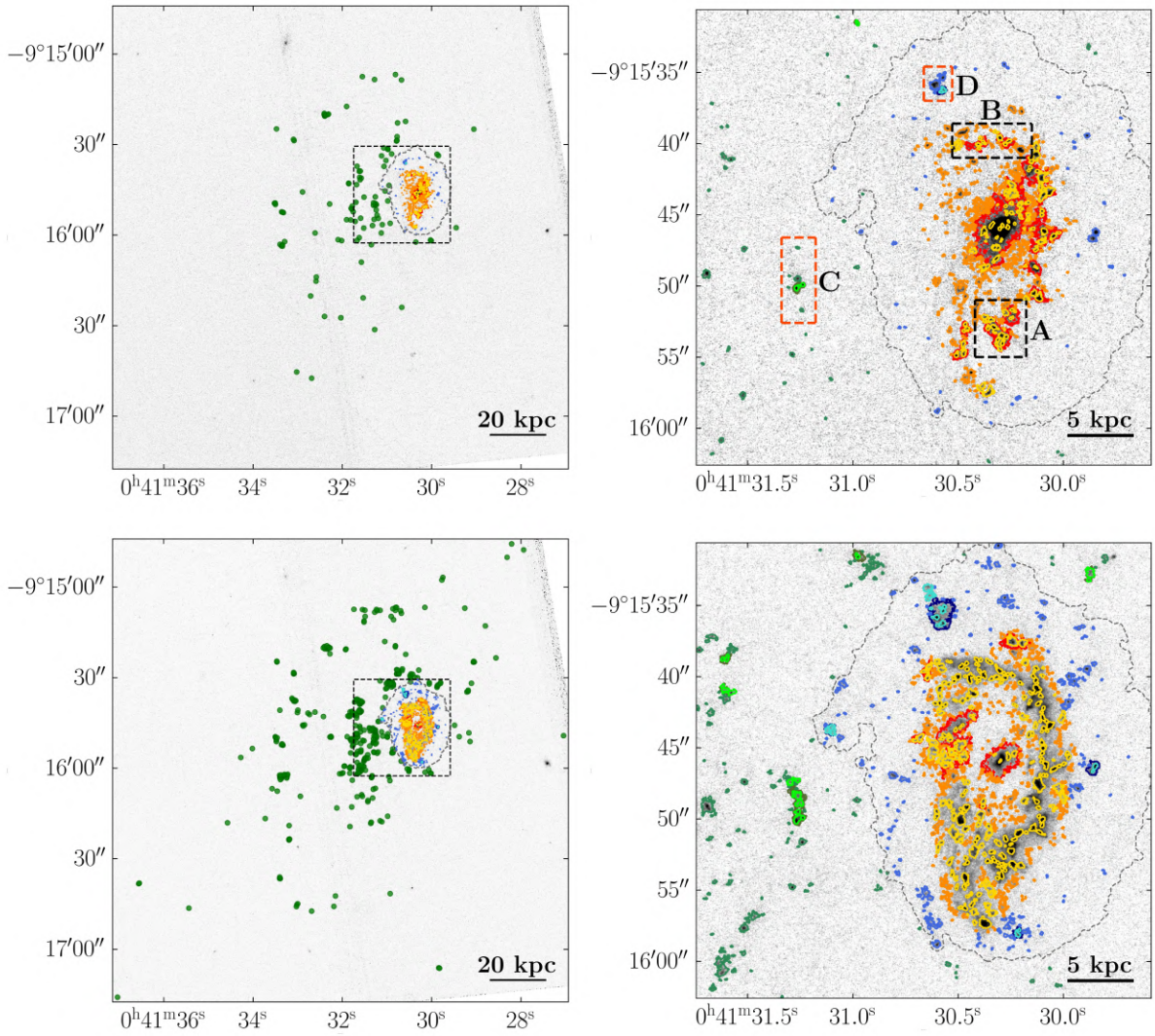

Figure 3.8: Map of the clumps detected in JO201, superimposed onto the image in the filter used for the detection. Upper panels: Hα-selected clumps. Lower panels: UV-selected clumps. Left panels: field of view including all the clumps. Right panel: zoomed-in version on the vicinity of the disk (highlighted in the left panel with the black dashed rectangle). Colors in the right panels represent the spatial category and the tree structure (Section 3.1.3 and 3.2.1): disk clumps are plotted in red (trunks which are not leaves), orange (trunks which are leaves) and yellow (leaves which are not trunks). Similarly, extraplanar clumps are plotted in dark blue, blue and light blue, and tail clumps are plotted in dark green, green and light green in right panels. The grey dashed contour is the galaxy disk contour (see Section 3.1.3. In the left panels, for the sake of clarity, the tail clumps are plotted as green dots of fixed size. The regions highlighted and labelled as A, B, C and D are shown in figure 3.9. Images credits to Giunchi et al. (2023a).

Avoiding AGN areas and including both resolved and unresolved clumps, $\sim 21\%$ of the Hα-selected and $\sim 7\%$ of the UV-selected clumps get excluded. The percentage is smaller in the latter, indicating that UV-selected clumps are more preferentially located out of AGN regions than Hα-selected clumps. Most of these are disk clumps, as expected, but a few of them can be found in the ionization cone of the AGN, whose extension can reach into

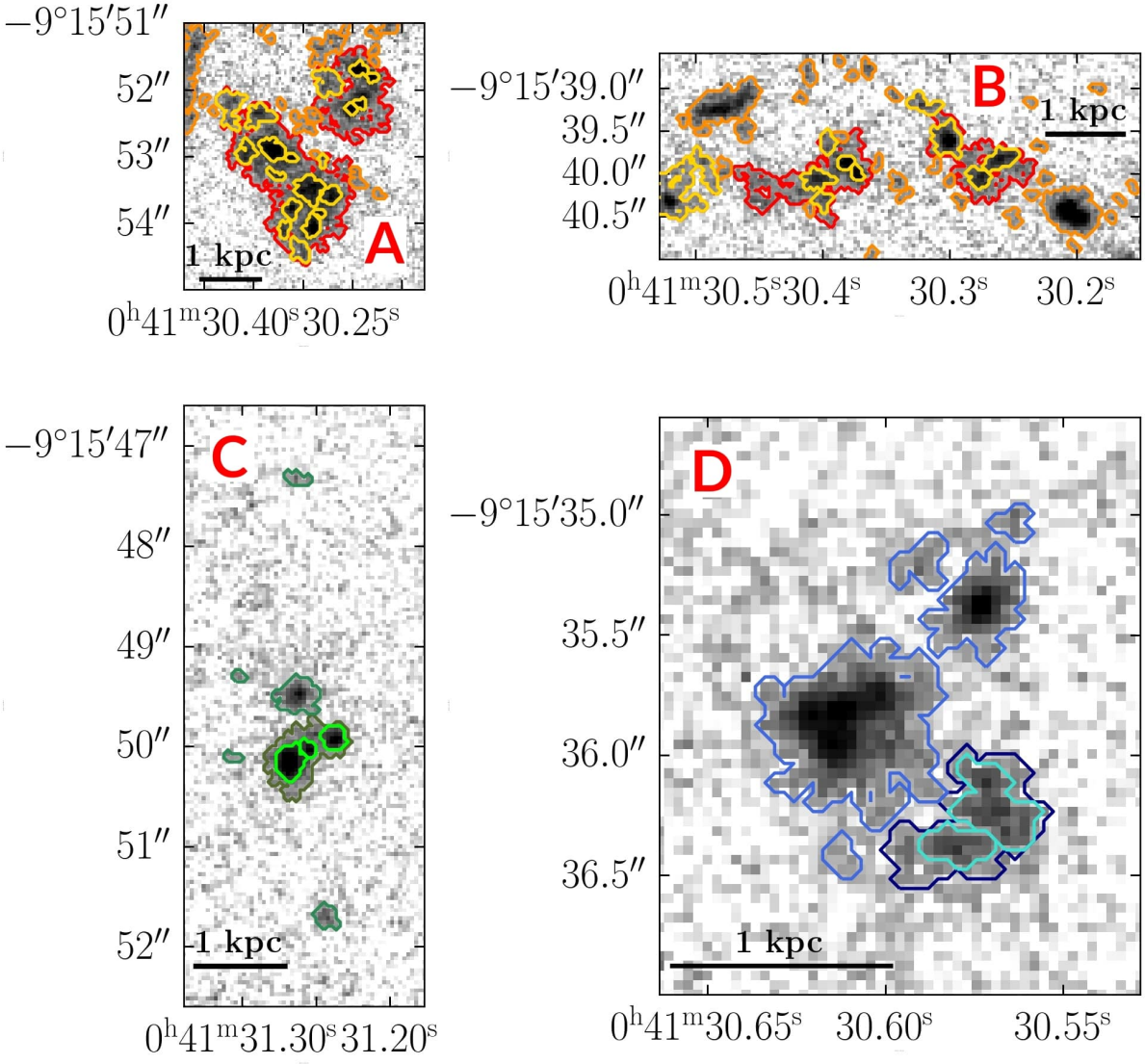

Figure 3.9: Hα images of the JO201 regions highlighted in the upper right panel of Figure 3.8. The colors are the same of Figure 3.8. Images credits to Giunchi et al. (2023a).

the extraplanar region. The exact numbers are listed in brackets in Table 3.1. Only 12% of Hα-selected and 16% of UV-selected clumps are spatially resolved, which means that the majority of the clumps have diameters smaller than $\sim$ 140 pc. Most of the resolved clumps are star-forming according to the BPT, except in the disk where about 25% of the Hα-resolved clumps are flagged as AGN or LINER.

In Figure 3.16 I plot the histograms of the number of clumps per galaxy, divided according to the selection band (Hα or UV) and the spatial category (disk, extraplanar and tail), together with the number of complexes.

In most cases disk clumps are much more numerous than extraplanar and tail clumps,

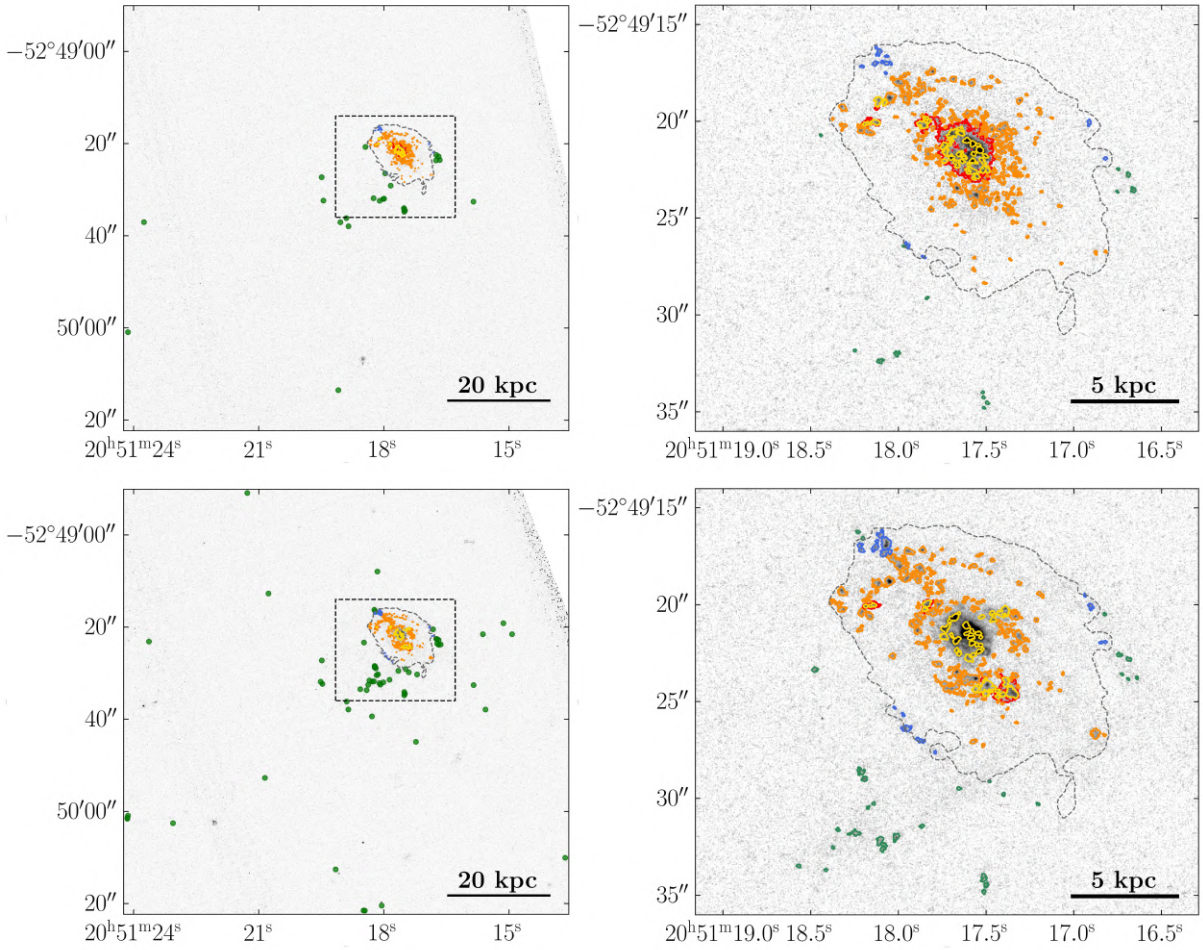

Figure 3.10: Same as Figure 3.8, but for JO175. Images credits to Giunchi et al. (2023a).

regardless of the selection filter, with the only exception being the UV-selected clumps in JW100, which is seen edge-on and is stripped mostly on the plane of the sky (Poggianti et al., 2019), thus in the most favorable conditions to appreciate the extraplanar clumps. For what concerns the number of extraplanar and tail clumps, the prevalence of one over the other depends on the galaxy: in JW100 the number of extraplanar clumps is much larger than that of tail clumps in both the selection filters, in JO204 and JO206 they are almost of the same number, while in the other galaxies tail clumps are more numerous than extraplanar. The number of clumps in each category clearly depends on both the disk inclination and the stripping direction with respect to the line of sight. Furthermore, with the only exception being disk clumps in JO175, for the same spatial category there are more UV-selected clumps than Hα-selected ones. This indicates that there are a number of stellar-only clumps, with little or no ionized gas left. The number of star-forming complexes in the tails of the galaxies is generally smaller than the number of tail UV-selected clumps, but larger than that of tail Hα-selected ones, with the only exception being JO206, suggesting that many complexes are matched only to UV-selected clumps, without any Hα counterpart.

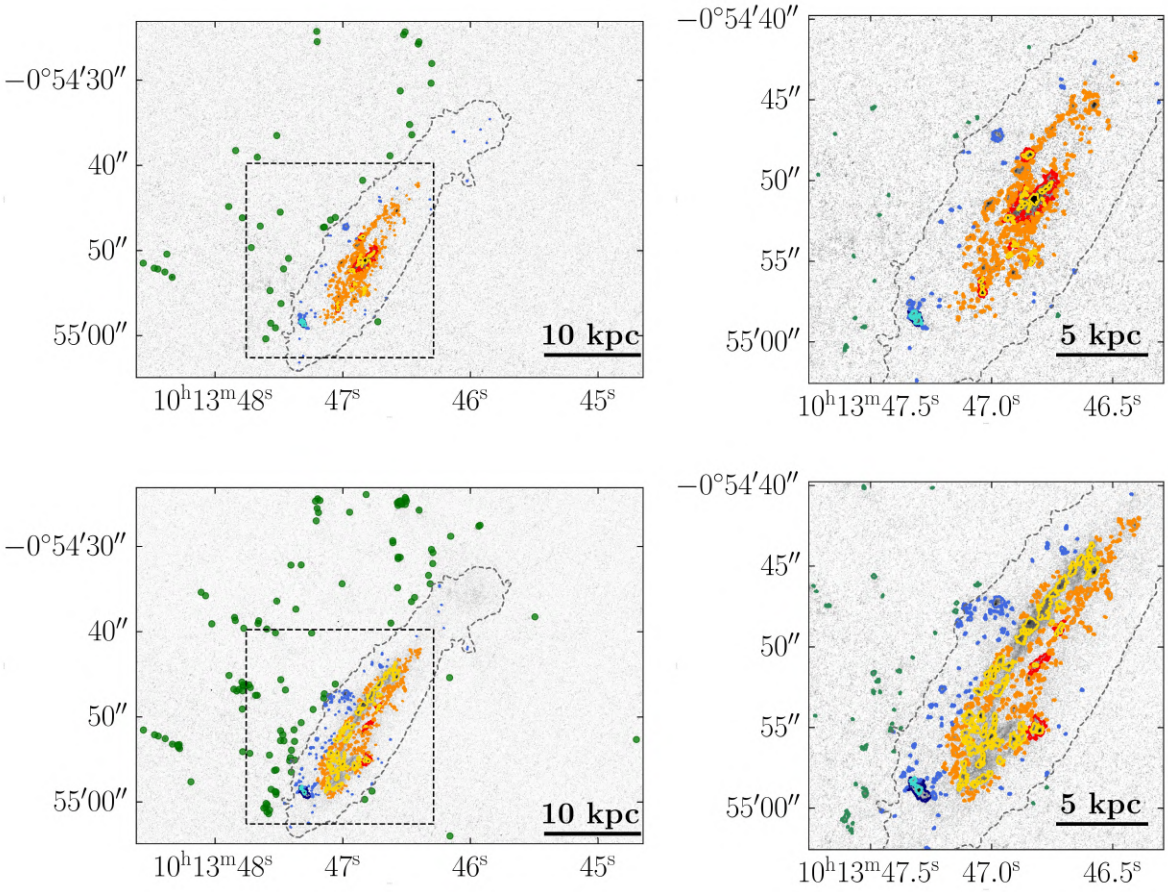

Figure 3.11: Same as Figure 3.8, but for JO204. Images credits to Giunchi et al. (2023a).

3.4. *Observed properties*

In this Section I list all the quantities and properties that I computed for each clump and that will be used in the following. Since one of the aims of this work is to study how clumps and complexes detected at different wavelength are related and clustered inside each other, some quantities are computed for the single clump/complex (Section 3.4.1), while others are computed only for the complexes since they are related to the clumps nested in them (Section 3.4.2).

3.4.1. *Single clump or complex quantities*

For all the detected clumps, the following quantities are computed by ASTRODENDRO:

- the intensity-weighted mean position (RA,Dec) of the clump, hereafter adopted as clump center.

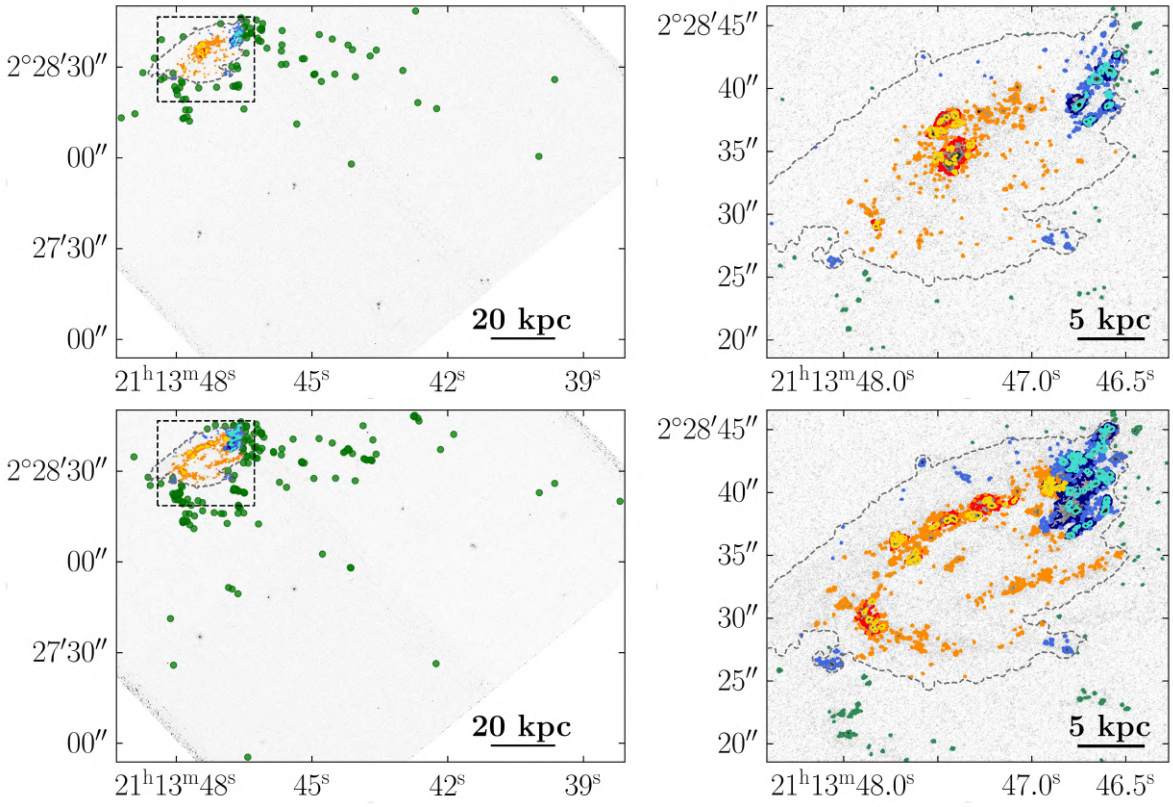

Figure 3.12: Same as Figure 3.8, but for JO206. Images credits to Giunchi et al. (2023a).

- Semi-major and semi-minor axes computed as standard deviations of the flux distribution of the clump in the direction of greatest elongation in the plane of the sky.
- The radius $r_{\rm core}$ computed as the geometric mean of the major and minor semi-axes.
- The exact area of the clump on the plane of the sky A.

In addition, I computed the following quantities:

- the flux densities for all the photometric bands, integrated over the clump area A. The flux uncertainties are computed summing two contributes in quadrature: the background noise, computed as a function of the clump area as described in Section 2.4, and the Poissonian uncertainty on the source counts converted then into flux considering the conversion factor PHOTFLAM, the exposure time and the Milky-Way dust attenuation.
- Hα or F275W luminosity ($L_{\rm H\alpha}$ and $L_{\rm F275W}$): calculated from the flux densities using the redshift of the cluster hosting the galaxy (column 10 in Table 2.1) for Hα- and UV-selected clumps, respectively. In order to get Hα luminosities from F680N$_{\rm line}$ filter, we compute Hα/(Hα + [N II]) for the Hα knots detected with MUSE in the galaxies of our sample (Poggianti et al., 2019). The median values obtained for each galaxies

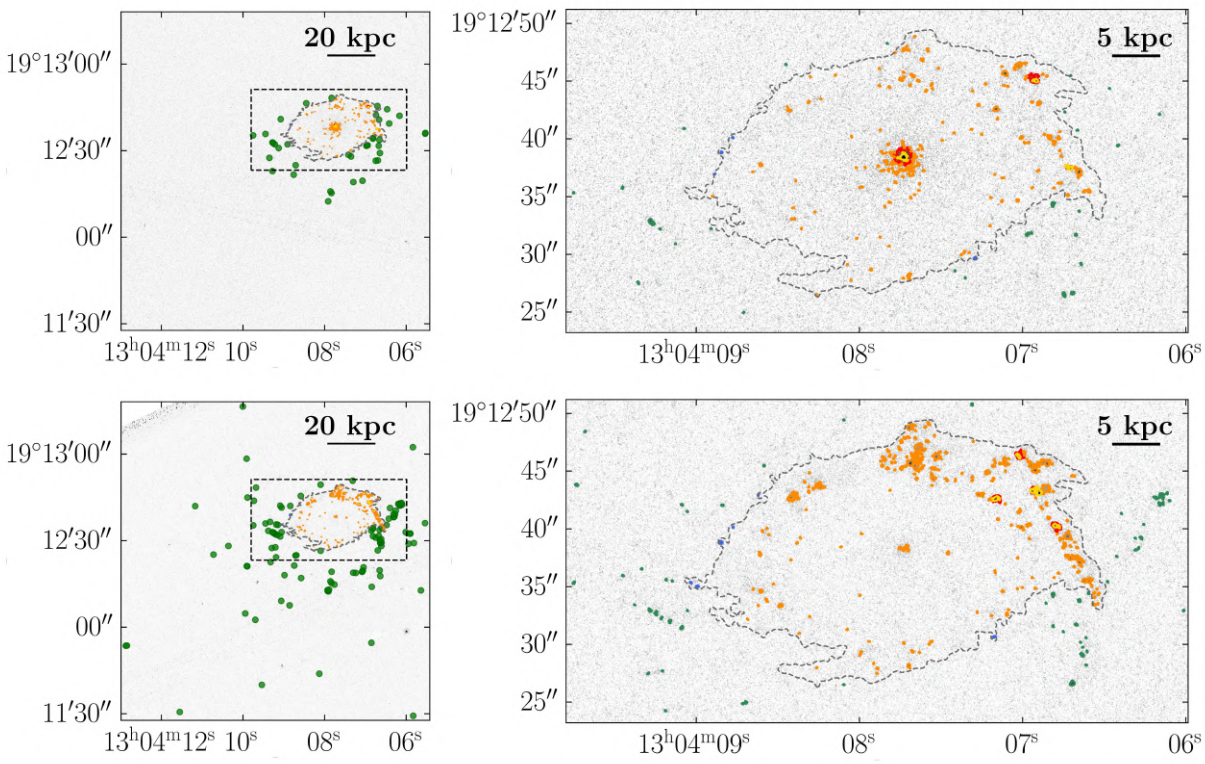

Figure 3.13: Same as Figure 3.8, but for JW39. Images credits to Giunchi et al. (2023a).

are listed in Table 2.1 and used to correct the F680N$_{\rm line}$ flux for the [N II] emission lines.

- Hα/UV ratio: computed as $L_{\rm H\alpha}/L_{\rm F275W}$ for all the clumps and complexes for which $L_{\rm H\alpha} > 0$ and the F275W signal-to-noise is larger than 2.

- $r_{\rm core,corr}$: PSF-corrected core radius. It is computed by subtracting in quadrature the σ of the PSF (FWHM/2.35 $\simeq$ 0.03 arcsec, see Section 2.1) to $r_{\rm core}$, under the assumption of a Gaussian density flux profile. The resulting angular radius is then converted in physical scale according to the redshift of the hosting cluster of each galaxy. For studying sizes, I define a sub-sample (*resolved sample*) of resolved clumps[5] by selecting those objects whose PSF-corrected core radius, $r_{\rm core,corr}$, exceeds the PSF FWHM (0.07 arcsec), which corresponds to $\sim$ 70 pc at the typical redshifts of our targets.

- The isophotal radius, defined as $r_{\rm iso} = (A/\pi)^{1/2}$.

- Size: defined as $2r_{\rm core,corr}$. This choice is supported by the fact that $r_{\rm core,corr}$ is defined by the flux distribution of the clump, therefore it is less sensitive to the flux threshold

[5]When possible, I substitute unresolved leaf clumps with its smallest, resolved, parent branch clump, if it does not contain any other resolved leaf clump.

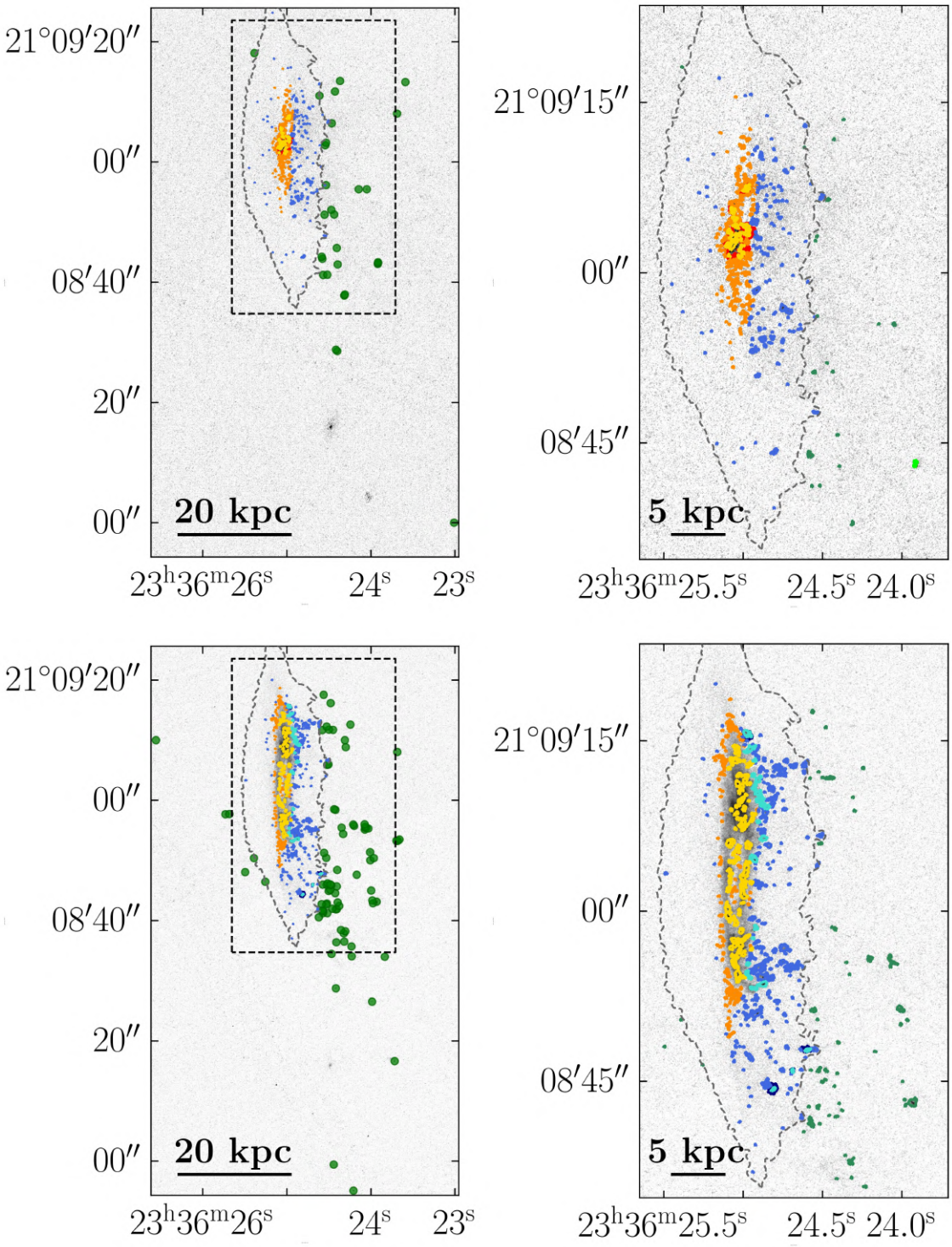

Figure 3.14: Same as Figure 3.8, but for JW100. Images credits to Giunchi et al. (2023a).

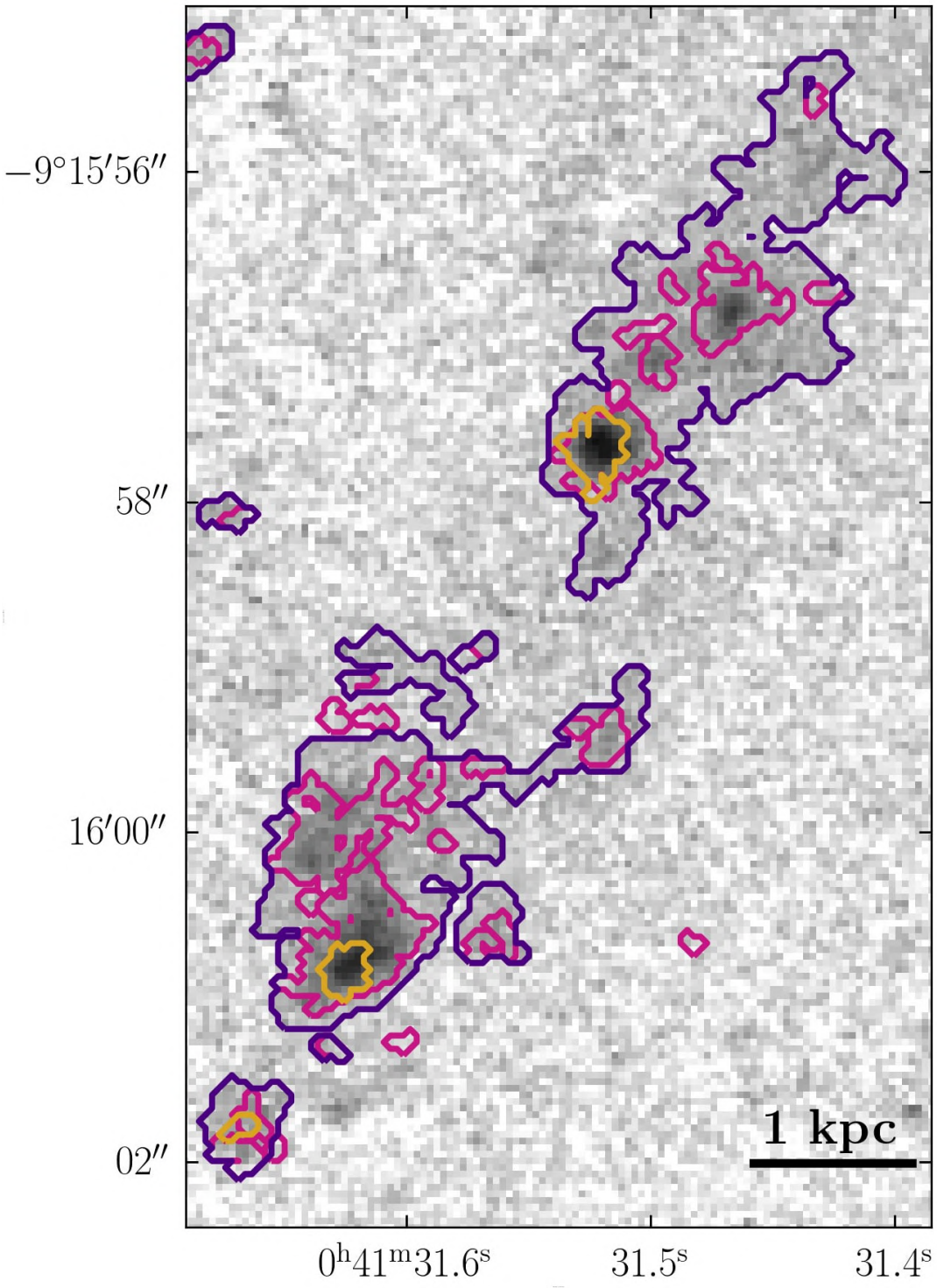

Figure 3.15: Zoomed-in F606W image of some star-forming complexes and clumps in JO201. Hα-selected clumps are plotted in dark orange, UV-selected clumps in violet and complexes in dark violet. Image from Giunchi et al. (2023a).

		LT sample				resolved sample			
Filter	gal	N_{LT}	N_d	N_e	N_t	n_{res}	n_d	n_e	n_t
(1)	(2)	(3)	(4)	(5)	(6)	(7)	(8)	(9)	(10)
	JO175	290(290)	252(252)	14(14)	24(24)	38(38)	37(37)	0(0)	1(1)
	JO201	663(476)	507(321)	51(49)	105(105)	115(88)	96(69)	4(4)	15(15)
	JO204	373(296)	290(219)	44(38)	39(39)	40(30)	32(23)	5(4)	3(3)
Hα	JO206	438(377)	234(173)	117(117)	87(87)	44(37)	24(17)	19(19)	1(1)
	JW39	235(168)	192(125)	4(4)	39(39)	14(12)	11(9)	0(0)	3(3)
	JW100	407(284)	233(139)	145(116)	29(29)	35(18)	24(9)	9(7)	2(2)
	tot	2406(1891)	1708(1229)	375(339)	323(323)	286(223)	224(164)	37(34)	25(25)
	JO175	287(287)	211(211)	17(17)	59(59)	47(47)	38(38)	2(2)	7(7)
	JO201	1244(1100)	659(518)	213(209)	372(372)	233(211)	143(122)	29(28)	61(61)
	JO204	531(475)	302(258)	110(102)	119(115)	82(78)	63(59)	9(9)	10(10)
UV	JO206	741(733)	392(384)	186(186)	163(163)	106(104)	51(49)	41(41)	14(14)
	JW39	355(349)	243(237)	6(6)	106(106)	31(31)	26(26)	0(0)	5(5)
	JW100	587(533)	214(178)	293(274)	80(80)	92(78)	48(36)	37(35)	7(7)
	tot	3745(3476)	2021(1787)	825(794)	899(895)	591(549)	369(330)	118(115)	104(104)

Table 3.1: Number of clumps detected in each galaxy and depending on the spatial category. From left to right: photometric band in which the clumps were detected (column 1), name of the galaxy (2), number of LT clumps (3), number of disk-LT clumps (4), number of extraplanar-LT clumps (5), number of tail-LT clumps (6), number of resolved clumps (7), number of resolved-disk clumps (8), number of resolved-extraplanar clumps (9), number of resolved-tail clumps (10). In brackets, the number of clumps in the each sample, but selected in order to avoid regions powered by AGN emission (see Section 3.2.2).

above which clumps are detected (Wisnioski et al., 2012). Similarly to Wisnioski et al. (2012), in Figure 3.17 I plot twice the PSF-corrected core radius against the isophotal radius, to show that these two quantities almost follow a 1:1 relation.[6]

- Axial ratio AR: ratio between the semi-minor and semi-major axes of the clump. According to this definition, elongated clumps have a smaller axial ratio than round ones.

- Tilt angle $\Delta\theta$: angle between the major axis of the clump/complex and the line connecting the center of the clumps to that of the galaxy. The angle is defined between 0 (semi-major axis aligned with the center of the galaxy) and 90 (semi-major axis perpendicular to the direction to the center of the galaxy) degrees. In Appendix A, the same quantity is computed as the angle between the major axis of the clump/complex and the local direction of the sub-tail the clump/complex belong to. Both definitions give consistent results.

- Projected distance D from the center of the galaxy: since the tail clumps are formed from the gas stripped from the galactic disk, it is not possible to infer their position

[6]In our size range, also Wisnioski et al. (2012) found that their isophotal radii are larger than core radii by a factor ~ 2.

		LT sample			resolved sample		
Filter	gal	A	B	C	A	B	C
(1)	(2)	(3)	(4)	(5)	(6)	(7)	(8)
	JO175	65(65)	214(214)	11(11)	31(31)	7(7)	0(0)
	JO201	206(165)	438(296)	19(15)	97(81)	18(7)	0(0)
	JO204	81(60)	287(233)	5(3)	36(29)	4(1)	0(0)
Hα	JO206	99(84)	318(274)	21(19)	41(34)	3(3)	0(0)
	JW39	27(20)	198(143)	10(5)	11(9)	3(3)	0(0)
	JW100	94(40)	299(232)	14(12)	29(13)	6(5)	0(0)
	tot	572(434)	1754(1392)	80(65)	245(197)	41(26)	0(0)
	JO175	74(74)	204(204)	9(9)	35(35)	7(7)	0(0)
	JO201	399(372)	779(670)	66(58)	198(180)	35(31)	0(0)
	JO204	106(102)	397(348)	28(25)	68(65)	14(13)	0(0)
UV	JO206	137(135)	573(568)	31(30)	82(80)	24(24)	0(0)
	JW39	55(55)	282(276)	18(18)	28(8)	3(3)	0(0)
	JW100	173(152)	392(362)	22(19)	80(67)	12(11)	0(0)
	tot	949(891)	2627(2428)	174(159)	491(455)	100(94)	0(0)

Table 3.2: Table with the number of clumps detected in each galaxy and depending on the ASTRODENDRO run. From left to right: the photometric band in which the clumps were detected (1), the name of the galaxy (2), the number of clumps in the LT sample detected in runs A (3), B (4) and C (5), the number of clumps in the resolved sample detected in runs A (6), B (7) and C (8). In brackets, the number of clumps in the same sample, but selected in order to avoid regions powered by AGN emission (see Section 3.2.2).

along the line of sight and therefore to de-project their position.

3.4.2. *Properties of the complexes depending on the nested clumps*

For each complex, I calculate the following quantities based on the properties of the associated clumps:

1. $N_{H\alpha}$ and N_{UV}: number of Hα- and UV-selected clumps hosted in each complex;
2. $f_{A(H\alpha)}$ and $f_{A(UV)}$: Hα and UV filling factor of the complexes. It quantifies the fraction of total area of the complex covered by the matched Hα- and UV-selected clumps (if any). It is computed only for resolved complexes as

$$f_A(j) = \frac{\sum_{i=1}^{N_j} A_{j,i}}{A_{compl}} \tag{3.1}$$

where j can refer either to Hα or UV. The filling factor is computed considering both resolved and unresolved matched clumps therefore the resulting value (if the complex contains at least one unresolved clump) is an upper limit on the intrinsic filling factor, as unresolved star-forming clumps could be smaller than the data resolution;

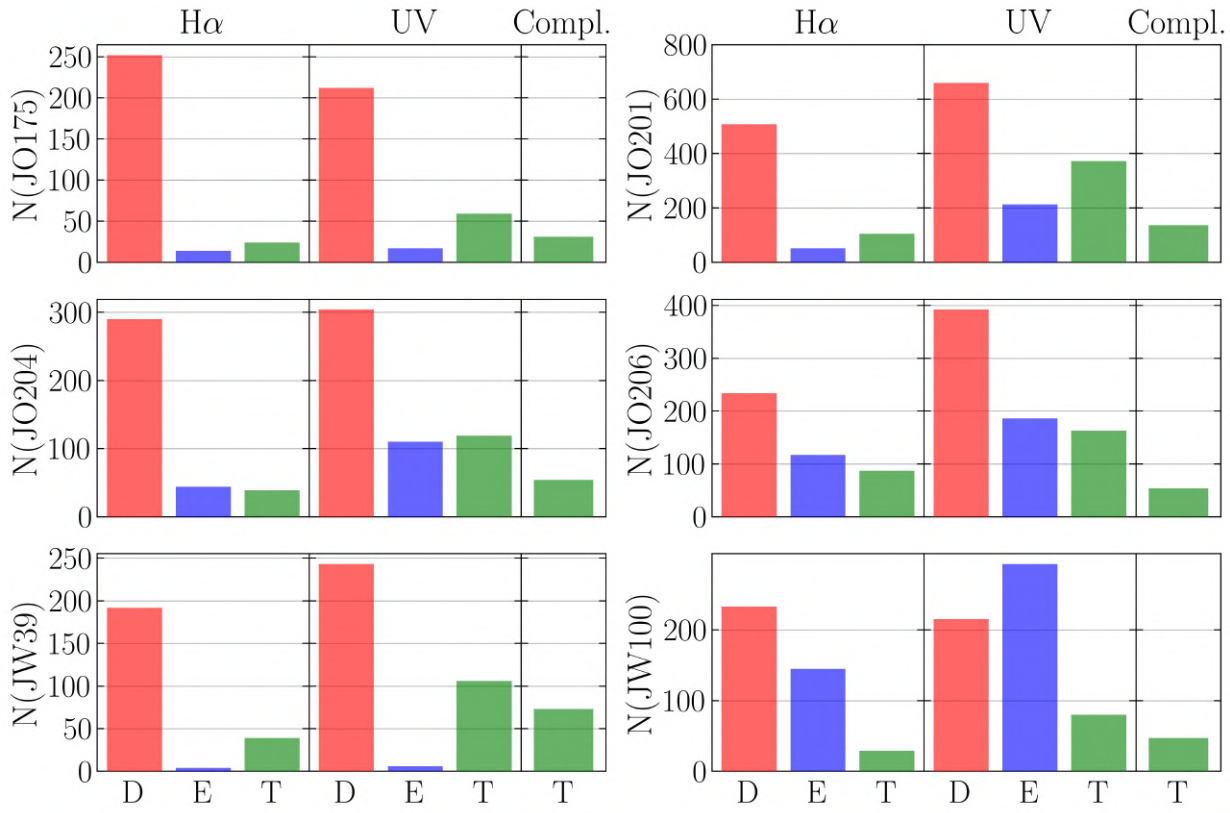

Figure 3.16: Histograms of the number of star-forming clumps and complexes in each galaxy, divided according to the selection filter and the spatial category. For each galaxy three panels are shown, with the number of Hα-selected clumps (left panel), UV-selected clumps (middle panel) and star-forming complexes (right panel), divided according to their spatial category: disk (red), extraplanar (blue) and tail (green). PLots from Giunchi et al. (2023a).

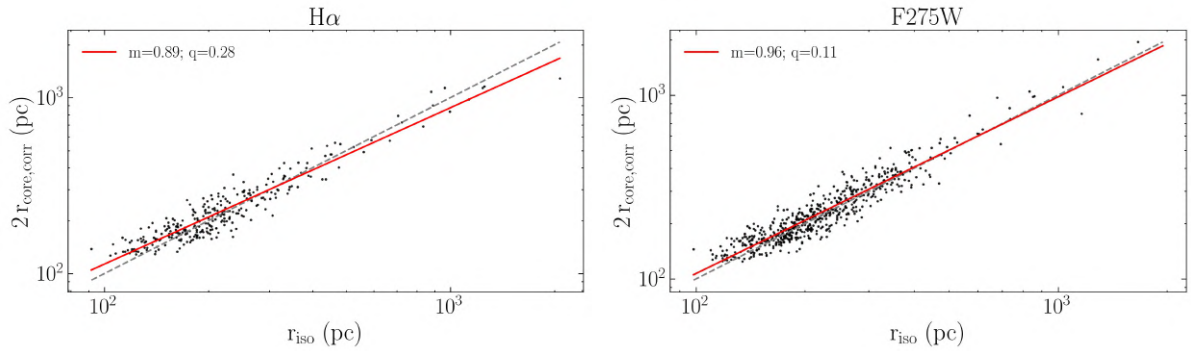

Figure 3.17: Comparison between the isophotal radius ($r_{\rm iso}$) and twice the PSF-corrected core radius ($2r_{\rm core,corr}$), defined in Section 3.4.1, both for Hα-resolved clumps (left panel) and UV-resolved clumps (right panel). The grey dashed line is the 1 : 1 relation, while the red solid line is the best-fitting line. The best-fitting line is in good agreement with the 1 : 1 relation, both for Hα- and UV-resolved clumps. Plot credits to Giunchi et al. (2023a).

3. r_{bc}(Hα) and r_{bc}(UV): respectively, the PSF-corrected core radius of the brightest Hα- and UV-resolved clump matched to a resolved complex.

Property	Symbol	Condition	Hα	UV	Compl.
Clump-galaxy distance	D	None	323	899	424
Clump/complex exact area	A_{exact}	Resolved	25	104	204
Axial ratio	AR	Resolved	25	104	204
Tilt angle	$\Delta\theta$	Resolved	25	104	204
F606W luminosity	L_{F606W}	$SNR_{F606W} > 2$	291	878	424
Hα-to-UV flux ratio	Hα/UV	$L_{H\alpha} > 0$ & $SNR_{F275W} > 2$	248	693	327
Number of matched Hα clumps	$N_{H\alpha}$	None	-	-	424
Number of matched UV clumps	N_{UV}	None	-	-	424
Hα clumps filling factor	$f_A(H\alpha)$	Resolved & $N_{H\alpha} > 0$	-	-	108
UV clumps filling factor	$f_A(UV)$	Resolved & $N_{UV} > 0$	-	-	192
Brightest resolved Hα clump	$r_{bc}(H\alpha)$	$N_{H\alpha} > 0$ & one resolved clump	-	-	20
Brightest resolved UV clump	$r_{bc}(UV)$	$N_{UV} > 0$ & one resolved clump	-	-	69

Table 3.3: Number of tail Hα clumps, UV clumps and star-forming complexes for which each property that is used in this work can be computed. Definitions of the quantities are given in Section 3.4.1 and 3.4.2.

For every quantity, Table 3.3 summarizes the number of Hα- and UV-selected clumps and optical complexes for which it is possible to derive the geometrical and luminosity properties described above.

3.4.3. *Estimate of masses and ages of the clumps*

In Chapter 6 I am going to study the mass function of the Hα- and UV-selected clumps observed in these galaxies. Details about clumps mass M_{cl} and mass-weighted age age_{mw} estimate are given in Werle et al. (2023), and the procedure is here briefly summarized.

First of all we selected only leaf clumps with SNR> 2 in all the filters. We used the SED fitting code Bagpipes (Bayesian Analysis of Galaxies for Physical Inference and Parameter EStimation, Carnall et al. 2018) to model the clumps stellar populations by exploiting all five photometric datapoints. We adopt the 2016 update of the simple stellar population (SSP) models from Bruzual & Charlot (2003) with a Kroupa (2001) IMF; the solar metallicity in these models is $Z_\odot = 0.017$. Adopting a Bayesian fitting technique, Bagpipes returns posterior probability distributions (PDFs) for each fitted quantity; in the following, the reference value of a physical property is computed as the median of its PDF.

Clumps star formation histories (SFHs) are modelled as a single delayed exponential (Carnall et al., 2019) of equation

$$\mathrm{SFR}(t) \propto \begin{cases} (t - t_0)e^{-\frac{t-t_0}{\tau}} & t \geq t_0 \\ 0 & t < t_0, \end{cases} \tag{3.2}$$

where t is the time since the Big Bang, t_0 the time when star formation starts (i.e. when the very first star formed) and τ is the timescale of the decline of star formation. This parametrization can be quite flexible because it is able to reproduce an instantaneous single burst for $\tau \sim 0$.

Dust is modelled using the Milky Way extinction curve from Cardelli, Clayton & Mathis (1989), adopting $R_V = 3.1$ and two foreground dust screens with different V-band extinction A_V, for stellar populations older and younger than 20 Myr. For stellar populations younger than 20 Myr, we included in the models emission lines and nebular continuum emission using CLOUDY (Ferland et al., 2017)).

Ages are allowed to vary between 0 and 500 Myr and the total mass assembled into stars is left to vary from 0 to $10^{10} M_\odot$.

The resulting fits underwent a series of quality-check controls. To evaluate how the underlying stellar populations belonging to the galaxy disk might affect our results (especially for extraplanar and disk clumps), a star formation history with two components was tested, to model both the young and old components. Whenever the addition of a second component led to unconstrained mass and age, the clump was discarded. In some cases, the fluxes of our models are outside the 2σ error bars of the observations for one or more filters, thus the fit cannot be considered satisfactory. After these cuts, our final sample contains 711 $H\alpha$-selected clumps (188 tail, 210 extraplanar, 313 disk), 1825 UV-selected clumps (593 tail, 677 extraplanar, 555 disk).

As an example, in Figure 3.18 I show representative cases of SED fitted with BAGPIPES for one Hα clump, one UV clump and one optical star-forming complex in JO201 (shown on the left), from Werle et al. (2023). For each of them, I show the datapoints, compared to the best-fitting spectrum and SED, which are in very good agreement.

3.5. *Clumps catalogs*

In Giunchi et al. (2023a) I released the catalogs of Hα- and UV-selected clumps, separately, as online Table. Each clump is univocally determined by the name of the galaxy, a letter (referred to the ASTRODENDRO run in which it has been detected, see Section 3.2.1) and an ID number. Then I included the RA and DEC coordinates, the luminosity in the selection filter (not corrected for self-extinction, but corrected for [N II] contribution in the case of Hα-selected clumps as described in Section 3.4), the morphological quantities (area, major and minor sigma, position angle, core radius and PSF-corrected core radius), the photometric fluxes and their errors in each band, including F680N continuum-subtracted (Hα + N II), a flag for the clump properties in the tree structure (0 trunks which are not leaves, 1 trunks which are also leaves, 2 branches, 4 leaves which are not trunks), a flag for the spatial category (0 tail, 1 extraplanar and 2 disk) and a flag for the BPT classification (0 no BPT diagram available, 1 star-forming, 2 composite, 3 AGN, 4 LINER). Details about how these quantities are computed are given in Sections 3.2.1 and 3.2.2.

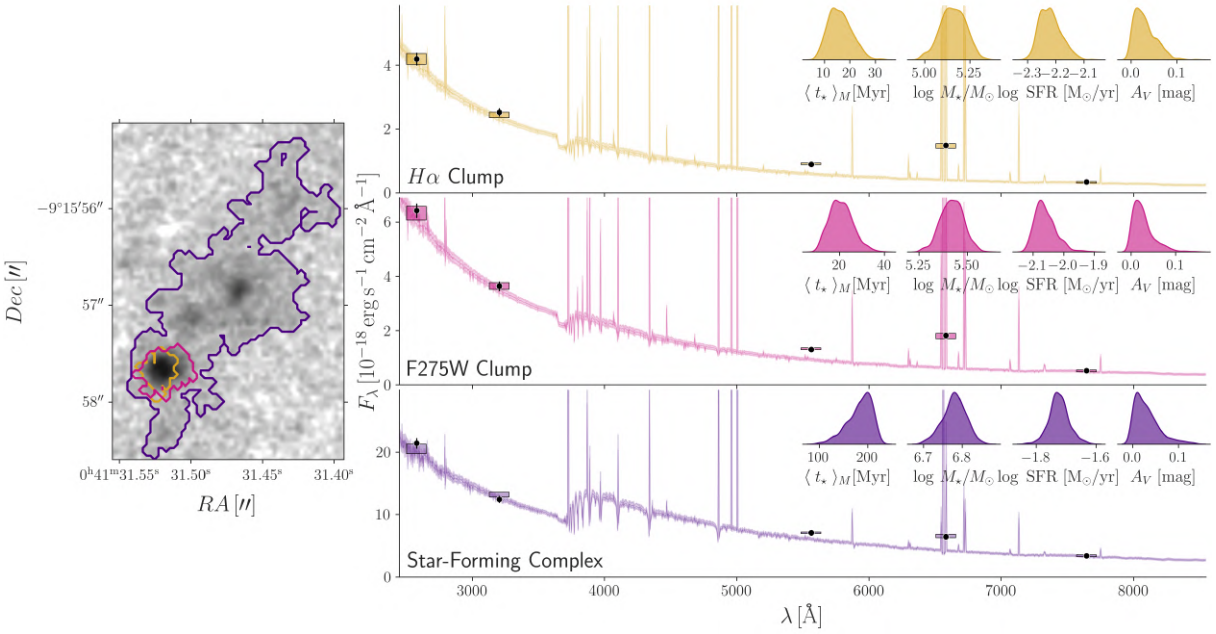

Figure 3.18: Examples of BAGPIPES fits for clumps selected from Hα, F275W and F606W images. On the left: F275W image of a region in the tail of JO201; regions in golden yellow, pink and purple indicate an Hα clump, a UV clump and a star-forming complex, respectively. On the right: BAGPIPES fits to the SED of the clumps and complexes highlighted in the image to the left; shaded region corresponds to the full range of the model spectra PDF and are plotted with the same color as the corresponding region in the image; black points with errorbars (often too small to be seen) indicate the observed photometric fluxes in the 5 *HST* bands used in this work. Colored rectangles show the region between the 1% and 99% percentiles of the photometric fluxes fitted by BAGPIPES. Inset plots in the right panels show the posterior PDFs of mass-weighted ages ($\langle t_* \rangle$), stellar masses ($\log M_*/\mathrm{M}_\odot$), star-formation rates (SFRs) and dust attenuation (A_V) derived for each object. Plot from Werle et al. (2023).

As an example, in Table 3.4 I report the first ten rows of the Hα-selected clumps catalog. For clarity, for some values not all the significant digits are reported.

ID_clump	galaxy	id_cat	_idx	RA	Dec	Lum	errL	A	$\sigma_{\rm M}$	$\sigma_{\rm m}$
				$^\circ$	$^\circ$	erg s^{-1}	erg s^{-1}	arcsec^2	$''$	$''$
JO175_A6_halpha	JO175	A	6	312.851	-52.834	3.264e+38	2.236e+37	0.040	0.071	0.041
JO175_A10_halpha	JO175	A	10	312.829	-52.827	6.320e+38	2.865e+37	0.061	0.091	0.046
JO175_A11_halpha	JO175	A	11	312.829	-52.827	1.979e+39	4.976e+37	0.173	0.137	0.080
JO175_A15_halpha	JO175	A	15	312.823	-52.824	1.068e+38	1.339e+37	0.016	0.060	0.026
JO175_A16_halpha	JO175	A	16	312.824	-52.823	3.202e+38	2.193e+37	0.038	0.055	0.047
JO175_A17_halpha	JO175	A	17	312.823	-52.823	8.186e+38	3.692e+37	0.106	0.111	0.088
JO175_A18_halpha	JO175	A	18	312.823	-52.823	2.851e+38	1.742e+37	0.022	0.050	0.025
JO175_A19_halpha	JO175	A	19	312.823	-52.823	3.118e+39	6.811e+37	0.336	0.267	0.123
JO175_A20_halpha	JO175	A	20	312.824	-52.823	1.183e+39	3.940e+37	0.112	0.094	0.080
JO175_A21_halpha	JO175	A	21	312.819	-52.823	2.433e+38	2.055e+37	0.035	0.059	0.055

Table 3.4: First ten rows of the catalog of Hα-selected clumps available online. For clarity, for some values not all the significant digits are reported. Columns from 1 to 11: ID of the clump (ID_clump), name of the host galaxy (galaxy), ASTRODENDRO run (id_cat, details in Section 3.2.1), clump id (_idx), coordinates of the center (RA and Dec), luminosity and uncertainty in the selection filter (Lum and errL, notice that Hα luminosity is in erg/s and corrected to remove [N II] emission, while UV luminosity is in erg/s/$\mathring{A}$), area A, semi-major axis (major_sigma, $\sigma_{\rm M}$), semi-minor axis (minor_sigma, $\sigma_{\rm m}$).

θ	$r_{\rm core}$	$r_{\rm core,corr}$	F275W	errF275W	F336W	errF336W
$^\circ$	$''$	kpc	erg	erg	erg	erg
			$\mathring{\rm A}\cdot{\rm s}\cdot{\rm cm}^2$	$\mathring{\rm A}\cdot{\rm s}\cdot{\rm cm}^2$	$\mathring{\rm A}\cdot{\rm s}\cdot{\rm cm}^2$	$\mathring{\rm A}\cdot{\rm s}\cdot{\rm cm}^2$
174.007	5.383e-02	4.027e-02	6.931e-19	4.989e-20	4.697e-19	3.332e-20
-155.162	6.429e-02	5.116e-02	1.321e-18	6.366e-20	8.863e-19	4.264e-20
-163.439	1.050e-01	9.040e-02	3.742e-18	1.092e-19	2.674e-18	7.370e-20
120.172	3.928e-02	2.300e-02	5.896e-20	2.790e-20	2.779e-20	1.809e-20
149.070	5.085e-02	3.701e-02	1.767e-19	4.521e-20	2.139e-19	3.051e-20
117.811	9.889e-02	8.468e-02	2.876e-18	8.714e-20	2.590e-18	6.171e-20
114.278	3.533e-02	1.706e-02	1.080e-19	3.385e-20	1.221e-19	2.281e-20
-149.026	1.810e-01	1.603e-01	5.979e-18	1.504e-19	5.986e-18	1.056e-19
118.371	8.677e-02	7.318e-02	2.055e-18	8.589e-20	2.233e-18	6.131e-20
106.350	5.689e-02	4.352e-02	1.504e-19	4.306e-20	1.526e-19	2.871e-20

Table 3.4: First ten rows of the Hα-selected clumps catalog. Columns from 12 to 18: position angle (θ), core radius ($r_{\rm core}$), PSF-corrected core raius ($r_{\rm core,corr}$), density flux and uncertainty in the filter F275W (F275W and errF275W), density flux and uncertainty in the filter F336W (F336W and errF336W).

F606W	errF606W	F680N	errF680N	F814W	errF814W
$\frac{\text{erg}}{\text{Å} \cdot \text{s} \cdot \text{cm}^2}$	$\frac{\text{erg}}{\text{Å} \cdot \text{s} \cdot \text{cm}^2}$	$\frac{\text{erg}}{\text{Å} \cdot \text{s} \cdot \text{cm}^2}$	$\frac{\text{erg}}{\text{Å} \cdot \text{s} \cdot \text{cm}^2}$	$\frac{\text{erg}}{\text{Å} \cdot \text{s} \cdot \text{cm}^2}$	$\frac{\text{erg}}{\text{Å} \cdot \text{s} \cdot \text{cm}^2}$
1.636e-19	7.199e-21	3.663e-19	1.761e-20	6.024e-20	8.368e-21
4.281e-19	1.003e-20	7.618e-19	2.318e-20	1.010e-19	1.050e-20
1.191e-18	1.703e-20	2.308e-18	4.012e-20	3.208e-19	1.820e-20
3.245e-20	3.987e-21	1.104e-19	1.035e-20	2.372e-20	5.095e-21
3.086e-19	8.181e-21	5.045e-19	1.843e-20	2.006e-19	9.345e-21
2.520e-18	1.948e-20	2.837e-18	3.703e-20	1.847e-18	2.083e-20
3.534e-19	7.613e-21	5.500e-19	1.626e-20	3.052e-19	8.726e-21
8.298e-18	3.536e-20	9.999e-18	6.858e-20	6.803e-18	3.914e-20
2.869e-18	2.062e-20	3.449e-18	3.973e-20	2.161e-18	2.211e-20
1.442e-19	6.735e-21	3.060e-19	1.633e-20	9.034e-20	8.150e-21

Table 3.4: First ten rows of the Hα-selected clumps catalog. Columns from 19 to 24: density flux and uncertainty in the filter F606W (F606W and errF606W), density flux and uncertainty in the filter F680N (F680N and errF680N), density flux and uncertainty in the filter F814W (F814W and errF814W).

F680N_line_flux	errF680N_line_flux	dendro_flag	tail_gal_flag	BPT_flag
$\frac{\text{erg}}{\text{Å} \cdot \text{s} \cdot \text{cm}^2}$	$\frac{\text{erg}}{\text{Å} \cdot \text{s} \cdot \text{cm}^2}$			
1.023e-16	7.008e-18	1	0	0
1.981e-16	8.981e-18	1	0	0
6.204e-16	1.560e-17	1	0	1
3.347e-17	4.198e-18	1	2	1
1.004e-16	6.875e-18	1	2	1
2.566e-16	1.157e-17	1	2	1
8.937e-17	5.459e-18	1	2	1
9.773e-16	2.135e-17	1	2	1
3.707e-16	1.235e-17	1	2	1
7.624e-17	6.440e-18	1	0	1

Table 3.4: First ten rows of the Hα-selected clumps catalog. Columns from 25 to 29: flux and uncertainty in continuum-subtracted F680N (F680N_line_flux and errF680N_line_flux, note the units are $\text{erg}\,\text{s}^{-1}\,\text{cm}^{-2}$ in this case), position of the clump in the tree hierarchy (dendro_flag), spatial category of the clump (tail_gal_flag), BPT category (BPT_flag).

Chapter 4

Characterization of luminosity and size of clumps and complexes

Throughout this Chapter I am going to show the results concerning the properties of the clumps, and in particular their luminosity and size. In Section 4.1 I compare the Hα luminosity of MUSE and HST both to validate the calibration of the HST data and to infer the amount of diffuse emission contained in the MUSE Hα knots presented in Poggianti et al. (2019); in Section 4.2 I characterize the luminosity and size distribution functions of clumps and complexes; finally, in Section 4.3 I show the results concerning the clumps luminosity-size relation, comparing our results with literature to infer the effect of ram-pressure stripping and environment on the properties of the clumps.

4.1. *Comparison with MUSE knots*

Hα MUSE knots (2.6.1) have already been used throughout this work to confirm the redshift of *HST* clumps in the tails. In this Section, I further exploit this sample by spatially matching it with the *HST* Hα-selected clumps, focusing only on the tail region (defined in Section 3.1.3). The total sample comprises 516 tail MUSE knots.

Due to the better resolution of *HST* with respect to the one of MUSE ($\sim$ 14 times better), I can resolve the emission coming from the MUSE knots, and confirm whether the emission was associated to a bright compact clump, a system of multiple clumps or if it comes from a diffuse component not associated to any *HST* clump. The spatial match is done by associating to a MUSE knot all the *HST* Hα clumps inside its area. In Figure 4.1 I show some representative cases of the variety of combinations that can be found when comparing MUSE knots and *HST* clumps co-spatiality, both in JO201. On the left I show a MUSE knot containing more than one *HST* clump, while on the right a system of knots with no (colored in blue) or one (in red) *HST* clump matched to them.

As a first step, I compare the MUSE knots Hα luminosity with the *HST* Hα one integrated inside the area defined by the size of the knot. I assume the MUSE luminosity to have no uncertainty, therefore the errors are given by the *HST* photometry. The results are shown in Figure 4.2, where I plot the difference between the MUSE and *HST* luminosities,

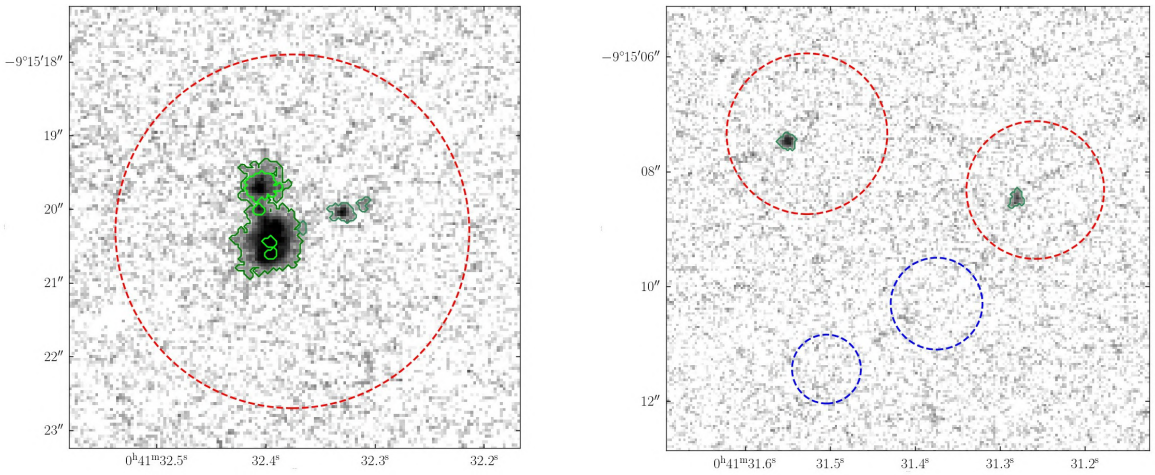

Figure 4.1: Textbook cases of the possible combinations of MUSE knots and *HST* Hα-selected clumps. The MUSE knots are plotted as circles on the *HST* Hα image. Both images are of JO201. Clumps are plotted in different shades of green according to their position in the ASTRODENDRO hierarchy (Section 3.2.1): dark green for trunks containing leaves, medium green for simple structures with no leaves inside, light green for leaves inside larger trunks.

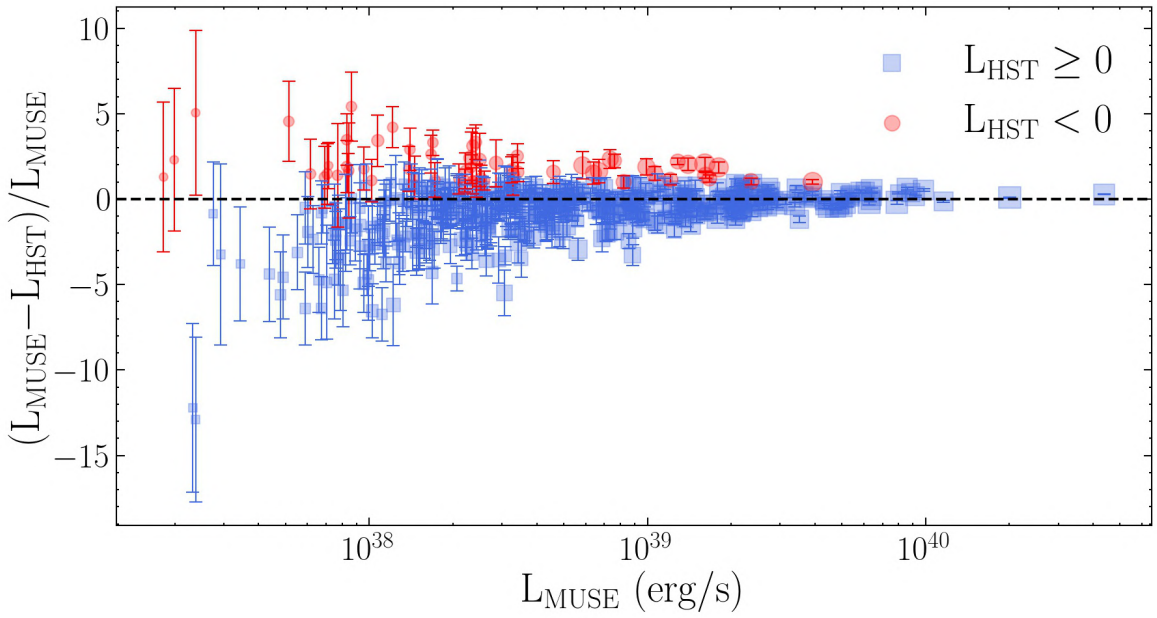

Figure 4.2: Difference between the MUSE knot Hα luminosity and *HST* Hα luminosity integrated inside the same area (defined by the size of the MUSE knot, described in Section 2.6.1), normalized to and plotted as a function of the MUSE luminosity. Knots with positive *HST* Hα luminosity are plotted as blue circles, as red squares if the Hα line is in absorption. The size of the markers is proportional to the knot size and the uncertainties are computed assuming no uncertainties on the MUSE luminosity. The dashed black line is plotted at 0, to mark the value at which the *HST* and MUSE luminosities are consistent with each other.

normalized to the MUSE one, as a function of the MUSE luminosity.

In 59 out of 516 knots the *HST* luminosity is negative (plotted in red) and therefore the difference with the MUSE luminosity is not very informative. However, I point out that the luminosities of $\sim 61\%$ of these knots are consistent within 1σ (the fraction arises

to 78% and 95% within 2 and 3σ, respectively). The existence of this sub-population of MUSE knots is likely due to the local fluctuations of the image background introduced by CTE (Section 2.4). Such fluctuations can be as large as 10% of the detection limit of the Hα maps (Section 2.4), which is negligible when considering compact and bright clumps in which, by construction, each pixel is at least 2 times brighter than the detection limit (Section 3.2.1). However, such systematic effect can bias the total flux when integrating the emission coming from large and low-surface brightness regions. Indeed, comparing the average surface brightness of the MUSE knots (computed as the MUSE Hα flux over the angular area of the knot) with the one obtained dividing the *HST* Hα detection limit (Section 2.4) by the area of an *HST* pixel ($0.016\,\mathrm{arcsec}^2$), we find that for $\sim$ 80% of the MUSE knots the surface brightness is smaller than 10% of the *HST* detection limit. Therefore the order of magnitude is compatible with the one of the background fluctuations, making the flux estimate of these diffuse region non-trivial. When removing such knots, the other knots luminosities (plotted in blue) show a good agreement, with increasing scatter as the knot gets fainter and smaller. There is a tendency for the *HST* luminosity to be brighter than the MUSE one, with the interquartile interval ranging from -1.297 to 0.135 and a median value equal to -0.431. Therefore it is rather common for the *HST* luminosity to be twice the MUSE one, notwithstanding the interquartile interval is still consistent with zero, at which the MUSE and Hα are consistent. Furthermore, as it can be seen in Figure 4.2, most of the knots that are overluminous in *HST* are still consistent with 0 within 1σ.

In order to explore the reasons behind this systematic effect, I divided the MUSE knots with positive *HST* emission between those matched to at least one *HST* Hα-selected clump (Section 3.3), which are called *full* knots and those with no *HST* counterpart (*empty* knots). In Figure 4.3, I show the luminosity difference between MUSE and *HST* relative to MUSE as a function of the diameter of the MUSE knot for empty (on the bottom left) and full (on the bottom right) knots. As one can notice, the median discrepancy for empty knots (-0.643, bottom left plot) is even larger than the median of the whole sample (-0.431). On the other hand, the median discrepancy for the full knots (-0.127, bottom right plot) is much more consistent with 0 and within the uncertainties by the assumptions we made when extracting the Hα emission line from the narrow-band filter (Section 2.3). Furthermore, the median profile of the empty knots is much more scattered than the profile of the full knots, which is more constant and consistent with 0. This confirms that the Hα flux of the MUSE regions in which there is a confirmed compact *HST* source is well recovered by *HST*. Finally, as shown in the histograms of the top panels, empty knots are typically smaller in size than full knots. Therefore we can conclude that the knots for which the discrepancy is larger and systematically in favor of *HST* are those with no *HST* counterpart. These knots look like bright sources in MUSE, but the absence of *HST* clumps inside them hints that they are more likely to be overluminous diffuse emission. Such regions should be characterized by a low surface brightness and that is why, in Figure 4.4, I show again the luminosity discrepancy for empty and full knots, but now as a function of the surface brightness, computed as $L_{\mathrm{MUSE}}/A_{\mathrm{knot}}$. As one can notice from the histograms in the upper panels, the empty knots have a systematic smaller surface brightness than the one of full knots. Moreover, the plots in the lower panels confirm that the discrepancy gets more negative for low values of surface brightness, a trend which is more evident for empty

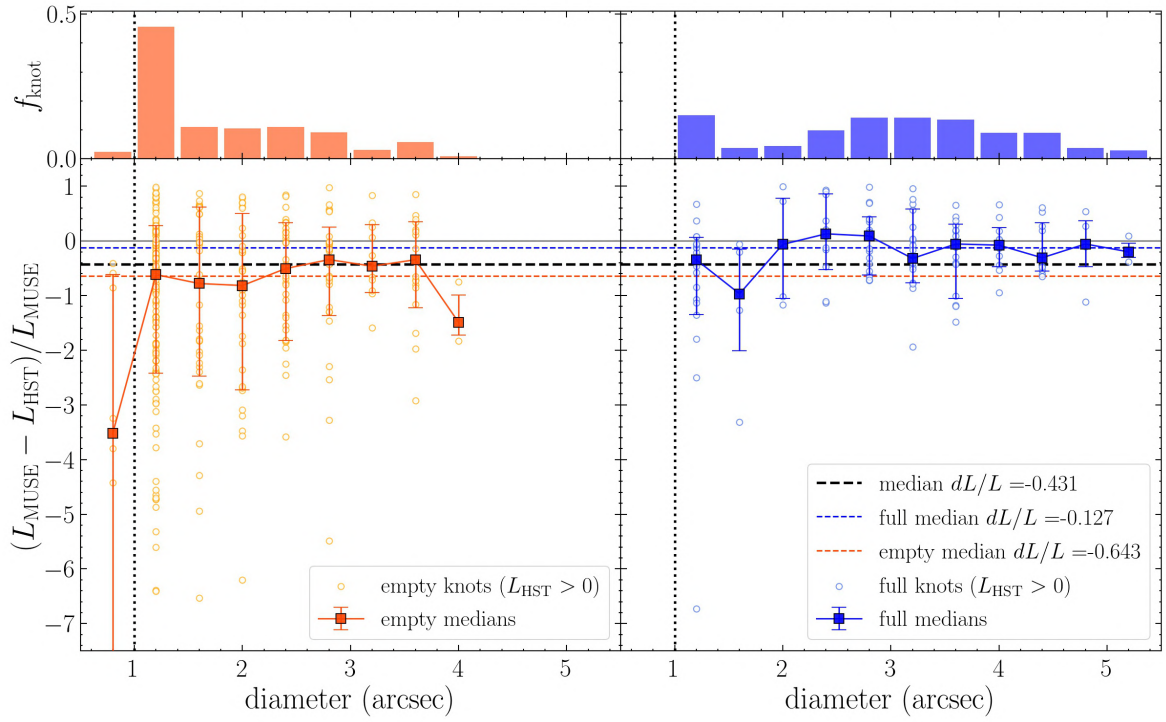

Figure 4.3: Top panels: histograms with the relative fraction in angular diameter of MUSE knots with no *HST* counterpart (to the left, in orange) and with at least on *HST* Hα-selected clump (to the right, in blue). Bottom panels: difference between the MUSE knot Hα luminosity and summed *HST* Hα luminosity of the Hα-selected clumps inside each knot, integrated inside the same area (defined by the size of the MUSE knot, described in Section 2.6.1), normalized to and plotted as a function of the angular diameter. Only knots with positive *HST* Hα emission are considered. Empty circles are the single knots, while the squared errorbars is the median profile of the luminosity difference as a function of the diameter. Dashed lines are: median values of the luminosity difference of the whole sample of knots (black), of the empty knots (orange) and of the full knots (blue).

clumps. The discrepancy observed at small surface brightness values and only for the most diffuse knots can be caused by two factors: the above-mentioned systematic effect of the image background, which can become not negligible for knots with surface brightness compatible with about 10% of the *HST* detection limit, and resolution effects. Indeed, the radius of the MUSE knots is the value at which the surface brightness of the knot gets comparable with the local background (Section 2.6.1); however, if the knot is small and comparable with the PSF of MUSE (1 arcsec of FWHM), the broadening effect of the PSF may bring a considerable amount of flux out of the circle defining the MUSE knot. This fraction of lost flux can be recovered when integrating within the same area in the *HST* images, for which the PSF is much smaller (0.07 arcsec of FWHM) and the broadening effect negligible. Finally, I point out the largest luminosity discrepancy is found for knots with $L_{\rm MUSE} \sim 10^{38}$ erg/s, for which the *HST* luminosity can get 3 times brighter than MUSE. However, this happens only in $\sim$ 6.6% of the cases, a negligible fraction of the whole sample.

I can now compute the difference between the luminosities of the MUSE knots and the *HST* clumps matched to them in order quantify the fraction of diffused component around the compact sources. I find 144 tail MUSE knots with an *HST* counterpart, about 27.9%

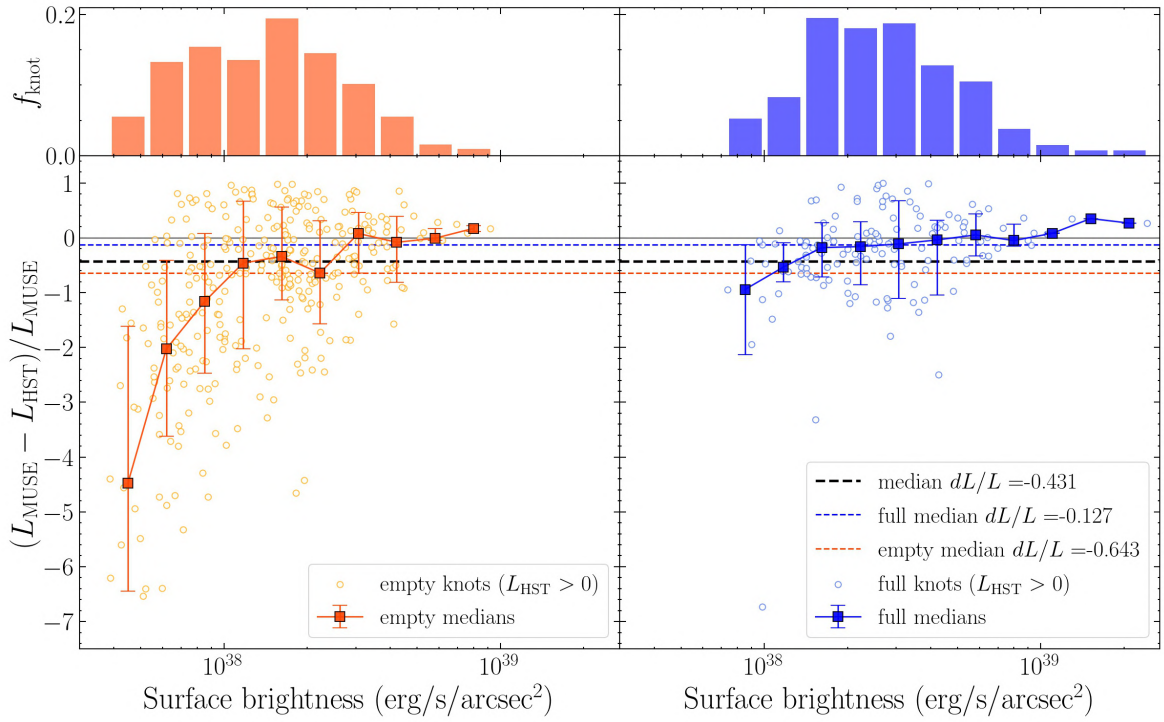

Figure 4.4: Same as Figure 4.3, but now the MUSE-*HST* luminosity difference is plotted as a function of the knot surface brightness.

of the whole sample of tail knots. That means that in more than two knots out of three, the emission that MUSE observed as compact and overluminous enough to be classified as a knot is not seen as compact by *HST* in Hα. Such emission can therefore be due to over-dense but still diffuse emission, or by clumps even smaller and fainter than the *HST* detection limit (Section 2.4).

For what concerns the MUSE knots with an *HST* counterpart, 61% (88/144) of them have only one matched *HST* clump, with a maximum of ten clumps matched to a single MUSE knot. Figure 4.5 shows the difference between the MUSE and the summed matched clumps luminosities relatively to the MUSE luminosity. By construction, in this case, it is impossible to have negative Hα *HST* luminosity. Uncertainties are computed propagating those of the matched clumps. Except for a few cases, the difference is between 0 and 1, with the interquartile interval ranging from 0.473 to 0.823 and a median of 0.700. I can therefore conclude that even when I have a match, the *HST* clumps can typically account at most for slightly more than half of the MUSE emission, with the residual one to be interpreted most likely either as a diffuse, or to a compact faint and unresolved component (as mentioned above).

4.2. *Distribution functions*

The luminosity (size) distribution function LDF (SDF) is defined as the number of sources per luminosity (size) bin normalized by the width of the luminosity (size) bin itself

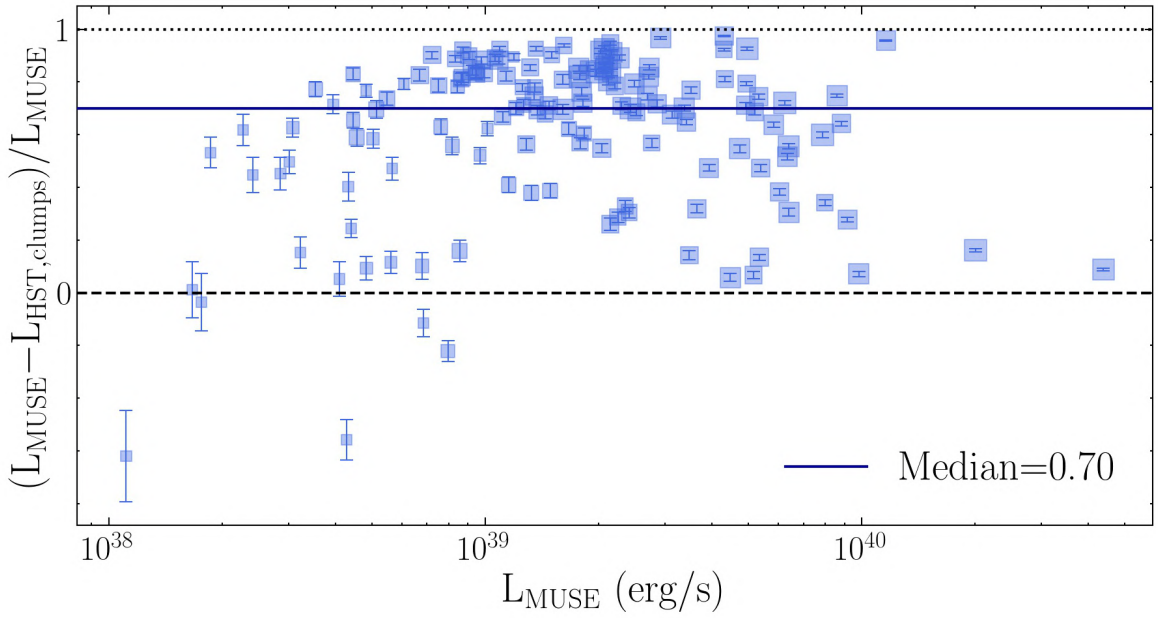

Figure 4.5: Difference between the MUSE knot Hα luminosity and summed *HST* Hα luminosity of the Hα-selected clumps inside each knot, integrated inside the same area (defined by the size of the MUSE knot, described in Section 2.6.1), normalized to and plotted as a function of the MUSE luminosity. The size of the squares is proportional to the knot size and the uncertainties are computed propagating the uncertainties on each clump luminosity. The dashed and dotted black lines are plotted in correspondence to the values 0 and 1, which are two extreme cases in which *HST* fully accounts for the MUSE emission or it is completely negligible, respectively. The blue solid line is the median value of the sample.

and by the total number of sources in the sample and is a useful tool to study the statistical properties of the star-forming clumps. As described is Section 1.4.1, they are typically well described by a power law and are good proxies of the environmental effects on the star-formation process and on the clustering properties of the clumps.

4.2.1. *Luminosity distribution functions*

Figure 4.6 and the left panel of Figure 4.7 show the histograms of the clumps in each spatial category and in each galaxy, binned in luminosity. The numbers of clumps and complexes are listed in Table 3.1 and Section 3.3. In particular I refer to the number of BPT-selected clumps, with no selection in size. The y-axis of plots are normalized by the total number of clumps in the spatial category and in the galaxy. Most Hα-selected clump distributions are peaked at values fainter than $\sim 10^{38}$ erg/s, at the faint-end of the luminosity dynamical range. The luminosities of the Hα-selected clumps are consistent with those of "giant" H II regions (like the Carina Nebula), whose Hα luminosities L(Hα) are typically 10^{37-39} erg/s, and "super giant" H II regions (like 30 Doradus in the Large Magellanic Cloud), with L(Hα) $> 10^{39}$ erg/s (Lee, Hwang & Lee, 2011). As expected, the faintest clumps are observed mostly in the closest galaxies of our sample (Table 2.1). JO201 stands out for its population of bright Hα-selected clumps, both in the disk and in the tail, while in the extraplanar regions the brightest clumps are those of JO206 (located in the crest to the top right of the disk, see Figure 3.12). Similar trends are found for

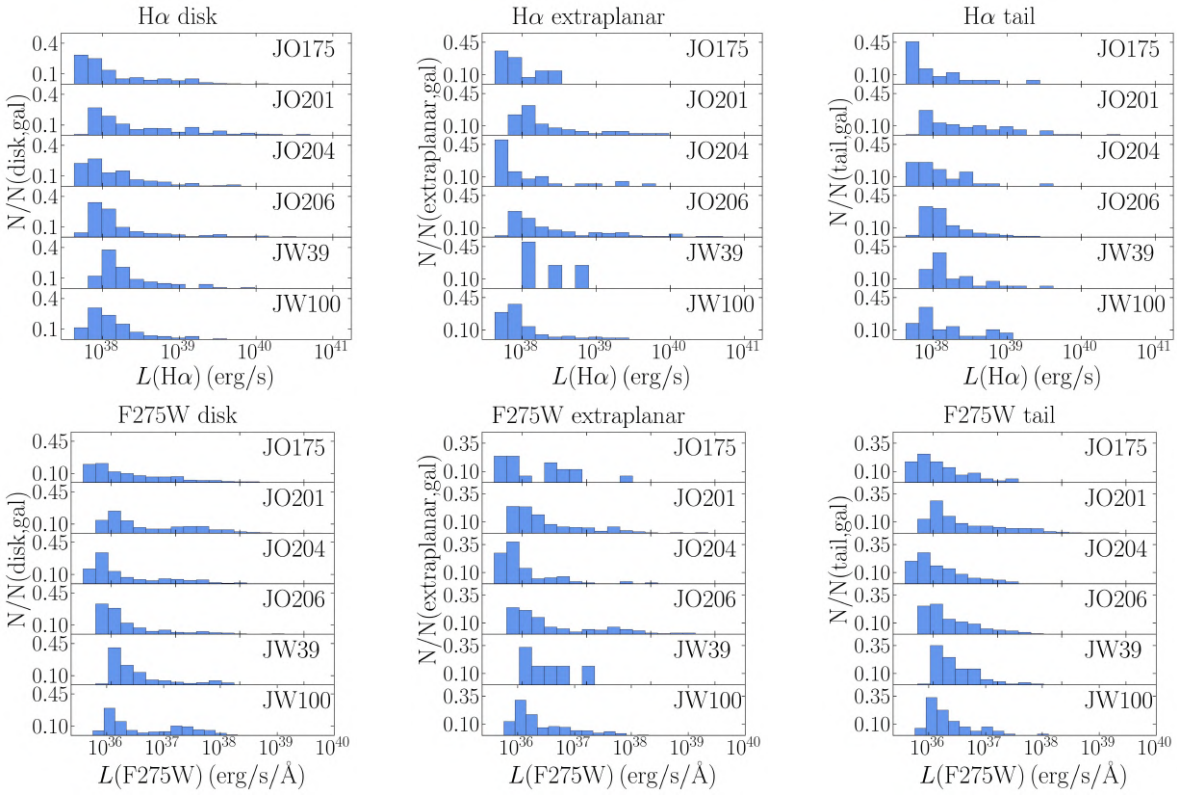

Figure 4.6: Fraction of Hα-selected (top row) and UV-selected (bottom row) clumps per spatial category and per galaxy. In each row, from left to right: disk, extraplanar and tail. Y-axis is normalized for the number of clumps in the galaxy and in the spatial category. Notice that the Hα luminosity of the Hα-selected clumps is the integrated emission of the Hα line, therefore in erg/s, while the UV luminosity of the UV-selected clumps is in erg/s/Å. Plots from Giunchi et al. (2023a).

UV-selected clumps. Also, I point out the hint for a bimodality in the distributions of the disk UV-selected clumps of JO201 and JW100 and of the extraplanar clumps of JO206. Finally, the star-forming complexes distributions are flatter than those of the clumps and do not peak at low luminosity like the clumps.

As done in Cook et al. (2016), throughout this work the datapoints of the luminosity distribution functions $\mathrm{d}\widetilde{\mathrm{N}}/\mathrm{d}L$ (LDF) are computed fixing the number of objects while varying the bin size, in order to obtain a robust representation of the distribution function. For our LDFs I choose 20 sources per bin. The luminosity of each bin is the central luminosity of the bin. As usually done in literature (Cook et al., 2016; Mascoop et al., 2021; Santoro et al., 2022), I fit only datapoints brighter than a given peak luminosity L_{peak}, under which the sample is considered incomplete. The selected datapoints are fitted[1] by a power law

$$p(L) = K\, L^{-\alpha} \quad \text{with } L \geq L_{\mathrm{peak}}, \tag{4.1}$$

where K is the normalization and α is the slope of the power law. L_{peak} is chosen for each

[1]Results do not change significantly either varying the number of clumps per bin between 5 and 50 or using a different fitting method which does not depend on the binning (PowerLaw, Alstott, Bullmore & Plenz 2014; Clauset, Shalizi & Newman 2009; Klaus, Yu & Plenz 2011).

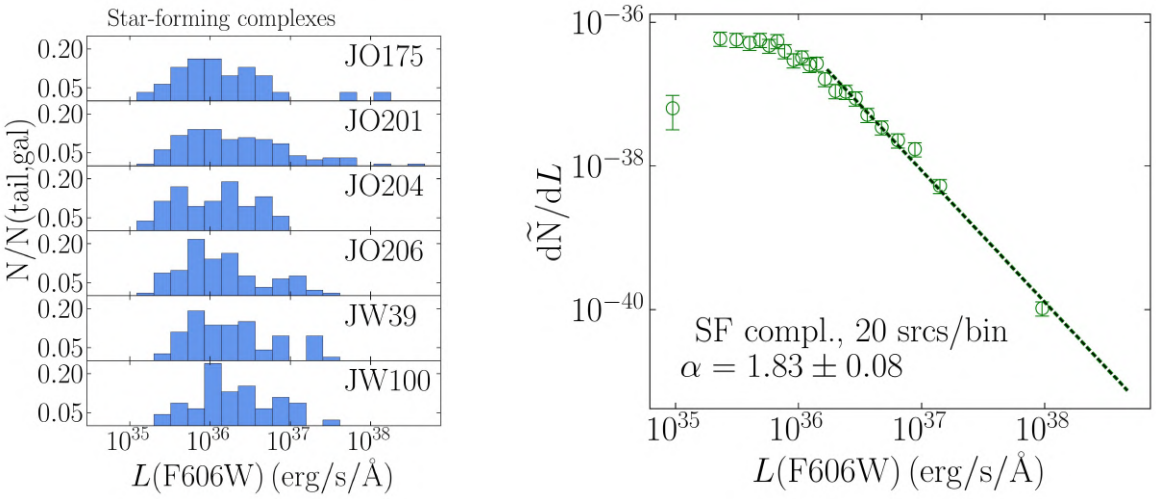

Figure 4.7: Left: same as Figure 4.6, but for star-forming complexes. Right: same as Figure 4.8, but for star-forming complexes. Plots taken from Giunchi et al. (2023a).

sub-sample starting from the peak value of the LDF and, if necessary, increasing it in order to avoid regions of the LDF particularly scattered (in which the sample starts being affected by incompleteness).

Hα-selected clumps, UV-selected clumps and star-forming complexes are fitted independently in each spatial category, in order to study variations in the properties of the LDFs as a consequence of RPS. I used the whole UV-selected and star-forming complexes samples, but only the BPT-selected Hα-selected clumps, in order to avoid AGN- and LINER-powered regions (see Section 3.2.2). Fits were performed using the CURVE_FIT method implemented in the SciPy[2] Python package, with uncertainties on the LDF computed as the Poisson noise of the number of objects in the bin.

In Figure 4.8 and on the right panel of Figure 4.7 I plot the observed LDFs together with the corresponding best-fitting power laws. Tail LDFs seem to be well described by a single power law, both for Hα- and UV-selected clumps.

In Table 4.1 I list the best-fitting values of the slope α and the normalization K, together with the peak luminosity $L_{\rm peak}$. Considering all the cases, the value of the slope α is in the range from 1.61 to 1.88, with a mean value of 1.79 ± 0.09 (1.84 ± 0.03 for Hα-selected clumps and 1.73 ± 0.09 for UV-selected clumps). The slopes are always smaller than 2, the theoretical value expected for a regime in which the collapse of the ISM into molecular clouds and then into stellar clumps is regulated by a scale-free turbulent cascade (Elmegreen, 2002, 2006). A flattening in the LDF can be caused both by a lack of faint clumps or by an excess of bright clumps; however, I can not exclude the effects of the blending of different clumps, that can cause two faint clumps to be counted as a single bright clump. In order to rule out the possibility that the inclusion in the sample of trunk clumps with sub-clumps can bias the results, I performed the same fits to the LDFs excluding them. Since this kind of trunks is $\sim 2\%$ of the whole sample, excluding them does not affect significantly the results and the leaf-only slopes are always consistent within 1σ with those obtained including both

[2]https://docs.scipy.org/doc/scipy/index.html

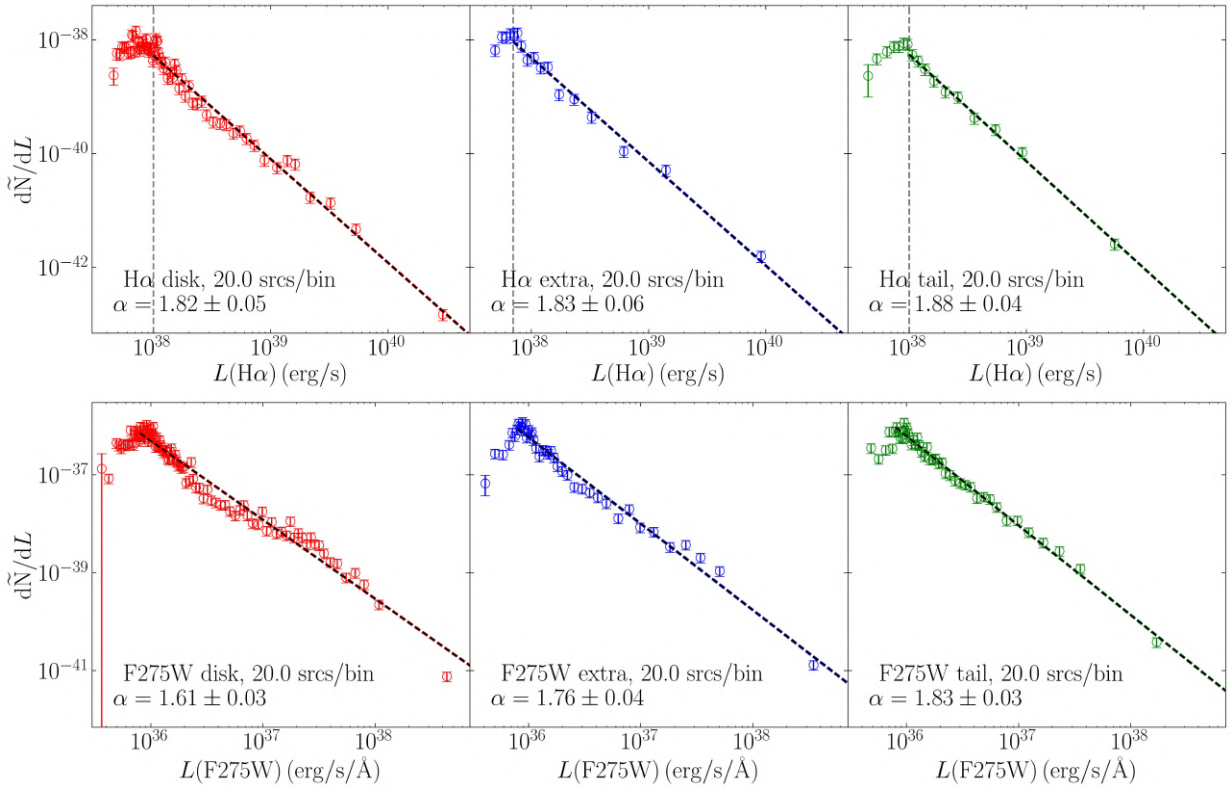

Figure 4.8: From Giunchi et al. (2023a). Luminosity distribution functions $\mathrm{d}\widetilde{\mathrm{N}}/\mathrm{d}L$ of Hα-selected (upper panels) and UV-selected (lower panels) clumps. Clumps are divided according to their spatial category: disk (left panels, in red), extraplanar (middle panels, in blue) and tail (right panels, in green). For each plot I show: the empirical LDF of the corresponding sample (open circles with errorbars), generated with equal-number bins (i.e. each bin contains the same number of objects, see Cook et al. 2016), and the best-fitting line (dashed line). The grey vertical lines correspond to the value of L_{peak}. Notice that the Hα luminosity of the Hα-selected clumps is the integrated emission of the Hα line, therefore in erg/s, while the UV luminosity of the UV-selected clumps is in erg/s/Å. Credits to Giunchi et al. (2023a).

trunks and leaves.

LDF slopes are consistent with previous results for H II regions (Kennicutt, Edgar & Hodge 1989; Santoro et al. 2022) and UV-selected young stellar clumps (Cook et al., 2016).

I also performed a *KS*-test on the luminosity distributions for pairs of spatial categories, for Hα- and UV-selected clumps separately, to infer whether the LDF significantly changes from one region to another. I compared the distributions above the maximum L_{peak} value above which all three sub-samples can be assumed to be complete. The resulting p-values are listed in Table 4.2 (first row) and are consistent with what one would expect when comparing the slopes of the LDFs. For Hα-selected clumps, where the slopes are consistent with each other within the errors, the KS-test cannot exclude that each pair of distributions are identical. For UV-selected clumps, the KS-test confirms significant differences for the pairs disk-extraplanar and disk-tail.

In the left panel of Figure 4.9 I show the comparison among the best-fitting slopes, as a function of the selection band and the spatial category. Both the UV and Hα slopes steepen going from disk, to extraplanar to tail regions, where the closest match with the expected

		α	K_L	$L_{\rm peak}$ [erg/s(/Å)]	$\alpha_{\rm s}$	$K_{\rm s}$	size$_{\rm peak}$ pc
(1)	(2)	(3)	(4)	(5)	(6)	(7)	(8)
	D	1.82 ± 0.05	30.9 ± 1.8	1×10^{38}	2.8 ± 0.2	4.2 ± 0.4	150
Hα	E	1.83 ± 0.06	31 ± 2	7×10^{37}	3.6 ± 0.6	6.4 ± 1.4	200
	T	1.88 ± 0.04	33.0 ± 1.6	1×10^{38}	4.4 ± 0.8	8 ± 2	160
	D	1.61 ± 0.03	21.8 ± 1.2	8×10^{35}	2.95 ± 0.16	4.6 ± 0.4	190
UV	E	1.76 ± 0.04	27.3 ± 1.6	8×10^{35}	2.9 ± 0.3	4.4 ± 0.7	200
	T	1.83 ± 0.03	26.9 ± 1.1	8×10^{35}	3.5 ± 0.4	5.9 ± 0.9	175
Complexes		1.83 ± 0.08	30 ± 3	1.7×10^{36}	-	-	-

Table 4.1: List of the best-fitting values of the LDFs and SDFs when fitted to the different samples of star-forming clumps and complexes. Column (1) refers to the clump selection photometric band. Column (2), from top to bottom: disk (D), extraplanar (E) and tail (T) sub-samples of Hα-selected and UV-selected clumps; the last row refers to star-forming complexes, which are only in the tails by construction. Columns (3), (4) and (5) contain the values of the best-fitting slopes α, the best-fitting normalization K_L and the peak luminosity $L_{\rm peak}$ arbitrarily chosen, over which datapoints are fitted (Equation 4.1). Notice that $L_{\rm peak}$ is in erg/s for Hα-selected clumps, whereas it is in erg/s/Å for UV-selected clumps and star-forming complexes. Columns (6), (7) and (8) list the same quantities (best-fitting slope α_s, best-fitting normalization K_s and peak size size$_{\rm peak}$), but for the SDFs.

	Hα			UV		
	D-E	D-T	E-T	D-E	D-T	E-T
(1)	(2)	(3)	(4)	(5)	(6)	(7)
Lum	0.792	0.350	0.254	0.004	2×10^{-8}	0.152
size	3×10^{-6}	0.613	0.012	7×10^{-5}	9×10^{-4}	0.002

Table 4.2: P-values of *KS*-tests (Section 4.2.1) for luminosity (first row) and size distributions (second row). Columns (2), (3) and (4) list the values for the Hα-selected clumps, when comparing disk and extraplanar clumps (D-E), disk and tail clumps (D-T) and extraplanar and tail clumps (E-T), respectively. Columns (5), (6) and (7) show the same results, but for UV-selected clumps. Hα-selected clumps are also selected to avoid AGN-powered regions when performing the *KS*-test on the luminosity distributions.

slope for a scale-free turbulent regime ($\alpha = 2$) is found.

Shallower LDFs are found in galaxies with high sSFR (Santoro et al., 2022), such as all our jellyfish galaxies (Vulcani et al., 2018), which may explain why our slopes are smaller than 2. Furthermore, as described in Section 1.4.1, past works (Cook et al., 2016; Messa et al., 2018; Santoro et al., 2022) find flatter LDFs in environments with a high SFR surface density $\Sigma_{\rm SFR}$. Projection effects and blending, which are more likely to affect the disk than the tails, have also been demonstrated to flatten the LDF (as demonstrated by Dessauges-Zavadsky & Adamo 2018 in the case of mass distribution function). Flatter slopes are also found in simulations that include the ageing effect of the most massive clumps (Gieles, 2009), which would be consistent with the fact that the slopes of the Hα-selected clumps (circles in Figure 4.9) are larger than those of the UV-selected clumps (squares) of the corresponding spatial category. It would be also confirmed by the slope of the star-forming complexes (all of which are located in the tails by construction), which is very close to that of tail UV-selected clumps.

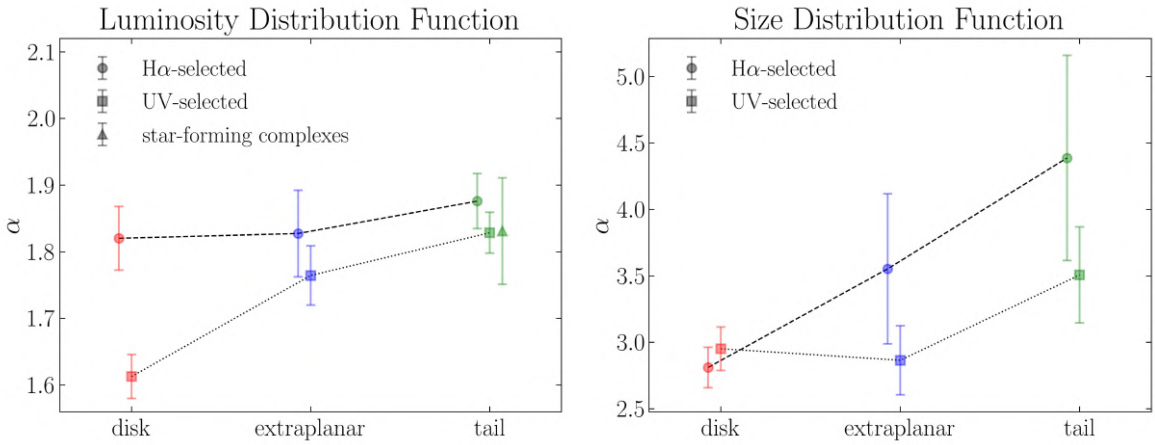

Figure 4.9: Comparison of the slopes of the LDFs (left panel) and SDFs (right panel) of star-forming clumps and star-forming complexes, both as a function of the selection band and the spatial category (see Table 4.1). Circles are Hα-selected clumps, squares are UV-selected clumps and triangles are star-forming complexes. Colors refers to the spatial category: red for disk, blue for extraplanar and green for tail. From Giunchi et al. (2023a).

My analysis therefore suggests that the tails contain proportionally more low-luminosity clumps than the disks, and the extraplanar regions are intermediate between the two. However, this difference is statistically significant only when comparing UV-selected disk clumps with the other spatial categories, while for Hα-selected clumps there are only hints of such trend (Figure 4.9). Furthermore, observational biases could explain the shallower LDF observed in disk clumps, since disk clumps are expected to be more affected by blending effects and underlying disk contamination, while the tail clumps are the least contaminated population, being isolated. Hence their observed LDF should be the closest to the intrinsic one. Indeed, it is the closest to the theoretical expected value of 2 (Elmegreen, 2006). Thus, we can conclude that the properties of the gas in which clumps are embedded are likely to play a minor role in influencing the LDF.

Deviation from single power law

Carefully inspecting Figure 4.8, it is evident that disk (and to some extent, also extraplanar) LDFs show some particular features, such as slope changes, plateaus and secondary peaks, hinting to the need of a more complex model rather than a single power law, as suggested by (Beckman et al., 2000) as a consequence of the transition from ionization to density bound (described in Section 1.4.1). To characterize these different regimes, disk LDFs are divided in three intervals: the faint-end interval, the plateau and the bright-end interval, each fitted with a power-law. Furthermore, for the Hα-selected LDF we fitted a power law also to datapoints brighter than 1.2×10^{39} erg/s, in correspondence of a secondary peak of the LDF[3] ("secondary-peak interval", hereafter).

[3]This secondary peak is dominated by clumps in JO201 (the galaxy with the largest amount of disk and tail clumps). Nonetheless, we do not have reasons to think there is a bias in luminosity artificially increasing the number of clumps at such luminosity, therefore it is a matter of interest to characterize this interval, too.

Phot. band	Parameters	Faint-end	Plateau	Bright-end	Secondary-peak
	α	2.7 ± 0.2	1.1 ± 0.4	1.82 ± 0.08	2.04 ± 0.08
Hα	$L_{\rm min}$ [erg/s]	1×10^{38}	2.7×10^{38}	5×10^{38}	1×10^{39}
	$L_{\rm max}$ [erg/s]	2.7×10^{38}	5×10^{38}	-	-
	α	2.24 ± 0.06	0.98 ± 0.14	2.31 ± 0.13	-
UV	$L_{\rm min}$ [erg/s/Å]	8×10^{35}	6×10^{36}	3×10^{37}	-
	$L_{\rm max}$ [erg/s/Å]	6×10^{36}	3×10^{37}	-	-

Table 4.3: Best-fitting slopes obtained when a set of power laws are fitted to the disk LDFs divided in intervals (Section 4.2.1). From left to right: clump selection photometric band (Phot. band); best-fitting slope α and luminosity range boundaries of the interval $L_{\rm min}$ and $L_{\rm max}$ (Parameters); names of the intervals (Faint-end, Plateau, Bright-end and Secondary-peak).

The best-fitting slopes and the luminosity intervals are shown in Table 4.3. In Figure 4.10 we show the best-fitting power laws superimposed onto the disk and extraplanar LDFs. The latter comparison was done in order to understand if also this spatial category could be characterized by the same regimes (we do not have enough statistics to divide the extraplanar LDFs in intervals and fit a power law in each of them).

For what concerns Hα-selected LDFs, the faint-end interval slope is steeper than that of the bright-end interval, hinting to a change in the properties of the clumps before and after the plateau. When considering the secondary-peak interval, the distribution gets steeper than for the bright-end interval, but still flatter than at the faint-end. When superimposing these results on the extraplanar LDF (right-end panels in Figure 4.10), one can notice that the faint- and bright-end best-fitting power laws describe quite well the distribution. On the other hand, the extraplanar LDF seems to lack the plateau and the secondary-peak, even though there are not enough datapoints in these intervals to exclude this hypothesis. Concerning the disk UV-selected LDF, the slopes in the faint- and bright-end intervals are consistent within the uncertainties. The plateau covers a wider luminosity range compared to the Hα plateau. The presence of a plateau in UV LDFs has never been observed before. Furthermore, the extraplanar LDF is well described by the results obtained for the disk, especially in the faint-end interval.

Whether these different regimes are an effect of the ageing or not is not clear yet. The position of the plateau in the disk Hα LDF is compatible with the change in the regime of the H II regions from *density bound* to *ionization bound* (Beckman et al., 2000). On the other hand, the slopes at the low and high luminosity ends are similar, while the Beckman et al. (2000) model predicts a steepening at bright luminosities, where H II regions are ionization bound. Moreover, our LDFs show the same plateau also in the disk UV-selected clumps, which should not be affected by the changing in the ionization regime.

4.2.2. *Size distribution functions*

In this Section I select Hα- and UV-resolved clumps, in order to have reliable estimates of the clump sizes. The analysis of the size distribution functions (SDFs hereafter) of the clumps is performed in the same way described in Section 4.2.1. The samples are binned using 15 sources per bin for disk clumps and 5 sources per bin for the extraplanar

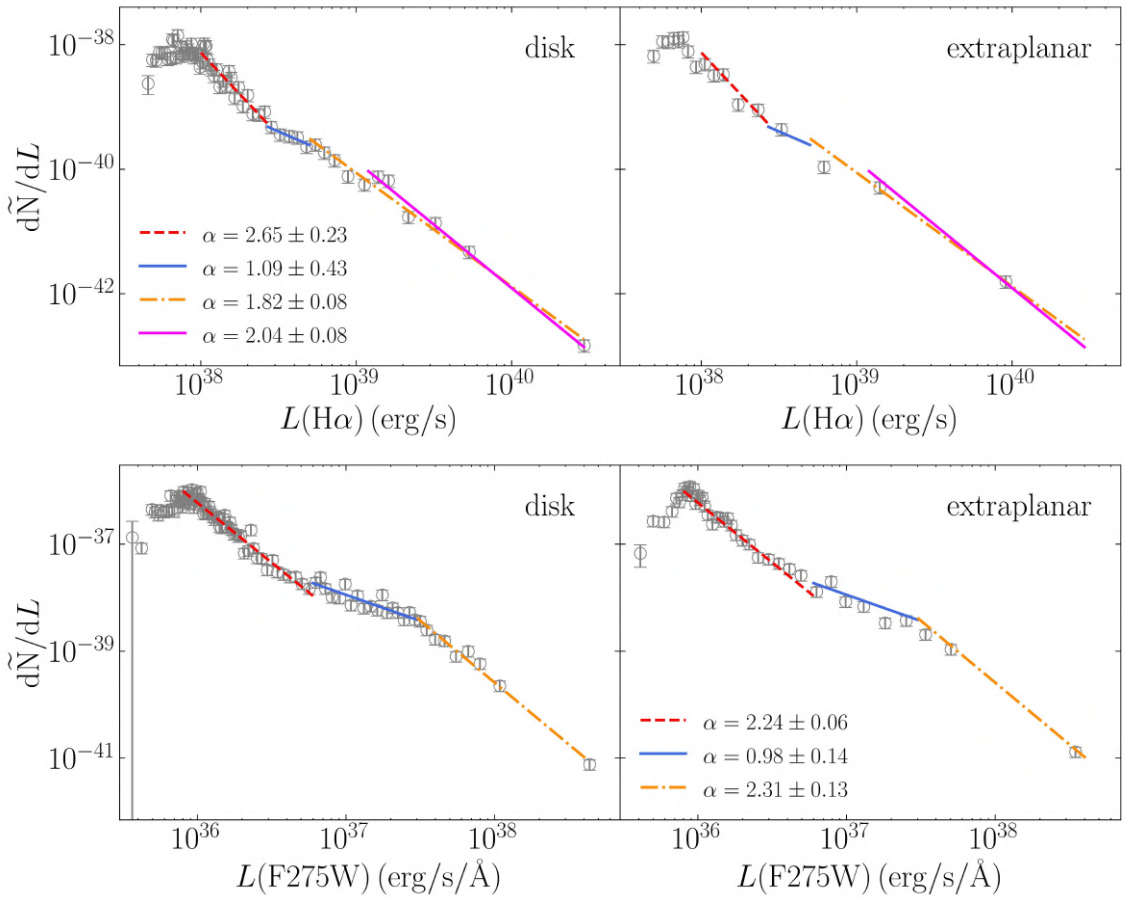

Figure 4.10: Luminosity distribution functions $d\widetilde{N}/dL$ of Hα-selected (upper panels) and UV-selected (lower panels) clumps fitted in intervals (defined as described in this Section). Clumps are divided in disk (left panels) and extraplanar (right panels). The fit in intervals is performed for the disk LDFs and superimposed to the extraplanar LDFs. The intervals are: faint end (red dashed line), plateau (blue solid line), bright end (yellow dash-dotted line), secondary peak (purple solid line, only for Hα clumps). Notice that the Hα luminosity of the Hα-selected clumps is the integrated emission of the Hα line, therefore in erg/s, while the UV luminosity of the UV-selected clumps is in erg/s/Å. Plot credits to Giunchi et al. (2023a).

and tail clumps, because of the low number of clumps in these spatial categories. SDFs are qualitatively similar to LDFs. Their intrinsic functional form is a power law, but incompleteness effects introduce a cutoff at small sizes. In analogy with what I did for the LDF (Equation 4.1), I define the peak value as $\mathrm{size}_{\mathrm{peak}}$ and I fit the datapoints above this value to a power law.

In Figure 4.11 the observed SDFs and the best-fitting model of each sub-sample are shown. For completeness, I plot also the SDF datapoints of unresolved clumps, for which I have only upper limits for the sizes (filled dots). In order to do that, SDFs are not normalized for the total number of clumps, since the normalization changes considering unresolved clumps or not. A single power law is likely to be a good representation of the resolved data, especially considering that the sample is about 15% of the one used to constrain the parameters of the LDFs (see Table 3.1). The loss of statistics can affect

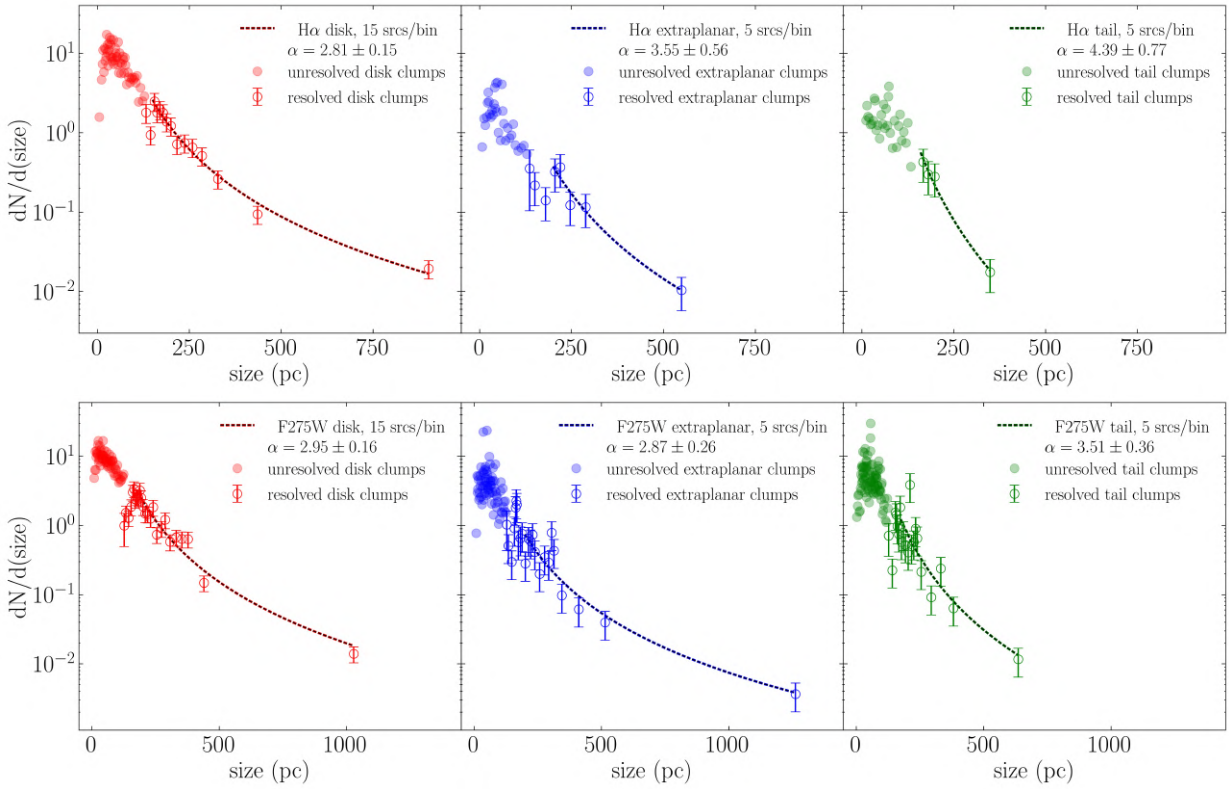

Figure 4.11: Size distribution functions for disk (red), extraplanar (blue) and tail (green) clumps. Top: Hα. Bottom: UV. Resolved clumps are shown as empty circles with 1σ errorbars, while unresolved clumps are plotted as filled circles without errorbars. In this case, SDFs are not normalized by the total number of clumps and the x-axis is in linear scale. Plot credits to Giunchi et al. (2023a).

especially the extraplanar and tail sub-samples, for which the regime in which the sample is complete includes just a few datapoints. The fitted power laws do not describe well the unresolved datapoints, as expected from incompleteness. Together with the fact that unresolved clumps have, by definition, no reliable size estimates, this incompatibility implies that I cannot draw any conclusion for sizes below ~ 140 pc.

The best-fitting slopes and normalizations, and the chosen $\text{size}_{\text{peak}}$ of each sub-sample are listed in columns (6), (7) and (8) of Table 4.1. The average slope is 3.3 ± 0.6 (3.6 ± 0.6 for Hα-resolved clumps and 3.1 ± 0.3 for UV-resolved clumps). Slopes of extraplanar and tail Hα-resolved clumps are consistent with the one found by Kennicutt & Hodge (1980) in the disk of a low-z spiral galaxy ($\alpha = 4.1$).

As done in Section 4.2.1 for LDFs, I computed the p-values from the KS statistics comparing the size distributions of pairs of spatial categories, keeping the two selection filters separated. Results are listed in Table 4.2 (second row). In this case, the KS finds significantly different distributions for all pairs, except for disk vs tail Hα-resolved clumps. However, both the slopes and the p-values have to be taken with caution, due to small numbers, especially in the tail clumps.

These distributions are found to be different from those inferred for the Hα clumps of these galaxies detected by Poggianti et al. (2019) from the MUSE Hα luminosities using the luminosity-size relation by Wisnioski et al. (2012): the expected median size was 440 pc

for clumps in the disks and 320 pc for clumps in the tails. Here, the median sizes are $\sim$ 210 pc, $\sim$ 211 pc, $\sim$ 180 pc for disk, extraplanar and tail Hα-resolved clumps, respectively, and $\sim$ 215 pc, $\sim$ 223 pc, $\sim$ 208 pc for disk, extraplanar and tail UV-resolved clumps. Consistently with what was inferred by Poggianti et al. (2019), clumps in the tails are smaller than those in the disk. Nonetheless, values found in this work are about half the size inferred in Poggianti et al. (2019). The explanation to this difference is strictly related to the differences between luminosity-size relation by Wisnioski et al. (2012) and the one obtained from our HST observations (see Section 4.3).

In the bottom panel of Figure 4.9 the slopes of the fit to the SDF of resolved clumps in each category are plotted. Also in the case of SDFs the slope of UV-resolved clumps are smaller (with the exception of disk clumps), even if consistent within errorbars, than those of Hα-resolved clumps. Moreover, disk and extraplanar UV-resolved slopes are almost equal, while in Hα there are hints of a steepening from disk to tail regions.

The slope increase can be partially explained based on the work in Gusev (2014), whose observations of the nearby galaxy NGC 628 demonstrated that the overall slope of SDFs reaches values between 4.5 and 6[4] when analysing the smallest structures of the star-forming regions (i.e. what we define as leaves in Section 3.2.1) or isolated objects. Instead, the slope decreases up to 2.5 once all the substructures of complex star-forming regions are taken into account. Our trend is analogous. I find steep slopes ($\sim 4.4 \pm 0.8$, consistent with 4.5) in the Hα tails, whose clumps have typically no or few substructures. On the other hand, the slope is smaller in the case of disk clumps, which are more structured than extraplanar and tail clumps. Therefore, including both trunks and leaves in the samples has little effects on the slope of tail clumps, while it may explain the flatter distribution found for disk clumps. Indeed, I observe steeper disk SDFs when using only the leaves (3.28 ± 0.28 in Hα and 3.22 ± 0.23 in UV). Alternatively, recent simulations of star forming regions in presence of different ambient pressures (Nath, Das & Oey, 2020) found slopes similar to the one of the disk SDFs, while they suggest the presence of a lower pressure environment in the tail. The pressure producing the measured steepening in the tail SDF would be one order of magnitude lower than the typical ICM pressure of our galaxies (Bartolini et al., 2022). Therefore the variation of the slope of the SDF across different environments seems to be different to that expected from environmental effects.

In conclusion, the largest clumps of our sample are found in the disk and in the extraplanar regions of our galaxies, whether I consider UV- or Hα-resolved clumps, and (as hinted by the *KS*-test), clumps of different spatial categories are likely to follow different SDFs with different slopes. The sizes of the clumps seem to be poorly affected by the environment in which they are embedded, ICM in the tails and ISM in the disks, and more linked to their clustering features.

[4]Gusev (2014) when fitting the cumulative distribution functions. Also, their slopes are defined as negative. Therefore the slopes in this work (α_s) and the slopes by Gusev (2014) (α_G) are connected by $\alpha_s = 1 - \alpha_G$.

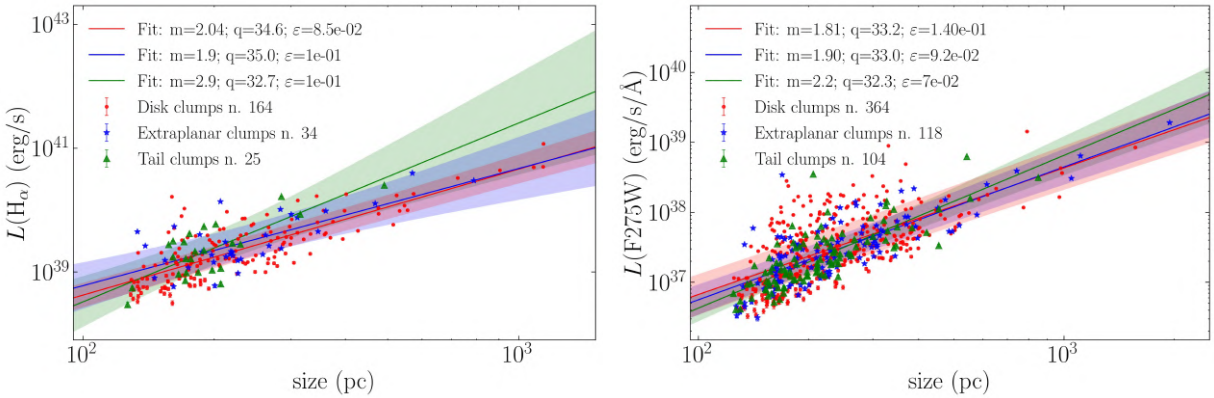

Figure 4.12: Luminosity-size relations for Hα-resolved clumps (on the left) and UV-resolved clumps (on the right). The clumps are plotted according to their spatial category: disk (red circles), extraplanar (blue stars), tail (green triangles). The best-fitting lines to the three categories are plotted as solid lines of the corresponding color. The shaded areas are the uncertainties on the fits at 2σ. Note that Hα luminosity is in erg/s, while F275W in erg/s/Å. Plots from Giunchi et al. (2023a).

4.3. *Luminosity-size relations*

In this Section I study the luminosity-size relation, both for Hα- and UV-resolved clumps. Here Hα-resolved clumps are BPT-selected to avoid AGN- and LINER-powered regions. To calculate the linear regression fits with the inclusion of an intrinsic scatter, I employed the Python software package LINMIX (Kelly, 2007). LINMIX implements a Markov Chain Monte Carlo (MCMC) algorithm to converge on the posterior and return a sample of sets of parameters drawn from the posterior distribution. The linear relation fitted by LINMIX is

$$\log L = m \log(size) + q + \mathrm{G}(\varepsilon), \tag{4.2}$$

where L is the luminosity of the clump in the filter in which it is selected, $size$ is the PSF-corrected core diameter, m is the angular coefficient of the correlation, q is the y-axis intercept and $\mathrm{G}(\varepsilon)$ is the intrinsic scatter, computed from a Gaussian distribution centered in $m\,\mathrm{Log}(size) + q$ with standard deviation ε.

In Figure 4.12 I plot the datapoints in the $(\mathrm{Log}L, \mathrm{Log}(size))$ plane and the best-fitting lines, both for Hα- and UV-resolved clumps (left and right panel, respectively). Clumps are divided according to their spatial position.

Best-fitting parameters are listed in Table 4.4. The average slope is 2.3 ± 0.4 for Hα-resolved and 1.97 ± 0.17 for UV-resolved clumps. The slopes for the disk and extraplanar Hα-resolved clumps are consistent within 1σ and close to 2, while the slope for the tail clumps is steeper. In UV, the slopes of all spatial categories are consistent with each other.

The Hα-resolved clumps have slopes consistent with 2 for disk and extraplanar clumps which, as discussed in Section 1.4.2, is either consistent with the model for the growth of ionized bubbles by Nath, Das & Oey (2020) and with the one discussed in Cosens et al. (2018) for clumps with a high star formation rate surface density (Σ_{SFR}). On the other hand, the slope of tail clumps is consistent with 3, as suggested by previous works (Beckman

	Hα			UV		
Spat. cat.	m	q	ε	m	q	ε
(1)	(2)	(3)	(4)	(5)	(6)	(7)
Disk	2.04 ± 0.12	34.6 ± 0.3	$(8.5 \pm 1.0) \times 10^{-2}$	1.81 ± 0.12	33.2 ± 0.3	$(14.0 \pm 1.0) \times 10^{-2}$
Extraplanar	1.9 ± 0.4	35.0 ± 0.8	$(10 \pm 3) \times 10^{-2}$	1.90 ± 0.14	33.0 ± 0.3	$(9.2 \pm 1.3) \times 10^{-2}$
Tail	2.9 ± 0.5	32.7 ± 1.2	$(10 \pm 3) \times 10^{-2}$	2.2 ± 0.2	32.3 ± 0.4	$(7 \pm 1) \times 10^{-2}$

Table 4.4: Best-fitting parameters (m, q, ε) (with 1σ uncertainties) of the luminosity-size linear relations (Equation 4.2) for Hα-resolved clumps (columns 2, 3, 4) and UV-resolved clumps (columns 5, 6, 7). Each spatial category (column 1) is fitted separately.

et al., 2000; Wisnioski et al., 2012) and by Cosens et al. (2018) for clumps in main-sequence galaxies.

We note that disk, extraplanar and tail clumps have similar Hα luminosities for a given size, therefore if disk and extraplanar clumps have enhanced $L_{\mathrm{H}\alpha}$, tail clumps should be enhanced as well. The enhancement in Hα emission for tail clumps would be possible even with a slope consistent with 3; as discussed in Section 1.4.2, the model by Cosens et al. (2018) predicts a flatter relation, but only if the clumps are located in the galactic plane. As the clumps become as large as the galactic scale height, they can grow only over the galactic plane, causing the change of slope from 3 to 2. However, clumps in the tails are located in a different environment, far from the galactic disk and can grow in all directions even if enhanced in Hα emission.

4.3.1. *Comparison with previous results*

In Figure 4.13 I compare the position of our Hα-resolved clumps in the $\log L - \log(size)$ with those presented in the literature. I show results from Fisher et al. (2017), who studied clumps belonging to turbulent, extremely Hα-bright DYNAMO galaxies, and those by Wisnioski et al. (2012), who studied $z \sim 0$, isolated, star-forming galaxies (Arsenault & Roy, 1988; Kennicutt et al., 2003; Rozas et al., 2006; Gallagher & Hunter, 1983; Monreal-Ibero, A. et al., 2007). I also show the best-fitting relations they present in their works.

Since both our luminosities and those computed by Wisnioski et al. (2012) are not dust-corrected, I re-added extinction caused by dust to the published dust-corrected luminosities of the DYNAMO clumps. Dust-extincted DYNAMO clumps are then fitted to a power law with slope fixed at 2, as done in Fisher et al. (2017).

As described in detail in Fisher et al. (2017), the radii of DYNAMO clumps were found fitting a 2D Gaussian to the light distribution, with the addition of a constant representing the local background level (Fisher et al., 2017). To make the comparison with DYNAMO as consistent as possible, I derive new PSF-corrected core radii (r_{gauss}) of our clumps fitting a 2D Gaussian+constant to our tail Hα-resolved clumps, which are more isolated and in a fainter local background than disk and extraplanar clumps. Then I visually select only clumps for which a fit is appropriate. For these clumps, I compute $r_{\mathrm{gauss}} - r_{\mathrm{core,corr}}$, finding that it does not correlate with $r_{\mathrm{core,corr}}$, it ranges between 0 and 50 pc and it has a median value of 25.5 pc. Assuming that this difference is a good representation of the value of $r_{\mathrm{gauss}} - r_{\mathrm{core,corr}}$ for all the Hα-resolved clumps of our sample, I computed a new PSF-

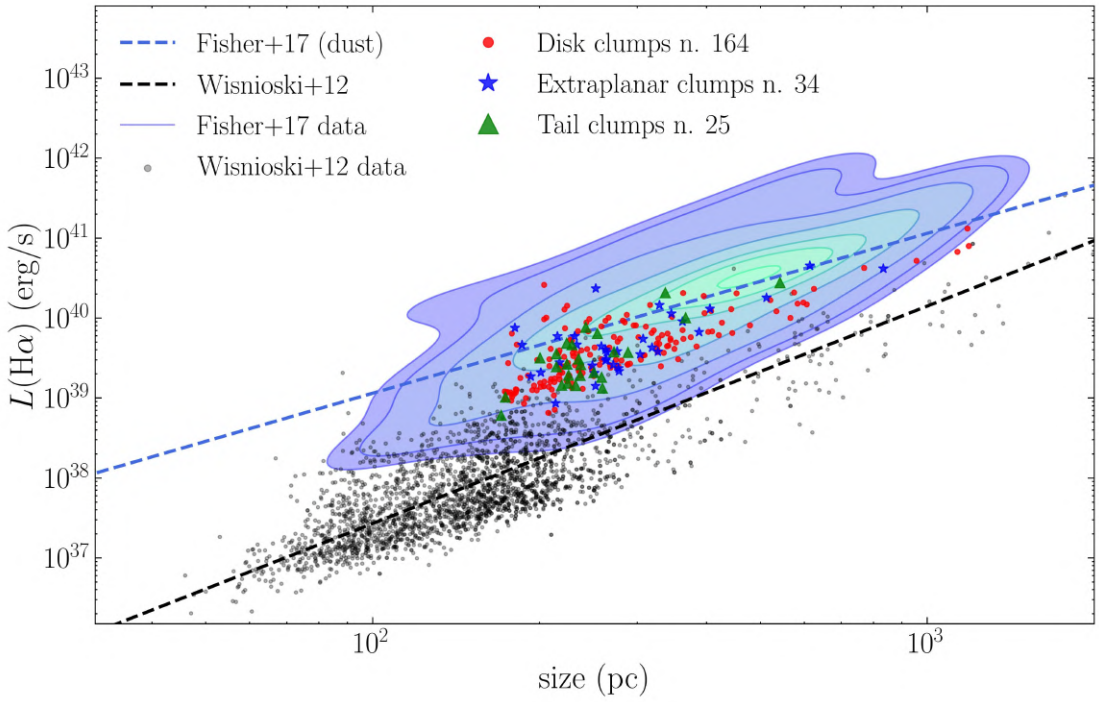

Figure 4.13: log(L(Hα)) − log(size) comparing our Hα-resolved clumps with those in DYNAMO starburst galaxies (Fisher et al. 2017, blue contours) and those in local, isolated, star-forming galaxies presented in Wisnioski et al. 2012 (Arsenault & Roy 1988; Kennicutt et al. 2003; Rozas et al. 2006; Gallagher & Hunter 1983; Monreal-Ibero, A. et al. 2007, black dots). Our clumps are plotted according to their spatial category: disk (red circles), extraplanar (blue stars), tail (green triangles). Our clump luminosities and sizes are corrected in order to make the comparison more trustworthy; for the same reason, DYNAMO clump luminosities are corrected re-adding the effects of dust extinction. The black dashed line is the best-fitting relation by Wisnioski et al. (2012), the blue dashed line is obtained fitting the dust-extincted DYNAMO clumps keeping the slope fixed at 2, as done in Fisher et al. (2017). Clumps in our sample lie in between the two sample, being close in particular to clumps in starburst galaxies. Plot credits to Giunchi et al. (2023a).

corrected core radius $\widetilde{r}_{\mathrm{core,corr}} = r_{\mathrm{core,corr}} + 25.5$ pc. Therefore the new sizes are $2\widetilde{r}_{\mathrm{core,corr}}$. The luminosities are re-computed integrating the light within a circle of radius $3\widetilde{r}_{\mathrm{core,corr}}$. The procedure adopted in Wisnioski et al. (2012) to compute luminosity and size is similar to the one applied in Fisher et al. (2017), though not identical. Therefore I can be confident that the corrections I applied to our clumps allow us to make a fair comparison also with the results by Wisnioski et al. (2012).

Our clumps lie between the Fisher and Wisnioski relations, being closer to the one obtained by Fisher et al. (2017), even though they have lower luminosities and sizes compared to the peak of their distribution. With respect to the Wisnioski clump distribution, our resolved clumps are on average larger and, at a given size, brighter. As shown by Johnson et al. (2017) and Cosens et al. (2018), DYNAMO clumps have both higher SFR and Σ_{SFR} than clumps in isolated spiral galaxies, as a consequence of the intense star formation of their host galaxies. Being closer to the DYNAMO sample in the luminosity-size relation may suggest our Hα-resolved clumps to have a high Σ_{SFR}, too (hints of that has already been found in Vulcani et al. 2020b, in which they studied the resolved SFR-stellar mass

relation for the MUSE Hα knots).

4.4. *Star-forming clumps and diffuse emission*

A major point that previous GASP observations could not address directly concerns the nature of the diffuse Hα emission observed in GASP galaxies (Tomičić et al., 2021a,b, and refs therein); in the tail, the diffuse emission (defined as the Hα component outside compact clumps) is found to be on average 50% and up to 80% in some galaxies (Poggianti et al., 2019). Diagnostic BPT diagrams based on [N II]/Hα line ratio indicate that the dominant ionization source of the diffuse emission is star formation; however MUSE data shows that other mechanisms are at play, like mixing of ICM and ISM, and shocks (Tomičić et al., 2021a,b). MUSE observations could not firmly establish whether the diffuse emission powered by sta formation was due to ionizing radiation escaped from the star-forming knots stars or from a population of smaller and undetected star forming clumps that are hiding within the diffuse Hα emission in the tails.

The clumps presented in the previous Chapter are identified either in UV or Hα with luminosity down to $\sim 10^{36}$ erg/s/Å in F275W and $\sim 10^{38}$ erg/s in Hα; these values are very close to the detection limit computed in Section 2.4. We did not detect any significant population of compact sources in UV nor in Hα in the tails outside of the star-forming knots detected with MUSE (see Poggianti et al., 2019). Hence we can safely conclude that the ionizing source of what was defined as diffuse ionized emission from MUSE data is not in-situ SF in clumps brighter than the detection limit of our HST observations.

Another interesting result from Sections 4.2.2 and 4.3 is that the sizes of the clumps in the tails measured from the HST observations are generally smaller than what was estimated in Poggianti et al. (2019) from MUSE observations using the luminosity-size relation for H II regions from Wisnioski et al. (2012). However, I found that at a given size, tail clumps are ~ 10 times brighter than the H II regions observed by Wisnioski et al. (2012). The paucity of very large star-forming clumps (larger than a few 100 pc) and/or the compactness of the star forming clumps in the tails might be connected with the peculiar physical condition in the ram pressure stripped gas which might affect the star-formation process; in principle, the collapse of molecular clouds and the star-formation processes could be influenced by thermal conduction from the ICM; however this effect could be mitigated or even prevented by magnetic fields (Müller et al., 2021; Ignesti et al., 2022b). The effect of the complex interplay between the stripped gas and the ICM would also affect the turbulence of the gas in the tails and hence the properties of the clustering hierarchy which should be hence linked to the environment and its pressure.

4.5. *Summary*

In this Chapter I have shown the results obtained for Hα and UV clumps in jellyfish galaxies for what concerns their luminosity and size distribution functions (LDFs and SDFs, respectively) and their luminosity-size relation. The comparison among clumps of different spatial categories (disk, extraplanar and tail) points out that the brightest and biggest

clumps of our sample are found in the disks.

When fitting the LDFs to a power law, I get an average slope of 1.79 ± 0.09, consistent with previous observations of clumps in main-sequence, merging and starburst galaxies. Being consistent also with the slope $(1.8 - 2)$ predicted by models and simulations, this result is evidence that even if gas is embedded in the ICM and is undergoing ram-pressure stripping, it collapses and forms stellar clumps according to a scale-free cascade driven by turbulence. In accordance with literature results, the SDF is flatter for the disk clumps, which are complex and clustered structures, than for the simple and far from each other tail clumps, ranging values between ~ 2.8 and ~ 4.5.

All the Hα clumps, whether they are in the disks or in the tails, show an enhanced Hα luminosity at a given size, when compared to the clumps in main-sequence galaxies, being closer to the clumps in starburst galaxies. Interestingly, no striking differences are found between disk and tail clumps, suggesting that the different environments in which they are embedded (ISM and ICM) play a minor role in influencing the star formation. Furthermore, the average best-fitting slope of the Hα luminosity-size relation is 2.3 ± 0.4, flatter than the slope 3 observed in clumps of main-sequence galaxies and consistent with the one observed in clumps in starburst galaxies, with enhanced star-formation rate surface density $\Sigma_{\rm SFR}$.

Therefore we can conclude that ram-pressure stripping is likely to enhance the clumps Hα luminosity (and possibly also $\Sigma_{\rm SFR}$) via gas compression, even if not as strongly as in starburst galaxies, yet not changing the clumps formation mechanism, still driven by the turbulent collapse.

Chapter 5

Morphology of clumps and complexes using a multi-wavelength approach

The main aim of this Chapter is to study the morphological properties of the clumps and complexes, especially in the tails, where they form from stripped gas, looking for the effects of ram-pressure stripping. Characterizing this large sample of objects, I aim at finding evidence that the fireball configuration (Section 1.5) systematically arises in the clumps of jellyfish galaxies. The Chapter is structured as follows: in Section 5.1 I analyze the axial ratios distributions of clumps and complexes in all disk, extraplanar and tail regions; in Section 5.2 I explore how the properties of the clumps are correlated to those of the complexes in which they are embedded, focusing on the number of matched clumps (Section 5.2.1) and on the filling factor (i.e. the fraction of optical area covered by the clumps, Section 5.2.2); in Section 5.3 I search for evidence of fireballs by rigorously defining the displacement of the Hα (or UV) emission and the center of the optical complex, and studying how the displacement is correlated to the properties of the complex; finally, Section 5.4 is focused on analyzing the possible correlations of the clump and complex properties and the distance from the host galaxy.

5.1. *Axial ratios of clumps and complexes*

The axial ratio of clumps and complexes can be a proxy of the effects of ram-pressure stripping on the gas that is forming stars. The fireball model (Section 1.5) predicts that stellar populations of different ages are formed displaced from each other and with a non-zero reciprocal velocity. In addition to that, the tidal field exerted by the parent galaxy may further increase the elongation of the stellar clumps. Therefore I expect our clump elongation to be larger than those observed in isolated galaxies.

In this Section we analyze the axial ratio for both Hα- and UV-resolved leaf clumps, as well as resolved star-forming complexes. As examples, I show in Figure 5.1 three UV-resolved clumps with increasing elongation (axial ratios 0.92, 0.60 and 0.24). The solid contour defines the area of the clump, while the dotted ellipse is defined from the semi-major and semi-minor axes of the clump, which also shows the position angle of the clump.

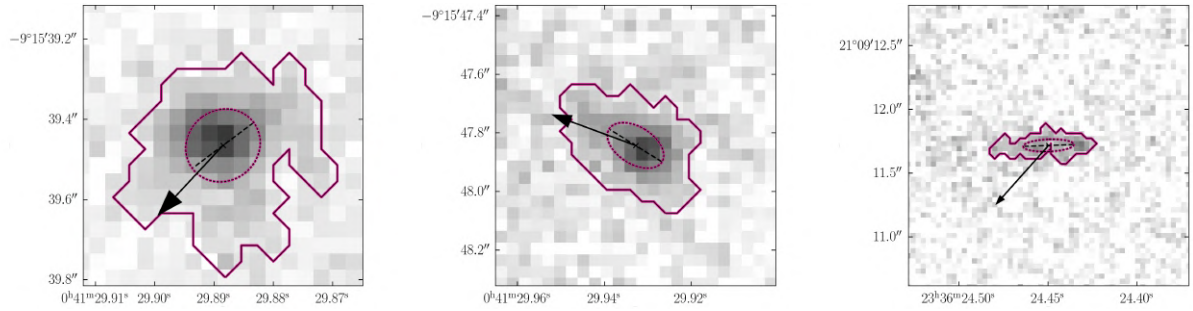

Figure 5.1: Images of 3 UV-resolved clumps. The solid contour defines the area of the clump, the dashed ellipse is defined by the major and minor axis. The dashed line is the major axis. The cross is the geometric center of the clump. The arrow points to the center of the hosting galaxy. The clumps are selected as examples of the variety of elongation we have: from left to right, the axial ratio (defined as the ratio of the semi-minor to the semi-major axes of the clump) decreases from 0.92, to 0.60, to 0.24. Images taken from Giunchi et al. (2023b).

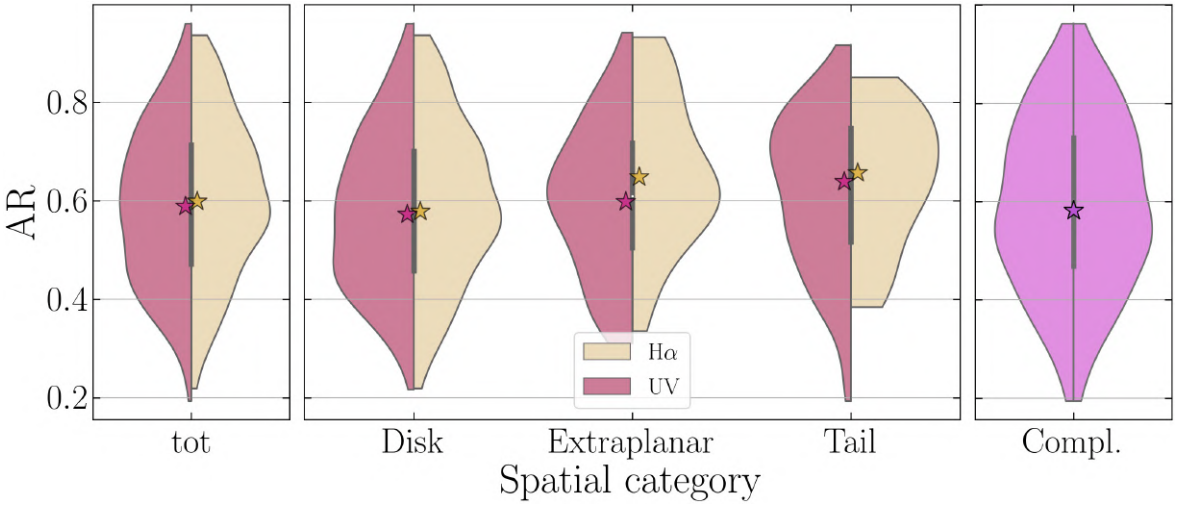

Figure 5.2: Violin plots of the axial ratio distributions of the star-forming clumps and complexes of our sample. Median values are plotted as stars, the dark vertical line shows the interquartile region. Left plot: distribution of the whole UV- (magenta) and Hα- (golden) resolved clumps. Middle plot: UV- (magenta) and Hα- (golden) resolved clumps are divided in spatial categories (disk, extraplanar and tail from left to right). Right plot: distribution of the resolved star-forming complexes. Credits to Giunchi et al. (2023b).

The arrow points towards the center of the galaxy, allowing a qualitative evaluation of the tilt angle.

In Figure 5.2 I show the violin plots of the axial ratio distributions of the Hα- and UV-resolved leaf clumps and of the resolved complexes. Median values are in the range $\sim 0.58 - 0.68$ for all the categories of clumps and complexes. I stress that the axial ratio of small clumps can be overestimated as a consequence of PSF, therefore these results should be taken as upper limits to the intrinsic median values.

I also performed a Kolmogorov-Smirnov test by separating Hα- from UV-selected clumps and complexes, in each of the three spatial categories (tail, extraplanar and disk). I do not find any difference among the sub-sample distributions of the axial ratio, with the only exception of UV-resolved disk and tail clumps. Nonetheless, I can still derive some conclusions by looking at the distributions in Figure 5.2. The median values and the peaks

of the distributions indicate that clumps tend to be rounder going from the disk to the tails. Furthermore, comparing disk and extraplanar clumps, the distribution becomes narrower, suggesting that there are less elongated clumps in the extraplanar regions than in the disk. Indeed, the peak shifts towards rounder clumps (especially in Hα). In the tails the trend of Hα-resolved clumps is even narrower and peaking at larger values of AR. The opposite seems happening for tail UV-resolved clumps, which are elongated (3.33% of the whole tail UV-resolved sample with AR$<$ 0.3).

In conclusion, I do not see any evidence that tail or extraplanar clumps are more elongated than clumps in the disk. In fact, they are round on average, except for a small fraction of UV-resolved clumps in the tails. However, I point out that also the star-forming complexes, located only in the tails by construction, can reach very low axial ratios. The optical emission comes from stars of different ages, from very young stars emitting in Hα and even in UV to stars older than 200 Myr that do not in Hα and are very faint in UV. Therefore the cases of strong elongation observed in the complexes are consistent with the fireball configuration (Section 1.5).

5.2. *Nesting of star-forming complexes in the tails*

In this Section I study the nesting properties of the star-forming complexes, by looking at the number of Hα- and UV-selected clumps they contain. I stress again that complexes are defined only in the tails, so all the results in this section refer to that spatial category. Clumps are matched to complexes as described in Section 3.2.3.

5.2.1. *Number of clumps within complexes*

In the top left panel of Figure 5.3 I plot the cumulative distributions of the complexes as a function of the number of hosted Hα- and UV-selected clumps: 96% of the complexes contain one or no Hα-selected clump and 3 UV-selected clumps at most. It is more common for a complex to host multiple UV-selected clumps rather than multiple Hα-selected clumps.

The complexes without Hα clumps are lacking bright H II regions, though they may still have a detectable diffuse Hα emission. Our Hα-clump detection procedure is sensitive to the emission powered by a single O class-star (see Figure 4.6).[1] The lack of O class-stars in these complexes can have two explanations: either star formation has stopped more than 20 Myr ago (all O class-stars have died, the clump is quenched/older), or star formation is still occurring but only stars with masses lower than O or bright B class-stars are currently forming (ongoing star formation with a top-light Initial Mass Function).

In Figure 5.4 I plot the number of matched Hα- and UV-selected clumps as a function of the following properties of the hosting complex described in Sections 3.4.1 and 3.4.2: optical luminosity $L_{\rm F606W}$, Hα/UV, the complex total area $A_{\rm compl}$, axial ratio AR and radius of the brightest matched clump r_{bc}. I also report the Pearson's coefficient r for each quantity and sample of clumps. The only significant correlations are found with $A_{\rm compl}$ and $L_{\rm F606W}$, for which the Pearson's coefficients are between 0.55 and 0.68 (depending on the

[1] An O5V star produces about 5.6×10^{49} ionizing photons per second, which for ionization bound conditions corresponds to an Hα luminosity of $5.6\times10^{37}\,{\rm erg\,s^{-1}}$.

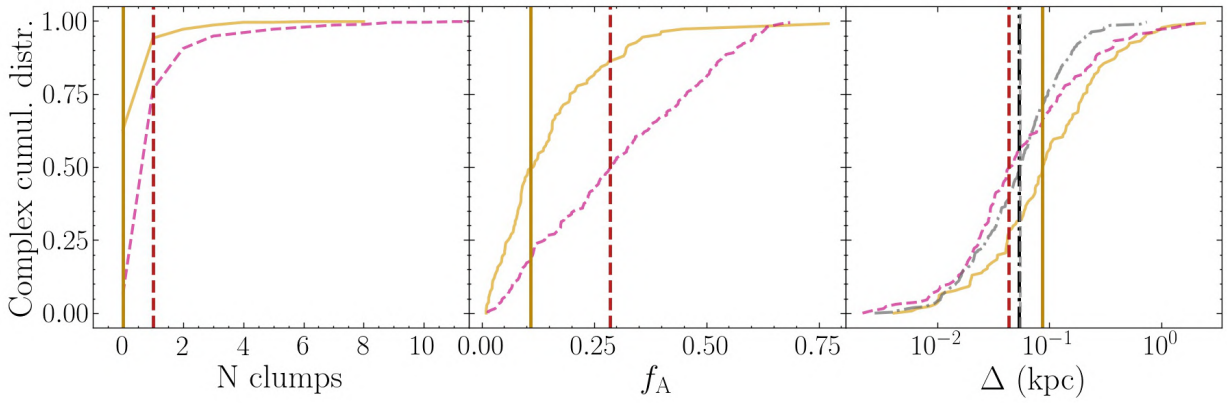

Figure 5.3: Cumulative distributions of the complexes per number of matched clumps (left panel, Section 5.2.1), clump filling factor (middle panel, Section 5.2.2) and clump-complex geometric center displacement (right panel, Section 5.3.1). Each quantity is computed for matched Hα-selected clumps (golden solid line) and UV-selected clumps (magenta dashed line). Furthermore, the displacement is computed considering separately UV-selected clumps in complexes with and without matched Hα clumps (the latter plotted as grey dotted-dashed line). Median values are plotted as dark golden solid, dark magenta dashed and, when present, black dotted-dashed vertical lines. In the right panel, the grey dashed line shows our minimum resolvable resolution for the center displacement (~ 0.055 kpc). Credits to Giunchi et al. (2023b).

chosen compared property and whether they have been computed on the matched Hα- or UV-selected clumps).

Since L_{F606W} traces also old stellar populations and therefore it is strictly connected to the mass of the complex, we conclude that massive, large and bright complexes host more clumps than low-mass, small and faint ones. However, the number of clumps is also weakly correlated to the size (Pearson's coefficient $0.49 - 0.57$), hinting that where clumps are numerous, they are also big. No other correlations are found between the number of hosted clumps and the properties of the complex.

5.2.2. *Filling factor* f_{A}

I now focus on the fraction of the total area of a complex that is filled with clumps, defined here as the filling factor (f_{A}). In particular, the comparison of UV- and Hα-selected clumps f_{A} gives hints about the morphological evolution of stellar populations of different age. In fact, as the clumps dynamically evolve, they can get more diffuse or evaporate (Fujii & Portegies Zwart, 2015), causing variations in their morphology and in many other properties. Furthermore, if the complexes follow fireball configuration (Section 1.5), then stars at different ages should occupy different regions of the complex, with young stars located further away from the galactic disk then old stars. Therefore the UV-selected clumps should cover a much larger area than the Hα-selected clumps, which are selected to span a shorter age range than Hα-selected clumps. The complex filling factors f_{A} computed with respect to Hα- and UV-selected clumps (Section 3.4.2) can be used to understand how the different generations of stars are spatially distributed with respect to each other.

In the middle panel of Figure 5.3 I plot the cumulative distributions of $f_{\mathrm{A}}(\mathrm{H}\alpha)$ and $f_{\mathrm{A}}(\mathrm{UV})$. UV-selected clumps are more likely to cover a larger area than Hα-selected clumps, 95% of which have a filling factor smaller than 0.4. Median values are 0.27 for UV-selected

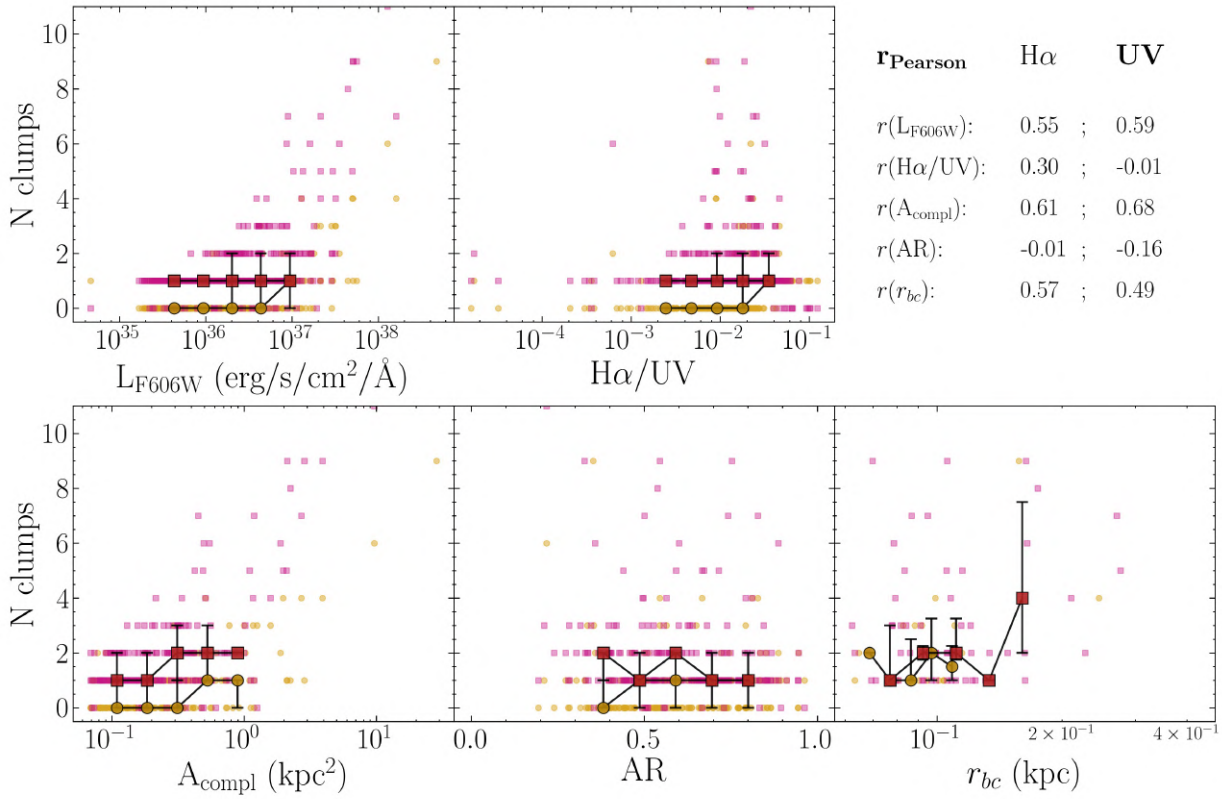

Figure 5.4: Plots of the number of matched Hα-selected clumps (golden dots) and UV-selected clumps (magenta squares) as a function of F606W luminosity L_{F606W} (top left), Hα-to-UV luminosity ratio Hα/UV (top middle), area A_{compl} (bottom left), axial ratio AR (bottom middle) and radius of the largest matched resolved clump (bottom right). Larger dark golden dots for Hα-selected clumps and dark magenta squares for UV-selected clumps show the median number of clumps per bin of the $x-$axis. The bins of the $x-$axis are equally spaced in linear or logarithmic scale according to the physical property. Error-bars show the quartiles of the distribution in the bin. On the top right I show the Pearson coefficient for each quantity and for Hα and UV matched clumps. For the sake of the clarity of the plots, I cut out one complex containing 21 clumps, which anyway does not affect our interpretation of the plots. Plots from Giunchi et al. (2023b).

clumps and 0.10 for Hα-selected clumps. This difference suggests that Hα-selected clumps typically occupy a small and compact region of their parent complexes, while UV-selected clumps are both larger and more numerous, as suggested also by the examples given in Figure 3.7. Furthermore, the UV cumulative distribution grows almost linearly, meaning that the distribution of f_A(UV) is flat up to 0.6.

To further investigate this behaviour, in Figure 5.5 we plot f_A as a function of the following properties of the hosting complex: L_{F606W}, Hα/UV, A_{compl}, AR and r_{bc}. Weak correlations are found with AR ($r = 0.28 - 0.32$) and Hα/UV ($r = 0.42$ for Hα clumps). No correlations are found with the area or the luminosity of the complex, nor with r_{bc}. However, I point out that the spread of the filling factor is large, even where we find a correlation. Since the filling factor correlates with the axial ratio of the complexes and not with their area, it is likely to be influenced mainly by the intrinsic morphology of the complexes: round complexes, regardless of the size, are better filled by clumps than elongated complexes.

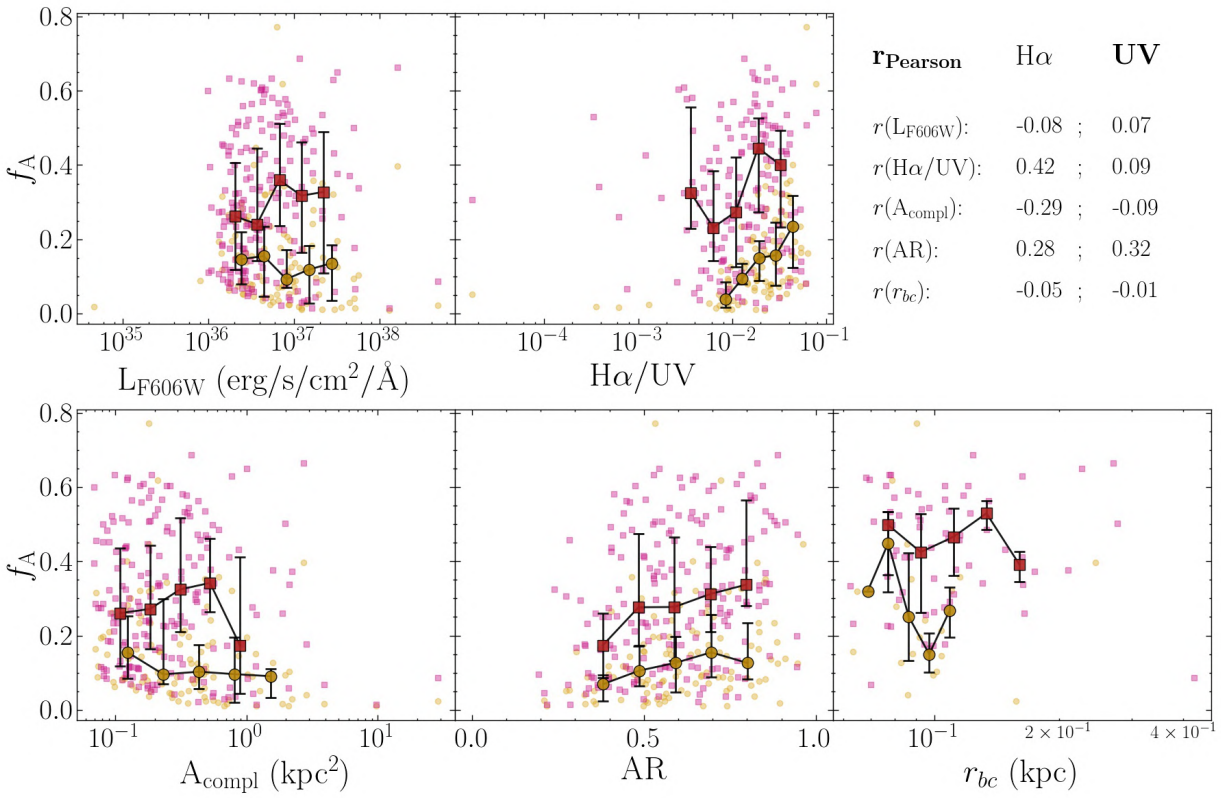

Figure 5.5: As Figure 5.4, but for Hα-selected clumps filling factor $f_{\rm A}$(Hα) (golden dots) and UV-selected clumps filling factor $f_{\rm A}$(UV) (magenta squares). Plots from Giunchi et al. (2023b).

In the top panel of Figure 5.6 I plot the PSF-corrected core radius of the brightest clump hosted by a complex as a function of the area of the complex itself. A good correlation is observed, both when looking at the Hα-resolved clumps and at the UV-resolved clumps ($r = 0.56$ and 0.76, respectively). Therefore large complexes both contain more and larger clumps than the small ones, rather than having more clumps with a constant size or a fixed number of clumps of increasing size.

However, I find that the filling factor does not correlate with $\rm A_{compl}$ and r_{bc} (Figure 5.5), and neither with the number of clumps, as shown in the bottom panel of Figure 5.6. Our conclusion is that, in large complexes, both the size and the number of the nested clumps increase in such a way that the filling factor is not correlated with the area of the complex. The only morphological quantity driving variations of the filling factor is the axial ratio of the complex: round complexes are more filled by clumps than elongated complexes. This effect may be due to differences in the RPS deceleration of round and elongated complexes, with the latter being more decelerated and resulting in higher reciprocal velocities among stars born at different times, with a consequent larger displacement among the stellar different generations. Otherwise, the difference may be caused by projection effects: the velocity of elongated complexes shall have the dominant component on the plane of the sky, while the round ones shall preferentially move along the line of sight.

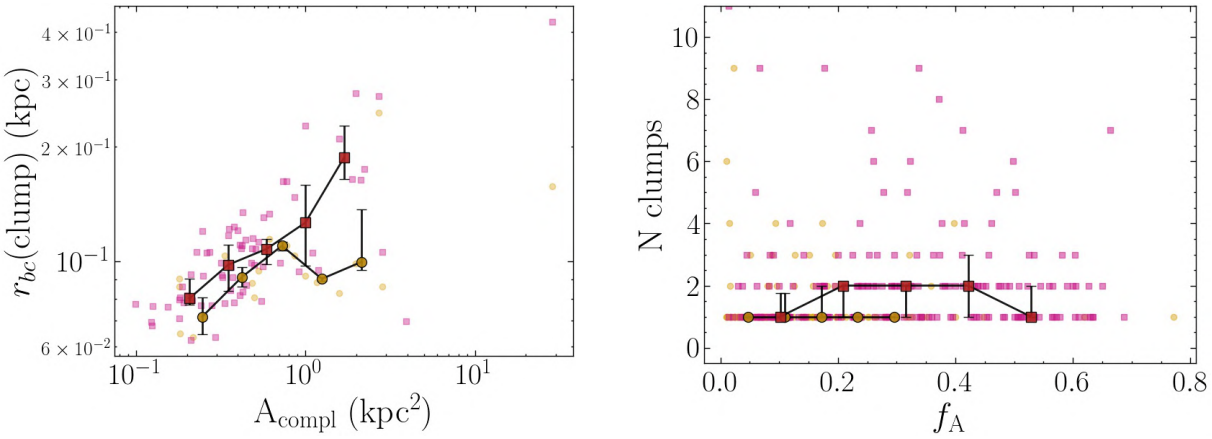

Figure 5.6: Left panel: PSF-corrected core radius of the brightest Hα-resolved (golden dots) and UV-resolved (magenta squares) clump matched to the complex area. Median profiles are plotted as dark golden dots for Hα-selected clumps and dark magenta squares for UV-selected clumps. Error-bars show the quartiles of the distribution in the bin. Right panel: same as the top panel, but for number of matched Hα-selected clumps as a function of the Hα filling factor (golden dots) and number of matched UV-selected clumps as a function of the UV filling factor (magenta squares). Plots taken from Giunchi et al. (2023b).

5.3. *Fireballs*

Throughout this Section I compare our results with previous fireballs observations in the tails of jellyfish galaxies, testing whether the expected configuration (Section 1.5 and Kenney et al. 2014; Jáchym et al. 2019) is systematically found also in our galaxy sample. To briefly summarize, the model of the *fireball* predicts that the age of the stellar populations formed in the stripped gas decreases with increasing distance from the galaxy disk. In the tails clumps are not embedded in the background disk optical emission, and therefore it is possible to find evidence of the fireball age gradient comparing Hα- and UV-selected clumps belonging to the same optical star-forming complex.

Figure 5.7 shows RGB images of eight clear examples of groups of fireballs, three in JO201, three in JO204 and two in JW100, respectively. In these RGB images (credits to ESA/Hubble & NASA) the UV and the Hα emission are strongly emphasized (in blue and red, respectively), while the other colors trace the optical light. The fireballs here highlighted are characterized by compact Hα emission, always displaced in the opposite direction with respect to the center of the galaxy. On the other hand the UV light, despite being more compact in correspondence of the Hα emission, is more diffuse and characterized by a long tail pointing towards the galaxy center. The optical emission is fainter and more diffuse than the UV one. In the case of JO201, the fireballs are elongated either along a direction aligned with the center of the galaxy or along the spiral arm-like sub-tails that are likely to characterize the large-scale morphology of the stripped material (in Appendix A I define the sub-tails for each galaxy and study possible trends along it). In a single fireball many compact Hα clumps are found. The fireballs seen in JO204 appear less diffuse and even more clustered than those observed in JO201, with smaller UV tails but more fragmented star-forming regions. On the other hand, JW100, shows either simple and long fireballs with one Hα clump located in the head of the system and a long UV tail (top

sub-image), or fireballs with many UV clumps aligned with each other and embedded in a more diffuse UV region.

In the next Section, I will quantify the displacement of the Hα- and UV-selected clumps with respect to the center of their star-forming complexes, to assess the fraction of complexes for which the displacement is oriented as expected by the fireball model, with the Hα-selected clumps displaced far from the galactic disk.

5.3.1. *Displacement of clumps inside complexes*

According to the fireball model, I expect the Hα emission to be displaced on one side of the star forming complexes defined by the F606W emission; the UV emission should be decentered as well, but less than the Hα one since it spans a wider age interval (10 Myr for Hα, 200 Myr for UV). To quantitatively estimate this effect, I computed the distance between the geometric centers of the complex and the brightest Hα-selected clump matched to it ($\Delta_{\mathrm{H}\alpha-\mathrm{opt}}$) and the brightest UV-selected clump ($\Delta_{\mathrm{UV}-\mathrm{opt}}$). This was done only for resolved star-forming complexes, in order to have a reliable and robust estimate of the position of the clumps nested inside them. I have shown in Section 3.4.2 that many complexes do not contain any Hα-selected clump, therefore in such cases we compute only $\Delta_{\mathrm{UV}-\mathrm{opt}}$, named $\Delta_{\mathrm{UV}-\mathrm{opt,noH}\alpha}$ hereafter, and keep these complexes separated from those containing both Hα- and UV-selected clumps.

The right panel of Figure 5.3 shows the cumulative distributions of the displacements $\Delta_{\mathrm{H}\alpha-\mathrm{opt}}$, $\Delta_{\mathrm{UV}-\mathrm{opt}}$ and $\Delta_{\mathrm{UV}-\mathrm{opt,noH}\alpha}$. The distribution of $\Delta_{\mathrm{H}\alpha-\mathrm{opt}}$ favors large displacement and indeed the median value (86.5 pc) is the largest among the three samples, while the one of $\Delta_{\mathrm{UV}-\mathrm{opt}}$ can reach very small values, of a few parsecs. The median value of $\Delta_{\mathrm{H}\alpha-\mathrm{opt}}$ is in good agreement with those observed by Kenney et al. (2014) for Hα-UV displacements ($80-100$ pc) of 10 clumps in IC3418. The UV displacement in complexes with no Hα-selected clumps, $\Delta_{\mathrm{UV}-\mathrm{opt,noH}\alpha}$, rises more steeply than the other two distributions and does not reach values larger than $700-800$ pc, even though the median displacement (53.8 pc) is larger than the one of $\Delta_{\mathrm{UV}-\mathrm{opt}}$ (43.3 pc). However, almost half of the distances are below the precision on the reciprocal position of the centers of the two components, which I quantified as the sum in quadrature of the size of two pixels (~ 0.055 kpc at z$\simeq 0.05$).

In order to understand what drives this trend, in Figure 5.8 I correlate the reciprocal distances with the usual complex properties. From these plots we can conclude that:

1. the best correlations are found with $\mathrm{A_{compl}}$ (Pearson's value 0.73) and L_{F606W} (0.61). The larger (and consequently also brighter) the complex, the larger the displacement. In particular, the largest values are reached by $\Delta_{\mathrm{H}\alpha-\mathrm{opt}}$, while $\Delta_{\mathrm{UV}-\mathrm{opt}}$ shows a similar but shallower trend and $\Delta_{\mathrm{UV}-\mathrm{opt,noH}\alpha}$ is flat;

2. a weak anti-correlation (Pearson's values ~ -0.38) is found with AR: the more elongated the complex, the larger the displacement. Also in this case, $\Delta_{\mathrm{H}\alpha-\mathrm{opt}}$ shows the steeper correlation, while $\Delta_{\mathrm{UV}-\mathrm{opt}}$ and $\Delta_{\mathrm{UV}-\mathrm{opt,noH}\alpha}$ have a similar, flatter trend;

3. when compared with Hα/UV, $\Delta_{\mathrm{UV}-\mathrm{opt,noH}\alpha}$ shows no correlation, while $\Delta_{\mathrm{H}\alpha-\mathrm{opt}}$ and $\Delta_{\mathrm{UV}-\mathrm{opt}}$ become smaller as Hα/UV increases;

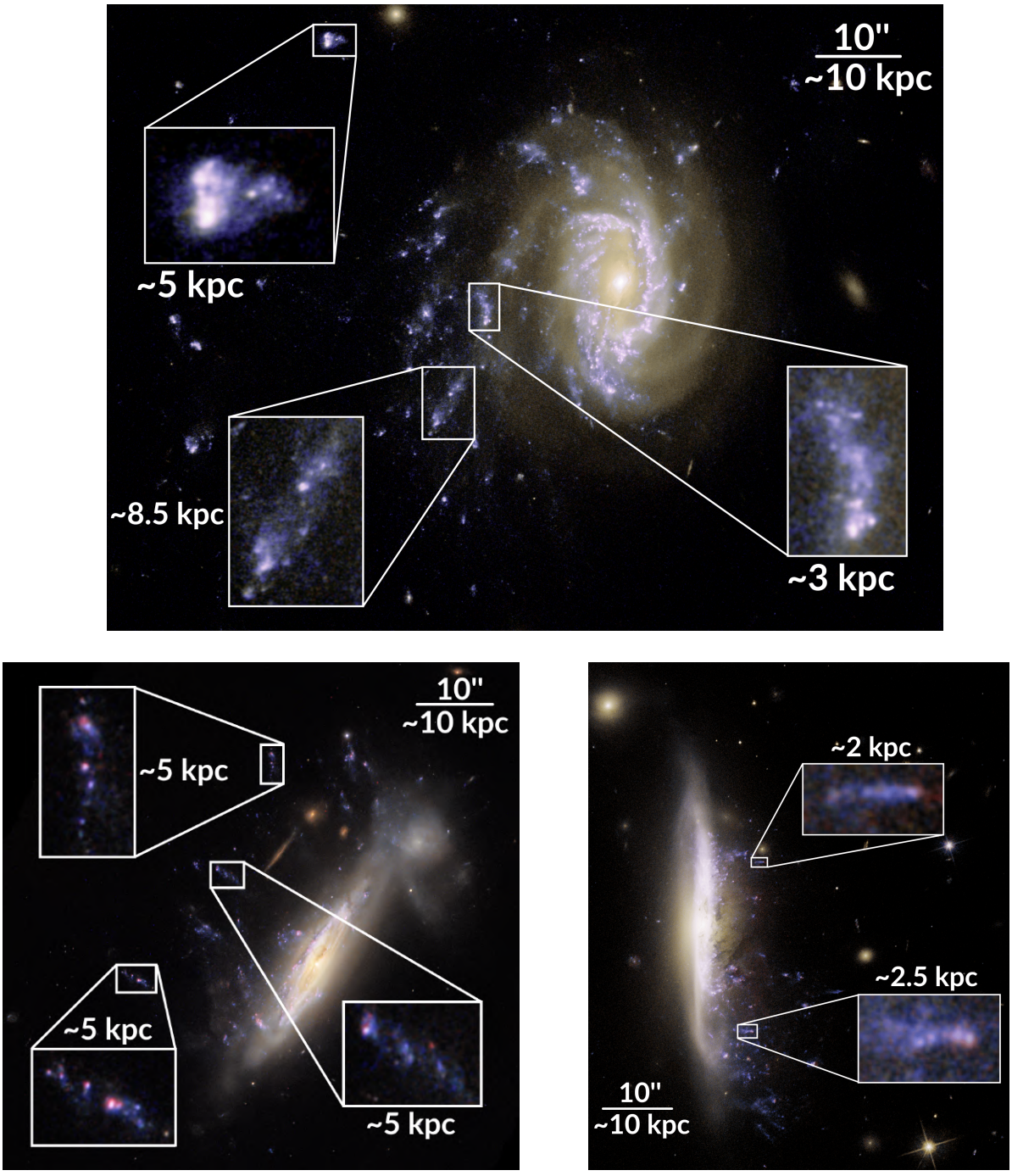

Figure 5.7: Color-composite images of JO201 (top), JO204 (left) and JW100 (right). The orange/yellow color traces the optical emission, the blue one is the UV emission. The red color is associated to Hα emission. Zoomed-in images show typical examples of fireball configurations of the star-forming clumps in the tails of these galaxies. Credits for images: ESA/Hubble & NASA, M. Gullieuszik and the GASP team.

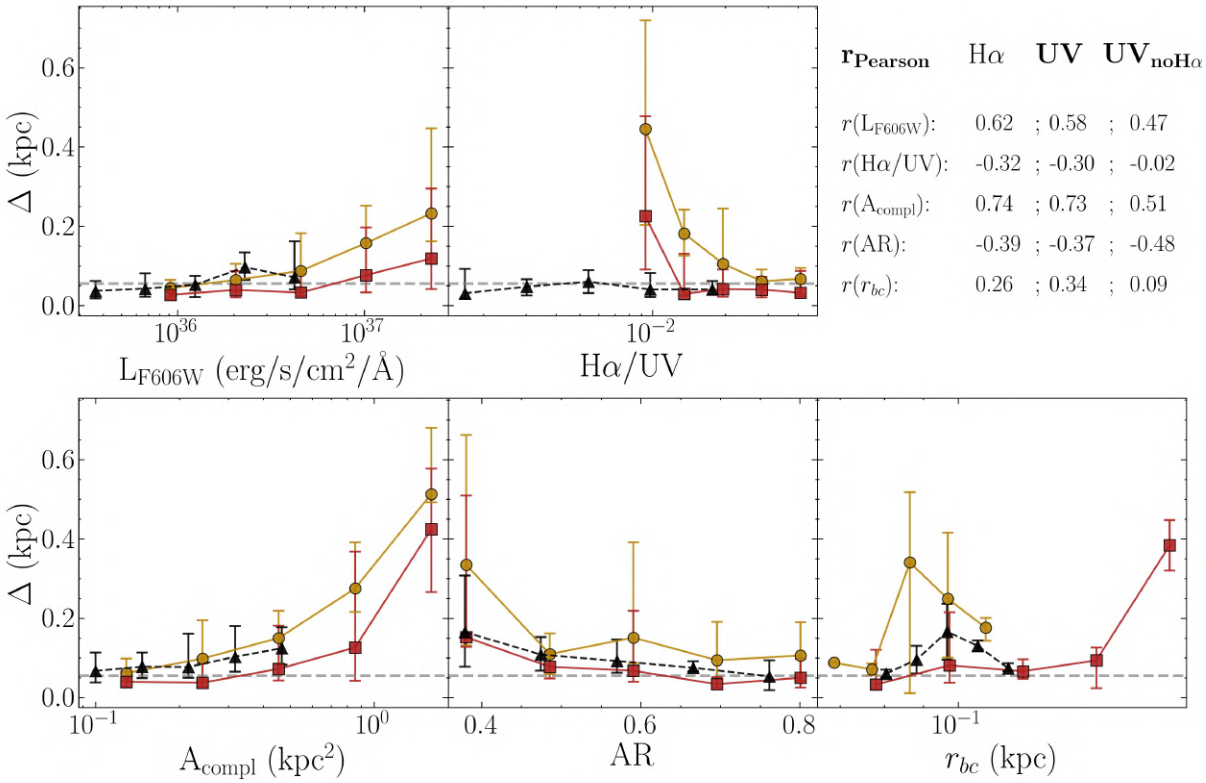

Figure 5.8: Plots of the center distances of the complexes as a function of F606W luminosity L_{F606W} (top left), Hα-to-UV ratio Hα/UV (top middle), area A_{compl} (bottom left), axial ratio AR (bottom central) and radius of the largest matched resolved clump (bottom right). I plot the median profiles of the center distances as golden dots for $\Delta_{H\alpha-opt}$, magenta squares for Δ_{UV-opt}, black triangle for $\Delta_{UV-opt,noH\alpha}$. Errorbars show the quartiles of the distribution in the bin. On the top right we show the Pearson coefficient for each quantity and for Hα and UV matched clumps. I also plot our resolution limit as a horizontal grey dashed line. Plots from Giunchi et al. (2023b).

4. no correlation is found with r_{bc}(clump), even if here the statistics may be too poor to drive any conclusion.

It is worth mentioning that in the cases of complex area and luminosity, $\Delta_{UV-opt,noH\alpha}$ overlaps remarkably well with $\Delta_{H\alpha-opt}$, at least in the range of values in which both complexes with and without Hα clumps are observed. Such good agreement suggests that the UV-only and UV+Hα complexes have similar morphological properties. As a consequence of passive ageing, the UV emission is now located only in the head of the fireball, where the youngest population resides and where younger complexes emit in Hα as well. That may explain why the morphological properties of the UV clumps in UV-only complexes resemble those of Hα clumps in the others. To fully answer to this question, a detailed analysis of the ages of these objects is necessary and will be perform in future works.

In conclusion, large and bright complexes with both Hα- and UV-selected clumps show clear signs of a displaced Hα emission, where the UV emission is more diffused and closer to the complex center, in accordance with the fireball model previously described. The displacement decreases with the complex axial ratio, suggesting that in elongated complexes the clumps tend to occupy one side of the complex, instead of being positioned at its center.

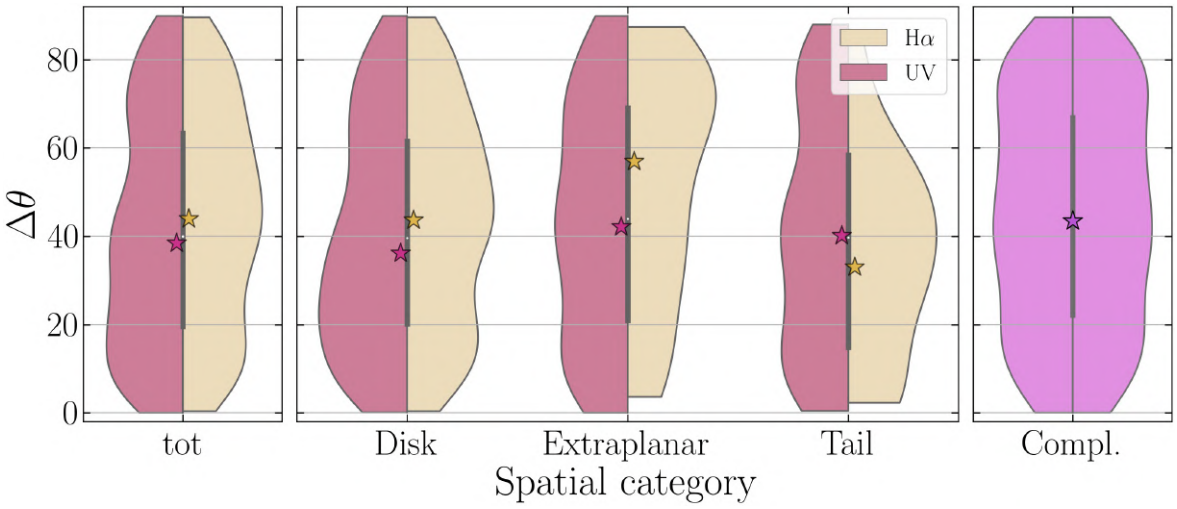

Figure 5.9: Same as Figure 5.2, but for tilt angle distributions of resolved clumps and complexes. Credits to Giunchi et al. (2023b).

5.3.2. *Alignment of clumps and complexes with the center of the galaxy*

If the fireball model holds, I might also expect the clumps and the complexes to be aligned along a common direction. For the following analysis, such direction is defined as the one to the center of the hosting galaxy, even if I tested also the directions of the sub-tails defined in Appendix A (Figure A.2), finding no substantial differences between the two.

In order to understand whether the clumps and the complexes are elongated along the direction to the galaxy center, we studied two possible proxies: 1) the distributions of the tilt angles of clumps and complexes $\Delta\theta$, defined in Section 3.4.1; 2) the comparison of projected distances from the center of the galaxy of the Hα, UV and optical centers of each complex, to understand whether the UV- and especially the Hα-selected clumps are further away from the disk than the optical emission, as expected by the fireball model.

In Figure 5.9 I show the violin plots of $\Delta\theta$ for the whole sample of clumps and complexes (left and right panel), and for the clumps divided in spatial category (middle panel). Distributions cover the whole range of possible values of $\Delta\theta$ and are almost flat. Median values are almost consistent with 40-45° in the majority of cases, the only exceptions being Hα-resolved extraplanar and tail clumps, for which I have a tendency for clumps with respectively large and small $\Delta\theta$.

The same distributions are studied for clumps of individual galaxies, at least for the cases in which the number of objects is sufficient to build a distribution. No major differences are found with the distributions obtained from the whole samples.

When comparing the projected distances from the center of the galaxy of the Hα, UV and optical centers of each complex, I select only those cases in which the displacement is larger than our precision on the reciprocal evaluation of the two centers (defined in Section 5.3.1 as the sum in quadrature of the size of two pixels, 0.055 kpc). Nonetheless, quantifying the fraction of complexes showing a fireball morphology is not trivial, due to the peculiar morphology of the complexes and the clumps inside them (as can be seen by

the RGB images). In 66/107 ($\simeq$ 62%) Hα-selected matched clumps and 104/187 ($\simeq$ 56%) UV-selected matched clumps, the clump center is farther than the one of the complex, hinting that the youngest stellar populations have a preferential direction of displacement, far from the galactic disk, as predicted indeed by the fireball model.

It is expected that, under fortunate geometrical alignment, such as ram-pressure stripping occurring on the plane of the sky, the fireball structure is observed, and the brightest Hα-selected clump is significantly more displaced than the brightest UV-selected clump inside the same complex. I have evidence of that from the RGB images already shown in Figure 5.7, with clear evidence of compact Hα emission (in red) embedded in diffuse UV emission (in blue), which shows a tail-like structure pointing towards the galaxy.

5.4. *Searching for trends in the tails*

In principle, the properties of clumps and complexes formed from stripped gas may depend on many factors: when the gas collapsed and how far from the disk, how long ago the clump/complex formed, what was the stage of stripping when the gas collapsed. These factors could influence the properties of a clump as a function of its distance from the galaxy, therefore it is interesting to analyze how the number and properties of clumps and complexes depend on the projected distance from the galaxy center. In doing this, I consider all galaxies together, after having checked that our trends are not biased by a single galaxy trend and that the same correlations (or absence of correlations) are found also when looking at individual galaxies.

In Figure 5.10 I plot the cumulative distribution of Hα- and UV-selected clumps and star-forming complexes in the tails as a function of the projected distance D from the hosting galaxy. The majority of clumps and complexes lie within 100 kpc from the galaxy center, with a median around 20-24 kpc. The median distance slightly increases from 20.34 kpc for Hα-selected clumps, to 22.25 kpc for UV-selected clumps, to 23.65 kpc for star-forming complexes In particular, Hα selected clumps are located, on average, closer to their galaxy disks, as shown by the median distances in Figure 5.10, suggesting that most of the star formation occurs soon after the gas is stripped.

I now focus on whether clump and complex characteristics depend on galactocentric distance. In Figure 5.11 I consider $L_{\rm F606W}$, Hα/UV, the clump/complex area A and AR. I do not find any evidence of trends for any clump/complex property as a function of distance. A possible reason behind the evident lack of trends in all the plots resides in the complexity of the star-formation process itself, which depends on a plethora of physical processes that might hide any simple correlation between the quantities I have studied.

I also study the trends with distance of the complex properties which are related to those of the matched clumps. In Figure 5.12 I plot the radial profiles of four complex quantities that can be derived considering the properties of the Hα- and UV-selected clumps matched to the complex: number of clumps, $f_{\rm A}$, radius of the brightest resolved matched clump, center distances ($\Delta_{\rm H\alpha-opt}$, $\Delta_{\rm UV-opt}$, $\Delta_{\rm UV-opt,noH\alpha}$, definitions in Section 5.3.1). The plots show the presence of two weak positive correlations with $f_{\rm A}$ and r_{bc}, especially for UV clumps. These trends may be a consequence of the fireball model: since the different generations of stars are characterized by a difference in velocity, the reciprocal distance

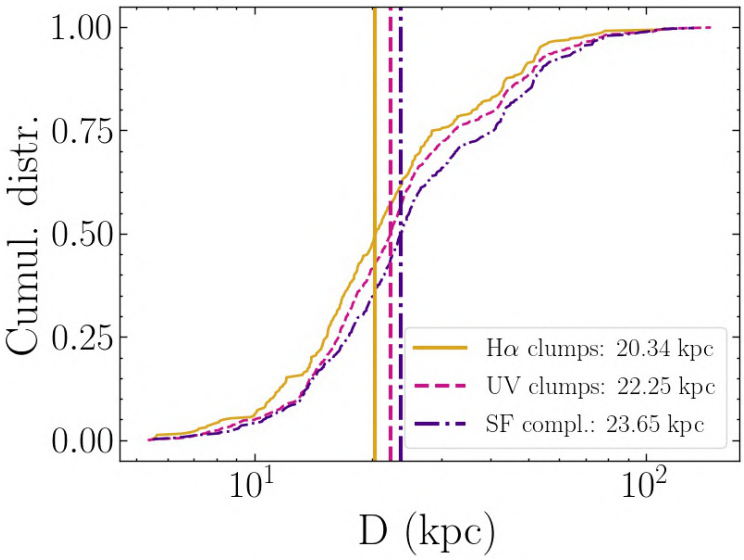

Figure 5.10: Cumulative distribution of tail Hα- and UV-selected clumps (solid golden and dashed purple, respectively) and star-forming complexes (dash-dotted violet) as a function of the distance. The median distances for each sample of clumps/complexes are plotted as vertical lines with same color and style as the corresponding cumulative distribution. Plots from Giunchi et al. (2023b).

among them increases with time, with the net result that the clump they form increases in size and better fill the complex to which it is matched. The same trends are studied computing the distance along their sub-tail (Figures A.3, A.4 and A.5), but no changes are found.

We conclude that the quantities related to the morphology of clumps and complexes and the clumps nesting in the complexes do not correlate with distance, probably as a consequence of the large variety of processes competing in driving and influencing the star formation. For the study of the properties of the stellar populations for each clump and complex, like the stellar mass, the star formation rate and the age, I refer to Werle et al. (2023).

5.5. *Summary*

In this Chapter I have characterized the morphological properties of the Hα and UV young star-forming clumps and optical complexes of our sample of jellyfish galaxies. I find that more than half of the optical complexes contain no Hα clumps, while most of them contain at least one UV clump. I have shown that the typical number and size of Hα and UV clumps is larger in big and bright optical complexes. Both these two quantities grow in such a way that the fraction of optical area covered by the clumps (i.e. the filling factor) is not correlated to the area of the complex. However, the median complex filling factor is larger for UV clumps (0.27) than for Hα clumps (0.10).

When studying the position of the clumps inside their complexes, Hα clumps, and UV clumps to a lesser extent, show a displacement from the complex center of $0.1 - 1$ kpc and, in $\sim 60\%$ of the cases, they are displaced away from the galactic disk. This is the first systematic evidence of the fireball configuration, already observed for a few cases in the tails of RPS galaxies, but now confirmed for a statistically relevant sample of clumps and

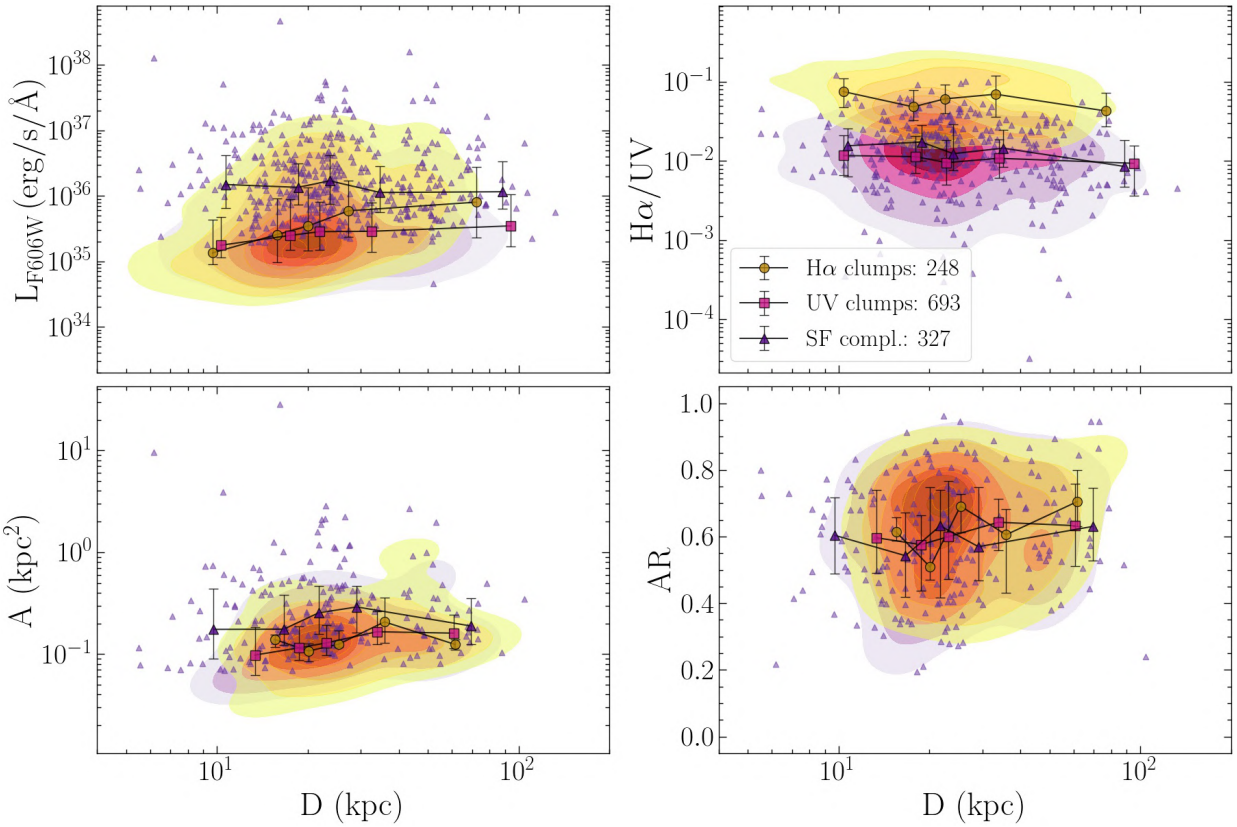

Figure 5.11: Plots of the following quantities as a function of the projected galactocentric distance: F606W luminosity L_{F606W} (top left), Hα-to-UV flux ratio Hα/UV (top right), area A (bottom left) and axial ratio (AR). Yellow-to-red and magenta contours are the Hα- and UV-selected/resolved clump density distribution, respectively. Star-forming complexes are plotted as violet triangles. Golden dots, purple squares and violet triangles are the median profiles of the Hα-selected/resolved clump, UV-selected/resolved clump and star-forming complex properties for bins containing an equal number of clumps/complexes, where the bars indicate the quartiles of the distribution. Plot credits to Giunchi et al. (2023b).

with a rigorous definition of the displacement.

Finally, the filling factor and the clump radius increase with the distance from the galactic disk, suggesting that the reciprocal displacement of the different stellar generations increases as a consequence of the velocity gradient caused by ram pressure.

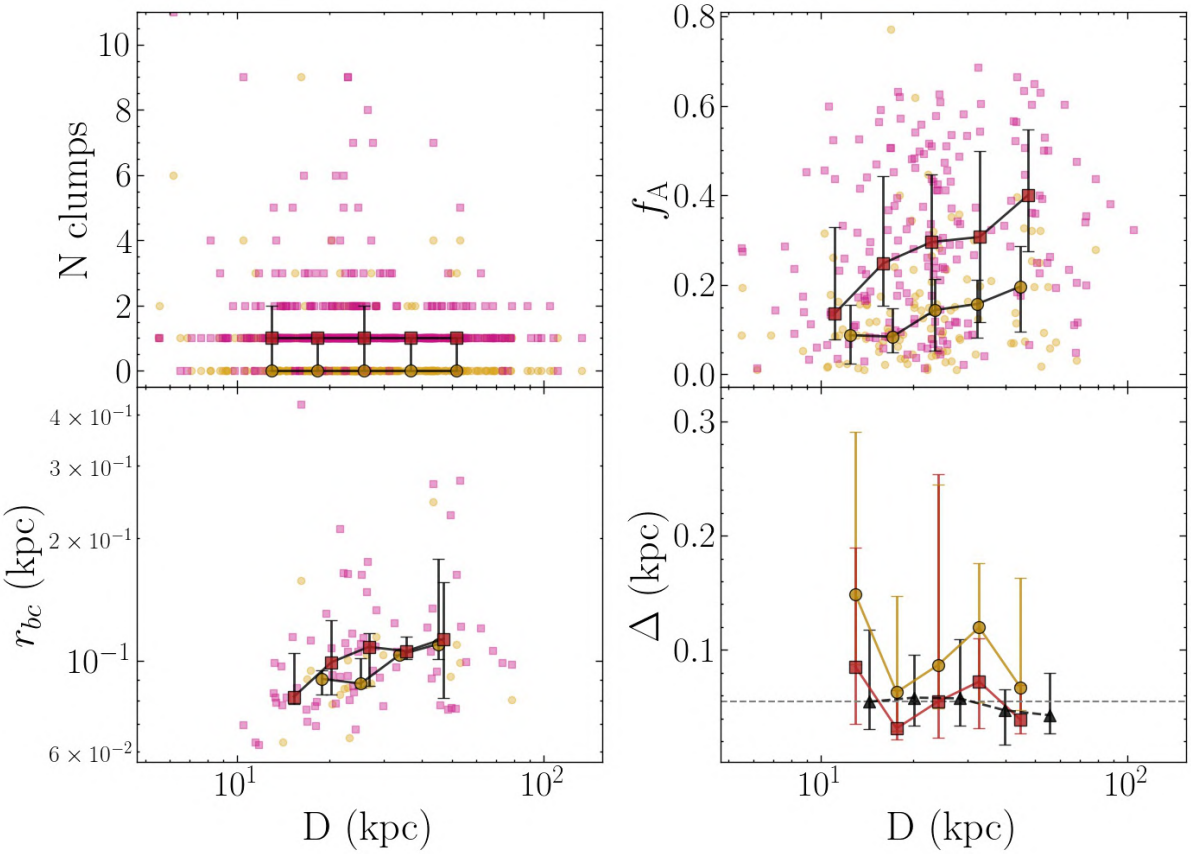

Figure 5.12: Trends with the projected galactocentric distance of the complex properties related to the matched clumps: golden dots when related to matched Hα-selected clumps, magenta squares to matched UV-selected clumps and black triangles, when present, to UV-selected clumps in complexes with no Hα-selected clumps. Median profiles are plotted as dark golden dots for Hα-selected clumps and magenta squares for UV-selected clumps. Error-bars show the quartiles of the distribution in the bin. The quantities on the y-axis are: number of matched clumps (top left); filling factor f_A (top right); radius of the brightest matched resolved clump r_{bc} (bottom left); geometric center displacements (bottom right, defined in Section 5.3.1, with our resolution limit of ~ 0.055 kpc plotted as horizontal dashed grey line). Plots taken from Giunchi et al. (2023b).

Chapter 6

Tail clumps mass function

The mass function, just like the luminosity function (Section 4.2.1), is an important tool to study the mechanism leading to the formation of clumps. As discussed in Section 1.4.1, models and observations of clumps in isolated main-sequence galaxies found evidence of a scale-free turbulent cascade driving the collapse of the ISM into molecular gas clouds and then young stellar clumps. In Section 4.2.1, I showed how the luminosity functions of the clumps observed in jellyfish galaxies, whether in the disks or in the tails, have slopes smaller than 2 (average value ~ 1.85), though consistent with literature and the turbulent scenario.

In this Chapter I push forward this analysis, studying the clumps mass function, which can be more directly compared with models and simulations. In order to properly retrieve the correct slope of the mass function, I am going to quantify the main effects that could bring to biased results, namely 1) the completeness of the sample as a function of the mass and 2) the systematic differences between the intrinsic mass of a clump and the observed mass, which highly depends on how the fluxes are computed and on the model adopted for the SED fitting. One way to model and quantify these effects is to create mock images of clumps with known input mass (and age), add them to the real images and perform again the same procedure adopted to detect the real clumps (Section 3.2) and obtain their masses (Section 3.4.3). Whether the mock clump is re-detected or not and (if it is) the comparison between input and output properties quantify the aforementioned sources of bias. Once these effects are properly modelled and taken into account, the fit to the mass function is performed in a Bayesian framework that is totally binning independent.

In this Chapter I present the results for the fits to the Hα- and UV-selected tail clumps for which we have robust estimate of the mass, which occurs when the clump has a signal-to-noise ratio larger than 2 in all the five available filters and the SED fit is in good agreement with the observed SED (details in Section 3.4.3). The catalog comprises 188 Hα- and 593 UV-selected clumps, respectively.

The Chapter is structured as follows: in Section 6.1 I obtain the intrinsic morphological shape of the clumps by stacking resolved, bright and isolated clumps; Section 6.2 is focused on the modelling of the Spectral Energy Distribution of the clumps as a function of their age and mass; in Section 6.3 I fit the clump size-mass relation, in order to be able to assign a physical size to the clumps for a given mass; Section 6.4 lists the steps followed to generate a

library of mock clumps images, which are re-observed and detected as described in Section 6.5. Once the mock clumps are re-observed, I use the information I got to model the mass completeness of the sample (Section 6.6) and the intrinsic-observed mass discrepancy (Section 6.7). Finally, the results of the fit of the Hα and UV tail mass functions are shown in Section 6.8.

6.1. *Characterization of the clumps morphology*

In order to generate a set of mock clumps, we need to characterize the typical morphology of Hα and UV clumps, respectively. Therefore I visually selected a set of 7(13) Hα-(UV-)resolved clumps, with SNR$>$ 2 in all five filters, isolated and with smooth and symmetric surface brightness profiles. For each selected clump I defined the largest possible square region including the clump as the only source. Then each clump undergoes the following steps:

1. the local background is fitted with a 2D polynomial function of 2nd degree and subtracted to the image. In order to exclude the clump, I masked out a region as large as the total area of the clump defined by ASTRODENDRO (Section 3.4.1) dilated by 3 pixels using the SCIPY function BINARY_DILATION[1].

2. The image is rotated to align the major axis of the clump to the $x-$axis and the minor axis to the $y-$axis (Section 3.4.1).

3. The physical scale of the image is normalized for the major axis along the $x-$axis and the minor axis along the $y-$axis. Since the size scales with the luminosity, as shown in Section 4.3, this normalization let us compare clumps of different sizes and axial ratios, also stretching the image to make the clumps as round as possible.

4. The image is converted from flux to surface brightness and resampled with smaller-size pixels.

5. The image is normalized for an effective surface brightness $\Sigma_{\rm eff} = F_{\rm bag}/{\rm A}_{\rm exact}$, where $F_{\rm bag}$ is the flux derived from the BAGPIPES best-fitting model of the clump[2] and ${\rm A}_{\rm exact}$ is the total area of the clump defined by ASTRODENDRO. Also this normalization is performed in order to make clumps of different luminosities comparable.

In this way, the rotated and normalized clumps are put in the same reference system, centered at the coordinates of the brightest pixel, and the stacked image is computed as the mean of all the images (where at least two images overlap). As an example, in Figure 6.1 the projections along the x- and y-axes of the UV stacked clump (left and right panel, respectively) are shown and compared with those of the clumps selected for the stacking.

[1] `https://docs.scipy.org/doc/scipy/reference/generated/scipy.ndimage.binary_dilation.html`

[2] We chose to use BAGPIPES fluxes, instead of the observed ones, as this choice let us better correlate the SED with the best-fitting mass and age of the clump, which are derived by BAGPIPES itself.

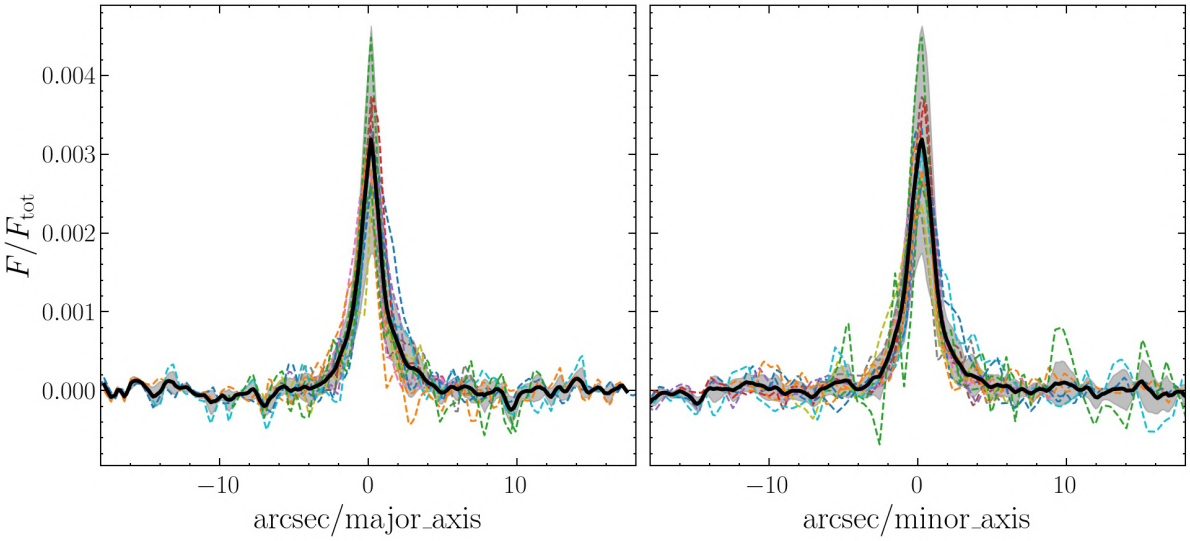

Figure 6.1: Projections along the x- (left panel) and y- (right panel) axis of the UV-resolved clumps selected for the stacking (dashed lines of varying colors) and the UV stacked clump (black solid line). The grey shaded area is the 1σ uncertainty of the stacked profile. The axes are normalized for scale quantities as described in Section 6.1.

The stacked image is then fitted with GALFIT[3], a tool fitting simultaneously one or more sources in an image adopting a large variety of models, adopting as a model the sum of two 2D Moffat functions, convolved for the WFC3 PSF of the proper filter (either F680N or F275W), available from TINYTIM (Krist, Hook & Stoehr, 2011). The surface brightness Σ of a 2D Moffat function is described by

$$\begin{cases} \Sigma(r) = \Sigma_0 \left[1 + \left(\dfrac{r}{r_d}\right)^2\right]^{-\gamma_{\rm M}} \\ \Sigma_0 = \dfrac{F_{\rm M}(\gamma_{\rm M} - 1)}{\pi r_d^2} \\ r_d = \dfrac{\rm FWHM_M}{2\sqrt{2^{1/\gamma_{\rm M}} - 1}} \end{cases} \tag{6.1}$$

where Σ_0 and r_d are the scale surface brightness and radius, respectively, defined by the total flux of the Moffat $F_{\rm M}$, the full-width at half-maximum $\rm FWHM_M$ and the concentration index $\gamma_{\rm M}$. Now, GALFIT is not able to fit normalized images in non-physical units, therefore I scaled the stacked image to the average flux and radius of the clumps selected to build the model. This choice will let me correctly evaluate the effects of the PSF on the shape of the clumps, which would be too strongly influenced by it (in case of clumps with the smallest flux and radius) or completely unaffected (in case of clumps with the largest flux and radius).

In Table 6.1 I list the best-fitting values of the morphological parameters of the Moffat functions, already re-normalized where needed. As an example, I also show the 2D maps

[3] `https://users.obs.carnegiescience.edu/peng/work/galfit/galfit.html`

	Hα		UV	
	Moffat 1	Moffat 2	Moffat 1	Moffat 2
(0)	(1)	(2)	(3)	(4)
$F_{\rm M}/F_{\rm tot}$	0.35 ± 0.16	0.65 ± 0.16	0.40 ± 0.06	0.60 ± 0.06
$\rm FWHM_{norm,M}$ (arcsec^{-1})	35 ± 28	131 ± 169	71 ± 32	175 ± 55
$\gamma_{\rm M}$	1.39 ± 0.31	10 ± 21	1.21 ± 0.22	4.7 ± 2.0

Table 6.1: Best-fitting parameters of the two 2D-Moffat functions used to model the stacked clumps. Column (0) contains the list of the parameters of each 2D-Moffat functions (equation 6.1): $F_{\rm M}/F_{\rm tot}$ is the total flux relatively to the sum of the two Moffat functions; $\rm FWHM_{norm,M}$ is the full-width at half-maximum normalized as described in Section 6.1; $\gamma_{\rm M}$ is the concentration index. Columns (1) – (2): best-fitting parameters for the Hα stacked clump; columns (3) – (4): best-fitting parameters for the UV stacked clump.

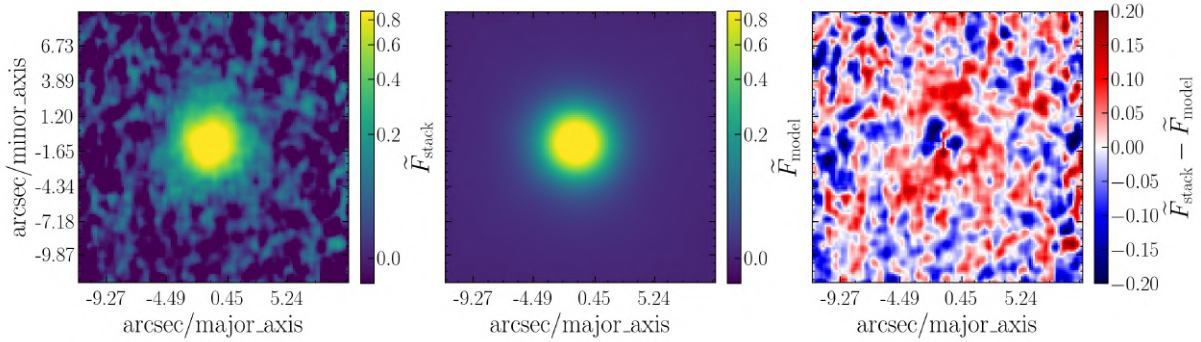

Figure 6.2: From left to right: UV stacked clump map, best-fitting model obtained with two 2D Moffat (parameters in Table 6.1), residuals. The axes and the fluxes are normalized to scale quantities as described in Section 6.1.

of the UV stacked clump compared with the best-fitting model, showing also the residual map, in Figure 6.2. In these maps the axes and $\widetilde{F}_{\rm stack}$ are re-normalized for the average core radius and total flux of the clumps used for the stacking, respectively, while the model flux $\widetilde{F}_{\rm model}$ is normalized for the total flux of the best-fitting model. Thanks to this procedure, I am able to create the mock image of a clump of any size, flux, axial ratio and position angle.

6.2. *Modelling the Spectral Energy Distribution*

The SED of a clump is comprised of many factors, primarily its age and mass. The former mainly drives the *shape* of the SED, i.e. the relative flux of the photometric bands with respect to each other. As discussed in Section 1.1, typical stellar populations younger than 10 Myr and 200 Myr are characterized by strong Hα-line emission and UV continuum, respectively. A clump with age in between 10 and 200 Myr, for example, will still be very bright in the F275W filter, but will have faint or no emission coming from Hα. If the clump is even older than 200 Myr, then, it will get progressively faint in the blue filters of our set.

Once the shape of the SED has been determined, it must be scaled to physical units by a factor which depends on the mass-to-light ratio, which is a function of the age of the

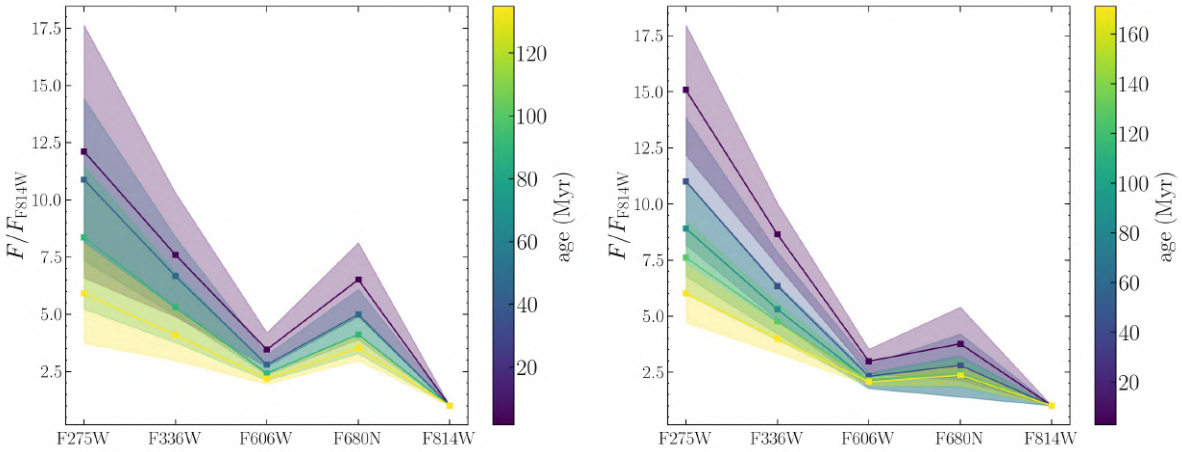

Figure 6.3: SED distribution of Hα (left panel) and UV (right panel) clumps normalized for the flux in the F814W filter. The clumps are divided in age bins (see the color bar on the right). Solid lines are the median SEDs in each age bins, while the shaded area covers the 1σ interval. Details about how these normalized SEDs are obtained are given in Section 6.2.1.

clump of which we want to create a mock image. The physical fluxes are then used to scale the normalized flux of the stacked clump defined in Section 6.1.

In the following Sections, I am going to show the procedures I followed to generate the SED of a mock clump, starting from its shape and then moving to its M/L. As already done to define the intrinsic shape of the clumps (Section 6.1), the procedure is followed independently for Hα and UV clumps.

6.2.1. *Shape of the Spectral Energy Distribution*

My aim is to generate a library of normalized SEDs of clumps at different ages, to be sampled reproducing the same age distribution as the one of the clumps I detected in our galaxies. Therefore I selected all the leaf tail clumps for which Bagpipes gives reliable estimates of stellar mass and mass-weighted age (Section 3.4.3), and binned them by age in logarithmic scale (5 bins for UV clumps and 4 bins for Hα clumps, in order to have a considerable number of clumps in each bin). Then the SED of each clump is normalized for the flux in the F814W filter, to make clumps of different masses comparable. For each age bin and photometric band, a flux distribution is built starting from the clumps normalized fluxes. This choice lets us assign to each age bin a median normalized flux with a scatter than can well reproduce the variations in the SEDs even among clumps of similar ages. In Figure 6.3 I show the results of the Hα and UV clumps normalized SEDs. As one can notice, the normalization for the F814W flux forces that filter to be anchored at 1, while the shapes of the SEDs follow pretty well the expected behaviour for the Hα-line emission and the near UV continuum, both getting fainter and fainter as the age bin includes clumps older than 10 and 200 Myr, respectively (Section 1.1).

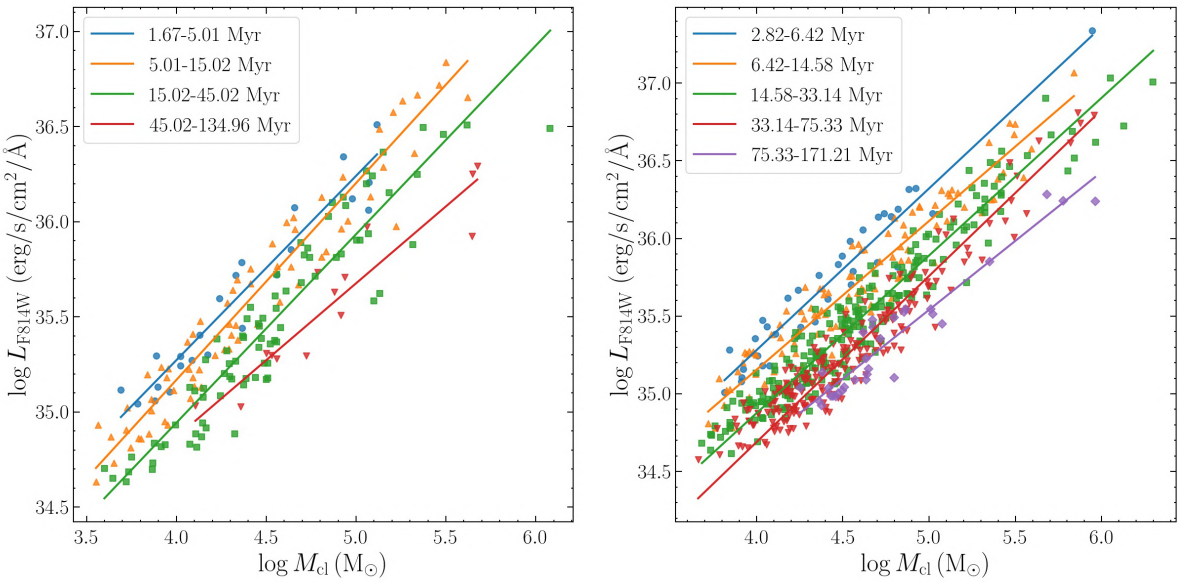

Figure 6.4: Clumps $\log L_{F814W} - \log M_{cl}$ plane (Hα clumps in the left panel, UV clumps in the right panel). Clumps are divided in age bins as described in Section 6.2.1 and plotted with different colors and shapes (see the legend). For each age bin, a linear fit to the clumps $\log L_{F814W} - \log M_{cl}$ is performed and plotted as solid line of the corresponding bin.

6.2.2. *Clumps mass-to-light ratios*

I define the mass-to-light ratio as the ratio between the clump stellar mass M_{cl} and the F814W luminosity L_{F814W}. M_{cl}/L_{F814W} is then computed for each age bin by performing a linear fit in the $\log M_{cl} - \log L_{F814W}$ plane. The linear fit is performed using the Bayesian fitting tool LINMIX (Kelly, 2007), including also the intrinsic scatter to the linear relation (Equation 4.2). Results are shown in Figure 6.4, where the Hα and UV clumps are also divided per age bins. As expected, the F814W at a given mass is larger for young clumps (i.e. small M_{cl}/L_{F814W}). That is, for a given clump mass and age, it is possible to assign to the clump the F814W luminosity, which is used to scale the normalized SED defined by its age (Section 6.2.1) to physical units.

6.3. *Radius-mass relation*

In order to assign a physical radius to the intrinsic profile obtained in Section 6.1, I fitted the core radius-mass relation with the Bayesian orthogonal linear fitting procedure firstly used in Posti et al. (2018) and described in Bacchini et al. (2019), which lets me introduce an intrinsic scatter in the clumps radius at a given mass. The likelihood $\log \mathcal{L}$ is

$$\log \mathcal{L}_{r-M} = -\frac{1}{2}\sum_{i=1}^{N_{cl}} \left[\frac{d_i^2}{\sigma_{tot}^2} + \ln(2\pi\sigma_{tot}^2) \right], \tag{6.2}$$

where N_{cl} is the number of resolved clumps that are fitted, d_i is the distance between a given data point $(\log \widetilde{M}_{cl}, \log \widetilde{r}_{core,corr})$ and the model $(\log \widetilde{M}_{cl}, m \log \widetilde{M}_{cl} + \widetilde{q})$. The total scatter

	m	q	σ_r
Hα	$(3.63 \pm 5.23) \times 10^{-2}$	-1.24 ± 0.02	$(3.30 \pm 1.82) \times 10^{-2}$
UV	$(1.75 \pm 0.27) \times 10^{-1}$	-1.93 ± 0.01	$(7.48 \pm 0.90) \times 10^{-2}$

Table 6.2: Best-fitting parameters of the Hα (top row) and UV (bottom row) clumps radius-mass relation, modelled as described in Section 6.3. The free parameters are the slope m, the intercept q and the radius intrinsic scatter σ_r.

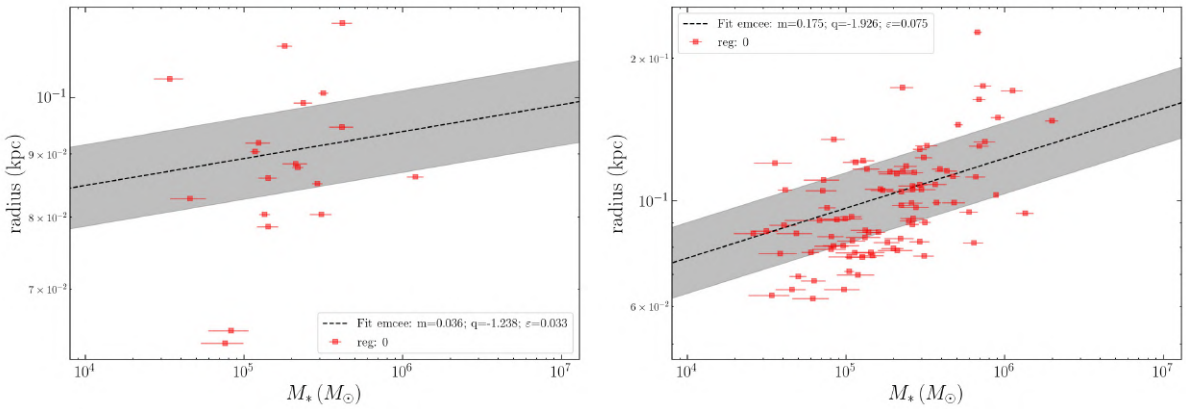

Figure 6.5: Core radius-mass relation for Hα (left) and UV (right) resolved clumps. Each clump is plotted as a red square with stellar mass uncertainties. The black dashed line is the best-fitting linear relation and the grey shaded region is the area covered considering the intrinsic scatter. Best-fitting parameters are obtained as described in Section 6.3.

is defined as $\sigma^2_{\rm tot} = \sigma^2_\perp + \sigma^2_{M_i,\perp} + \sigma^2_{r_i,\perp}$, where $\sigma_\perp$ is the orthogonal intrinsic scatter, while $\sigma_{M_i,\perp} = \sigma_{M_i} \sin\theta$ and $\sigma_{r_i,\perp} = \sigma_{r_i} \cos\theta$ are the projections of the $\log \widetilde{M}_{\rm cl}$ and $\log \widetilde{r}_{\rm core,corr}$ uncertainties σ_{M_i} and σ_{r_i}, respectively ($\theta = \arctan m$). Before the fitting, the data points are shifted by their median values to remove the covariance between m and q (which becomes $\widetilde{q}$ after the shift).

The space of the free parameters is explored by means of a Markov chain Monte Carlo (MCMC), using the python tool EMCEE (Foreman-Mackey et al., 2013). I considered the median of the parameters distributions as the best-fitting parameters and are listed in Table 6.2 in the form (m, q, σ_r), which are the parameters needed to infer the clumps size at a given mass. In Figure 6.5 the size-mass log-plane is shown; I note a strong correlation for UV clumps, while the correlation for Hα clumps is quite weak. However, the fitting procedure I followed allows me to model the large scatter observed for Hα clumps as the intrinsic scatter of the relation and therefore the variety of possible radii that a clump of a given mass can have.

6.4. *Mock clumps generation*

In the previous Sections, I have defined all the quantities necessary to generate mock images in all the *HST* filters for a clump with given mass, age and axial ratio. I have generated a set of 1000 Hα clumps and 1000 UV clumps for each galaxy, for which the input parameters listed above are defined as follows:

1. The clump stellar mass $M_{\rm cl}$ is extracted from a flat distribution ranging from the minimum to the maximum clump stellar mass derived from the real clumps. This choice gives me the same statistics at all masses when studying the mass completeness and discrepancy (Section 6).

2. Age and axial ratio are extracted from the corresponding distribution of real clumps. In this case it is my interest to simulate these quantities in the most realistic way; for example, an old clump may be more difficult to detect than a young clump with the same mass, therefore the relative fraction of clumps with a certain age affects how likely clumps with a certain mass are to be lost.

Once the intrinsic properties of the clumps are defined, I can derive the observables:

1. By means of the size-mass relation, at a given mass I can derive the value of $r_{\rm core,corr}$ (Section 6.3), which is converted to angular scale given the redshift of the galaxy. The intrinsic scatter of the linear relation is taken into account with a Gaussian extraction. The inferred core radius is used to assign a physical angular scale to the clump intrinsic profile (Section 6.1), which is then convoluted for the *HST* PSF.

2. The clump image is stretched for the extracted axial ratio and rotated by a position angle uniformly extracted between 0 and 2π.

3. The shape of the SED of the clump is inferred from the age as follows. As described in Section 6.2.1, for each age bin and photometric filter I derived a distribution of normalized fluxes; after uniformly extracting a random number between 0 and 1, I take the normalized flux in each filter at the percentile corresponding to the number extracted. By doing this, I am able to reproduce the variety of SED shapes present in each bin.

4. Given the mass and the age, I derive $M_{\rm cl}/L_{\rm F814W}$ (Section 6.2.2) and convert it to F814W flux, which let me scale the normalized SED previously determined to a physical quantity. Given the fluxes in the 5 photometric filters, I generate an image of the clump for each filter, by multiplying the clump intrinsic profile for the corresponding flux.

5. The clump images of each filter are convoluted for the corresponding PSF curve.

That is, I created a library of 1000 mock Hα clumps (and 1000 mock UV) for each galaxy, each of which constituted by 5 images. As examples, I show in Figure 6.6 three F275W mock images of UV mock clumps generated to belong to JO201. One can notice the growing size of the image, due to the varying size of the mock clumps, and the variety of elongations and position angles.

6.5. *Re-observation of the mock clumps*

The aim of these mock observations is to quantify the effects of background noise and contamination by background and foreground sources on the detection of clumps in the

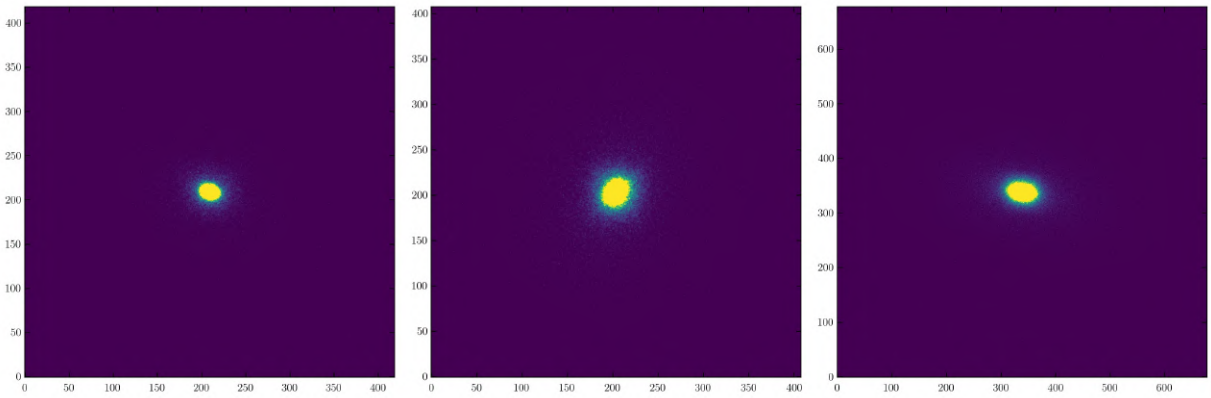

Figure 6.6: Examples of F275W mock images of three UV clumps generated for JO201 as described in Section 6.4.

tails of the jellyfish galaxies of our sample. The classical way to mimic the same conditions affecting the galaxy real images consists of adding the mock clumps images to the real images themselves, perform the same procedure adopted to detect the real clumps and check whether mock clumps are re-detected and what their output properties are.

In order to evenly cover the area of the image where the clump detection was run, the field of view of each galaxy (Table 2.3) is divided in a grid of $N_{\rm cell}$ squared cells (700 pixels in size for JO175, JO206 and JW100, 800 for JO201, JO204, JW39). Then a number of mock clumps equal to the number of cells is randomly extracted by the corresponding library (Section 6.4) and added to each cell. The center of the clump is randomly extracted within a square region of size 350/400 pixels (half of the cell size) centered in the corresponding cell This is done in order to fully explore the background conditions inside a certain cell, still avoiding the mock clump to be placed at the border of it and possibly overlap with other adjacent mock clumps. Furthermore, the center of the mock clump can not be inside the galactic optical disk. For the subsequent mock observation, the cell grid is shifted both along RA and Dec by 350/400 pixels, again to exhaustively explore the whole galactic FOV. As examples, in Figure 6.7 I show the first two mock observations for JO201, where one can notice where the mock clumps are added, how the FOV is divided in cells and how the grid is shifted in the second mock observation. In order to have a statistically robust estimate of the completeness and input-output discrepancy in the whole mass interval, I need to run at least 1000 clumps per galaxy, which result in $N_{\rm mock} = 1000/N_{\rm cell}$ mock observations (rounded up).

Once the mock image is ready, I re-ran the clumps detection (Section 3.2.1). From now on, I will call this catalog the *new* catalog, while the one of Section 3.5, with only real clumps, is the *original* catalog. The new catalog is matched with the original one to find re-detected real clumps and remove them from the new catalog, in order to keep in the new catalog only re-detected mock clump candidates. A new clump is flagged as a *re-detected* original clump, and removed by the new catalog, if the center of an original clump is within a circle centered in the center of a new clump and with radius equal to the new clump core radius (defined as in Section 3.4.1), and their fluxes are comparable within a factor 2. The remaining new clumps are matched with the mock clumps that were added to the

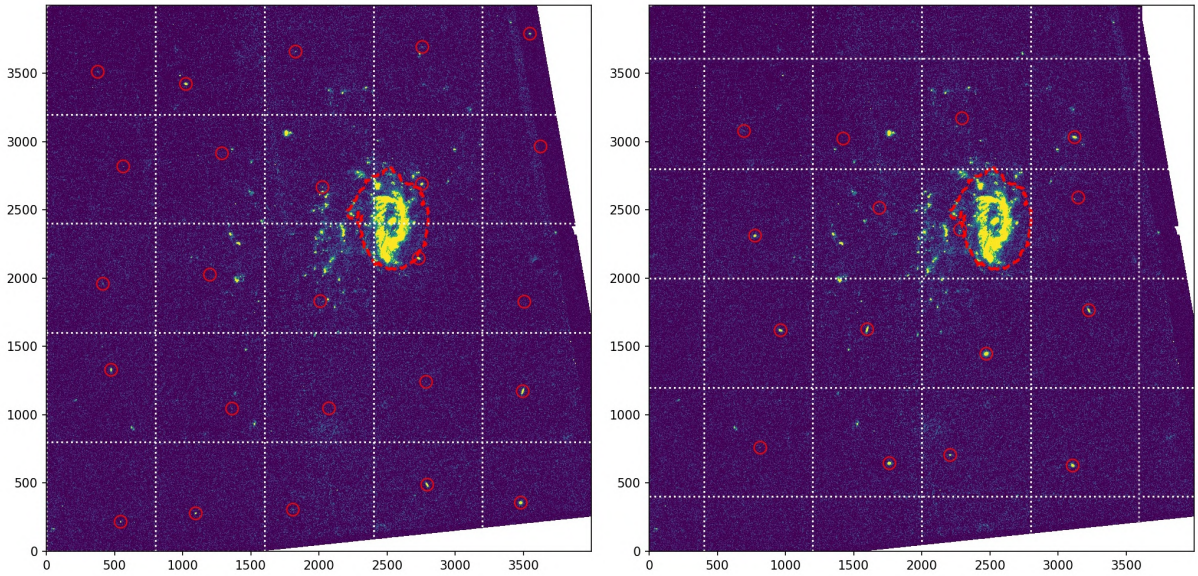

Figure 6.7: First two F275W mock images generated for JO201 following the prescription in Section 6.5. The white dashed lines define the grid in which the FOV is divided, while the red dashed contour is the optical disk (Section 3.1.3). The mock clumps that are added to the real images are inside the red circles.

image, and if the center of a mock clump is within the area of a new clump, the new clump is flagged as a re-detected mock clump. All the other new clumps are removed from the catalog. Input mock clumps not matched to any new clump are flagged as not-detected. Finally, the mass and mass-weighted age of the re-detected mock clumps are derived with BAGPIPES in the same way described in Section 3.4.3.

After having followed these steps, out of 6125 Hα and 6125 UV clumps, we re-detected and computed stellar masses for 3416 and 2982 clumps, respectively.

To summarize, at the end of this process I can study the fraction of lost mock clumps as a function of their input mass while, for those that are re-detected, I can compare the input mass with the one resulting from BAGPIPES.

6.6. *Completeness*

I define the completeness as the fraction of re-detected clumps per input mass. I modelled it as a logistic function, a sigmoid function having a characteristic S-shaped curve, monotonically increasing from an asymptotic value (for $x \to -\infty$) to another (for $x \to +\infty$). The equation describing the logistic function is

$$C(\log m_{\rm in}) = \frac{k}{[1 + e^{-p(\log m_{\rm in} - \log m_{\rm in,0})}]}, \tag{6.3}$$

where $m_{\rm in}$ is the input mass, k is the value of the asymptotic value for $m_{\rm in} \to +\infty$, p regulates the sharpness of the increase of the function and $m_{\rm in,0}$ is the input mass value at which $C(\log m_{\rm in,0}) = k/(1 + e)$.

	k	p	$\log m_{\rm in,0}$	a	b	c	d	e
	10^{-1}				10^{-1}	10^{-3}	10^{-1}	10^{-3}
(0)	(1)	(2)	(3)	(4)	(5)	(6)	(7)	(8)
Hα	9.91 ± 0.02	4.85 ± 0.16	4.77 ± 0.01	2.63 ± 0.15	3.8 ± 0.6	33 ± 5	2.6 ± 0.2	-9.3 ± 3.3
UV	9.87 ± 0.04	3.88 ± 0.13	5.02 ± 0.01	1.77 ± 0.20	7.6 ± 0.7	-5.2 ± 6.0	5.3 ± 0.2	-61 ± 3

Table 6.3: Best-fitting parameters of the completeness and input-output discrepancy functions for Hα (first row) and UV (second row) mock clumps. The two functions are modelled as described in Sections 6.6 and 6.7. Column (0) refers to the mock clumps that are fitted (either Hα or UV). Columns (1) to (3): free parameters of the completeness $(k, p, \log m_{\rm in,0})$ as described in Equation 6.3, i.e. the maximum value, the stepness of the rise and the input mass at which the rise starts. Columns (4) to (8): free parameters of the input-output function as in Equation 6.6, where (a, b, c) describe the input-output correlation and (d, e) the intrinsic scatter of the correlation.

The space of the free parameters $(k, p, \log m_{\rm in,0})$ is explored by means of a Markov chain Monte Carlo, using the python tool EMCEE (Foreman-Mackey et al., 2013) to maximize the likelihood

$$\log \mathcal{L}_C = \sum_{i=1}^{N_{\rm det}} C(\log m_{{\rm in},i}) + \sum_{j=1}^{N_{\rm not-det}} [1 - C(\log m_{{\rm in},j})], \tag{6.4}$$

where $N_{\rm det}$ and $N_{\rm not-det}$ are the numbers of re-detected and not detected mock clumps added to the mock observations, respectively, while $m_{{\rm in},i}$ and $m_{{\rm in},j}$ are the input stellar masses of the $i-$th re-detected and j-th not detected mock clumps, respectively. I define the best-fitting parameters as the median of the parameters distributions obtained by exploring the parameter space to maximize $\log \mathcal{L}_C$ and listed in the first three rows of Table 6.3.

Now, correcting for the not-detected clumps when the completeness is below 0.5, i.e. where more half of the clumps are lost, may not bring to robust estimates. Therefore I forced the completeness to 0 for input masses below the value $m_{\rm in,1/2}$ at which $C(\log m_{\rm in,1/2}) = 0.5$. Therefore the operative completeness $\widetilde{C}(\log m_{\rm in})$ I am going to use is

$$\begin{cases} C(\log m_{\rm in}) & \text{for} \quad \log m_{\rm in} \geq \log m_{\rm in,1/2} \\ 0 & \text{for} \quad \log m_{\rm in} < \log m_{\rm in,1/2} \end{cases} \tag{6.5}$$

In Figure 6.8 I show the Hα and UV best-fitting completeness functions (where the dashed line is the profile of $C(\log m_{\rm in})$ before forcing it to 0). For a visual comparison, I overplotted the observed input mass completeness; this is computed by binning the mock clumps in input mass, assigning to the $k-$th bin a value $C_k = N_{{\rm det},k}/N_k$, where N_k and $N_{{\rm det},k}$ are the total number and the number of re-detected clumps in the $k-$th bin, respectively. Note that the fitting procedure I followed (Equation 6.4) is binning independent, therefore the observed binned completeness is shown only as a reference. Both for Hα and UV clumps, the best-fitting function well reproduce the results from the mock observations, which show how low-mass clumps are more likely to be lost, as expected.

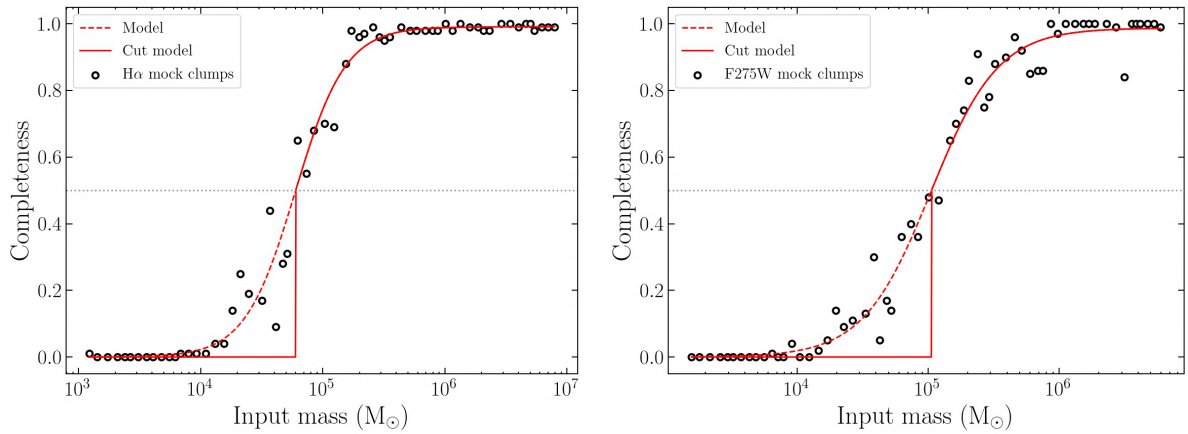

Figure 6.8: Input mass completeness of Hα (left panel) and UV (right panel) mock clumps. The red solid line is the best-fitting model computed as in Equation 6.5, while the red dashed line show the prosecution of the model if the function were not forced to 0 for values below 0.5 (Section 6.6). The threshold values of 0.5, below which the function is forced to 0, is plotted as a grey dotted line. The black empty circles are the binned mass completeness derived from the mock clumps.

6.7. *Intrinsic and observed mass discrepancy*

Our capability of recovering the intrinsic mass of a star-forming clump is always affected by the noise of the image, which especially affects the faint regions of the clump. The comparison between the intrinsic mass of the mock clumps and the observed value can quantify this effect. Furthermore, this study is important in order to evaluate whether the definition of clump observed mass, which depends both on the definitions of the clump fluxes (Section 3.4.1) and the models used to infer the mass (Section 3.4.3), is affected by systematic effects.

In Figure 6.9 I show as dots the comparison between observed and intrinsic mass of the re-detected mock clumps, both for Hα and UV clumps. Note that for high masses there is a good agreement between them, while at low masses the observed mass is systematically smaller than the intrinsic one. I modelled the distribution of $(\log m_{\rm obs}, \log m_{\rm in})$ datapoints as a quadratic relation F with linearly decreasing scatter σ depending on the observed mass $\log m_{\rm obs}$:

$$\begin{cases} F(\log m_{\rm obs}) = a + b \cdot \log m_{\rm obs} + c \cdot (\log m_{\rm obs})^2 + g[0, \sigma(\log m_{\rm obs})] \\ \sigma(\log m_{\rm obs}) = d + e \cdot \log m_{\rm obs} \end{cases} \tag{6.6}$$

The best-fitting values of the free parameters (a, b, c, d, e) are the median values of the distributions, obtained maximizing a likelihood written as in Equation 6.2. In this case $N_{\rm cl}$ is the number of re-detected mock clumps, $d_i^2 = \log m_{{\rm in},i}^2 - [a + b \cdot \log m_{{\rm obs},i} + c \cdot (\log m_{\rm obs})^2]^2$ is the distance between the $i-$th input mass and the one inferred from the model, and $\sigma_{\rm tot} = \sigma(\log m_{{\rm obs},i})$ is the intrinsic scatter at the $i-$th observed mass. Again, the parameter space is explored by means of EMCEE. The best-fitting parameters are listed in the last five columns of Table 6.3 and the model distributions are shown in Figure 6.9, where one can see that they well describe the mock clumps distributions.

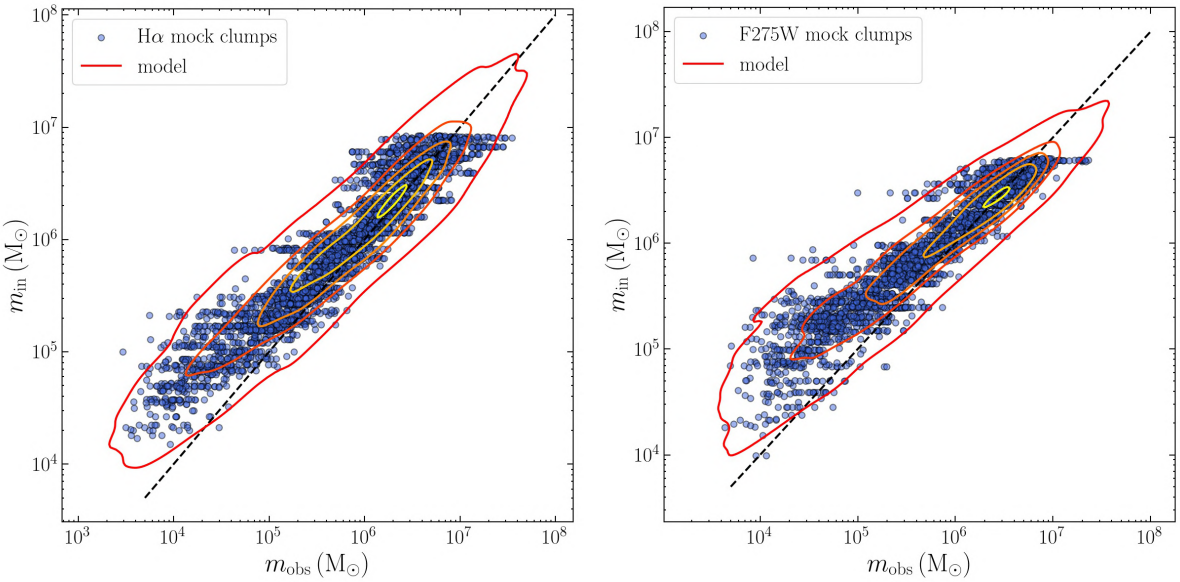

Figure 6.9: Discrepancy between observed (x-axis) and intrinsic (y-axis) mass for Hα (left panel) and UV (right panel) re-detected mock clumps. Each clump is plotted as a blue dot. The black dashed line is the 1 : 1 relation. The red contours are computed from the best-fitting model describing the clumps distribution (Equation 6.6).

Thanks to this model, at a given clump observed mass $\log m_{{\rm obs},j}$ I define a Gaussian distribution $G_j(\log m_{\rm in})$ with mean and standard deviation given by Equation 6.6, which describes the distribution of possible intrinsic masses that can result in the observed mass $\log m_{{\rm obs},j}$.

6.8. *Modelling the mass function*

The fitting to the mass function (MF) must take into account the effects that I have quantified in the previous sections; the number of clumps with a certain mass is affected by completeness, so a certain fraction of them may be lost, and a clump with a given observed mass may have a different input mass, which is the real value on which the MF depends. The likelihood I used to explore the parameter space is

$$\log \mathcal{L}_{\rm MF}(\boldsymbol{\theta}) = N_{\rm cl}\,\pi(\boldsymbol{\theta}) + \\ + \sum_{i=1}^{N_{\rm cl}} \log\left\{ \int_{\log m_{{\rm in},1/2}}^{+\infty} {\rm MF}(\log m_{\rm in}, \boldsymbol{\theta})\, G_i(\log m_{\rm in})\, \widetilde{C}(\log m_{\rm in})\, d\log m_{\rm in} \right\}, \tag{6.7}$$

where $N_{\rm cl}$ is the number of real UV or Hα clumps with reliable mass estimates (Section 3.4.3), ${\rm MF}(\log m_{\rm in}, \boldsymbol{\theta})$ is the MF with free parameters $\boldsymbol{\theta}$, $\pi(\boldsymbol{\theta})$ is the prior of the parameters (which depends on the parameters of the MF), $G_i(\log m_{\rm in})$ is the input mass distribution of the $i-$th observed mass $\log m_{{\rm obs},i}$ (Section 6.7) and $\widetilde{C}(\log m_{\rm in})$ is the completeness (Section 6.6). Note that the integral over input masses is done only for values larger than $\log m_{{\rm in},1/2}$,

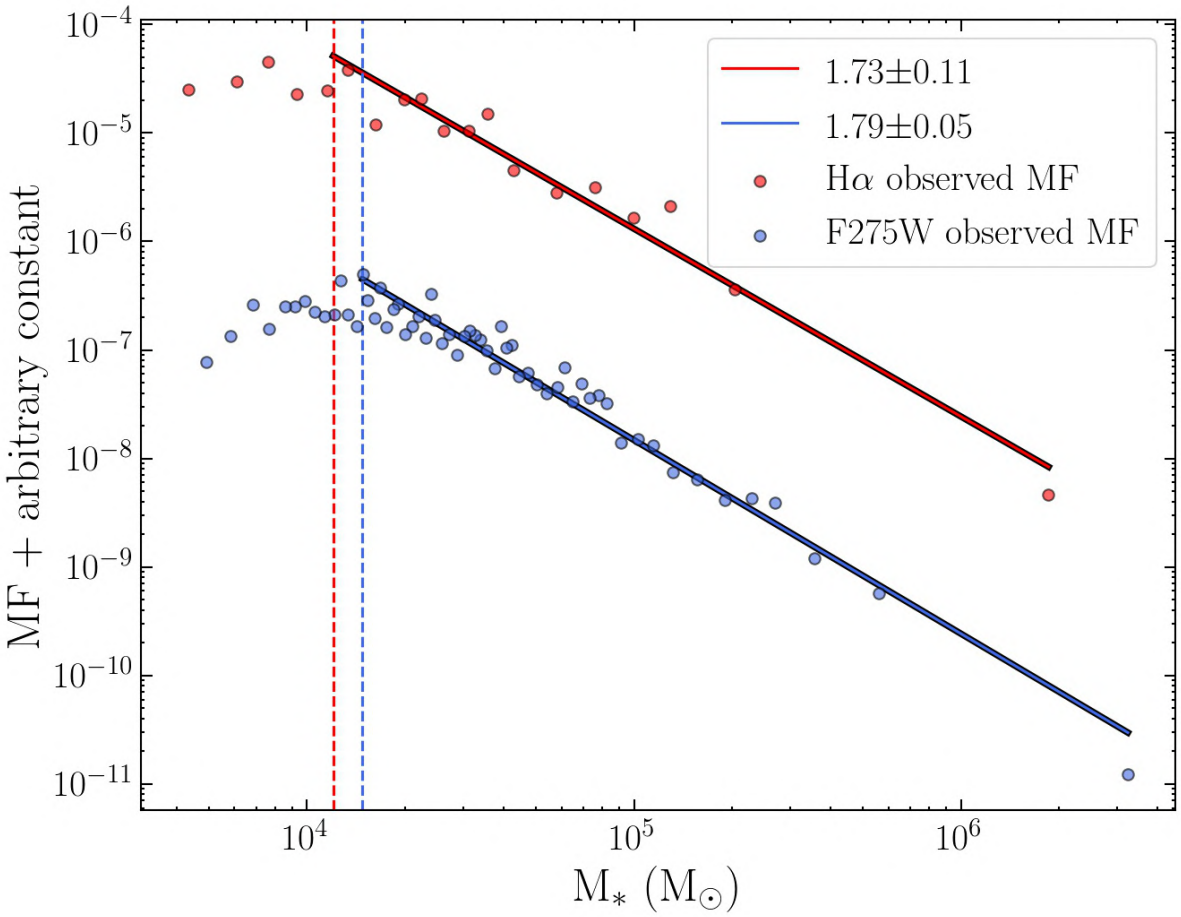

Figure 6.10: Plots of the observed mass function of the Hα (red dots) and UV (blue dots) tail clumps. The clumps are binned in the same way done in Section 4.8, with ten clumps per bin. The solid lines are the best-fitting single power laws (slopes in legend), while the vertical dashed lines are the mass thresholds above which the fit is performed.

avoiding a mass regime in which the fit is highly affected by incompleteness. The likelihood is maximized and the parameter space explored by means of EMCEE. The MF model I fitted is a single power law, with only the slope α as a free parameter (Equation 1.4). The best-fitting slopes are defined as the median values of the parameter distributions and are 2.07 ± 0.10 and 2.28 ± 0.08 for Hα and UV tail clumps, respectively.

In order to test how the mass completeness and discrepancy affect the results, I fitted the observed MF in the same way done in Section 4.8 for the luminosity distribution function, fitting the binned observed MF with a power law for masses above the peak of the binned distribution. Figure 6.10 shows the results for both Hα and UV tail clumps: even if the distribution is well described by a single power law, having neglected the two effects above mentioned the best-fitting slopes are smaller: 1.73 ± 0.11 for Hα tail clumps and 1.79 ± 0.05 for UV tail clumps. This test demonstrates that the completeness and the discrepancy between intrinsic and observed mass can not be neglected when fitting the MF.

The slopes obtained sampling the likelihood in Equation 6.7 are in good agreement with models and previous observations (Section 1.4.1); the Hα slope is consistent with 2

and therefore with many previous works (Zhang & Fall, 1999; Hunter et al., 2003; de Grijs et al., 2003; Gieles et al., 2006; Adamo et al., 2017; Messa et al., 2017; Messa et al., 2018; Rodruck et al., 2023; Livermore et al., 2012). As suggested by models (Elmegreen, 2002, 2006) and simulations (Hennebelle & Audit, 2007; Audit & Hennebelle, 2010; Fensch et al., 2023), this result confirms that also star-forming clumps in the tails, formed from stripped gas and embedded in the hot and high-pressure ICM, form as a consequence of a turbulent scale-free collapse of the ISM into molecular clouds and then stellar clumps. The UV slope is steeper and therefore compatible with models predicting this evolution of the slope as a function of the ageing and dynamical evolution of the clumps (Fujii & Portegies Zwart, 2015).

Chapter 7

Conclusions

In this thesis I presented UVIS *HST* observations of 6 galaxies (JO175, JO201, JO204, JO206, JW39, JW100) undergoing strong ram-pressure stripping (RPS), exerted by the ICM, at redshift $z \sim 0.05$ from the GASP survey (Poggianti et al., 2017b). These so-called jellyfish galaxies were selected for hosting a large number of MUSE Hα star-forming knots in the tails of stripped gas (see Poggianti et al., 2019). The targets were observed in four photometric broad-bands covering a spectral range from UV to the I-band restframe (F275W, F336W, F606W and F814W) and a narrow band one (F680N) covering Hα emission at their redshift.

The main goal of this observing programme is to study the physics of young stellar clumps formation and morphological evolution in the context of galaxies undergoing RPS and embedded in the hot and high-pressure ICM. Furthermore, these datas complement the large dataset collected within the GASP project, which is based on MUSE observations and that was then followed-up with multiwavelength observations with JVLA, APEX and ALMA, MeerKAT, LOFAR, UVIT, and archival Chandra X-ray data to probe molecular and neutral gas, as well as UV and X-ray emission. The main limitation of these data is the spatial resolution, which is of the order of 1 arcsec or larger for all observations, corresponding to ~ 1 kpc. The *HST* observations presented here allow studies of GASP galaxies with unprecedented spatial resolution (0.07 arcsec $\simeq$ 70 pc); this is a critical aspect, in particular to characterize star-forming regions which are in general small sources with sub-kpc scales. Moreover, these observations provide deep UV data that would strongly constrain the properties of young stellar populations, as well as Hα data probing the ionized gas.

The first step consisted of the reduction the raw HST data, removing bad pixels and cosmic rays to obtain the scientific images, and the extraction of the Hα-line maps. I put careful attention in the removal of cosmic rays, which otherwise can be easily mistaken for compact bright sources, and in the correct estimate of the Hα line, considering the effects of other lines, including [N II], [O III] and Hβ.

The visual inspection of the images pointed out how ram pressure shapes the morphology of the clumps and of the outskirts of the galactic disks. The clumps in the tails are typically simple structures, and especially in Hα they appear very compact, while in the F275W filter they also show a variety of diffused emission departing from the bright peak of the

emission and elongated in the direction of the motion of the galaxy in the ICM. Implicitly, such difference also confirms that stellar structures in the tails of jellyfish galaxies are not simple stellar populations. Moreover, the clumps tend to be aligned along a few (2 to 6) long filamentary sub-tails, which can either be quite linear, like straight tentacles (like in JO204, JO206 and JW100), or more similar to extensions of the spiral arms of the disk (in JO175, JO201 and JW39). On the other hand, clumps in the galactic disk are clustered in large and bright regions following the spiral arm distribution, with complex structures and clumps nested inside each other. The regions of the disk firstly experiencing the effects of ram pressure show bright UV and Hα compact sources, displaced from the dust absorption lanes, which are most likely pushed away by ram pressure.

The comparison with MUSE ancillary data did not unveil a considerable number of compact Hα or UV sources outside the MUSE Hα knots observed at $\sim$ 1 kpc-resolution. This is true also in the regions of the tails in which MUSE revealed the presence of diffused Hα emission powered by massive stars, confirming that ionizing source of this diffuse gas component is not in-situ star formation above the UVIS detection limit ($L_{\mathrm{H}\alpha} = 10^{38}$ erg/s at 2σ). Furthermore, nearly all MUSE knots correspond to single compact and bright *HST* sources, with also many cases in which no Hα bright sources are observed inside MUSE knots.

For the next step I created a robust catalog of Hα and UV star-forming clumps, and optical star-forming complexes, to be publicly released, giving to this work also legacy value. In order to study the effects of the environment on the properties of the clumps, I divided them in disk clumps, still inside the optical galactic disk and showing no signs of ram pressure; extraplanar clumps, if they are still inside the optical galactic disk but formed from gas already experiencing stripping, as demonstrated by their elongated and disturbed morphology; and tail clumps, outside the galactic disk and clearly formed from stripped gas. The final samples comprise 2406 Hα-selected clumps (1708 disk clumps, 375 extraplanar clumps and 323 tail clumps), 3745 UV-selected clumps (2021 disk clumps, 825 extraplanar clumps and 899 tail clumps) and 424 star-forming complexes (located only in the tails by construction). The covered luminosity range goes from $\sim 3 \times 10^{38}$ to $\sim 4 \times 10^{40}$ erg/s in Hα, and from $\sim 3 \times 10^{36}$ to $\sim 2 \times 10^{39}$ erg/s/Å in UV. On average, $\sim$ 15% of them are resolved, meaning that most of the clumps have sizes smaller than $\sim$ 140 pc.

I studied the luminosity and size distribution functions of the star-forming clumps, where a power-law fit confirms that their formation channel is the same observed in isolated galaxies. Indeed the average slope of the luminosity distribution functions (LDFs) is 1.79 ± 0.09, close to the theoretical prediction of 2 for models in which the ISM collapses following a scale-free cascade driven by turbulence, where dense and cold molecular gas clouds are the final stage of this collapse, where stellar clumps form. Literature results confirm that this is the driving mechanism of clumps formation in both main-sequence and starburst galaxies, and my results testify that even clumps born from gas embedded in ICM and undergoing RPS form in the same way.

Also the size distribution functions (SDFs) are consistent with previous results, which showed that regions where clumps show a high level of complexity have a flatter SDF than

regions where clumps are simple and isolated. Here I obtain the same trend, with small slopes (~ 3) for both Hα and UV disk clumps and large ones (~ 4.5) in the tails.

The luminosity-size relation shows that clumps in jellyfish galaxies have enhanced $L_{\mathrm{H}\alpha}$ and star-formation rate surface density Σ_{SFR}. These conclusions are hinted by the best-fitting slope to the correlation observed for resolved clumps and by the comparison with Hα clumps in literature. The former has an average value of 2.3 ± 0.4, smaller than the one derived for clumps in main-sequence galaxies (~ 3) and consistent with the one obtained for clumps in starburst galaxies, which are known to be enhanced both in $L_{\mathrm{H}\alpha}$ and Σ_{SFR}. The latter shows how our clumps have brighter Hα-line emission at a fixed size than those in main-sequence galaxies, although smaller than those in starburst galaxies. Furthermore, I found no striking difference among disk, extraplanar and tail clumps, testifying that, even if tail clumps are embedded in the ICM, they formed in the same way as clumps formed in the galactic disk and surrounded by the ISM. These results suggest that although RPS does not change the formation mechanism of the clumps, it is able to trigger the formation of stars in structures that are more compact than those observed in isolated galaxies.

I obtained the first systematic evidence of fireballs in the tails of jellyfish galaxies. As previously obtained by multiwavelength studies of a few dozens of tail clumps, RPS should induce a morphological configuration in which the furthest regions of a clump are populated by younger stars than those close to the galactic disk, as a consequence of the fact that ram pressure acts only on the gaseous component, ignoring the stellar one. However, previous studies found evidence of this fireball configuration only by low-resolution observations of the neutral and molecular gas in the tails, or by analyzing one-by-one the morphology of UV and Hα clumps. In this work, the strong available statistics let me define in a rigorous way the displacement of UV and Hα clumps inside the optical complexes in which they are nested. By doing this I demonstrated that, even if complexes and clumps are characterized by a variety of shapes, there is a systematic trend according to which Hα and UV clumps are located on one side of the complex hosting them, especially if it is large, bright and elongated. Furthermore, UV clumps, tracing also stars older than those traced by Hα clumps, are more numerous, cover a larger area of the optical complex and are systematically less displaced than Hα clumps. These results hint that the fireball configuration is not a minor effect of RPS; on the contrary, it is a common feature affecting the spatial distribution and relative velocity of the different stellar generations in complexes, which can not be neglected when characterizing them.

Finally, I derived the mass function of tail clumps, further confirming that their formation channel is the same observed in main-sequence galaxies. Also in this case the mass function was fitted with a power law. However, before doing it, I corrected it taking into account two main effects able to bias the resulting slope: the mass completeness and discrepancy between the intrinsic mass of a clump and its estimate from observations. By means of a Bayesian fit, I obtained best-fitting slopes of 2.07 ± 0.10 and 2.28 ± 0.08 for Hα and UV tail clumps, respectively. This is a strong evidence that stellar clumps firstly form as the final stage of the turbulent collapse of the gas even when the gas is embedded in

the ICM, and then evolve either loosing the most massive clumps, which causes the slope increase.

To conclude, by means of a statistically robust sample of star-forming clumps and complexes, I have demonstrated that RPS is able to enhance the star formation even at the level of the single clumps, yet not changing the clumps formation mechanism, and to induce a peculiar fireball configuration in the clumps in the tails, which must be taken into account when characterizing them, especially if one aims at understanding the fate of these structures.

7.1. *Outlook and future work*

In Chapter 6, I performed a Bayesian fit to the tail clumps mass function which accounted for the completeness and the discrepancy between intrinsic and observed mass. I aim at applying the same procedure to disk and extraplanar clumps: the study of Hα and UV clumps in the different spatial categories will improve the study done for luminosity functions and possibly further confirm that clumps in jellyfish galaxy form following a turbulent scale-free cascade just like clumps in isolated main-sequence galaxies.

The next step will be the study of the fate of the $10^{5-6}\,M_\odot$ star-forming complexes observed in the tails of these galaxies. The main aspects that must be taken into account for this work are the self-gravity of the complex, the tidal field of the parent galaxy and the non-zero relative velocity among stars of different age, as predicted by the fireball model. I aim at utilizing a semi-analytical model that takes into account these effects to efficiently explore a large interval of parameters and define the conditions under which a complex remains self-gravitating or not and bound to the parent galaxy or not. If the complex fades away on short timescales, it can contribute to the stellar halo of its galaxy or to the intracluster light. On the other hand, if the complex survives as a compact object for a relevant amount of time, it may become a satellite of its parent galaxy and be possibly accreted by it, or it may escape the gravity of its parent galaxy and become an independent dark matter-free ultra-diffuse dwarf galaxy orbiting inside the galaxy cluster.

This last scenario is finding confirmation in observations of UDGs lacking of dark matter (Lelli et al., 2015; Ploeckinger et al., 2018) and in the recent observation of a relatively young ($\sim$ 1 Gyr) dwarf galaxy observed in the tail of a jellyfish galaxy (Iodice et al., 2021). Pushed by these results, I participate as a co-I to a recently submitted proposal for the VLT Survey Telescope (VST) with the aim of getting deep images of 7 clusters at intermediate-low redshift ($\sim$ 0.05), exploiting the large FOV of VST ($1^\circ \times 1^\circ$) to cover at least one virial radius for each cluster and get an exhaustive census of their dwarf galaxy populations.

Finally, the results obtained by the PHANGS collaboration are showing how combined multi-wavelength observations of resolved clumps in Hα, UV, polycyclic aromatic hydrocarbon (PAH) and CO can put strong constraints on the timescales for the formation of stellar clumps, their decoupling from the molecular gas cloud from which they formed and the disruption of the cloud as a consequence of stellar feedback (Kruijssen & Longmore, 2014; Kruijssen et al., 2018; Kruijssen et al., 2019; Chevance et al., 2021; Kim et al., 2022). Moved from the interest in understanding whether these timescales change for clumps born from

gas experiencing strong ram-pressure, I submitted as PI a proposal to get JWST-NIRCam $\sim 100\,pc-$resolved photometric data of the disks and the tails of JO201 and JW100. Observing the PAH emission lines we will put also strong constraints on the star formation efficiency (SFE) of these clumps, to be compared with clumps in different environments. Furthermore, $\sim 1\,kpc$-resolution ALMA data of JO201 and JW100 showed that the former is characterized by very compact CO knots usually co-spatial with the MUSE Hα knots, while in JW100 the emission is much more diffused and the SFE low. Comparing the high-resolution results of these two galaxies with each other can shed light on the reasons why they are showing such different molecular gas properties and whether these properties hold also in smaller compact regions.

Acknowledgments

I would like to warmly thank my supervisors Bianca, Marco and Alessia for everything they taught to me in these years and for being incredible guide. Thanks to you now I know what kind of astronomer I aim at being. I would like to thank Ariel Werle, Claudia Scarlata, Anita Zanella and Daniela Calzetti for their fundamental support throughout these years, and the whole GASP team for the useful discussions and comments. A final thank to Emily Wisnioski and Deanne Fisher for providing me the data from their papers, and my internal and external evaluators for having accepted my request and for their useful comments. This thesis is based on observations made with the NASA/ESA Hubble Space Telescope obtained from the Space Telescope Science Institute, which is operated by the Association of Universities for Research in Astronomy, Inc., under NASA contract NAS 5-26555. These observations are under the programme GO-16223. All the *HST* data used in this work can be found in MAST: `http://dx.doi.org/10.17909/tms2-9250`. This thesis used also observations collected at the European Organization for Astronomical Research in the Southern Hemisphere associated with the ESO programme 196.B-0578. This project has received funding from the European Research Council (ERC) under the European Union's Horizon 2020 research and innovation programme (grant agreement No. 833824) and "INAF main-streams" funding programme (PI B. Vulcani). This research made use of Astropy, a community developed core Python package for Astronomy by the Astropy Collaboration (2018).

Appendix A

Appendix: sub-tails definition

Since I am interested in studying the distribution of the properties of the clumps along the tails, for each galaxy the UV-selected clumps aligned to each other forming a chain and with a similar gas kinematics are grouped in sub-tails (Figure A.1). MUSE maps of the gas kinematics are presented and discussed in Poggianti et al. (2017a), Poggianti et al. (2017b), Bellhouse et al. (2017) and Gullieuszik et al. (2017). To properly estimate the projected distance of a clump from the galaxy along each sub-tail, I defined the sub-tails according to the following two definitions, according to the stripping morphology:

1. linear: as done in Franchetto et al. (2021), the positions of the clumps in the plane of the sky are fitted with a line. The distances of the clumps are computed projecting the clump positions onto the best-fitting line and fixing the zero-point to the projection of the first clump of the sub-tail. This definition is adopted for JO204, JO206 and JW100 (i. e. the nearly edge-on galaxies);

2. logarithmic spiral arm-like: in this case, I followed the same procedure described in Bellhouse et al. (2021). Each galaxy F275W image is deprojected according to the axial ratios measured in Franchetto et al. (2020), by scaling the distances along the dimension of the kinematic minor axis. The position in the plane of the sky of each pixel is then converted in spherical polar coordinates according to its radial distance from the centre of the galaxy and azimuthal position. In this space (in particular in the $\log r - \theta$ plane), structures with a logarithmic spiral shape appear as straight lines, and therefore I manually fit a line to the tails of the galaxies[1]. As explained in Bellhouse et al. (2021), I opted for a manual method because the tails of these galaxies are characterized by very disturbed and peculiar morphologies, which are not easily fitted using an automated process. When possible, I used the same curves fitted in Bellhouse et al. (2021), adding new ones where necessary. Finally, for each sub-tail, clumps are projected onto their spiral arm, and their distances are computed from these points to the zero-point, defined as the projection of the first clump of the

[1]We point out that the deprojection cannot take into account the vertical distance of the clumps in the tails from the plane of the disk, as the distance among the tail clumps and between the clumps and the galaxy cannot be recovered.

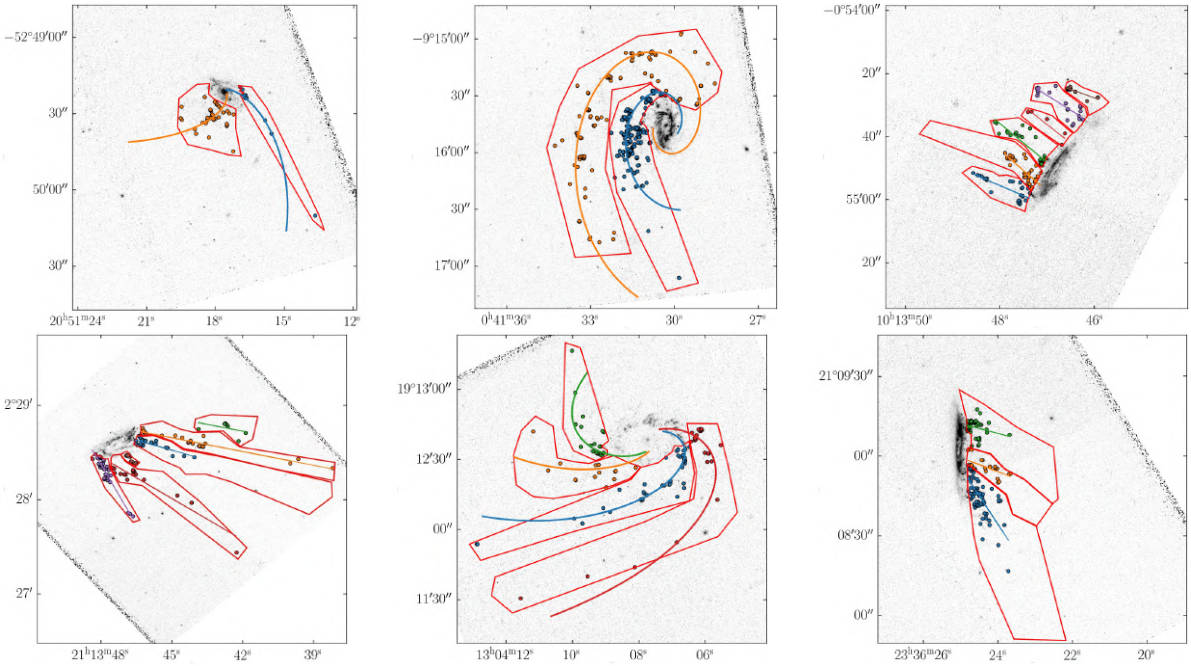

Figure A.1: F275W maps of the six galaxies of our sample. Top row (from left to right): JO175, JO201, JO204; bottom row: (from left to right): JO206, JW39, JW100. In different colors I plot the sub-tails I defined for each galaxy: the dots are the UV-selected clumps I used to trace the regions (solid, closed regions) defining the sub-tails; the best-fitting trajectories of the sub-tails are plotted as solid lines (as straight lines or spiral arms, according to the choice made in Section A). The red dots are the zero-points of the sub-tails, from which the distances of the clumps along the sub-tails are computed. Each sub-tail is flagged with a number.

sub-tail. This definition is adopted for JO175, JO201 and JW39 (i. e. the nearly face-on galaxies).

The distances are then converted in kpc according to the redshift of the galaxy cluster.

The sub-tails are adopted to re-compute the tilt angles of clumps and complexes (Section 5.3.2) and the trends with the distance in Section 5.4. Note that, using only clumps included in sub-tails, this sample has no disk clumps and just a fraction of the extraplanar clumps (6 in Hα, 21 in UV). In Figure A.2 I show the tilt angle distribution of clumps and complexes along the direction defined by the sub-tails. By comparing this plot with the corresponding one in Section 5.3.2 (Figure 5.9), no major differences are observed, especially considering the poor statistics available for the extraplanar clumps. The only hint of a difference is in the complex distribution: even if the median value is still consistent with 45°, the distribution is less flat than in Figure 5.9, with an over-abundance of complexes at low values, meaning that they are particularly well aligned to the sub-tail direction.

Figure A.3 shows the cumulative distribution of clumps and complexes as a function of the sub-tail distance. The corresponding plot of Section 5.4, obtained for the projected galactocentric distance (Figure 5.10), shows a trend according to which Hα clumps are typically closer to the galactic disk than UV clumps, with optical complexes even further away than UV clumps. This trend is completely lost with the sub-tail distance; even if the cumulative distribution may suggest that Hα clumps are still located at slightly smaller

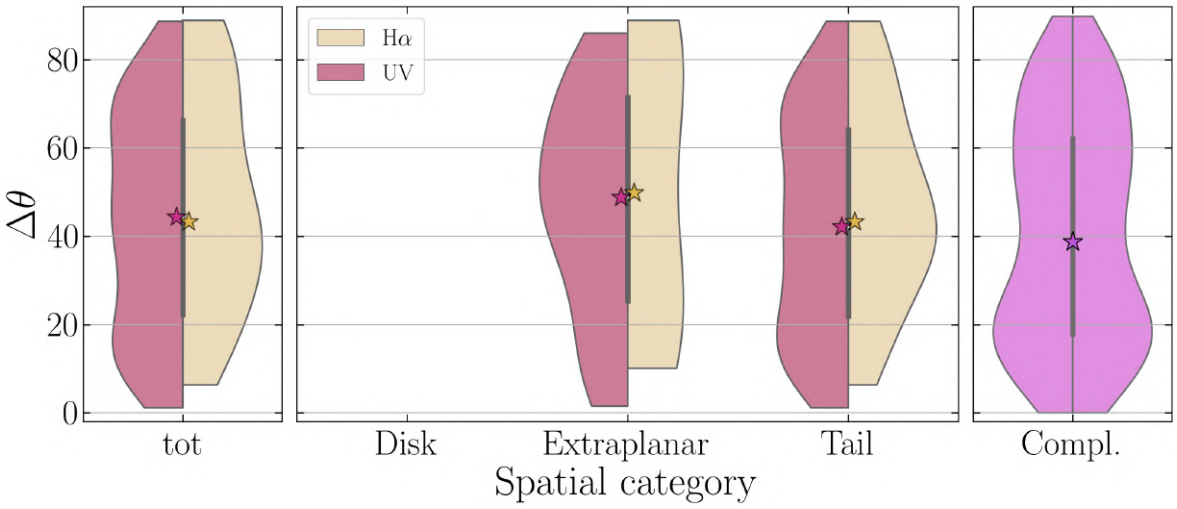

Figure A.2: Same as Figure 5.9, but for tilt angle distributions of resolved clumps and complexes computed with along the local direction of the sub-tail.

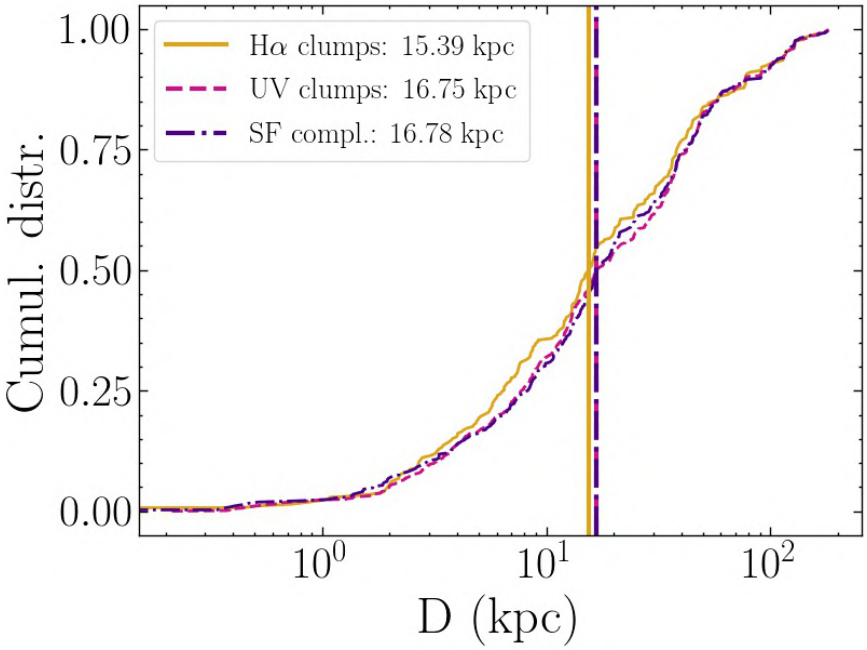

Figure A.3: Same as Figure 5.10, but the distance is computed along the sub-tails.

distances than UV clumps and optical complexes, the median values are indistinguishable. Furthermore, UV clump and optical complex distributions are almost perfectly overlapped along the whole distance interval.

In Figures A.4 and A.5 I show the trends with the sub-tail distance of the properties of clumps and complexes. The former includes the optical luminosity L_{F606W}, the Hα-to-UV ratio Hα/UV, the area of the clump/complex A and the axial ratio AR (all defined in Section 3.4.1). The latter shows the properties of the complexes in relation to those of the clumps nested inside them: the number of clumps, the filling factor f_{A}, the radius of the brightest resolved clump r_{bc} (all defined in Section 3.4.2) and the center displacements Δ (Section 5.3.1). By comparing these plots with the corresponding ones (Figures 5.11 and

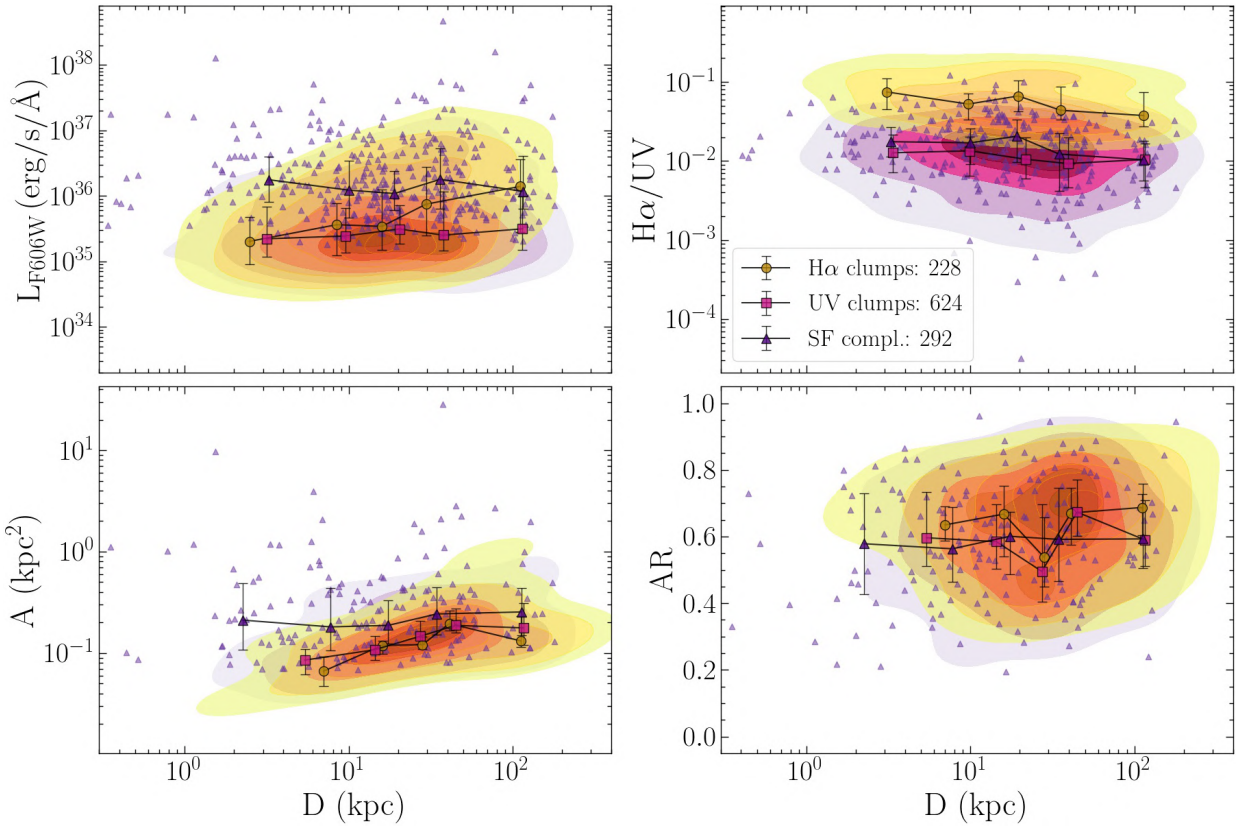

Figure A.4: Same as Figure 5.11, but the distance is computed along the sub-tails.

5.12) in Section 5.4, computed adopting the projected galactocentric distance, no striking differences are observed. The only negligible variations one can notice are in the trends of f_A, which gets slightly flatter, and of r_{bc}, which is slightly steeper.

Therefore I can conclude that computing tilt angles and distances with respect to this set sub-tails, defined according to the spatial distribution of the *HST* clumps and to the MUSE kinematics of the ionized gas, do not introduce any improvement in the observed trends, still probably highly affected by projection effects.

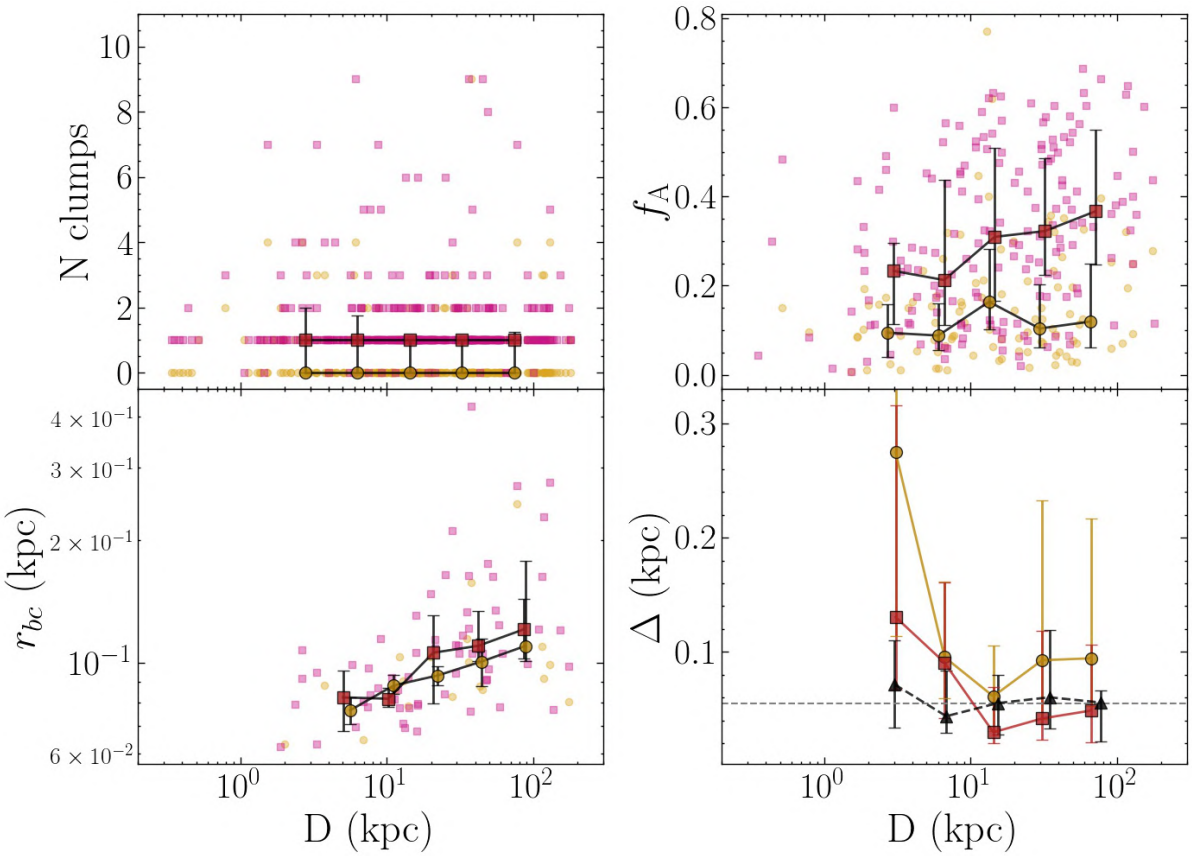

Figure A.5: Same as Figure 5.12, but the distance is computed along the sub-tails.

Bibliography

Abadi M. G., Moore B., Bower R. G., 1999, MNRAS, 308, 947

Abramson A., Kenney J. D. P., 2014, AJ, 147, 63

Abruzzo M. W., Bryan G. L., Fielding D. B., 2022, ApJ, 925, 199

Adamo A. et al., 2017, ApJ, 841, 131

Akerman N., Tonnesen S., Poggianti B. M., Smith R., Marasco A., 2023a, ApJ, 948, 18

Akerman N., Tonnesen S., Poggianti B. M., Smith R., Marasco A., Kulier A., Müller A., Vulcani B., 2023b, MNRAS

Alstott J., Bullmore E., Plenz D., 2014, PLoS ONE, 9, e85777

and A. M. Price-Whelan et al., 2018, The Astronomical Journal, 156, 123

Anglés-Alcázar D., Faucher-Giguère C.-A., Kereš D., Hopkins P. F., Quataert E., Murray N., 2017, MNRAS, 470, 4698

Arsenault R., Roy J. R., 1988, A&A, 201, 199

Audit E., Hennebelle P., 2010, A&A, 511, A76

Bacchini C., Fraternali F., Iorio G., Pezzulli G., 2019, A&A, 622, A64

Bacchini C. et al., 2023, ApJ, 950, 24

Bacon R. et al., 2010, in Ground-based and Airborne Instrumentation for Astronomy III, McLean I. S., Ramsay S. K., Takami H., eds., Vol. 7735, International Society for Optics and Photonics, SPIE, pp. 131 – 139

Baldwin J. A., Phillips M. M., Terlevich R., 1981, PASP, 93, 5

Balogh M. L., Navarro J. F., Morris S. L., 2000, ApJ, 540, 113

Bartolini C. et al., 2022, ApJ, 936, 74

Bastian N. et al., 2012, MNRAS, 419, 2606

Bastian N., Ercolano B., Gieles M., Rosolowsky E., Scheepmaker R. A., Gutermuth R., Efremov Y., 2007, MNRAS, 379, 1302

Beckman J. E., Rozas M., Zurita A., Watson R. A., Knapen J. H., 2000, AJ, 119, 2728

Bekki K., Couch W. J., 2003, The Astrophysical Journal, 596, L13

Bellhouse C. et al., 2017, ApJ, 844, 49

Bellhouse C. et al., 2019, MNRAS, 485, 1157

Bellhouse C. et al., 2021, MNRAS, 500, 1285

Biviano A. et al., 2017, A&A, 607, A81

Blanton M. R., Eisenstein D., Hogg D. W., Schlegel D. J., Brinkmann J., 2005, The Astrophysical Journal, 629, 143

Borissova J., Kurtev R., Georgiev L., Rosado M., 2004, A&A, 413, 889

Boselli A., Cortese L., Boquien M., Boissier S., Catinella B., Gavazzi G., Lagos C., Saintonge A., 2014, A&A, 564, A67

Boselli A. et al., 2018, A&A, 614, A56

Boselli A. et al., 2020, A&A, 634, L1

Boselli A., Fossati M., Sun M., 2022, A&ARv, 30, 3

Boselli A., Gavazzi G., 2006, PASP, 118, 517

Boselli A., Gavazzi G., 2014, A&ARv, 22, 74

Boselli A. et al., 2021, A&A, 646, A139

Bouché N. et al., 2010, ApJ, 718, 1001

Bournaud F., Elmegreen B. G., Elmegreen D. M., 2007, The Astrophysical Journal, 670, 237

Bournaud F. et al., 2013, The Astrophysical Journal, 780, 57

Bresolin F. et al., 1998, AJ, 116, 119

Bresolin F., Kennicutt, Robert C. J., Stetson P. B., 1996, AJ, 112, 1009

Bressert E. et al., 2010, MNRAS, 409, L54

Brinchmann J., Charlot S., White S. D. M., Tremonti C., Kauffmann G., Heckman T., Brinkmann J., 2004, MNRAS, 351, 1151

Bruevich V. V., Gusev A. S., Guslyakova S. A., 2011, Astronomy Reports, 55, 310

Bruzual G., Charlot S., 2003, MNRAS, 344, 1000

Byrd G., Valtonen M., 1990, ApJ, 350, 89

Calzetti D. et al., 2015, AJ, 149, 51

Campitiello M. G. et al., 2021, ApJ, 911, 144

Canning R. E. A. et al., 2014, MNRAS, 444, 336

Cardelli J. A., Clayton G. C., Mathis J. S., 1989, ApJ, 345, 245

Carnall A. C., Leja J., Johnson B. D., McLure R. J., Dunlop J. S., Conroy C., 2019, ApJ, 873, 44

Carnall A. C., McLure R. J., Dunlop J. S., Davé R., 2018, MNRAS

Casertano S. et al., 2000, AJ, 120, 2747

Catinella B. et al., 2013, Monthly Notices of the Royal Astronomical Society, 436, 34

Cava A. et al., 2009, A&A, 495, 707

Cava A., Schaerer D., Richard J., Pérez-González P. G., Dessauges-Zavadsky M., Mayer L., Tamburello V., 2018, Nature Astronomy, 2, 76

Cavaliere A., Fusco-Femiano R., 1976, A&A, 49, 137

Ceverino D., Dekel A., Bournaud F., 2010, Monthly Notices of the Royal Astronomical Society, 404, 2151

Chabrier G., 2003, PASP, 115, 763

Chevance M. et al., 2021, Monthly Notices of the Royal Astronomical Society, 509, 272

Christensen C. R., Davé R., Governato F., Pontzen A., Brooks A., Munshi F., Quinn T., Wadsley J., 2016, ApJ, 824, 57

Clauset A., Shalizi C. R., Newman M. E. J., 2009, SIAM Review, 51, 661

Cole S., Lacey C. G., Baugh C. M., Frenk C. S., 2000, MNRAS, 319, 168

Conselice C. J. et al., 2004, The Astrophysical Journal, 600, L139

Consolandi G., Gavazzi G., Fossati M., Fumagalli M., Boselli A., Yagi M., Yoshida M., 2017, A&A, 606, A83

Cook D. O., Dale D. A., Lee J. C., Thilker D., Calzetti D., Kennicutt R. C., 2016, MNRAS, 462, 3766

Cortese L., Catinella B., Smith R., 2021, Publ. Astron. Soc. Australia, 38, e035

Cortese L. et al., 2007, MNRAS, 376, 157

Cosens M. et al., 2018, ApJ, 869, 11

Cowie L. L., Songaila A., 1977, Nature, 266, 501

Cowie L. L., Songaila A., Hu E. M., Cohen J. G., 1996, AJ, 112, 839

Cox A. N., Becker S. A., Pesnell W. D., 2000, in Allen's Astrophysical Quantities, Cox A. N., ed., p. 499

Cramer W. J., Kenney J. D. P., Sun M., Crowl H., Yagi M., Jáchym P., Roediger E., Waldron W., 2019, ApJ, 870, 63

Daddi E. et al., 2007, ApJ, 670, 156

Davé R., Finlator K., Oppenheimer B. D., 2012, MNRAS, 421, 98

Davies R. et al., 2020, MNRAS, 498, 4150

de Grijs R., Anders P., 2006, MNRAS, 366, 295

de Grijs R., Anders P., Bastian N., Lynds R., Lamers H. J. G. L. M., O'Neil E. J., 2003, MNRAS, 343, 1285

De Lucia G., Blaizot J., 2007, MNRAS, 375, 2

De Lucia G., Springel V., White S. D. M., Croton D., Kauffmann G., 2006, MNRAS, 366, 499

Deb T. et al., 2020, MNRAS, 494, 5029

Dessauges-Zavadsky M., Adamo A., 2018, MNRAS, 479, L118

Dessauges-Zavadsky M., Schaerer D., Cava A., Mayer L., Tamburello V., 2017, The Astrophysical Journal Letters, 836, L22

Dressler A., 1980, ApJ, 236, 351

Dressler A. et al., 1997, ApJ, 490, 577

Dutton A. A., van den Bosch F. C., Dekel A., 2010, MNRAS, 405, 1690

Elbaz D. et al., 2007, A&A, 468, 33

Elmegreen B. G., 2002, ApJ, 564, 773

Elmegreen B. G., 2006, ApJ, 648, 572

Elmegreen B. G., Bournaud F., Elmegreen D. M., 2008, The Astrophysical Journal, 688, 67

Elmegreen B. G., Elmegreen D. M., 2005, The Astrophysical Journal, 627, 632

Elmegreen B. G., Elmegreen D. M., Fernandez M. X., Lemonias J. J., 2009, The Astrophysical Journal, 692, 12

Elmegreen B. G., Falgarone E., 1996, ApJ, 471, 816

Elmegreen D. M. et al., 2014, The Astrophysical Journal, 787, L15

Elmegreen D. M., Elmegreen B. G., Ravindranath S., Coe D. A., 2007, ApJ, 658, 763

Faber S. M., Trager S. C., Gonzalez J. J., Worthey G., 1995, in Stellar Populations, van der Kruit P. C., Gilmore G., eds., Vol. 164, p. 249

Farrens S. et al., 2020, Astronomy and Computing, 32, 100402

Fensch J., Bournaud F., Brucy N., Dubois Y., Hennebelle P., Rosdahl J., 2023, A&A, 672, A193

Ferland G. J. et al., 2017, Rev. Mex. Astron. Astrofis., 53, 385

Ferrière K. M., 2001, Reviews of Modern Physics, 73, 1031

Fisher D. B. et al., 2017, The Astrophysical Journal Letters, 839, L5

Fisher D. B. et al., 2017, MNRAS, 464, 491

Foreman-Mackey D., Hogg D. W., Lang D., Goodman J., 2013, PASP, 125, 306

Förster Schreiber N. M. et al., 2011, ApJ, 739, 45

Fossati M., Fumagalli M., Boselli A., Gavazzi G., Sun M., Wilman D. J., 2016, MNRAS, 455, 2028

Franchetto A. et al., 2021, ApJ, 922, L6

Franchetto A. et al., 2020, ApJ, 895, 106

Fritz J. et al., 2017, ApJ, 848, 132

Fujii M. S., Portegies Zwart S., 2015, MNRAS, 449, 726

Fujita S. S. et al., 2003, The Astrophysical Journal, 586, L115

Fumagalli M., Krumholz M. R., Prochaska J. X., Gavazzi G., Boselli A., 2009, The Astrophysical Journal, 697, 1811

Gabor J. M., Bournaud F., 2013, Monthly Notices of the Royal Astronomical Society, 434, 606

Gallagher J. S., Hunter D. A., 1983, ApJ, 274, 141

Gamow G., 1938, Physical Review, 53, 595

Gavazzi G., Cortese L., Boselli A., Iglesias-Paramo J., Vílchez J. M., Carrasco L., 2003, The Astrophysical Journal, 597, 210

Genel S. et al., 2011, The Astrophysical Journal, 745, 11

Genzel R. et al., 2008, The Astrophysical Journal, 687, 59

Genzel R. et al., 2011, The Astrophysical Journal, 733, 101

George K. et al., 2019, MNRAS, 487, 3102

George K. et al., 2018, Monthly Notices of the Royal Astronomical Society, 479, 4126

George K. et al., 2023, MNRAS, 519, 2426

Gieles M., 2009, Ap&SS, 324, 299

Gieles M., Larsen S. S., Scheepmaker R. A., Bastian N., Haas M. R., Lamers H. J. G. L. M., 2006, A&A, 446, L9

Giunchi E. et al., 2023a, ApJ, 949, 72

Giunchi E. et al., 2023b, ApJ, 958, 73

Göller J., Joshi G., Rohr E., Zinger E., Pillepich A., 2023, arXiv e-prints, arXiv:2304.09199

Gonzaga S., Hack W., Fruchter A., Mack J., 2012, The DrizzlePac Handbook

Goto T., Yamauchi C., Fujita Y., Okamura S., Sekiguchi M., Smail I., Bernardi M., Gomez P. L., 2003, Monthly Notices of the Royal Astronomical Society, 346, 601

Gouliermis D. A. et al., 2017, Monthly Notices of the Royal Astronomical Society, 468, 509

Gouliermis D. A., Schmeja S., Klessen R. S., de Blok W. J. G., Walter F., 2010, ApJ, 725, 1717

Gouliermis D. A. et al., 2015, MNRAS, 452, 3508

Grasha K. et al., 2017, ApJ, 842, 25

Green A. W. et al., 2013, Monthly Notices of the Royal Astronomical Society, 437, 1070

Gronke M., Oh S. P., 2018, MNRAS, 480, L111

Gullieuszik M. et al., 2023, ApJ, 945, 54

Gullieuszik M. et al., 2020, ApJ, 899, 13

Gullieuszik M. et al., 2017, ApJ, 846, 27

Gunn J. E., Gott, J. Richard I., 1972, ApJ, 176, 1

Guo Y., Giavalisco M., Ferguson H. C., Cassata P., Koekemoer A. M., 2012, The Astrophysical Journal, 757, 120

Guo Y. et al., 2018, ApJ, 853, 108

Gusev A. S., 2002, Astronomical and Astrophysical Transactions, 21, 75

Gusev A. S., 2014, MNRAS, 442, 3711

Gómez P. L. et al., 2003, The Astrophysical Journal, 584, 210

Haas M. R., Gieles M., Scheepmaker R. A., Larsen S. S., Lamers H. J. G. L. M., 2008, A&A, 487, 937

Haydon D. T., Kruijssen J. M. D., Chevance M., Hygate A. P. S., Krumholz M. R., Schruba A., Longmore S. N., 2020, MNRAS, 498, 235

Haynes M. P., Giovanelli R., 1984, AJ, 89, 758

Hennebelle P., Audit E., 2007, A&A, 465, 431

Hopkins P. F., Kereš D., Murray N., Quataert E., Hernquist L., 2012, Monthly Notices of the Royal Astronomical Society, 427, 968

Hubble E. P., 1926, ApJ, 64, 321

Hubble E. P., 1936, Realm of the Nebulae

Humphreys R. M., Davidson K., 1979, ApJ, 232, 409

Hunter D. A., Elmegreen B. G., Dupuy T. J., Mortonson M., 2003, AJ, 126, 1836

Iben I., Renzini A., 1984, Phys. Rep., 105, 329

Iben, Icko J., 1965, ApJ, 141, 993

Ignesti A. et al., 2023, ApJ, 956, 122

Ignesti A. et al., 2022a, ApJ, 937, 58

Ignesti A. et al., 2022b, ApJ, 924, 64

Iodice E. et al., 2021, A&A, 652, L11

Jáchym P. et al., 2017, ApJ, 839, 114

Jaffé Y. L. et al., 2018, MNRAS, 476, 4753

Jeans J. H., 1902, Philosophical Transactions of the Royal Society of London. Series A, Containing Papers of a Mathematical or Physical Character, 199, 1

Johnson T. L. et al., 2017, ApJ, 843, L21

Jones T. A., Swinbank A. M., Ellis R. S., Richard J., Stark D. P., 2010, Monthly Notices of the Royal Astronomical Society, 404, 1247

Jáchym P. et al., 2019, The Astrophysical Journal, 883, 145

Kapferer W., Sluka C., Schindler S., Ferrari C., Ziegler B., 2009, A&A, 499, 87

Kauffmann G. et al., 2003, MNRAS, 346, 1055

Kauffmann G., White S. D. M., Guiderdoni B., 1993, MNRAS, 264, 201

Kawata D., Mulchaey J. S., 2008, ApJ, 672, L103

Keel W. C. et al., 2015, AJ, 149, 155

Kelly B. C., 2007, ApJ, 665, 1489

Kenney J. D. P., Abramson A., Bravo-Alfaro H., 2015, AJ, 150, 59

Kenney J. D. P., Geha M., Jáchym P., Crowl H. H., Dague W., Chung A., van Gorkom J., Vollmer B., 2014, ApJ, 780, 119

Kennicutt, Robert C. J., 1998, ARA&A, 36, 189

Kennicutt, Robert C. J. et al., 2003, PASP, 115, 928

Kennicutt, Robert C. J., Edgar B. K., Hodge P. W., 1989, ApJ, 337, 761

Kennicutt R. C., Evans N. J., 2012, ARA&A, 50, 531

Kennicutt R. C., Hodge P. W., 1980, ApJ, 241, 573

Kewley L. J., Heisler C. A., Dopita M. A., Lumsden S., 2001, ApJS, 132, 37

Kim J. et al., 2022, Monthly Notices of the Royal Astronomical Society, 516, 3006

Klaus A., Yu S., Plenz D., 2011, PLoS ONE, 6, e19779

Koopmann R. A., Kenney J. D. P., 2004, ApJ, 613, 866

Kormendy J., Bender R., 2012, ApJS, 198, 2

Krist J. E., Hook R. N., Stoehr F., 2011, in Society of Photo-Optical Instrumentation Engineers (SPIE) Conference Series, Vol. 8127, Optical Modeling and Performance Predictions

V, Kahan M. A., ed., p. 81270J

Kroupa P., 2001, MNRAS, 322, 231

Kroupa P., Weidner C., 2003, ApJ, 598, 1076

Kruijssen J. M. D., Longmore S. N., 2014, Monthly Notices of the Royal Astronomical Society, 439, 3239

Kruijssen J. M. D. et al., 2019, Nature, 569, 519

Kruijssen J. M. D., Schruba A., Hygate A. P. S., Hu C.-Y., Haydon D. T., Longmore S. N., 2018, Monthly Notices of the Royal Astronomical Society, 479, 1866

Krumholz M. R., Dekel A., 2012, ApJ, 753, 16

Kulier A. et al., 2023, ApJ, 954, 177

Lada C. J., Lada E. A., 2003, ARA&A, 41, 57

Laganá T. F., Martinet N., Durret F., Lima Neto G. B., Maughan B., Zhang Y. Y., 2013, A&A, 555, A66

Larsen S. S., 2002, AJ, 124, 1393

Larson R. B., Tinsley B. M., Caldwell C. N., 1980, ApJ, 237, 692

Lee J. C. et al., 2022, ApJS, 258, 10

Lee J. H., Hwang N., Lee M. G., 2011, The Astrophysical Journal, 735, 75

Leisawitz D. et al., 2019, in Society of Photo-Optical Instrumentation Engineers (SPIE) Conference Series, Vol. 11115, UV/Optical/IR Space Telescopes and Instruments: Innovative Technologies and Concepts IX, Barto A. A., Breckinridge J. B., Stahl H. P., eds., p. 111150Q

Lelli F., Duc P.-A., Brinks E., McGaugh S. S., 2015, Galaxies, 3, 184

Lewis I. et al., 2002, MNRAS, 334, 673

Liu G., Calzetti D., Kennicutt, Robert C. J., Schinnerer E., Sofue Y., Komugi S., Egusa F., Scoville N. Z., 2013, ApJ, 772, 27

Livermore R. C. et al., 2012, MNRAS, 427, 688

Lourenço A. C. C. et al., 2023, MNRAS, 526, 4831

Luber N. et al., 2022, ApJ, 927, 39

Ma J., Maksym W. P., Fabbiano G., Elvis M., Storchi-Bergmann T., Karovska M., Wang J., Travascio A., 2021, ApJ, 908, 155

MacKenty J. W., Maíz-Apellániz J., Pickens C. E., Norman C. A., Walborn N. R., 2000, AJ, 120, 3007

Magnier E. A. et al., 1993, A&A, 278, 36

Mandelker N., Dekel A., Ceverino D., Tweed D., Moody C. E., Primack J., 2014, Monthly Notices of the Royal Astronomical Society, 443, 3675

Mascoop J. L., Anderson L. D., Wenger T. V., Makai Z., Armentrout W. P., Balser D. S., Bania T. M., 2021, ApJ, 910, 159

Merluzzi P. et al., 2013, MNRAS, 429, 1747

Merritt D., 1983, ApJ, 264, 24

Messa M. et al., 2018, MNRAS, 477, 1683

Messa M., Adamo A., Östlin G., Melinder J., Hayes M., Bridge J. S., Cannon J., 2019, MNRAS, 487, 4238

Messa M. et al., 2017, Monthly Notices of the Royal Astronomical Society, 473, 996

Meštrić U. et al., 2022, arXiv e-prints, arXiv:2202.09377

Mo H., van den Bosch F. C., White S., 2010, Galaxy Formation and Evolution

Monreal-Ibero, A., Colina, L., Arribas, S., García-Marín, M., 2007, A&A, 472, 421

Moore B., Katz N., Lake G., Dressler A., Oemler A., 1996, Nature, 379, 613

Moore B., Lake G., Katz N., 1998, ApJ, 495, 139

Moretti A. et al., 2018, Monthly Notices of the Royal Astronomical Society, 480, 2508

Moretti A. et al., 2020, ApJ, 889, 9

Müller A. et al., 2021, Nature Astronomy, 5, 159

Murata K. L. et al., 2014, The Astrophysical Journal, 786, 15

Murray N., Quataert E., Thompson T. A., 2009, The Astrophysical Journal, 709, 191

Nath B. B., Das P., Oey M. S., 2020, MNRAS, 493, 1034

Noeske K. G. et al., 2007, ApJ, 660, L43

Oemler, Augustus J., 1974, ApJ, 194, 1

Oklopčić A., Hopkins P. F., Feldmann R., Kereš D., Faucher-Giguère C.-A., Murray N., 2016, Monthly Notices of the Royal Astronomical Society, 465, 952

Osterbrock D. E., 1989, Astrophysics of gaseous nebulae and active galactic nuclei

Ostriker E. C., Shetty R., 2011, The Astrophysical Journal, 731, 41

Owers M. S. et al., 2019, ApJ, 873, 52

Pannella M. et al., 2015, ApJ, 807, 141

Peluso G., Radovich M., Moretti A., Mingozzi M., Vulcani B., Poggianti B. M., Marasco A., Gullieuszik M., 2023, ApJ, 958, 147

Peluso G. et al., 2022, ApJ, 927, 130

Peng Y.-j. et al., 2010, ApJ, 721, 193

Pietrzyński G., Gieren W., Fouqué P., Pont F., 2001, A&A, 371, 497

Pietrzyński G., Ulaczyk K., Gieren W., Bresolin F., Kudritzki R. P., 2005, A&A, 440, 783

Ploeckinger S., Sharma K., Schaye J., Crain R. A., Schaller M., Barber C., 2018, MNRAS, 474, 580

Poggianti B. M. et al., 2016, AJ, 151, 78

Poggianti B. M. et al., 2019, MNRAS, 482, 4466

Poggianti B. M. et al., 2019, The Astrophysical Journal, 887, 155

Poggianti B. M. et al., 2017a, Nature, 548, 304

Poggianti B. M. et al., 2017b, ApJ, 844, 48

Portegies Zwart S. F., McMillan S. L. W., Gieles M., 2010, ARA&A, 48, 431

Posti L., Fraternali F., Di Teodoro E. M., Pezzulli G., 2018, A&A, 612, L6

Postman M. et al., 2005, ApJ, 623, 721

Postman M., Geller M. J., 1984, ApJ, 281, 95

Radovich M., Poggianti B., Jaffé Y. L., Moretti A., Bettoni D., Gullieuszik M., Vulcani B., Fritz J., 2019, MNRAS, 486, 486

Ramatsoku M. et al., 2020, A&A, 640, A22

Ramatsoku M. et al., 2019, MNRAS, 487, 4580

Rasera Y., Teyssier R., 2006, A&A, 445, 1

Rodruck M. et al., 2023, MNRAS, 526, 2341

Roediger E., Bruggen M., Owers M. S., Ebeling H., Sun M., 2014, MNRAS, 443, L114

Rozas M., Richer M. G., López J. A., Relaño M., Beckman J. E., 2006, A&A, 455, 539

Salaris M., Cassisi S., 2005, Evolution of Stars and Stellar Populations

Salim S. et al., 2007, ApJS, 173, 267

Salpeter E. E., 1955, ApJ, 121, 161

Sanchez-Garcia O. et al., 2023, arXiv e-prints, arXiv:2301.06612

Sancisi R., Fraternali F., Oosterloo T., van der Hulst T., 2008, A&ARv, 15, 189

Santoro F. et al., 2022, A&A, 658, A188

Sarazin C. L., 1986, Reviews of Modern Physics, 58, 1

Schlafly E. F., Finkbeiner D. P., 2011, ApJ, 737, 103

Schlegel D. J., Finkbeiner D. P., Davis M., 1998, ApJ, 500, 525

Schneider P., 2015, Extragalactic Astronomy and Cosmology: An Introduction

Semelin B., Combes F., 2005, A&A, 441, 55

Sharp R. G., Bland-Hawthorn J., 2010, ApJ, 711, 818

Shibuya T., Ouchi M., Kubo M., Harikane Y., 2016, The Astrophysical Journal, 821, 72

Smith R. et al., 2022, ApJ, 934, 86

Smith R. J. et al., 2010, MNRAS, 408, 1417

Solanes J. M., Manrique A., García-Gómez C., González-Casado G., Giovanelli R., Haynes M. P., 2001, The Astrophysical Journal, 548, 97

Speagle J. S., Steinhardt C. L., Capak P. L., Silverman J. D., 2014, ApJS, 214, 15

Storey P. J., Zeippen C. J., 2000, MNRAS, 312, 813

Stroemgren B., 1933, Publikationer og mindre Meddeler fra Kobenhavns Observatorium, 86, 1

Strömgren B., 1939, ApJ, 89, 526

STScI Development Team, 2020, stsynphot: synphot for HST and JWST

Sun M. et al., 2021, Nature Astronomy, 6, 270

Tadaki K., Kodama T., Tanaka I., Hayashi M., Koyama Y., Shimakawa R., 2013, The Astrophysical Journal, 780, 77

Tamburello V., Mayer L., Shen S., Wadsley J., 2015, Monthly Notices of the Royal Astronomical Society, 453, 2490

Tan B., Oh S. P., Gronke M., 2022, arXiv e-prints, arXiv:2210.06493
Tomičić N. et al., 2021a, ApJ, 907, 22
Tomičić N. et al., 2021b, ApJ, 922, 131
Tomičić N. et al., 2018, The Astrophysical Journal Letters, 869, L38
Tonnesen S., 2019, ApJ, 874, 161
Tonnesen S., Bryan G. L., 2010, ApJ, 709, 1203
Tonnesen S., Bryan G. L., 2012, MNRAS, 422, 1609
Toomre A., Toomre J., 1972, ApJ, 178, 623
van der Walt S. et al., 2014, PeerJ
Venemans B. P. et al., 2005, A&A, 431, 793
Vulcani B. et al., 2020a, ApJ, 892, 146
Vulcani B. et al., 2018, ApJ, 866, L25
Vulcani B. et al., 2021, ApJ, 914, 27
Vulcani B. et al., 2019, MNRAS, 488, 1597
Vulcani B. et al., 2020b, ApJ, 899, 98
Waldron W. et al., 2023, MNRAS, 522, 173
Werle A. et al., 2023, arXiv e-prints, arXiv:2312.06879
Werle A. et al., 2022, ApJ, 930, 43
Whitaker K. E. et al., 2014, ApJ, 795, 104
White S. D. M., Frenk C. S., 1991, ApJ, 379, 52
Whitmore B. C., Chandar R., Bowers A. S., Larsen S., Lindsay K., Ansari A., Evans J., 2014, AJ, 147, 78
Whitmore B. C., Gilmore D. M., Jones C., 1993, ApJ, 407, 489
Wisnioski E., Glazebrook K., Blake C., Poole G. B., Green A. W., Wyder T., Martin C., 2012, MNRAS, 422, 3339
Wisnioski E. et al., 2011, Monthly Notices of the Royal Astronomical Society, 417, 2601
Wuyts S. et al., 2012, The Astrophysical Journal, 753, 114
Yan H. et al., 2023, ApJS, 269, 43
Yoshida M., Yagi M., Komiyama Y., Furusawa H., Kashikawa N., Hattori T., Okamura S., 2012, ApJ, 749, 43
Yoshida M. et al., 2008, ApJ, 688, 918
Zanella A. et al., 2015, Nature, 521, 54
Zanella A. et al., 2019, MNRAS, 489, 2792
Zhang Q., Fall S. M., 1999, ApJ, 527, L81